PHASE BASED GUIDED WAVE METHODS FOR DAMAGE MAPPING IN MULTILAYERED STRUCTURES

A Dissertation
Presented to
The Academic Faculty

By

Aaron Darnton

In Partial Fulfillment
of the Requirements for the Degree
Doctor of Philosophy in the
George W. Woodruff School of Mechanical Engineering

Georgia Institute of Technology

December 2016

PHASE BASED GUIDED WAVE METHODS FOR DAMAGE MAPPING IN MULTILAYERED STRUCTURES

Approved by:

Dr. Massimo Ruzzene, Advisor
School of Aerospace Engineering
School of Mechanical Engineering
Georgia Institute of Technology

Dr. Karim Sabra
School of Mechanical Engineering
Georgia Institute of Technology

Dr. Michael Leamy
School of Mechanical Engineering
Georgia Institute of Technology

Dr. Jennifer Michaels
School of Electrical and Computer Engineering
Georgia Institute of Technology

Dr. Andrew Hull
Undersea Warfare Weapons, Vehicles and Defensive Systems Department
Naval Undersea Warfare Center, Division Newport

Date Approved: 16 August 2016

ACKNOWLEDGEMENTS

First and foremost, I would like to thank my adviser Dr. Massimo Ruzzene. His counsel and guidance was critical to this work as well as my education, professional development and personal growth.

To my committee members, Dr. Karim Sabra, Dr. Michael Leamy, Dr. Jennifer Michaels, and Dr. Andrew Hull, I am especially grateful for your time and input to this work. Beyond that, I have spent time with all of you outside of your participation on my committee, either through coursework, conferences or collaborative work; I have enjoyed these interactions and consider them important parts of my professional and personal development.

My attendance at the Georgia Institute of Technology would not have been possible without the support of Kevin Kerstetter, Glenn Payette, Tim Krell, Doug Ray and Neil Dubois. I thank you all for supporting me in my endeavor to return to school.

To my lab mates, Olivier and Marshall, the conversation and comradery were critical to the survival aspect of graduate studies. I would also like to thank Hannah, Giuseppe, William, Matteo, Raj, and Guglielmo.

Thank you to my family; you have been a tremendous source of support. In particular, to my wife Kim, your unshaking willingness to support this adventure cannot be understated. For that, I am forever grateful.

And to our new son Hudson, you are an endless source of encouragement.

Thank you,

TABLE OF CONTENTS

LIST OF TABLES

LIST OF FIGURES

SUMMARY

This thesis presents two novel methods for mapping damage in plates along with a concept for optical acquisition of guided waves in plates. These contributions directly tackle challenges with fielding guided wave methods for use in Non-Destructive Evaluation. Non-Destructive Evaluation's core purpose is to assess the integrity of a system or component without destroying it. There are a bevy of approaches for doing so. In the case of large plate-like structures such as the skin of an aircraft or superstructure of ship, guided waves offer unique advantages to other methods. First, they propagate over long distances, making them suitable for big structures. Second, they are dependent on both geometrical and material properties of the plate. This makes them sensitive to a wide range of defects including cracks, delaminations and porosity that occur below the surface of the plate and thus are not visible to an observer.

For a variety of reasons, guided wave techniques are rarely used in practice. The first challenge is the difficulty in acquiring the data. Measurement of the full wavefield typically requires a Scanning Laser Doppler Vibrometer or a scanning ultrasonic receiver. Neither of these approaches is well suited to field use. The second challenge is that many guided wave methods make use of models or baseline measurements that are sensitive to environmental changes and changes in boundary condition, making it difficult to use baseline measurements or models.

This work will approach both of these difficulties. First, the methods developed will minimize the use of models and exclude the use of baseline measurements. The Two-Dimensional Phase Gradient method utilizes the linear relationship between phase and space to trace reflected waves back to the damage. It is shown to be effective for identifying and mapping cracks. The second method, the Phase Congruency for Damage Mapping method utilizes complex components of a signal decomposition to locate damage. It is successful at mapping a wider range of

characteristics including delaminations, geometrical changes in the sample, mass additions and impact damage in addition to cracks. These methods improve robustness by excluding baseline measurement and limiting the use of models as well as increase the level of information available to a Non-Destructive Evaluation practitioner by developing a map of damage rather than simple detecting and locating the damage.

The second main contribution of this work is a framework for a novel optical method for acquiring guided wave signals in plates. This preliminary investigation shows that high speed cameras are capable of capturing full guided wave fields in far less time than a comparable Scanning Laser Doppler Vibrometer acquisition. The method is developed and demonstrated on three samples: an isotropic, quasi-isotropic and orthotropic plate. Analysis of the captured data revealed that the guided wave was in fact captured although at very low signal to noise ratios. The framework presented in this thesis demonstrates the feasibility of such a method.

The work presented on wavefield analysis improves robustness by not utilizing models or baselines in either method. Second, these methods map damage as opposed to just locating damage thus increasing the information extracted from the data. The framework for optical acquisition provides a path for greatly reducing the acquisition time for guided wave wavefields. Both of these contributions are important steps on the path to developing robust guided wave methods that are suitable for field use.

CHAPTER I

INTRODUCTION

1.1 Overview

This thesis develops novel methods for assessing damage in plates with a particular focus on cracks, delaminations and impact damages in isotropic and composite type materials using guided waves (GW). This area of work falls within the broad area of Non-Destructive Evaluation (NDE). In this chapter gives a brief overview of NDE and its applications to inspecting plate-like structures. The discussion focuses on the basic differences between the major classes of inspection techniques within the NDE field. Following this, an overview of GW and the current state of GW research will be presented. Subsequently the rational for using phase in the spatial domain for post-processing the measured wavefields is explained. The primary experimental set-up used in this work will be given next. Finally, the objectives and contributions of this thesis are previewed.

1.2 Non-Destructive Evaluation

Detecting physical defects in mechanical structures has been an important task in civilian safety with origins in the industrial revolution. The advent of mechanical machinery in the presence of large groups of people put new emphasis on determining the integrity of such systems. In particular critical failures in industrial boilers and railroads drove the development of what is now known as Non-Destructive Evaluation (NDE) [2, 3]. Non-Destructive Evaluation typically involves systematic assessments of a system's material condition both at the onset of the system's life (e.g. during and immediately after manufacturing) and periodic inspections throughout the life of the system. For this reason, the testing cannot be destructive. While the exterior of a component may be inspected visually, the interior requires other methods of inspection. To this end, many methods have been developed that assess the interior of specimens. This work will focus on assessing the interior of plate-like structures, in particular, fiber – matrix composite materials. However, the methods apply to any plate-like structure.

Non-Destructive-Testing's most basic and common form is visual inspection. The US Department of Transportation's Federal Aviation Administration notes that within its scope of concern, the vast majority of inspections can be accomplished visually [4]. Other approaches utilized digital imaging and processing for automated variations of visual inspection [5-7]. Further penetrant testing can augment visual testing by enhancing the visibility of surface penetrating features such as cracks or porosity [8]. While relatively easy to grasp and implement, these techniques are confined to damage that is apparent on the surface of the specimen. This typically restricts the inspection to cracks, gross separation of layered components, surface breaking porosity or similar defects. Visual inspection can identify markers of internal damage due to impacts or otherwise, but direct detection is not possible. From a practical perspective, access to the specimen can further limit the region of the specimen available for inspection.

Methods that detect internal damage include Eddy Current Testing (ECT). This technique is based on electromagnetic induction, thus is suited to conductive materials. Based on the understanding of electromagnetism developed in the 19th century, Dr. Freidrich Forster pushed ECT into a form suitable for industrial use shortly after World War II [9, 10]. Eddy Current Testing is based on detecting disturbances in the eddy current produced by an alternating current in a conductive coil. Through detection of these changes, information about the condition of the specimen can be deduced. However, there are challenges with this method. The primary limitations of this method are the depth of defects that can be detected and the requirement for the specimen to be conductive [10].

Infrared thermography inspections serve as an alternative non-contact NDE method. Infrared techniques grew out of developments in thermal sensor technology driven by the United

States Military from World War II well into the late 20th century [11]. Infrared thermography utilizes surface temperatures to image defects in a specimen. Infrared thermography methods can be grouped into two categories: passive techniques using thermal energy inherent to the specimen and active techniques which utilizes heat from an external source [12, 13]. Alternatively, vibrothermography uses vibrations to detect defects. Friction at the defect causes local thermal gradients which can be detected and quantified [11]. These techniques are limited in the depth of defect that can be detected as well as the ability to heat the specimen [11].

An alternative to ECT and infrared thermography is radiographic testing. This method can produce a two-dimensional (2-D) image of the specimen, or a three-dimensional representation of the specimen using Computed Tomography (CT) much like what is done in the medical field. The primary benefit of this method is that it allows inspection through the thickness of a part unlike the previously described methods. The first radiography experiments were published in 1896 and demonstrated both medical and non-medical applications [14]. Within thirty years, inspection applications including casting inspection, weld inspection, metallic contamination detection, materials testing, even detecting fraudulent artworks had been considered and evaluated [15]. However, radiation is generally not safe for humans, thus precautions must be taken.

Acoustic based inspection as an NDT method was conceived in 1929 by Sergei Y. Sokolov for testing castings using pulse-echo ultrasonics (Fig. 1.1) [16]. Ultrasonic testing continued to be developed due to the unique set of advantages they hold over other NDE methods. The most important is its sensitivity to internal discontinuities. Unlike visual inspections (manual or automated), acoustic techniques are sensitive to internal damage [5-7]. Further, acoustic waves are sensitive to internal flaws throughout the thickness [12, 13]. Acoustic waves propagate through all elastic materials making their application more general than methods such as electro-magnetic methods which require conductive specimens [17]. Finally, acoustic waves pose no danger to operators unlike radiography methods [5].

In traditional ultrasonic methods, elastic waves are induced in a specimen via a transmitting transducer, allowed to propagate through the specimen, and then received by a receiving transducer. This approach is well researched and utilized in many industries. The most straightforward applications are pulse-echo configurations. In pulse-echo ultrasonics the time of flight for an acoustic pulse passing through the sample under test is measured. The wave is reflected by a change in impedance that is typically either a known sample boundary (e.g. part edge) or an unknown defect. This method only reveals information about the specimen directly below the transducer. The time domain response for a single point (Fig. 1.1) is known as an A-scan. B-Scans are a collection of time series for points in a line to compile a time-space representation of the response signal. To create a 2-D representation of a specimen, a collection of times series from points on 2-D grid are collected and plotted. This is known as a C-scan. Alternatives to normal incidence pulse-echo inspection are oblique incidence excitation. This typically requires separate transmitting and receiving sensors and takes advantage of reflections to inspect places not otherwise accessible to normal incidence pulse-echo methods.

1.3 Guided Wave Methods

Ultrasonic methods discussed in the previous section focused on bulk waves techniques. An

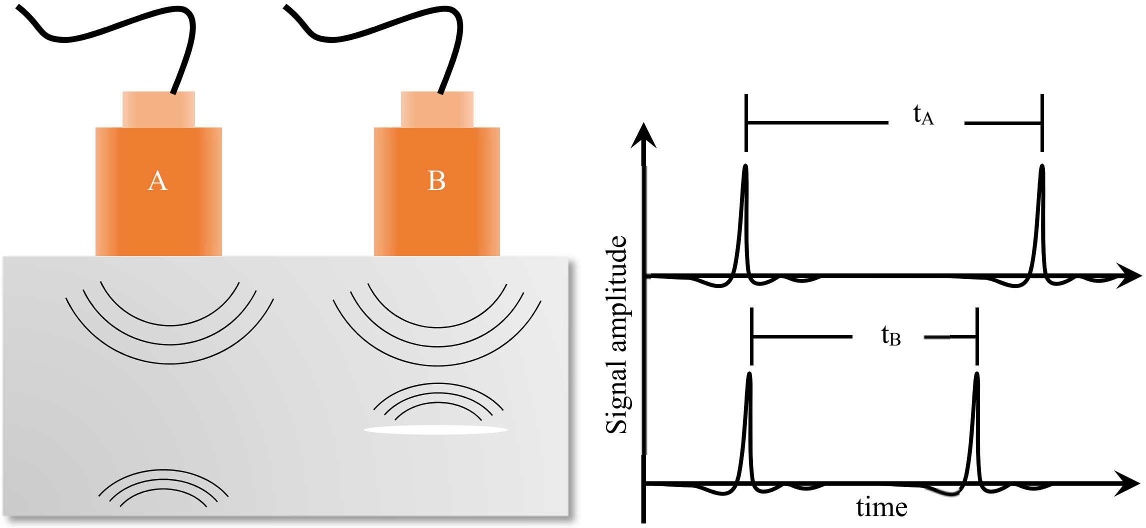

Figure 1.1 Typical pulse-echo ultrasonic testing

alternative to traditional ultrasonic methods are GW methods. To facilitate discussion of GW methods as well as to provide a foundation for the GW methods developed in this work, a brief overview of GW and the current state of GW research is presented in this section.

1.3.1 Overview of Guided Waves

As the name implies, GWs take advantage of bounded structures, such as plates, rods or pipes that guide the propagation of the wave. Guided waves are unique in that they have lower attenuation rates than bulk waves used in traditional ultrasonic methods [18]. Additionally, they are sensitive to boundary conditions, thickness changes and material property changes [19]; this can be an asset or a hindrance. Lamb Waves are a subset of the GW that propagate in plate-like structures and are often used as idealizations for waves in plate-like structures as will be done in this work.

Lamb Waves are dependent on both the bulk longitudinal and transverse wave properties of the subject material as well as the thickness of the plate. This dependency makes Lamb Waves suitable for inferring properties of the specimen. If Lamb Waves are excited and characterized in a specimen, an assessment of one or more of these properties can be made. This quality makes them an ideal NDE tool. The Rayleigh-Lamb frequency-wavenumber equations link the material properties and plate thickness to the frequency and wavenumber of the wave. The Rayleigh-Lamb frequency-wavenumber equations assume a homogeneous, isotropic plate with stress free boundaries. With these assumptions, two modes types can be excited in the plate, a symmetric and asymmetric mode. The Rayleigh-Lamb frequency-wavenumber equations for these two modes types are.

Symmetric Modes:

$$\frac{\tan(qh)}{\tan(ph)} = -\frac{4k^2pq}{(q^2-k^2)^2} \tag{1.1}$$

Asymmetric Modes:

$$\frac{tan(qh)}{tan(ph)} = -\frac{(q^2 - k^2)^2}{4k^2pq} \tag{1.2}$$

where,

$$p^2 = \sqrt{\frac{\omega^2}{c_L^2} - k^2} \tag{1.3}$$

$$q^2 = \sqrt{\frac{\omega^2}{c_T^2} - k^2}$$

These two equations relate frequency and wavenumber for a given set of material properties (found in parameters p and q) and thickness, $(2h)$. For any real frequency there are an infinite set of complex wavenumbers that satisfy Eqns. (1.1) and (1.2). The complex and imaginary wavenumbers represent decaying and evanescent solutions. The real wavenumbers represent propagating waves and are known as the dispersion curves. An example set of dispersion curves is given in Fig. 1.2. For a given frequency a minimum two solutions are present and at higher frequencies more solutions are present. This means that multiple modes are present for any given frequency. In this work, the frequencies considered are below the cut-off frequency for the first asymmetric mode, A_1, ensuring that only the two fundamental modes are present, the A_0, and S_0.

The key reason for reviewing the development of the frequency-wavenumber relationship is that the wavenumbers associated with any frequency depend on the material properties and the plate's thickness. These relationships will be used throughout this work. First, in 2-D PG method, frequency – wavenumber relationships will be used to isolate individual modes. Second, in the Phase Congruency for Damage Mapping, the changes in wavenumber due to the presence of damage or geometric changes will be used to identify the boundaries of these effected areas. Lastly, these relationships are used to verify the existence of a GW in the optical measurement approach.

The Rayleigh-Lamb frequency-wavenumber equations assumed homogeneous, isotropic media. For anisotropic and multi-layered media other methods are needed to determine the dispersion curves. This work will utilize the Semi-Analytic Finite Element method [20]. In this approach, the plate is discretized in the thickness direction. This allows each layer to be modeled independently with homogenous properties. Then the problem is recast as an eigenvalue problem and solved to obtain the dispersion curves for the plate. The discretization in the thickness direction makes it ideal for composite plates hence its use in this work.

1.3.2 Guided Wave for NDE

Guided waves have been known for nearly a century. In 1917 Horace Lamb first suggested that GW may propagate in a thin plate [19], but it was not until 1961 that Lamb Waves were verified experimentally [21]. From there, research included applications to NDE [22, 23].

Current research is driven in large part by expanded use of composites across a wide range of industries [24]. Composites require new methods of inspection for two reasons. The first is that composites are gaining use in structurally significant areas [25]. These areas include airplane wings

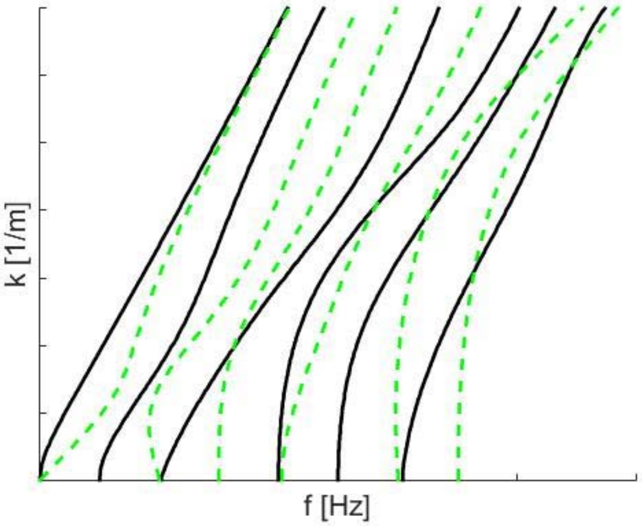

Figure 1.2 Example dispersion relations (dashed lines: symmetric modes, solid lines: asymmetric modes).

and fuselages [26], major components of maritime hull structures and superstructures [27], as well as the main body of spacecraft [28]. These components are both large and critical to structural integrity. Additionally, composites are prone to internal defects due to their layered construction [29]. For example, delaminations can be present in a specimen but not visible from the exterior. Finally, composites are typically highly attenuative, meaning the amplitude of acoustic waves decreases rapidly with distance. Guided Waves are well suited for these conditions as they can inspect the full thickness of a specimen and propagate over long distances.

Many of the early GW methods were analogous to the pulse-echo ultrasonic techniques. In these types of techniques, GW were primarily used for their long propagation distances to detect defects in pipes [30, 31], and railroad rails[32]. Some plate and beam structures were considered as well [22, 33-36]. These pulse-echo type methods focused on time of flight and did not make use of the rich information available in the full wavefield.

Other focus areas for GW research include investigating how GW interact with damage [37-39]. These investigations in scattering have been used to inform modeling [34, 40]. Guided Waves have also been proposed for assessing bond characteristics [33, 41-45]. These approaches generally focused on GW transferred across the bond. The changes in the signal were then correlated to the presence of defects in the bond. Again, these methods focused primarily on pitch and catch measurement arrangements that do not consider the behavior of the wave in space.

Recent work on GW has focused on moving from idealized geometries and damage models towards more real world configurations. Some authors have investigated of GW propagation in non-planar geometries [46, 47]. The goal of the work in these studies to extend previous work on plates to real-world geometries such as bent plates and plates with stiffeners. Others have focused on considering more realistic damage models [48]. By including more complexities in both sample geometry and damage, more real-world relevance is introduced to the research.

In the vast majority of GW research, the focus has been on the time domain. However, the spatial and wavenumber domain contain information that is not available in the time and frequency domain. Damage not only causes reflections but can cause local changes in wavenumber [39] that can be exploited [49, 50]. Recent work that has focused on the spatial information in wavefields focused on wavenumber analysis [50-52]. These methods use the wavefield over a delamination to characterize the damage taking advantage of the spatial variations in the wavenumber domain. The analysis methods in this work will also focus on identifying changes in the wavenumber domain

1.4 Measurement of Guided Wavefields

A common method for measuring wavefields is to collect a set of individual time series on a grid of measurement points covering the area (Fig. 1.3). These can then be assembled into a matrix with dimensions of space and time. For typical engineering plates, wavelengths are relatively small, on the order of a few centimeters or less, thus requiring a dense grid of measurement points. To achieve this grid density mechanical scanning systems are common.

One common method utilizes a traditional ultrasonic receiver on a computer-controlled gantry. In this method, the gantry positions the receiving sensor at each position on the grid. At each location, a sending transducer generates a GW in the specimen, while the receiving transducer records a time history of the plate's surface displacements at the given point. Once each of the time series is collected, the data can then be assembled into a multi-dimensional matrix with time and space dimensions. This method is typically used with non-contact transducers with either air or water as a coupling medium between the transducer and plate. Air coupled transducers are simple to set up but are limited in their ability to transfer energy into the specimen. Water coupled transducers are far more efficient at transmitting energy into the specimen but require submersion tanks or continuous water streams that must be dealt with.

There are two primary shortcomings in this approach. This first is the requirement for a high degree of repeatability. Since the spatial domain is assembled point-by-point with a series of time separated measurements, the excitation event must be repeated for each time series collected. Thus the excitation must be highly repeatable. The second is the difficulty posed by non-planar surfaces. To accommodate these geometries complex five-dimensional sensor manipulation is required.

The problem posed by complex geometries can largely be overcome by using Scanning Laser Doppler Vibrometers (SLVD). In these systems, a laser beam is used to measure the velocity of the sample's surface normal to the laser beam. In general, these systems can be located several meters from the sample. Thus complex geometries are no longer an impediment so long as the laser beam's reflection can be directed back to the laser head (via retro-reflective surface treatments or otherwise).

An SLDV will be the primary measurement device in this work. Measurements are made following the configuration depicted in Fig. 1.4. The SLDV (Polytec PSV 400) and excitation method are an integrated system. A function generator (Agilent 3320A) is used to generate the excitation signal. This signal is then amplified (E&I 1040L) and sent to a piezoelectric device to excite wavefield in the plate. The function generator triggers the SLDV to begin measuring the

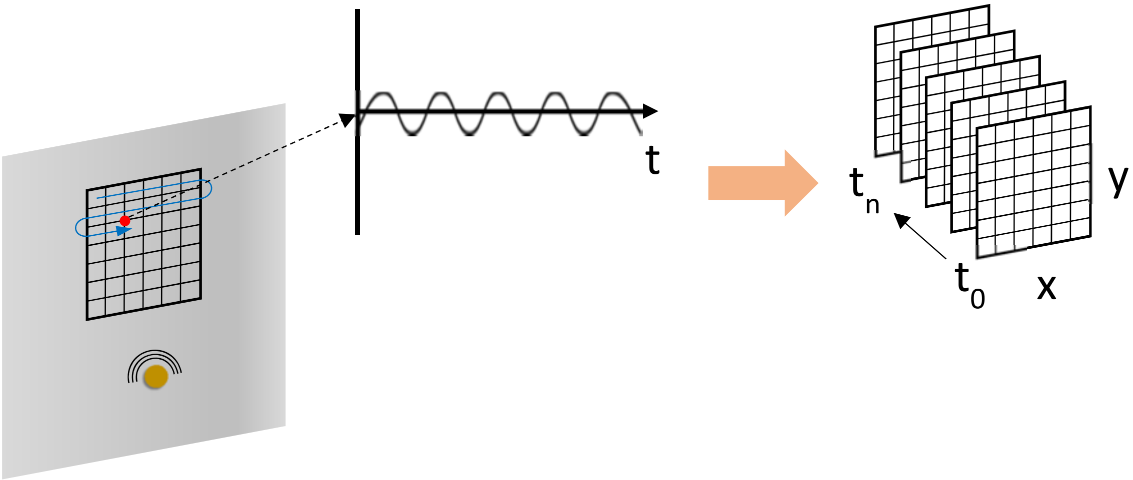

Figure 1.3 Schematic of scanning grid

plate's response. The SLDV records a time series for each point before moving on to the next point and repeating the measurement. These time histories are then synchronized in time resulting in a three-dimensional matrix representing the space-time evolution of the wave.

Two different types of transducers are used to excite wavefields in this work. The first type are simple piezoelectric ceramic disks. The disks are permanently adhered to the plate with an epoxy. The disks are polarized in the radial direction so that an application of voltage across the disc resulted in radial strains that are transmitted to the plate via the epoxy. These transducers are designed to be used well below the first resonance frequency in either the thickness or radial direction. This allows a broad range of frequencies to be excited but with relatively low amplitudes.

The second type of excitation device is an ultrasonic resonance transducer. This transducer, in contrast to the ceramic disk, is relatively large, heavy and designed to be used at its resonant frequencies. As such, this transducer is ideal for exciting large amplitude waves but only at the

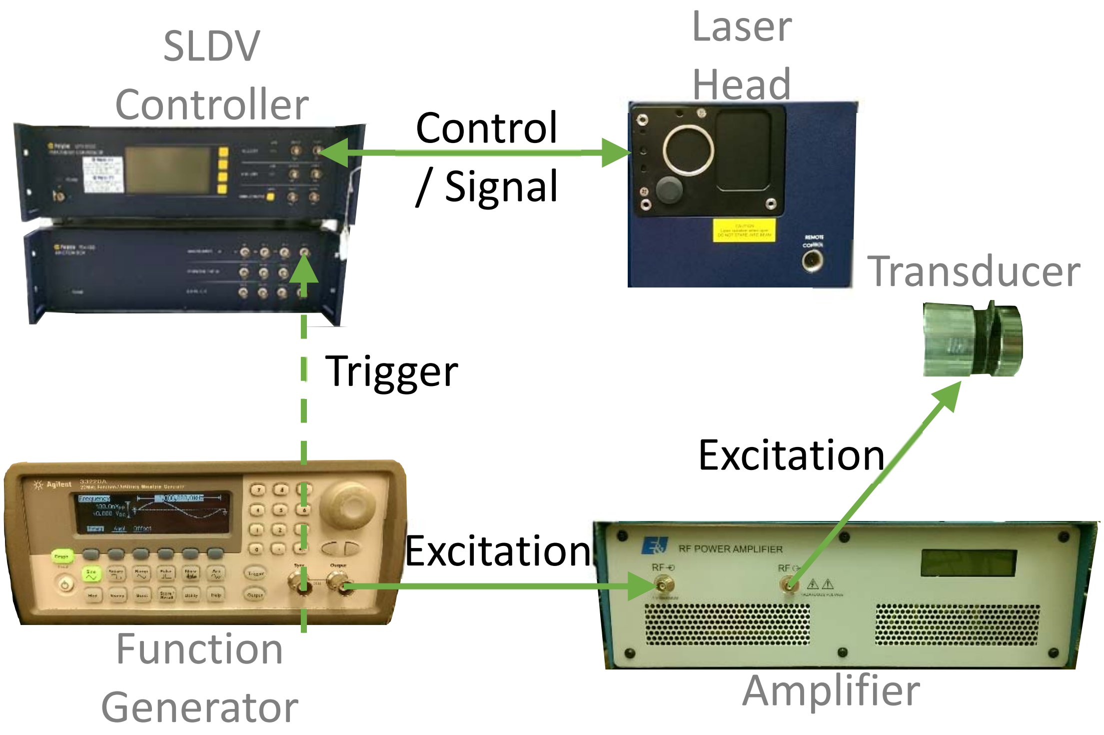

Figure 1.4 Schematic of Experimental Set-up

system's resonant frequencies. These transducers are clamped to the specimen with shear gel between the plate and transducer, so they can easily be removed.

The measurement system outlined above is the primary experimental set-up used in this work. The characteristics of the system require repeatable excitation but allow large amounts of flexibility in the size and shape of the measurement area, the density of the sample grid and sampling frequency. Chapter 5 will outline a new alternative framework for measuring GW that captures motion of the entire measurement field simultaneously. This chapter will explore an optical method for measuring GW as well as investigate methods for improving the sensitivity to GW.

1.5 Phase Based Methods

Both traditional and GW based acoustic techniques typically utilize the amplitude of a signal rather than the phase [36, 53-55]. The phase in this case refers to the position of the rotational vector describing a harmonic component of the measured signal in the complex plane. The phase of the component is the argument of the oscillatory term (complex exponential or trigonometric function) that describes the signal analytically. In contrast, the amplitude, which does not typically oscillate, is found as a scaling parameter applied to the oscillatory component. Neither of these values can be measured directly, rather they are inferred from measurements of a real valued parameter, usually displacement or velocity of a point on the specimen. While amplitude based analysis procedures are most common, a few phase based methods have been developed.

A relatively early method utilizing the phase of the received signal is split-spectrum analysis [56, 57]. This method operates in the time domain on a received signal for a pulse-echo measurement. The method breaks the signal into several parts via a wavelet transform then attempts to discriminate between grain noise and flaws by the breadth in the frequency spectrum of the received signal. More recently, an approach similar to beam forming was employed to determine the bearing of a reflection from damage [58, 59]. The most recent addition to the set of phased based methods is phase coherence imaging proposed by Camocho et. al. [60]. This method utilizes phase to improve the signal to noise ratio (SNR) and angular resolution of a beamforming array. It utilizes a pulse echo technique with a phased transducer array to detect damage through the thickness of a specimen.

These methods all utilize phase in the temporal domain to discern location of the reflector. The methods proposed here take advantage of phase in the spatial domain. By taking advantage of the signals spatial information maps of damage can be created since the spatial frequency, or wavenumber, is sensitive to defects. Examples include when there is a change in wavenumber, due to a delamination [39, 50] or change in thickness [61], or a reflection caused by many types of defects [54, 62]. This sensitivity to wavenumber is not available in the temporal domain. By analyzing the phase in the spatial domain, detecting and mapping the location of changes in wavenumber can be used to create maps of the damage.

1.6 Objectives

There are two objectives in this work. The first objective is to propose novel phased base methods for mapping damage in plates using full wavefield measurement. These methods should minimize or exclude the use of models or baselines so that they are robust to changes and variations in material properties and conditions. Two parallel approaches are developed to meet this objective. The first is the 2-D PG method; the second is the Phase Congruency for damage mapping method. These two methods make use of phase in the spatial domain to generate maps of damage.

The second objective is to explore a novel method for measuring GW using optical means. This type of method can acquire a full wavefield in a single recording. However, the GW in the optically collected image is very low amplitude relative to the information defining the static image. Thus methods to improve the sensitivity are proposed as well. The optical measurement method and analysis approach together demonstrate the feasibility of using optical means to measure wavefields.

1.7 Contributions

This work develops two phase-based methods for damage mapping along with a framework for a new approach for GW acquisition. This first damage mapping method is well suited to crack like damage and the second is applicable to mapping a larger range of damage types including delaminations, notches, and impact damage as well as geometrical changes. The GW acquisition approach utilizes an optical camera to acquire the wavefield.

The first damage mapping method is the 2-D PG approach. This method is ideal for locating and mapping crack-like linear damage. Earlier works developed a one-dimensional (1-D) PG method [63]. This work extends the method to two dimensions. The method utilizes the slope of the phase to locate discontinuities. The extension to 2-D requires two contributions. The first is to leverage previous work on phase unwrapping [64]. The second contribution was developing a novel method of discerning the source from the edge of the wavefield. These individual elements are combined to create a method for determining the location of damage in a wavefield.

The second mapping method developed in this work is the Phase Congruency method for damage mapping. This method is adapted from an image processing method for edge detection [65]. Edges in images are simply discontinuities in the luminance gradient. Similarly, damage often manifests itself as discontinuities in the wavefield by causing a reflection, change in wavenumber or both. By modifying the image processing method and applying it to GW wavefields maps of damage can be produced.

The third contribution of this work is exploration of a novel method of capturing wavefields. There are no methods presently that capture the entire spatial domain of the wavefield at once. All methods utilize in some fashion a scanning grid, collecting individual time histories one at a time. In this work, a novel optical method is explored that measures the entire spatial domain of the wavefield at once, thus greatly reducing acquisition time. In principle, the entire scan area can be collected with one excitation-measurement event. However, to reduce uncorrelated noise, this work utilizes multiple captures and averaging to improve the signal-to-noise ratio.

Although none of these methods are mature enough for field use, these three contributions make progress towards improving methods available to NDE practitioners. Damage maps provide more information to evaluate and assess the severity of damage while the optical measurement approach would improve feasibility of GW for field use with its flexibility and the reduction of acquisition time.

1.8 Organization of Work

This work is divided into four chapters. The first chapter will present the work done on the first damage mapping method, the 2-D PG method. First, a review of the 1-D PG method as previously presented will be summarized. Next, the extension to 2-D is developed. Finally, results of numerical and experimental evaluations are illustrated along with a discussion of the results and some concluding remarks. The following chapter presents the Phase Congruency for damage mapping method. Previous work on PC for edge detection in images is given first as a foundation. Following this, the method is analyzed with respect to wavefield analysis and modifications are made to tailor the method to GW. The method is then evaluated against a series of increasingly complex wavefields from numerical simulations and experimental measurements in the fourth chapter. This chapter also considers opportunities for characterization of damage. Finally, a novel method of wavefield acquisition through optical means is discussed in the fifth chapter. The exploration of this technique is an experimental so the concept is presented first, followed by a discussion of the analysis technique. Finally, results are presented from the experimental datasets. The last chapter summarizes the work presented as well as provides some remarks on possible paths forward for future developments.

CHAPTER II

TWO-DIMENSIONAL PHASE GRADIENT APPROACH

2.1 Chapter Overview

The first method evaluated for mapping damage is the Two-Dimensional Phase Gradient approach. This method makes use of the linear relationship between wavenumber and space. Therefore, as the wave evolves in space, the wavenumber-space product grows linearly. In the context of GW interrogation of a specimen, damage can be mapped using this linear relationship. This method will be evaluated on two types of defect. The first is crack-type defects simulated with a notch and the second is delamination-type defects simulated by decoupling layers of a composite plate.

This chapter begins with an overview of the 1-D PG approach developed by Ayers et. al. [63]. Then the extension to 2-D will be presented followed by results for numerical and experimental cases.

2.2 Phase Gradient for One-Dimensional Fields

In this section the concept for the 1-D PG method is briefly reviewed [63].

2.2.1 Concept

Consider a generic 1-D wave propagating at frequency, ω_0 with no attenuation. The wave can be represented as the real component of the complex exponential,

$$u(x,t) = \mathcal{R}\left\{Ae^{i(\omega_0 t - kx)}\right\} \tag{2.1}$$

Here $u(x,t)$ is a generic dynamic variable (e.g. surface displacement, velocity, etc.), A is the amplitude of the wave, and k is the spatial frequency or wavenumber.

The phase of the wave is the argument of the exponential. There is a clear linear relationship between phase and position,

$$arg\big(u(x,t)\big) = \omega_0 t - kx \tag{2.2}$$

For a wave that originates at x_s and propagates in the positive x-direction, the signal can be described as follows,

$$u(x,t) = \begin{cases} \mathcal{R}\{Ae^{i(\omega_0 t - k(x_s - x) + \Phi)}\} & x \geq x_s \\ 0 & x < x_s \end{cases} \tag{2.3}$$

where the phase offset Φ , is introduced to account for any constant phase source that may arise for a propagating wave (e.g. complex reflection coefficients, enforcement of interface conditions, etc.). The phase of this signal is then,

$$arg\big(u(x,t)\big) = \begin{cases} \omega_0 t - k(x_s - x) + \Phi & x \geq x_s \\ 0 & x < x_s \end{cases} \tag{2.4}$$

To the left of the signal's source, the signal has zero magnitude, therefore there can be no meaningful description of the phase. For this reason, the phase value at locations where no wave is present is conventionally set to zero. To the right, the phase has a linear relationship kx with space.

The Fourier Transform (FT) in time of the signal in Eqn. (2.3) yields a signal in the space-frequency domain

$$\tilde{u}(x,\omega_0) = \mathcal{F}_t\big(u(x,t)\big) = \begin{cases} Ae^{i(-k(x_s - x) + \Phi)} & x \geq x_s \\ 0 & x < x_s \end{cases} \tag{2.5}$$

where the phase in the Fourier domain is given by,

$$arg\big(\tilde{u}(x,\omega_0)\big) = \begin{cases} kx + \Phi - kx_s & x \geq x_s \\ 0 & x < x_s \end{cases} \tag{2.6}$$

The phase to left of the source has a constant value of zero. To the right, the phase is made up of two terms, one constant ($\Phi - kx_s$) and one linear (kx) yielding an overall linear relationship with space in this domain. Taking first derivative of the phase in space yields,

$$\frac{\partial}{\partial x} arg\big(\tilde{u}(x,\omega_0)\big) = \begin{cases} k & x \geq x_s \\ 0 & x < x_s \end{cases} \tag{2.7}$$

By differentiating the phase as a function of space, the phase terms that are constant in space, $(\Phi - kx_s)$, go to zero. This leaves only one term, k, which is a constant. Therefore taking the second derivative of the phase results in a Dirac Delta function located at the change between the portion with zero slope and the linear portion.

$$\frac{\partial^2}{\partial x^2} arg\big(\tilde{u}(x,\omega_0)\big) = \delta(x_s - x) \tag{2.8}$$

The change identified by the Dirac Delta function at $x = x_s$ effectively identifies wave's source. Identifying the source of the wave is the fundamental basis of the PG method. By reducing the more complicated wavefields due to GW to a single harmonic component such that Eqn. (2.4) is a reasonable approximation of the reduced wavefield, the FT, estimation of phase and localization equivalent to Eqns. (2.5)-(2.8) can be performed to locate damage. This is the basic concept of the PG method.

2.2.2 Phase Unwrapping

In the preceding analysis, phase is assumed to be a continuous function of space. However, if one infers the phase from the measured value of displacement, one would find that the phase is only unique over a 2π interval. Considering the signal defined by Eqn. (2.3) (Fig. 2.1 (a)) the phase extracted from the signal is seen in Fig. 2.1 (b). The repeating nature of the sinusoid prevents unique solutions to phase outside any 2π interval. To obtain the continuous form used in the above analysis the measured phase must be unwrapped. To unwrap the phase, several methods are available, although many can be traced back to the Itor method [64].

$$\varphi(\vec{x}) = \int_C \nabla\varphi \cdot d\vec{x} + \varphi(\vec{x}_s) \tag{2.9}$$

The equation first takes the gradient of the phase, φ, as a function of space then integrates the gradient along a path to remove the discontinuities from the wrapped phase. For a 1-D signal there is only one path for evaluating the integral thus evaluating Eqn. (2.9) is straightforward. For analytic signals, the method reconstructs a smooth phase curve over space. General 1-D unwrapping algorithms for discrete data begin at the first phase value in the domain and scan along the domain for discontinuities greater than π then adds or subtracts 2π to the node at the discontinuity and all following nodes. The unwrapped phase corresponding to the signal in Fig. 2.1 (a) is illustrated in Fig. 2.1 (b) as the dashed line. The discontinuities in the wrapped phased are eliminated in the unwrapped phase.

2.2.3 Application to multi-modal wavefields

The previous section describes the PG concept in the context of a wavefield with only a single harmonic component in a portion of the wavefield. In practice, the wavefield is a multimodal GW wavefield. At the surface, displacements due to the GW can be represented as a summation of multiple harmonic components acting on discrete portions of the wavefield. In this work, excitation frequencies are well below the first cut-off frequency, thus the model can be simplified to include only two modes, the fundamental symmetric, S_0, and antisymmetric, A_0, modes. In this example, it

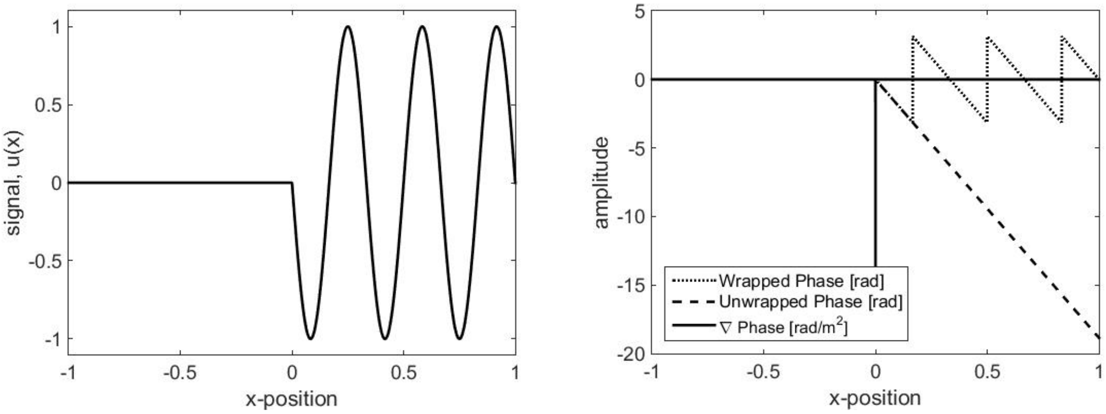

(a) (b)

Figure 2.1 The 1-D signal given by Eqn. (2.3) (a) and its wrapped phase (dotted line),unwrapped phase (dashed line) and second derivative (solid line) (b) is assumed that the source is to the left of the inspection area at $x = x_s$ and launches only the A$_0$ mode. The sample is also assumed to be of infinite length so that there are no reflected waves from boundaries.

It is known that the GW will interact with damaged such as notches or delamination [62, 66] resulting in both reflected and transmitted waves. Additionally, damage will cause converted modes to appear. Therefore, if damage is assumed to be located at $x = 0$ in the field of measurement, the incident A$_0$ mode will result in four new components following interaction with the damage: reflected A$_0$, transmitted A$_0$, transmitted S$_0$ and reflected S$_0$. Assuming the dynamic variable to be the out of plane surface displacements,

$$u(x,t) = \begin{cases} \mathcal{R}\left\{\left(\tilde{A}_{A_0^i} e^{-ik_{A_0}x} + \tilde{A}_{S_0^r} e^{ik_{S_0}x} + \tilde{A}_{A_0^r} e^{ik_{A_0}x}\right) e^{i\omega_0 t}\right\}, & x < 0 \\ \mathcal{R}\left\{\left(\tilde{A}_{S_0^t} e^{-ik_{S_0}x} + \tilde{A}_{A_0^t} e^{-ik_{A_0}x}\right) e^{i\omega_0 t}\right\}, & x \geq 0 \end{cases} \tag{2.10}$$

Here, $\mathcal{R}\{\,\}$, denotes the real part of the complex exponentials describing each wave component. The subscripts refer to the mode with the superscripts, i, r and t referring to the incident, reflected and transmitted components respectively. The wavenumbers k_{S_0}, and k_{A_0}, are the wavenumbers associated with their respective modes at the excitation frequency ω_0.

To utilize the concepts from the previous section the wavefield must be reduced to a single wavefield component. To do so, a 2-D FT is taken of Eqn. (2.10). It can be reasonably approximated as

$$
\begin{aligned}
\widetilde{U}(\omega,k) = \Big[&\tilde{A}_{A_0^{i+t}}\delta\big(k+k_{A_0}\big) + \tilde{A}_{S_0^t}\delta\big(k+k_{S_0}\big) + \tilde{A}_{A_0^r}\delta\big(k-k_{A_0}\big) \\
&+ \tilde{A}_{S_0^r}\delta\big(k-k_{S_0}\big)\Big]\,\delta(\omega-\omega_0) \\
&+ \Big[\tilde{A}^*_{A_0^{i+t}}\delta\big(k-k_{A_0}\big) + \tilde{A}^*_{S_0^t}\delta\big(k-k_{S_0}\big) + \tilde{A}^*_{A_0^r}\delta\big(k+k_{A_0}\big) \\
&+ \tilde{A}^*_{S_0^r}\delta\big(k+k_{S_0}\big)\Big]\,\delta(\omega+\omega_0)
\end{aligned}
\tag{2.11}
$$

In this form, the wavefield is broken down in to eight complex components filling the four quadrants of the frequency-wavenumber domain (see Fig. 2.2). The reflected wave for each mode is represented by conjugate pairs in quadrants II, and IV ($+\omega, -k$ and $-\omega, +k$), while the incident and transmitted mode are contained in quadrants I and III ($+\omega, +k$ and $-\omega, -k$). This observation can be used to separate the reflected wave from the incident and transmitted wave via directional filtering [67]. By applying a filter in the frequency-wavenumber domain to isolate the second and fourth quadrants the wavefield can be reduced to only the reflected modes.

To separate the A$_0$ and S$_0$ mode, modal filtering is used [68]. By applying a filter that passes the area around the reflected A$_0$ modes at $(\omega_0, -k_{A_0})$ and $(-\omega_0, k_{A_0})$ yet excludes the signal content

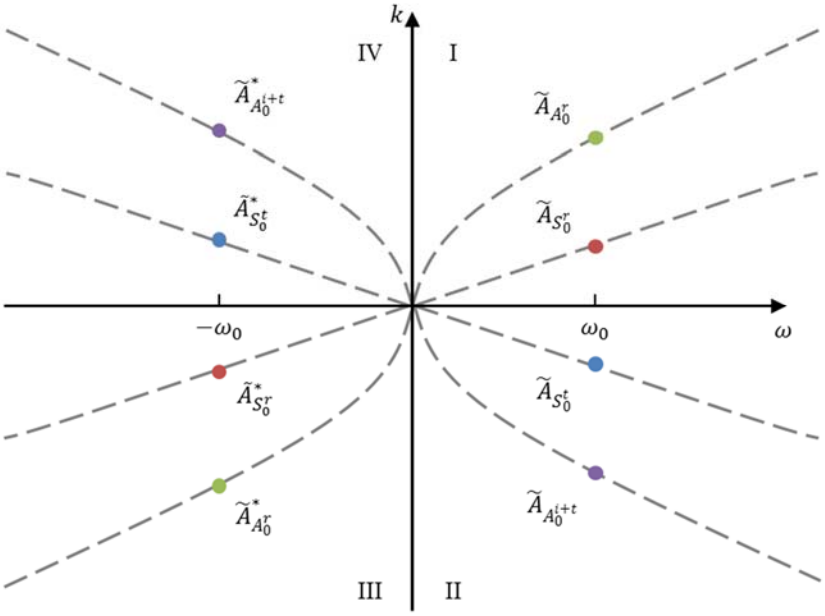

Figure 2.2 Cartoon of Eqn. (2.11)

associated with the S₀ mode at $(\omega_0, -k_{S_0})$ and $(-\omega_0, k_{S_0})$ the A₀ mode can be extracted. At this point, the wavefield is reduced to the wavefield in Eqn. (2.3) where $x_s = 0$ is the location of the damage and is revealed by the delta function of Eqn. (2.8).

2.2.4 1-D PG Example Model

To illustrate the 1-D PG method, a simple example is given using synthetic data. The dataset is generated from the following analytical expression.

$$u(x,t) = \begin{cases} u_i(x,t) + \frac{1}{2}u_{rS_0}(x,t) + \frac{1}{2}u_{rA_0}(x,t), & x < x_s \\ u_{tS_0}(x,t) + u_{tA_0}(x,t), & x \geq x_s \end{cases} \tag{2.12}$$

where each component is described by the real part of the complex exponential windowed by a raised cosine function. The real part of the term is denoted by $\mathcal{R}\{\,\}$

$$u_i(x,t) = \mathcal{R}\left\{\frac{1}{2}\left(1 - e^{i\left(\frac{\omega}{4}\left(t - \frac{x}{c_{gA_0}}\right)\right)}\right)e^{i\left(\omega\left(t - \frac{x}{c_{pA_0}}\right) - \frac{\pi}{2}\right)}\right\} \tag{2.13}$$

$$for \quad \frac{x}{c_{gA_0}} \leq t \leq \frac{x}{c_{gA_0}} + \frac{8\pi}{\omega}$$

$$u_{tS_0}(x,t) = \mathcal{R}\left\{\frac{1}{2}\left(1 - e^{i\left(\frac{\omega}{4}\left(t - \frac{x_s'}{c_{gA_0}} - \frac{x_s}{c_{gA_0}}\right)\right)}\right)e^{i\left(\omega\left(t - \frac{x_s'}{c_{pA_0}} - \frac{x_s}{c_{pA_0}} - \frac{\pi}{2}\right)\right)}\right\} \tag{2.14}$$

$$for \quad \frac{x_s'}{c_{gA_0}} + \frac{x_s}{c_{gS_0}} \leq t \leq \frac{x_s'}{c_{gA_0}} + \frac{x_s}{c_{gS_0}} + \frac{8\pi}{\omega}$$

$$u_{tA_0}(x,t) = \mathcal{R}\left\{\frac{1}{2}\left(1 - e^{i\left(\frac{\omega}{4}\left(t - \frac{x_s'}{c_{gA_0}} - \frac{x_s}{c_{gA_0}}\right)\right)}\right)e^{i\left(\omega\left(t - \frac{x_s'}{c_{pA_0}} - \frac{x_s}{c_{pA_0}} - -\frac{\pi}{2}\right)\right)}\right\} \tag{2.15}$$

$$for \quad \frac{x_s'}{c_{gA_0}} + \frac{x_s}{c_{gA_0}} \leq t \leq \frac{x_s'}{c_{gA_0}} + \frac{x_s}{c_{gA_0}} + \frac{8\pi}{\omega}$$

$$u_{rS_0}(x,t) = \mathcal{R}\left\{\frac{1}{2}\left(1 - e^{i\left(\frac{\omega}{4}\left(t+\frac{x_s'}{c_{gA_0}}+\frac{x_s}{c_{gS_0}}\right)\right)}\right)e^{i\left(\omega\left(t+\frac{x_s'}{c_{pA_0}}+\frac{x_s}{c_{pS_0}}--\frac{\pi}{2}\right)\right)}\right\} \tag{2.16}$$

$$for \quad \frac{x_s'}{c_{gS_0}}+\frac{x_s}{c_{gS_0}} \leq t \leq \frac{x_s'}{c_{gS_0}}+\frac{x_s}{c_{gS_0}}+\frac{8\pi}{\omega}$$

$$u_{rA_0}(x,t) = \mathcal{R}\left\{\frac{1}{2}\left(1 - e^{i\left(\frac{\omega}{4}\left(t+\frac{x_s'}{c_{gA_0}}+\frac{x_s}{c_{gA_0}}\right)\right)}\right)e^{i\left(\omega\left(t+\frac{x_s'}{c_{pA_0}}+\frac{x_s}{c_{pA_0}}--\frac{\pi}{2}\right)\right)}\right\} \tag{2.17}$$

$$for \quad \frac{x_s'}{c_{gA_0}}+\frac{x_s}{c_{gA_0}} \leq t \leq \frac{x_s'}{c_{gA_0}}+\frac{x_s}{c_{gA_0}}+\frac{8\pi}{\omega}$$

The incident wave propagates up to point $x = x_s$ then split into four components. The reflected modes have a relative position, $x_s' = x_s - x$. Nominal properties for an aluminum plate 2 mm thick will be used with an excitation frequency of 200 kHz. At this excitation frequency, the A_0 and S_0 mode the following wave speeds:

- A_0 mode: c_g 2784 m/s, c_p 1737 m/s
- S_0 mode: c_g 5334 m/s, c_p 5359 m/s.

Figure 2.3 (a) illustrates the synthetic data that served as the input to the 1-D PG 1process in the time domain and in the Fourier Domain (b).

2.2.5 1-D PG Process

The 1-D PG process has three main steps outlined in Fig. 2.4. The first step is to perform modal separation in the Fourier Domain. The signal in the Fourier Domain is seen in Fig. 2.3 (b). The contour lines indicate the signal's FT while the solid black lines are the computed dispersion curves. The dispersion curves can be determined by a hybrid analytical-numerical method such as the Semi-Analytical Finite Element (SAFE) method developed by Liu and Achenbach [69], the computer program DISPERSE [70], or experimentally by methods like those of Lee and Ko [71]. This work utilized the SAFE method.

The first filtering step is to remove the incident wave. This is done by simply removing the content in the first and third quadrants of the Fourier Domain with the following filter

$$W_d(\omega,k) = \begin{cases} 1, & \omega k < 0 \\ 0, & \omega k \geq 0 \end{cases} \tag{2.18}$$

This filter is then multiplied by the signal in the Fourier Domain.

$$\widetilde{U}_d(\omega,k) = W_d(\omega,k)\widetilde{U}(k,\omega) \tag{2.19}$$

The result is the filtered signal in the Fourier Domain seen in Fig. 2.5 (a) along with a single time slice of its time domain counterpart in Fig. 2.5 (b)

The second filtering step is to remove the S₀ mode. In this example, a constant width Tukey filter is used and is defined relative to the dispersion curves of the mode.

$$W_m(\omega,k) = \begin{cases} 0, & 0.5 < \xi \\ \frac{1}{2}\Big(1-\cos\big(4\pi\xi(\omega,k)\big)\Big), & 0.25 < \xi \leq 0.5 \\ 1, & \xi \leq 0.25 \end{cases} \tag{2.20}$$

where,

$$\xi(\omega,k) = \frac{|k_c(\omega) - k|}{w} \tag{2.21}$$

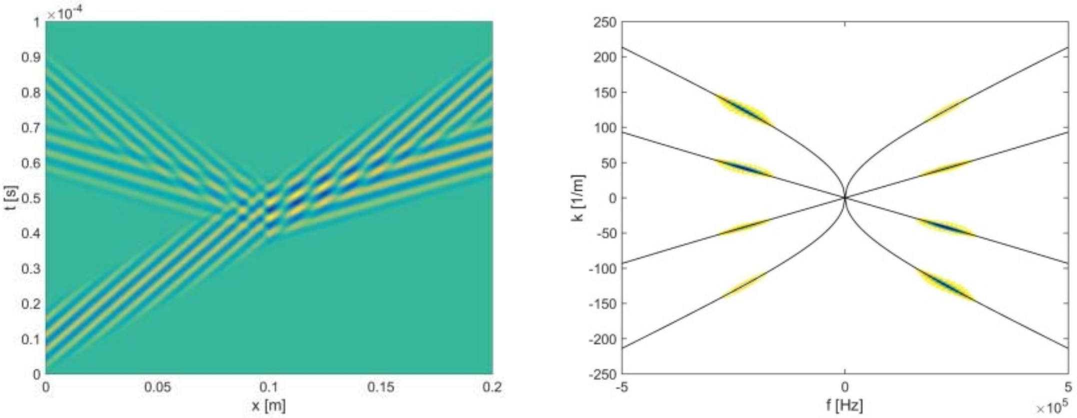

(a) (b)

Figure 2.3 Displacements for 1-D example in the spatial-temporal domain (a) and in the Fourier Domain (b)

Here, k_c is the analytically calculated wavenumber for the A_0 mode at a given frequency and w is a width parameter governing the width of the Tukey window. This filter is then multiplied by Eqn. (2.19),

$$\widetilde{U}_{dm}(\omega, k) = W_m(\omega, k)\widetilde{U}_d(k, \omega) \qquad (2.22)$$

The filtered signal is seen in Fig. 2.5 (c) along with a single snapshot of its time domain counterpart in Fig. 2.5 (d).

With only a single mode in the wavefield, the filtered temporal-spatial domain data is transformed with a FT at the incident frequency. This result is complex so the phase is taken directly from the signal. The phase at very low values is not meaningful as it represents only the small values resulting from the FT and Inverse Fourier Transform (IFT) and not the actual signal. For this reason, points with amplitudes below 40% of the full signal amplitude are set to zero phase.

At this point the signal is unwrapped. The wrapped and unwrapped phase are seen in Fig. 2.6 (a) and (b) respectively along with the second derivative of the signal (c). It is clear that the second derivative of the signal locates the scatterer at $x = 0.1$ [m].

This example demonstrated the two main components of the PG method: reduction of the GW wavefield and source identification. Two key features of this approach that are attractive for

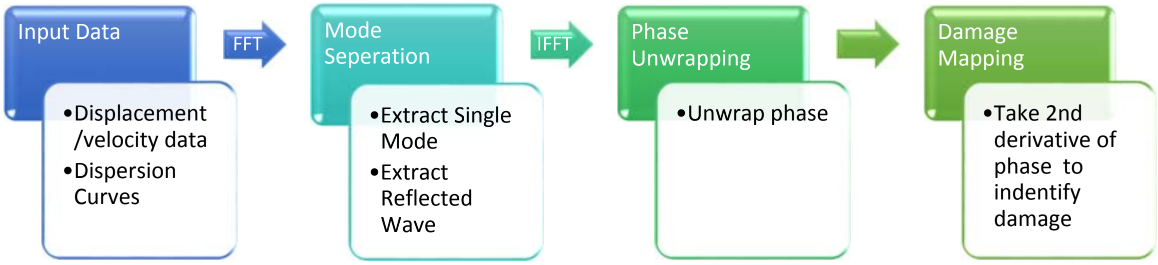

Figure 2.4 Schematic of the PG procedure

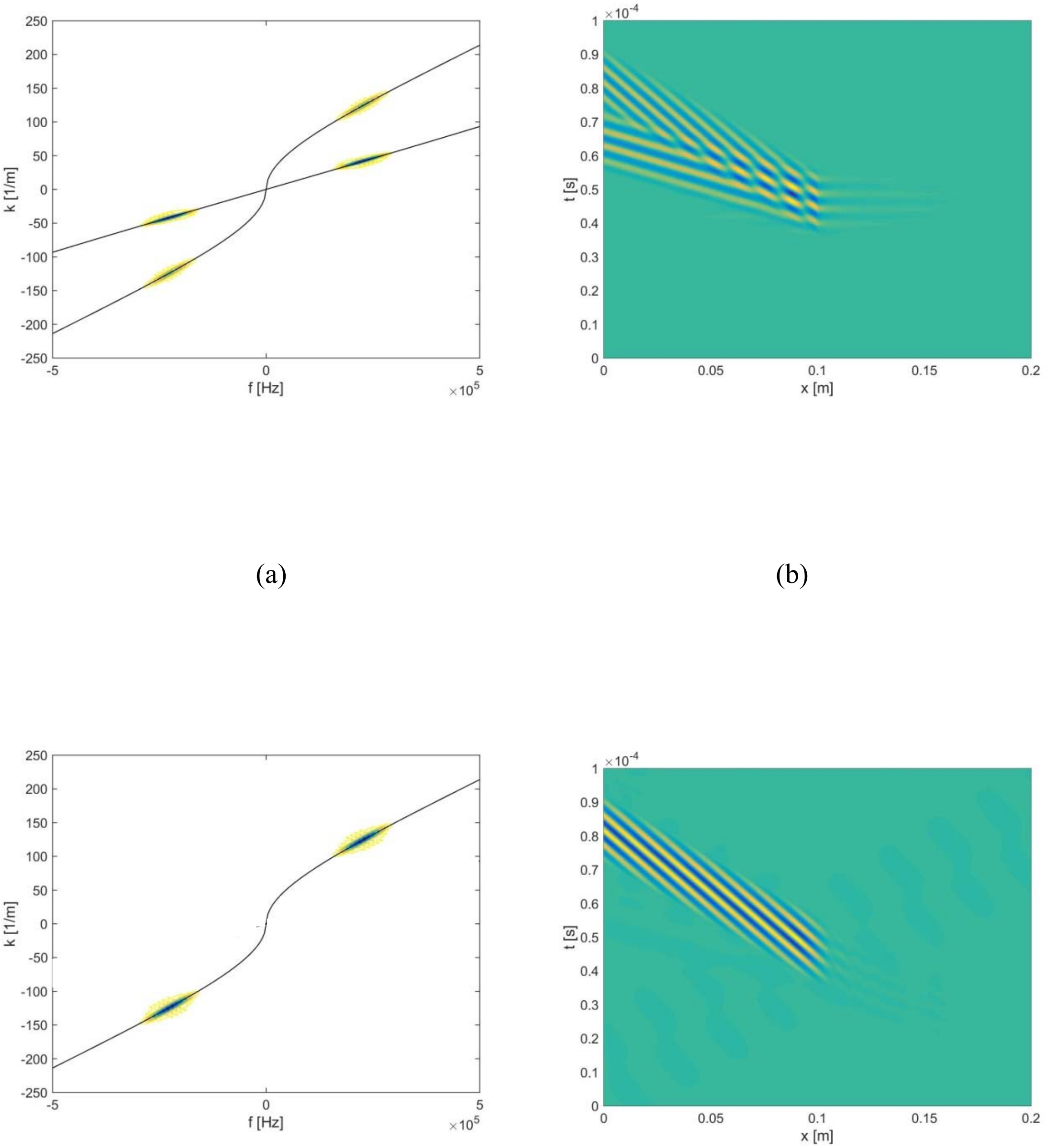

(a) (b)

(c) (d)

Figure 2.5 Displacements for 1-D example after directional filtering in the spatial-temporal domain (a) and in the Fourier Domain (b) and after modal filtering in the spatial-temporal domain (c) and in the Fourier Domain (d)

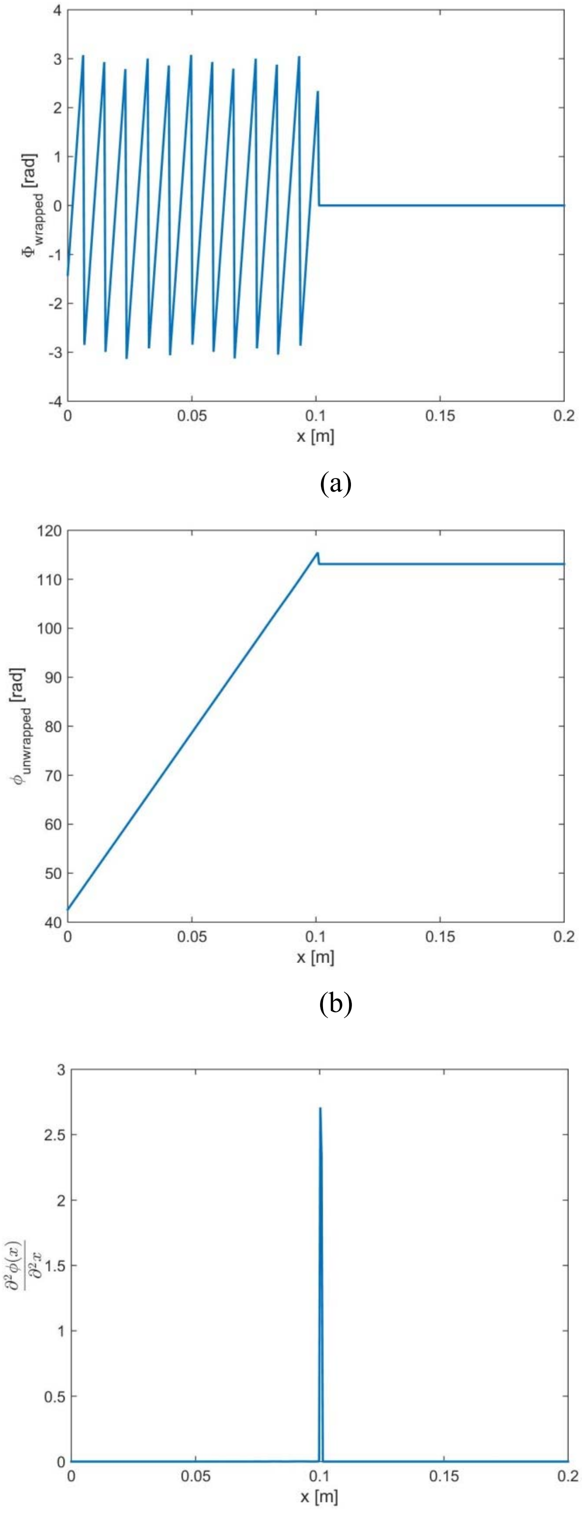

(a)

(b)

(c)

Figure 2.6 The wrapped phase of the signal (a), unwrapped phase (b) and second derivative of phase (c) damage mapping are seen as well:

1. there is no dependence on absolute phase values, and
2. there is no dependence on amplitude of the signal.

The fact that the method is not dependent on the absolute phase values is important since measured phase values are non-unique. Therefore, shifts in phase due to choice of starting point in the unwrapping process or due to complex reflection or transmission coefficients are not important. Second, the method does not depend on the amplitude of the wave as a function of space or due to mode conversion.

2.3 Two-dimensional Phase Gradient

Conceptually the extension to 2-D wavefields is very similar in concept to the 1-D case. This section begins by defining a 2-D wavefield analogous to the 1-D wavefield in Eqn. (2.10). Then, separation of modes in the 2-D space will be presented. Once the wavefield is reduced to a single harmonic component, the technique for unwrapping the phase will be presented along with a method for deducing the source's location. Finally, an example will be given to illustrate the procedure.

2.3.1 Representation of a Two-Dimensional Propagating Wave

Unlike the one-dimensional case, a model of the wavefield can be approximated by three harmonic components: an incident wave, two scattered waves.

$$\begin{aligned} u(\vec{x},t) = \mathcal{R}\Big\{\Big(&\tilde{A}_{S_0^i}(r_i,\theta_i)e^{-ik_{S_0}(\theta_i)r_i}+\tilde{A}_{S_0^s}(r_s,\theta_s)e^{ik_{S_0}(\theta_s)r_s} \\ &+ \tilde{A}_{A_0^s}(r_s,\theta_s)e^{ik_{A_0}(\theta_s)r_s}\Big)\, e^{i\omega_0 t}\Big\} \end{aligned} \tag{2.23}$$

Assuming a Cartesian coordinate system with $\vec{x} = (x, y)$ as the observation point and $\vec{x}_i = (x_i, y_i)$ as the source location of the incident wave while, $\vec{x}_s = (x_s, y_s)$ is the location of the scatter

(Fig. 2.7). These in turn yield propagation distances, $r_i = |\vec{x}_i - \vec{x}|$, the distance between the incident wave's source and the observation point and $r_s = |\vec{x}_s - \vec{x}|$, the distance between the scatterer and the observation point. The wavenumber $k_{A_0|S_0}(\theta)$ allows directionally dependent wavenumbers, thus admitting orthotropic materials. Here θ is defined as the angle of bearing between the source indicated by the subscript and observation point with respect to a reference datum.

In this case, the source and scattered wave amplitudes are allowed to vary in the angular direction. In contrast to the 1-D case, the amplitude is not constant but rather a function of propagation distance r. As in the 1-D case, damping is ignored.

Approximating the FT of Eqn. (2.23) as,

$$\begin{aligned}\widetilde{U}(\omega, k_x, k_y) = &\left[\tilde{A}_{A_0^{i+s}}(\theta)\delta\left(\vec{k} + \vec{k}_{A_0}\right) + \tilde{A}_{S_0^s}(\theta)\delta\left(\vec{k} + \vec{k}_{S_0}\right) + \right]\delta(\omega - \omega_0) \\ &+ \left[\tilde{A}^*_{A_0^{i+s}}(\theta)\delta\left(\vec{k} - \vec{k}_{A_0}\right) + \tilde{A}^*_{S_0^s}(\theta)\delta\left(\vec{k} - \vec{k}_{S_0}\right)\right]\delta(\omega + \omega_0)\end{aligned} \tag{2.24}$$

where,

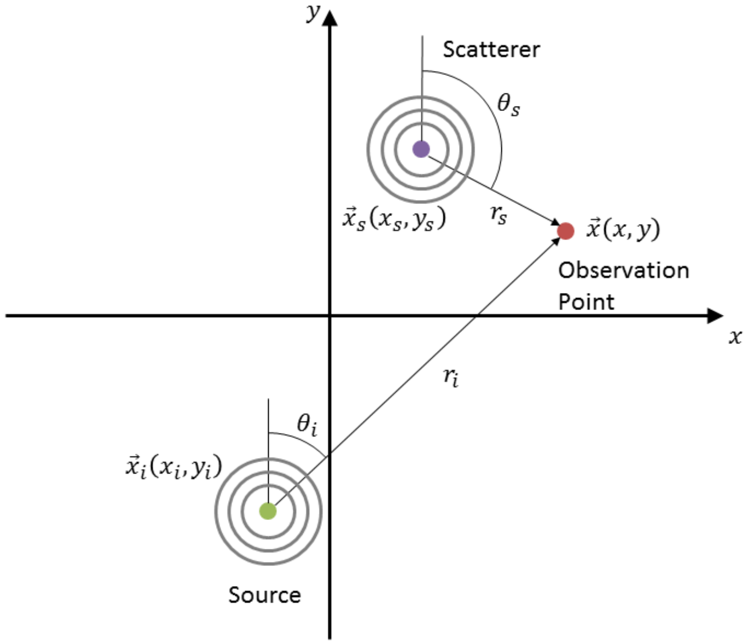

Figure 2.7 Definition of variables

$$\vec{k} = (k_x, k_y) \tag{2.25}$$

$$\vec{k}_{A_0}(\theta) = \left(k_{A_0}(\theta)\sin(\theta), k_{A_0}(\theta)\cos(\theta)\right) \tag{2.26}$$

$$\vec{k}_{S_0}(\theta) = \left(k_{S_0}(\theta)\sin(\theta), k_{S_0}(\theta)\cos(\theta)\right) \tag{2.27}$$

there are four terms in the expression. These terms again form complex conjugate pairs across the zero frequency plane. Figure 2.8 illustrates Eqn. (2.24) along with the dispersion curves for the frequency slice $\omega = \omega_0$. Comparing this to the analogous 1-D case in Fig. 2.2, rather than two sets of four discrete point, there are two sets of two curves. These curves have a directional dependence linked to the spatial orientation by the angle θ. This implies that if the angle between the source and observation point in the spatial-temporal domain is θ, the corresponding wavenumber will be oriented at θ from the k_y axis in the Fourier Domain.

2.3.2 2-D Phase Unwrapping

As was the case in the 1-D method, the phase must be unwrapped to obtain a continuous phase field. Phase unwrapping is more challenging in 2-D than in 1-D because in 2-D there are a wide range of path choices to evaluate the integral in Eqn. (2.9). This work will use an existing method to define the path of called the Quality Guided Phase Unwrapping method [64]. The method relies on a quality metric to guide the path of unwrapping. Once the path is determined, the problem is a

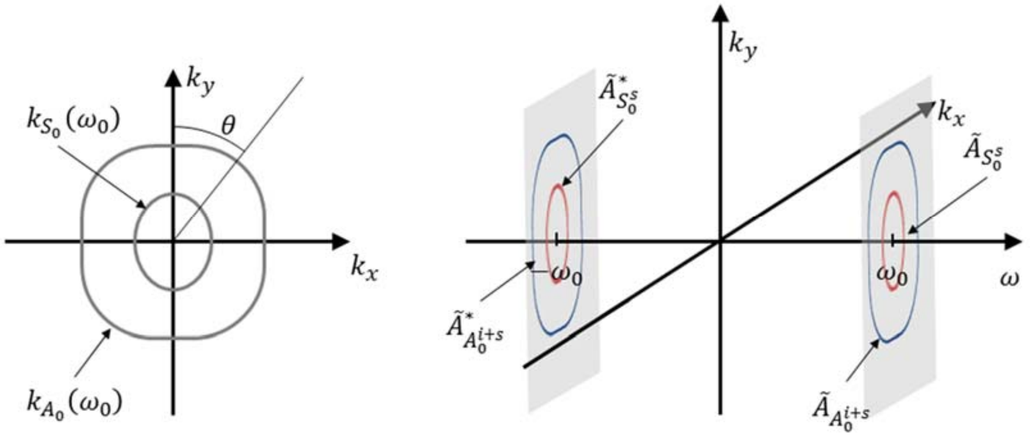

Figure 2.8 Cartoon of Eqns. (2.26) and (2.27) (a), and Eqn. (2.24) (b)

1-D problem along the integration path therefore any 1-D unwrapping method can be used.

The Quality Guided Phase Unwrapping method uses one of several metrics to determine the path of integration in Eqn. (2.9). In this work, the Phase Derivative Variation (PDV) measure is used as the quality metric since the phase of the GW is expected to have a constant gradient, therefore has minimal variance. The PDV measure uses local variance in phase gradient as the quality metric. The quality metric $Q[n,m]$ is calculated at each point as [64].

$$Q[n,m] = \sigma_x^2[n,m] + \sigma_y^2[n,m] \tag{2.28}$$

where,

$$\sigma_x^2[n,m] = \left((\Delta_x\varphi[n-1,m])^2 + (\Delta_x\varphi[n+1,m])^2 + (\Delta_x\varphi[n,m-1])^2 + (\Delta_x\varphi[n,m+1])^2\right)^{-\frac{1}{2}} \tag{2.29}$$

$$\sigma_y^2[n,m] = \left(\left(\Delta_y\varphi[n-1,m]\right)^2 + \left(\Delta_y\varphi[n+1,m]\right)^2 + \left(\Delta_y\varphi[n,m-1]\right)^2 + \left(\Delta_y\varphi[n,m+1]\right)^2\right)^{-\frac{1}{2}} \tag{2.30}$$

and the gradients, $\Delta_x\varphi$ and $\Delta_y\varphi$ are calculated along the x- and y-directions respectively using a numerical central differencing of locally unwrapped phase. The locally unwrapped phase is simply the three points used in the central differencing method unwrapped using any standard 1-D unwrapping routine as described in Section 2.2.2.

The PDV quality metric is well suited to the expected form of GW data. Since adjacent points will have a linear relationship in space, then the derivative of the phase will nominally have no difference in gradient. Therefore any points with high variance must constitute discontinuities in the phase field.

Once the quality is determined for the whole domain, a starting point for the unwrapping procedure is selected in an area of high-quality phase. This point is considered unwrapped and the remaining elements are unwrapped relative to this point's phase. This point is also the initial active node in the process described below. From this point, the algorithm determines the path of unwrapping using the following steps:

1. The elements neighboring the active element is added to a list of adjoining elements.
2. The adjoining element with the lowest PDV is selected and set as the active point and removed from the list of adjoining elements.
3. This point is then unwrapped relative to an adjacent element that has already been unwrapped using any 1-D unwrapping method.
4. Return to step one and repeat until all elements are unwrapped.

As an example, two successive repetitions of the process laid out above are performed on the contrived set of phase values illustrated in Fig. 2.9. The phase is zero around the perimeter. In the interior, the phase changes in the y-direction crossing from $-\pi$ to π at the midpoint representing a wrapping discontinuity. Figure 2.10 (a) illustrates the phase derivative variance as calculated for the phase field in Fig. 2.9 using Eqns. (2.28)-(2.30). The node outlined in red indicates the active node while the nodes outlined in yellow indicate the nodes on the adjoined nodes list. The adjoined nodes are all the nodes adjacent to previously unwrapped nodes. As this is the initiation step, the adjoined list is comprised of all four nodes that boarder the active node. Since this is the initiation step, the active node is declared unwrapped. Its initial wrapped phase value and serves as the starting point for the remaining iterations of the unwrapping procedure. Figure 2.10 (b) shows the results of the unwrapping procedure after the initiation step. There is only one node with a phase value in this plot since only the active node from the initiation step is considered unwrapped.

From here, the PDV values of the nodes on the adjoined list are considered and the lowest PDV value is selected as the active node. Figure 2.10 (c) shows the active node in the second step outlined in red, while the previously unwrapped nodes are outlined in green. The red node is unwrapped using a 1-D unwrapping algorithm relative to any of the adjacent nodes that have been previously unwrapped. The list of adjoined nodes is then updated and the new list of adjoined cells is denoted by the nodes outlined in yellow in Fig. 2.10 (c). The results of the unwrapping thus far are seen in Fig. 2.10 (d). Figure 2.10 (e)-(f) show the results of the second iteration. Once all nodes have been unwrapped, the resulting unwrapped phase plot is seen in Fig. 2.11. Now the phase is smoothly varying in the center section while the surrounding section remains a constant value on the border.

This simple example illustrates the unwrapping procedure. The unwrapping itself is still performed utilizing a 1-D unwrapping method. The Quality Guided Phase Unwrapping method simply defines the path of unwrapping based on a local quality metric. The method is initiated at a point of high quality phase and then proceeds along a path defined by the highest quality adjacent node remaining to be unwrapped.

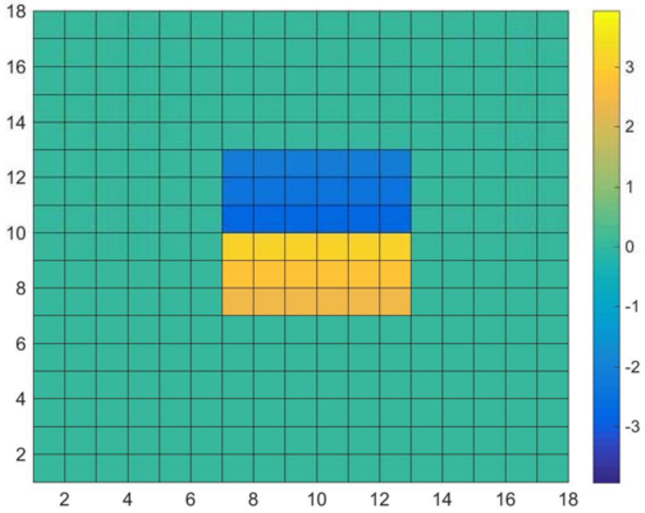

Figure 2.9 Wrapped phase values for unwrapping example.

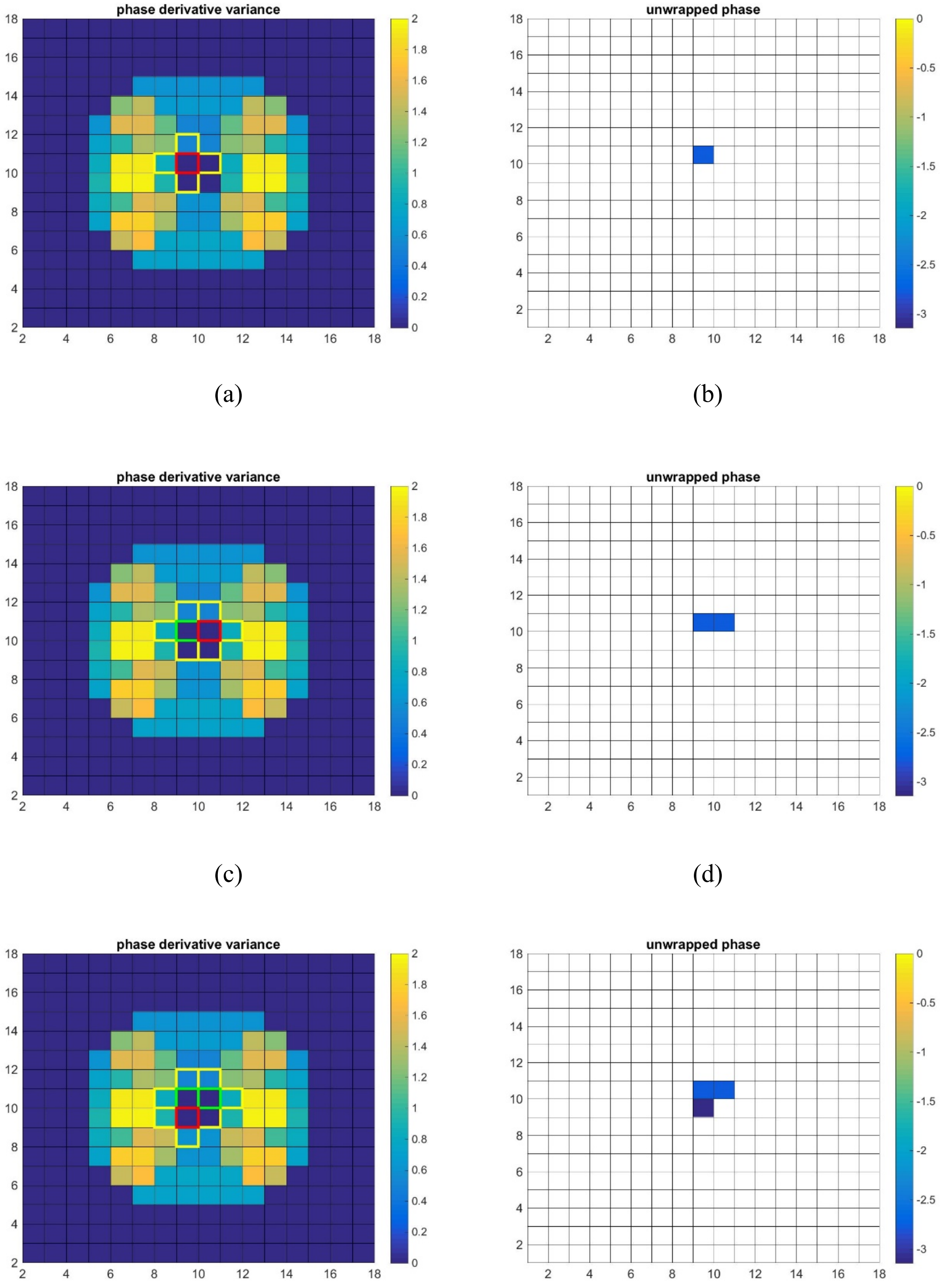

(a) (b)

(c) (d)

(e) (f)

Figure 2.10 The initial phase derivative plots and unwrapped phase of the initial point (a)-(b) and two successive iterations (b)-(f).

2.3.3 Mode Separation

In the previous section, an analytical model of a GW wavefield was defined. As in the 1-D case, this wavefield must be reduced to one wave component. This is done analogously to what was done in the 1-D case; first, a single mode is isolated then the reflected wave is separated from the incident wave.

As in the 1-D case, the method as described by Michaels et. al. [68] will be used to extract a single mode. Defining a Tukey filter in the radial direction that is centered on the dispersion curve for a particular mode, a single mode can be isolated in the wavenumber – wavenumber domain as a function of frequency as defined by Michaels et. al. [68]. To extract the filtered, mode the signal, $\widetilde{U}(\omega, k_x, k_y)$, is multiplied by the filter, $W_M(\omega, k_x, k_y)$, in the Fourier Domain,

$$\widetilde{U}_M(\omega, k_x, k_y) = \widetilde{U}(\omega, k_x, k_y) W_M(\omega, k_x, k_y) \tag{2.31}$$

Removal of the incident wave also occurs in the Fourier domain. In this work, all wavefields are rotated such that the vector between the source and center of the inspection area are aligned with the negative y-axis to simplify the directional filtering. By aligning the propagation direction with the y-axis the directional filtering window described by Ruzzene [67] can be

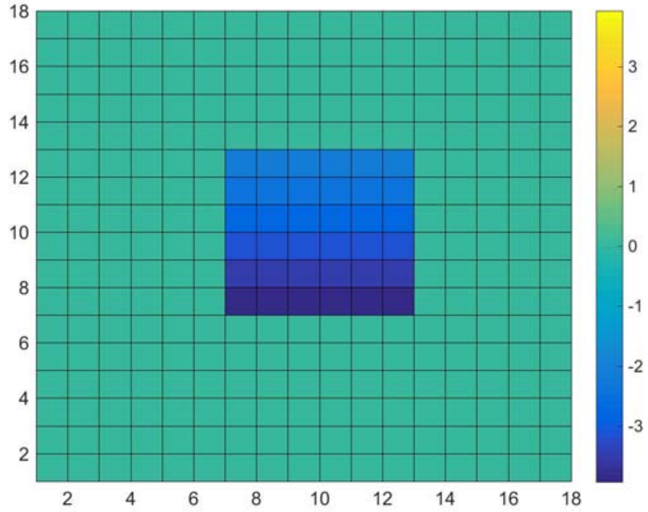

Figure 2.11 Example of the unwrapped phase.

simplified to the following binary filter in the three-dimensional Fourier space

$$W_{\mathrm{D}}(k_x, k_y, \omega) = \begin{cases} 1, & k_y\omega < 0 \\ 0, & k_y\omega \geq 0 \end{cases} \tag{2.32}$$

Rigid body motion and DC offsets are typically not present in transient wave datasets, so the filter value is set to zero on the axis as well as in the quadrants representing the incident wave. The simple binary filter can be used since the datasets contain only transient oscillatory components that center the wave information at the wavenumber and excitation frequency of the wave, well away from the zero axes for typical measurement grids. Should these assumptions fail, an analogous tapered window, such as a Tukey window could be used. Applying the directional filter in the Fourier Domain,

$$\widetilde{U}_{MD}(\omega, k_x, k_y) = \widetilde{U}_M(\omega, k_x, k_y) W_D(\omega, k_x, k_y) \tag{2.33}$$

At this point, an IFT is performed to return to the spatial-temporal domain. For sake of example, it will be assumed that the reflected A_0 mode will is the extracted mode.

$$u_{A_0^r}(x, y, t) = \mathcal{F}_{3D}^{-1}\{\widetilde{U}_{MD}(\omega, k_x, k_y)\} \tag{2.34}$$

The resulting wavefield contains only a single mode propagating in a single direction. The phase can now be extracted and unwrapped.

2.4 Source Location

Following the mode reduction and directional filtering, the FT in time of the signal in Eqn. (2.34) is given with the following time independent description of the signal at the center frequency of the excitation signal,

$$\tilde{u}_{A_0^r}(x, y, \omega_0) = \mathcal{F}_t\left(u_{A_0^r}(x, y, t)\right) = \begin{cases} \tilde{A}_{A_0^r}(r_s, \omega_0) e^{i(-k_{A_0}(\theta_s, \omega_0) r_s)}, & y > y_s \\ 0, & y \leq y_s \end{cases} \tag{2.35}$$

This form includes the assumption that $y_i > y_s$, and that the directional filtering is performed with filters aligned with the coordinate system as indicated in Eqn. (2.32). The directional filtering and assumption of source location results in the reflected wave only being present for $y > y_s$. The medium is assumed to be infinite thus there are no edge reflections. With these assumptions, the phase of this signal is,

$$\varphi(x,y) = arg\left(\tilde{u}_{A_0^r}(x,y;\omega_0)\right) = \begin{cases} -k_{A_0}(\theta_s,\omega_0)r_s + \Phi, & y > y_s \\ 0, & y \le y_s \end{cases} \tag{2.36}$$

Again, Φ accounts for any constant phase associated with the complex coefficient, $\tilde{A}_{A_0^r}(r_s,\omega_0)$.

Following the example of the 1-D case, the Laplacian in the Cartesian coordinate system results in the following,

$$\nabla^2\varphi(x,y) = \delta(y_s - y) \tag{2.37}$$

This delta function identifies the boundary of the reflected wavefield as defined by Eqn. (2.35). The boundary contains both the scatter at $\vec{x}_s$ as well as boundary of the wavefield at $y = y_s$. The goal is to find just the source, so additional means are needed to discriminate the wave's source from the remainder of the wavefield boundary. To resolve this, the gradient vector is considered. To begin Eqn. (2.36) is recast in a 2-D polar coordinate system centered on the scatter,

$$\varphi(r_s,\theta_s) = \begin{cases} -k_{A_0}(\theta_s,\omega_0)r_s + \Phi, & y > y_s \\ 0, & y \le y_s \end{cases} \tag{2.38}$$

This is trivial as the only spatially varying components depend only on the distance from the scatter and the angle of bearing relative to the scatter.

Considering only the non-zero portion for simplicity and taking the gradient in 2-D polar coordinates

$$\nabla\varphi'(r_s,\theta_s) = -k_{A_0}(\theta_s,\omega_0)\mathbf{e}_{r_s} - \frac{\partial k_{A_0}(\theta_s,\omega_0)}{\partial\theta_s} r_s \mathbf{e}_{\theta_s} \tag{2.39}$$

Here the unit vectors $\mathbf{e}_{r_s}$ and $\mathbf{e}_{\theta_s}$ are the radial and angular unit vectors relative to the location of the scatterer. There are two components to the gradient vector. The first is a radial component that points in the negative radial direction thus, it will always point towards the scatterer. The second component is dependent on the change of wavenumber as a function of angular direction. For isotropic materials, this term is zero. Many composites are quasi-isotropic, thus this term will be very small. However, this term is a function of the distance from the scatterer and will therefore decrease to zero as one moves radially toward the source no matter the dependence of wavenumber on angular orientation. Therefore, if one moves along a path defined by the gradient vectors of the phase field, it must lead to the wave's source.

To implement this, a numerical marching scheme is employed. This scheme evaluates the gradient vector and takes incremental steps, Δs, in the direction of the gradient vector.

$$\begin{Bmatrix} x_{i+1} \\ y_{i+1} \end{Bmatrix} = \frac{\Delta s}{|\nabla \varphi(\vec{x})|} \begin{Bmatrix} \dfrac{\partial \varphi(\vec{x})}{\partial x} \\ \dfrac{\partial \varphi(\vec{x})}{\partial y} \end{Bmatrix} + \begin{Bmatrix} x_i \\ y_i \end{Bmatrix} \tag{2.40}$$

The marching schemes starts from a point in space, (x_i, y_i) and moves a distance Δs in the direction of the phase gradient to the new location, (x_{i+1}, y_{i+1}). Repeating this procedure creates a set of points defining a path towards the scatterer. By selecting a number of point the boundary of the field and then employing the marching scheme from each of these points, a series of individual paths are created. Evaluating the phase along these paths, these data series can then be treated as a set of independent 1-D cases and evaluated per Eqn. (2.8).

2.5 2-D Phase Gradient Example

This section gives an example of the 2-D Phase Gradient using a synthetic dataset to illustrate the process. The process for analyzing a 2-D wavefield has the same steps as those indicated in Fig. 2.4. The main difference is the 2-D phase unwrapping algorithm and process for generating the path for evaluating second derivative. To illustrate the process for a 2-D field, a set of synthetically generated data is analyzed. The wavefield is generated from the following set of equations that are a transient analog to the form presented in Eqn. (2.23).

$$u(\vec{x},t) = \frac{1}{\sqrt{r_i}} u_{S_0^i}(r_i,\theta_i,t) + A(r_s,\theta_s,) u_{S_0^s}(r_s,\theta_s,t) + A(r_s,\theta_s) u_{A_0^s}(r_s,\theta_s,t) \tag{2.41}$$

where,

$$u_{A_0^i}(r_i,\theta_i) = \mathcal{R}\left\{\frac{1}{2}\left(1 - e^{i\left(\frac{\omega}{4}\left(t - \frac{r_i}{c_{gA_0}}\right)\right)}\right) e^{i\left(\omega\left(t - \frac{r_i}{c_{pA_0}}\right) - \frac{\pi}{2}\right)}\right\} \tag{2.42}$$

$$for \qquad \frac{r_i}{c_{gA_0}} \le t \le \frac{r_i}{c_{gA_0}} + \frac{8\pi}{\omega}$$

$$u_{A_0^s}(r_s,\theta_s) = \mathcal{R}\left\{\frac{1}{2}\left(1 - e^{i\left(\frac{\omega}{4}\left(t - \frac{r_{is}}{c_{gA_0}} - \frac{r_s}{c_{gA_0}}\right)\right)}\right) e^{i\left(\omega\left(t - \frac{r_{is}}{c_{pA_0}} - \frac{r_s}{c_{pA_0}}\right) - \frac{\pi}{2}\right)}\right\}$$

$$for \qquad \frac{r_{is}}{c_{gA_0}} + \frac{r_s}{c_{gA_0}} \le t \le \frac{r_{is}}{c_{gA_0}} + \frac{r_s}{c_{gA_0}} + \frac{8\pi}{\omega} \tag{2.43}$$

$$u_{S_0^s}(r_s,\theta_s) = \mathcal{R}\left\{\frac{1}{2}\left(1 - e^{i\left(\frac{\omega}{4}\left(t - \frac{r_{is}}{c_{gA_0}} - \frac{r_s}{c_{gS_0}}\right)\right)}\right) e^{i\left(\omega\left(t - \frac{r_{is}}{c_{pA_0}} - \frac{r_s}{c_{pS_0}}\right) - \frac{\pi}{2}\right)}\right\}$$

$$for \qquad \frac{r_{is}}{c_{gA_0}} + \frac{r_s}{c_{gS_0}} \le t \le \frac{r_{is}}{c_{gA_0}} + \frac{r_s}{c_{gS_0}} + \frac{8\pi}{\omega} \tag{2.44}$$

and,

$$r'_s = r_{is} + r_s \tag{2.45}$$

$$r_{is} = |\vec{x}_i + \vec{x}_s| \tag{2.46}$$

$$A(r_s, \theta_s) = \frac{\left(1 + \sin\left(2\theta_s - \frac{\pi}{2}\right)\right)}{2\sqrt{r'_s}} \tag{2.47}$$

The expressions utilize the notation as described in Section 2.3.1 and illustrated in Fig. 2.12. The source and scatterer are located at $\vec{x}_i = (0.10, 0.33)$ m, and $\vec{x}_i = (0.10, 0.08)$ m respectively. Both source and scatter include a spreading term. The scatter also contains an angular amplitude variation to simulate the radiation patterns of an actual scatterer. As before the properties are,

- A_0 mode: c_g 2784 m/s, c_p 1737 m/s
- S_0 mode: c_g 5334 m/s, c_p 5359 m/s

simulating a 2 mm thick aluminum plate at 200 kHz. The excitation is a four-cycle tone burst. The simulated analysis area is outlined with the dashed line where $h = 0.2$ m.

A snapshot of the raw data and the FT of the data taken at the $k_x = 0$ 1/m orientation is shown in Fig. 2.13. A 3-D Tukey window is used to reduce leakage since FTs are used throughout

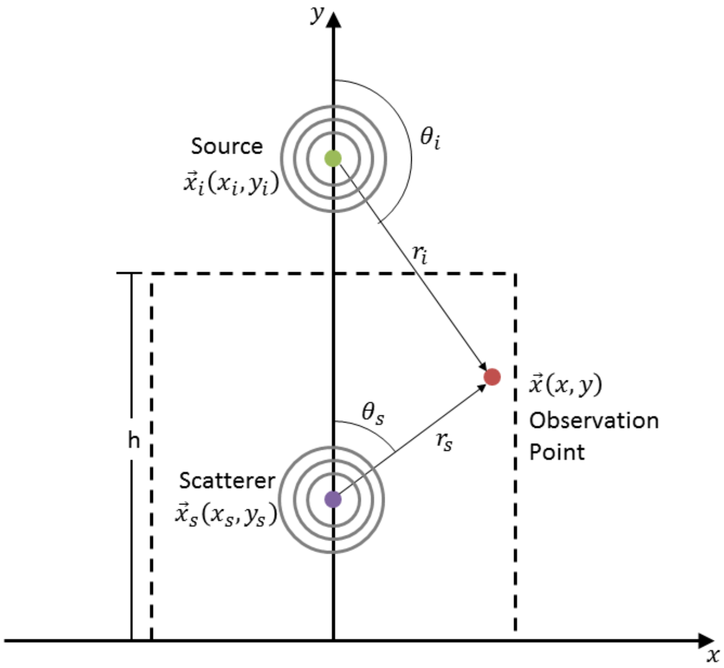

Figure 2.12 Schematic of synthetic dataset

the analysis. The first step in filtering the data is to separate the modes. This is done in the same fashion as the 1-D case using the Tukey filter. Multiplying this window by the signal in the 3-D Fourier Domain isolates just one mode. For this example, the A_0 mode is retained. Following this, the directional separation is performed using the filter described in Eqn. (2.32). The results of these two operations are seen in the four panels of Fig. 2.14.

At this point the signal is transformed back into temporal-spatial domain and a FT is taken in the time domain at the excitation frequency. This results in a single 2-D dataset with two spatial dimensions with complex displacements. Phase values for nodes whose amplitude are 15% of the global maximum value amplitude were set to zero. These points correspond to the area $y \leq y_s$ and only have non-zero amplitudes as a result of the FT and IFT used in the mode reduction and directional filtering. The wrapped phase can be taken directly from these complex values. The phase is then unwrapped following the method described in Section 2.3.2 utilizing open source code developed by Spottiswoode [72] implementing the Quality Guided Phase Unwrapping method with the Phase Derivative Variance quality metric [64].

The phase is extracted and unwrapped for the center frequency of the excitation and the

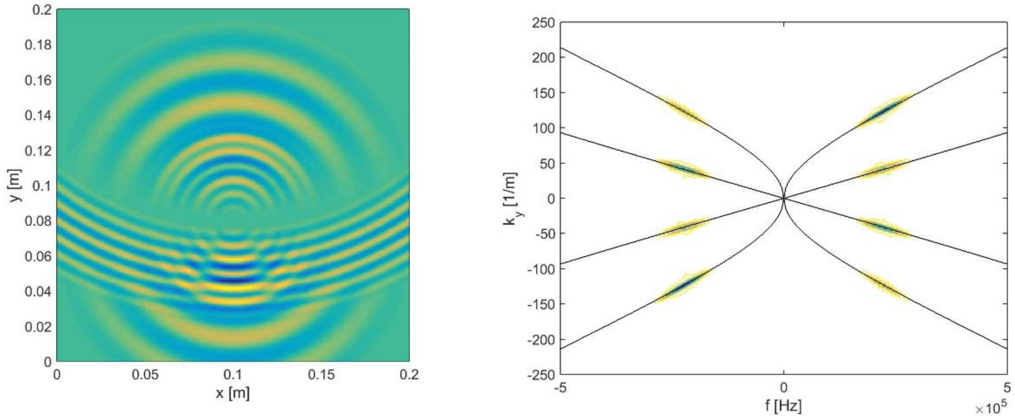

(a) (b)

Figure 2.13 Displacements for 2-D example in the spatial-temporal domain at t = 7.8e-5 s(a) and in the Fourier Domain (b) at $k_x = 0$

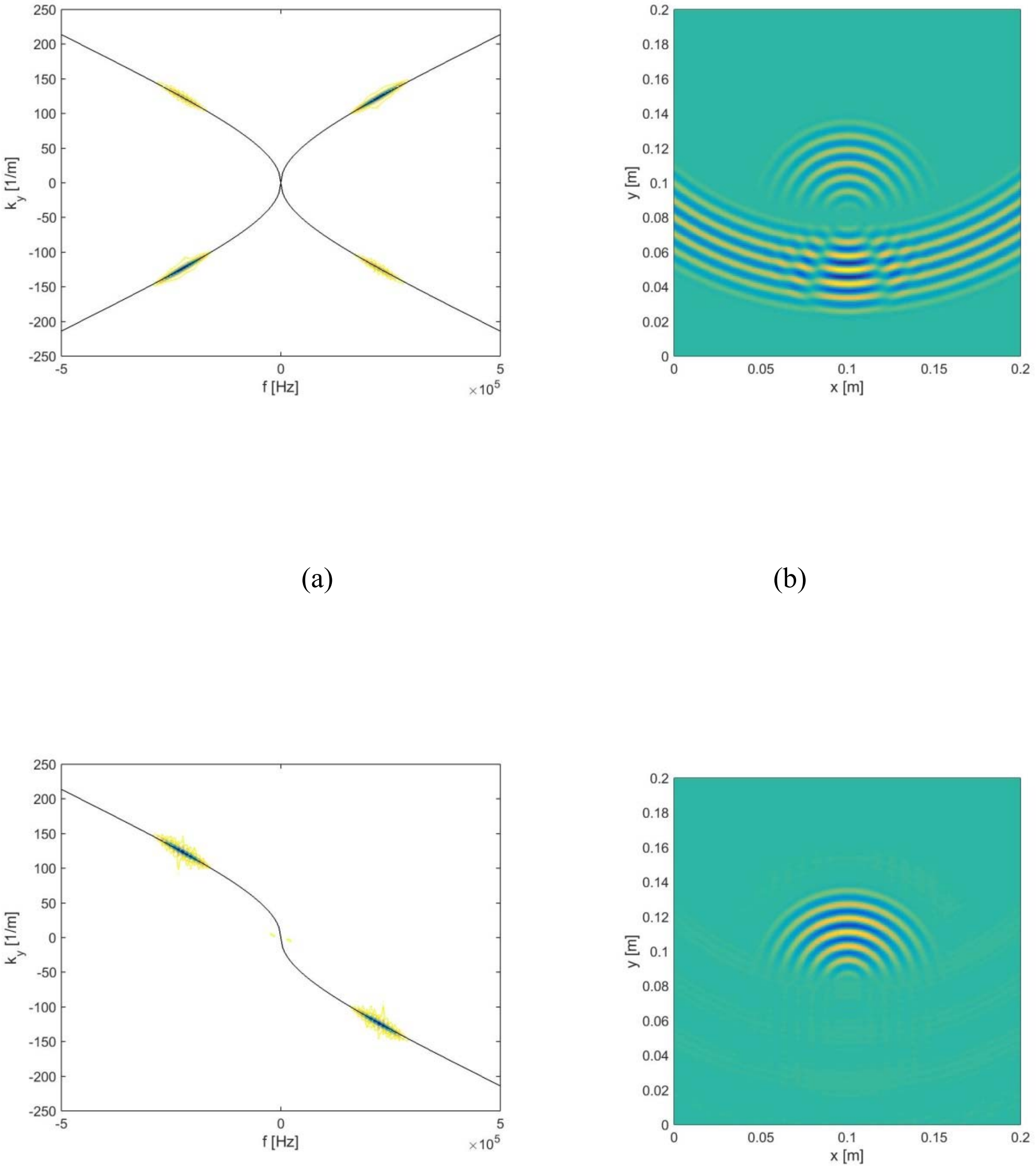

(a) (b)

(c) (d)

Figure 2.14 Displacements for 2-D example after modal filtering in the spatial-temporal domain (a) and in the Fourier Domain (b) and after directional filtering in the spatial-temporal domain (c) and in the Fourier Domain (d) two frequency bins on either side of the excitation frequency in the method as described in Section 2.3.2. These three phase planes are then averaged to reduce noise in the phase plane.

With the unwrapped phase, a set of nine seed points are set along the top edge of the analyzed area. These points serve as the starting point for the marching scheme given by Eqn. (2.40). The step size for the marching scheme was 0.5 mm. Since each step does not necessarily fall on a node, linear interpolations of the phase gradient is made to obtain the gradient vector at each new step location. Since the phase field is expected to have a linear variance with space, this is an appropriate interpolation method.

As this marching scheme progresses, the second derivative of the phase along this line is computed. The marching scheme terminates when a spike in the absolute value of the second derivative is reached. The termination point is retained and a point cloud was created to denote the location and extent of the scatterer. The results of the phase unwrapping, marching scheme and termination point cloud are seen in Fig. 2.15. The contour lines in the top panel (a) are the unwrapped phase field. The path of the marching scheme is given by the dashed black lines and the termination points given by the gray dots. The lower panel (b) just has the termination points given by the gray dots and location of source given by the black x.

The results clearly converge on the location of the scatter. In the subsequent section the method will be evaluated on numerical and experimental datasets as it was described in this section.

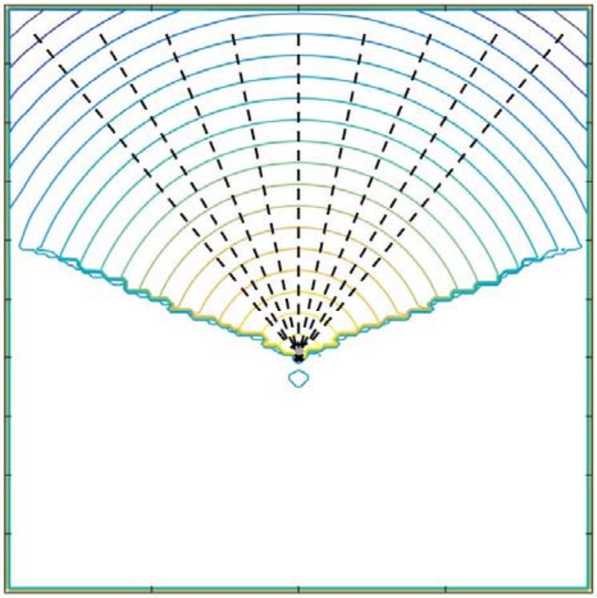

(a)

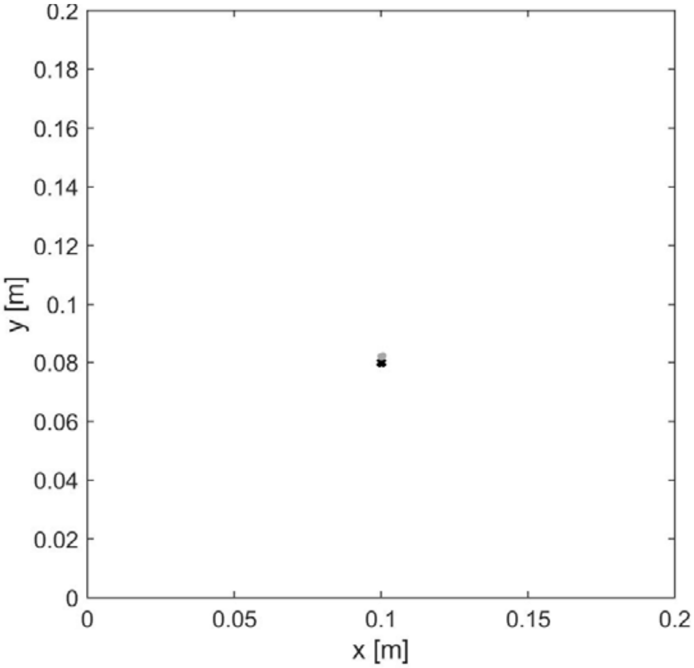

(b)

Figure 2.15 Results for the 2-D example.

2.6 Numerical Results

To validate the PG approach for 2-D wavefields, two damage types are considered: a notch and a delamination. The notch represents a surface breaking crack, while the delamination represents a separation between layers of the composite structure. This section presents the numerical models and their results.

2.6.1 Notched Plate

A notch in an isotropic material is considered first. The notch is formed by making a rectangular cut in a model of an aluminum plate. Due to the symmetry of the problem only of half the plate is modeled. Figure 2.16 (a) illustrates the dimensions of the plate as well as the simulated scanned region. The dashed line indicates the line of symmetry utilized in modeling. Table 2.1 lists the properties used for the materials considered in this chapter. The numerical model is created using ABAQUS/CAE interface [73]. The model is meshed with C3D8R, eight node rectangular, reduced integration, hourglass controlled elements. The regular geometry allows rectangular elements with 0.78 x 0.78 mm dimensions. The plate is discretized into five elements in the thickness direction.

The thickness of the elements varies with notch depth such that the elements align with the bottom of the notch. Figure 2.16 (b) shows an enlarged view of the notch in the meshed numerical model. Three defect depths are simulated: 0.8 mm, 1.2 mm and 1.4 mm with the plate thickness being 2.0mm making them 40%, 60% and 70% of the thickness of the plate. The notch is 12.5 mm long and 2 mm wide.

To excite the plate, a concentrated forced is applied on the node at the intersection of the plate’s edge and centerline. A transient four-cycle tone burst at 200 kHz is used to excite the plate. Pin constraints at each corner constrain any rigid body motion of the plate. The explicit solver uses a 2e-8 s step increment and runs for 100,000 iterations for a total of 200 μs. This time

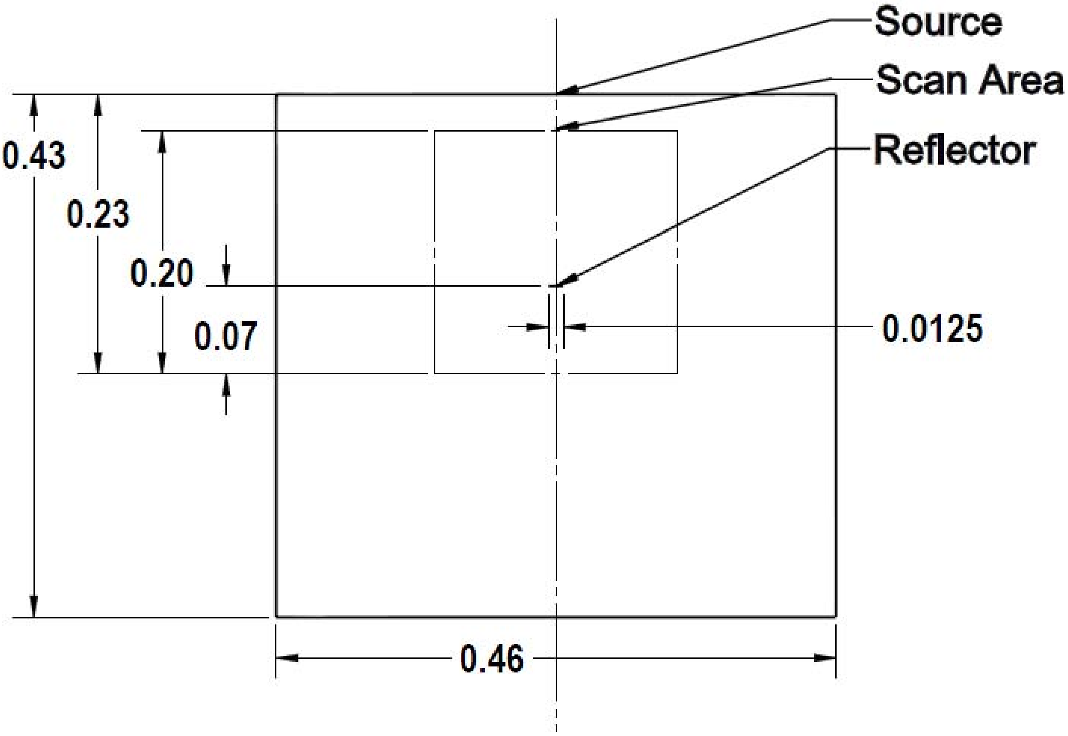

(a)

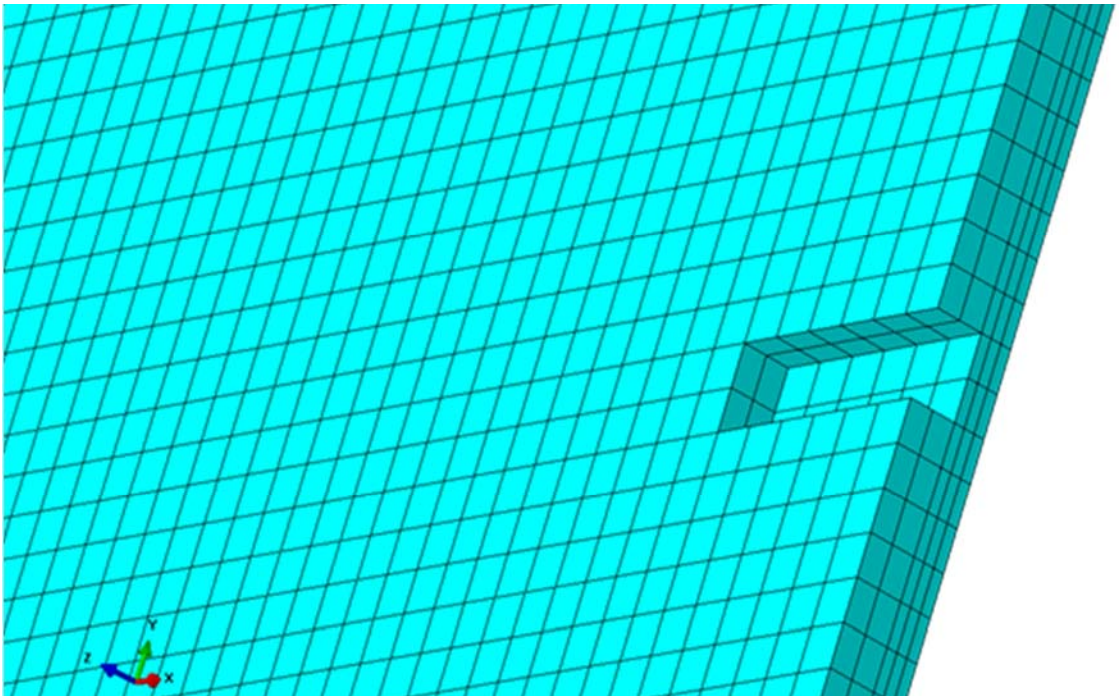

(b)

Figure 2.16 Layout of notched plate (a) (dimensions in m) and an illustration of the model of the notch (b).

Table 2.1 Table of plate properties

	Young's Modulus [GPa]			*Shear Modulus [GPa]*			*Poisson's Ratio*			*Density [kg/m^3]*
	E_1	E_2	E_3	G_{12}	G_{23}	G_{31}	ν_{12}	ν_{23}	ν_{31}	ρ
Aluminum	71.0			26.5			0.34			2700
Fiberglass	47.8	13.6	13.6	5.9	5.2	5.9	0.257	0.3	0.257	1980

step is far finer than what is necessary for analysis so the time dimension is decimated by a factor of 20 and truncated at 1.2 μs giving a total of 300 time steps.

The normal surface displacements from the numerical simulation are used to evaluate the PG method. The surface displacements at a single time slice as well as the FT of the data for the plate with the 1.4 mm deep notch are seen in Fig. 2.17 (a) and (b). With the data in the Fourier Domain, the directional separation and mode isolation is performed per Section 2.3.3. The results of these operations are seen in Fig. 2.17 (c) and (d). Since the modes are well separated in the Fourier Domain the results of the mode reduction are quite good.

Following this, the phase unwrapping procedure described in Section 2.3.3 is used to create the continuous phase field for three frequency bins: the frequency bin at the excitation frequency and the bins immediately above and below this frequency. Unwrapping three frequencies allows them to be averaged to reduce noise in the phase field. For illustrative purposes Fig. 2.18 shows the unwrapped phase along the centerline of the plate. The unwrapped phase of each of the three frequencies (solid lines) are shown along with the averaged value (x markers). The slope of the phase compares favorably with the prediction by the SAFE method (dashed line in Fig. 2.18) of the wavenumber at the center frequency of the signal. The slopes associated with each of the three frequencies is 116.06, 113.05, and 110.10 1/m as compared with 117.97, 115.00 and 112.01 1/m predicted with SAFE. The phase plot is smooth and continuous indicating that the phase

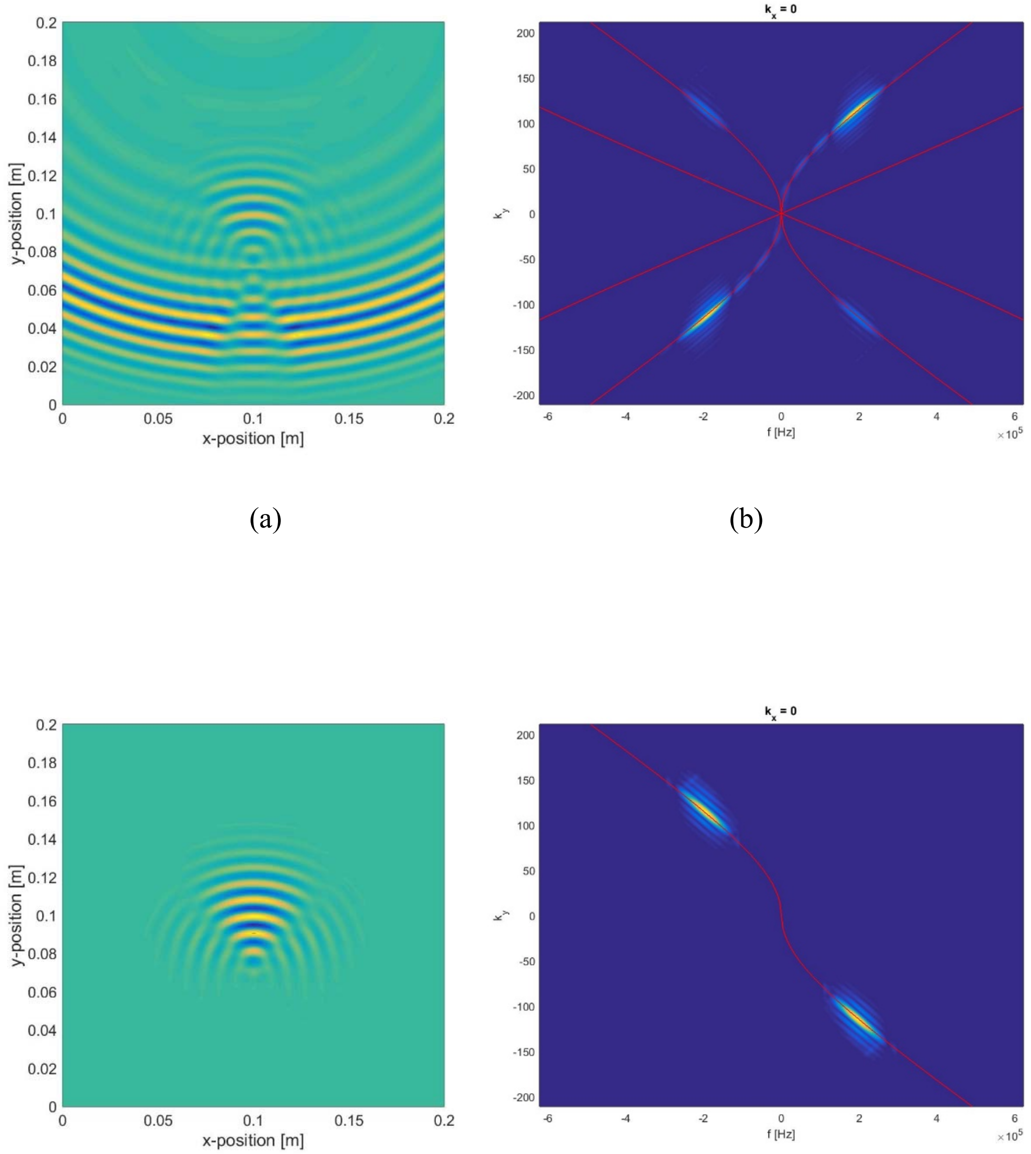

(a) (b)

(c) (d)

Figure 2.17 Displacements for numerical notched plate before filtering in the spatial-temporal domain (a) and in the Fourier Domain (b) and after directional and modal filtering in the spatial-temporal domain (c) and in the Fourier Domain (d) unwrapping performed as expected.

The three unwrapped phase fields are averaged resulting in the contours seen in Fig. 2.19 for all three notch depths. The contours denote the unwrapped phase field. Consistent with the results in Fig. 2.18, the slope of the phase is constant as is evident by the even spacing of the contour lines. The dashed lines give the path determined by the marching method, Eqn. (2.40). The constant slope of the unwrapped phase is evident in these lines since they converge directly on the notch location indicated by the horizontal gray line.

The paths defined by the marching scheme formed a set of 1-D paths along which the second derivative of the phase is taken. The gray dots indicate the location of the spike in the second derivative. These points create a point cloud estimating the shape of the defect. For all three depths, the points clearly indicate the notches location and span.

The major components of the phase unwrapping method perform as expected. The mode filtering isolated the reflected A_0 mode as indicated by both the constant slope and the value of the slope in Fig. 2.18 compared to the slope predicted by SAFE. The 2-D PG method correctly

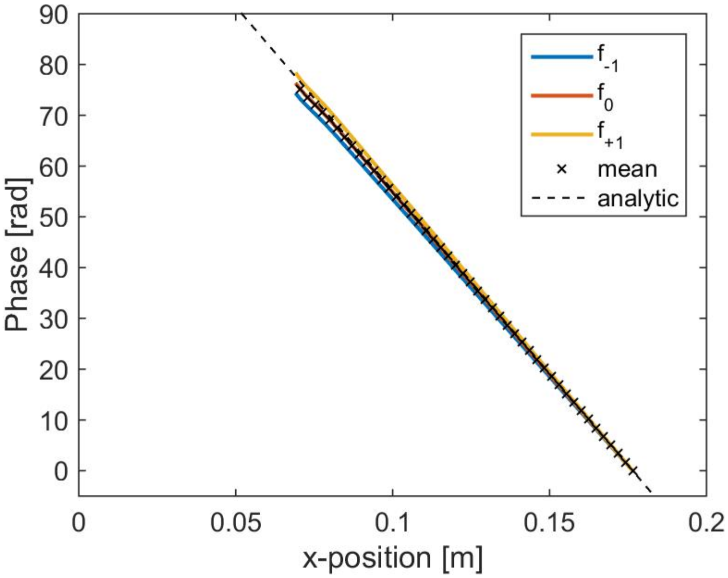

Figure 2.18 Phase unwrapping for 1.4 mm notch depth along plate centerline.

estimates the location and shape of the defect for all three depths seen in Fig. 2.19.

2.6.2 Composite with Delamination

The numerical model for the delamination simulates a quasi-isotropic fiberglass plate. The plate is made up of eight layers with the following layup orientation: [0°, 90°, 45°, -45°]$_s$. The properties relative to the ply orientation are given in Table 2.1. To simulate a delamination the nodes between layers two and three are decoupled in a circular area as depicted in Fig. 2.20. Figure 2.10 also illustrates the location of the source and the scanned region of the plate. The corners of the plate are pinned to prevent rigid body motion. The surface displacements of the model are extracted from the solution obtained with ABAQUS' Standard Explicit solver. The mesh for this model uses 0.25 mm x 0.25 mm x 0.2 mm C3D8R, eight node rectangular, reduced integration, hourglass controlled elements. The grid spacing is finer than necessary for the PG analysis so the data is down sampled and truncated to a 162 x 188 point grid with nominally 1 mm grid spacing corresponding to a roughly 0.16 m x 0.19 m grid. The excitation frequency for this model is 100 kHz four cycle tone burst. For the explicit solver, 512 3.14e-7 s time increments are used giving a total time of 150 μs. The data is truncated at 123 μs to reduce the size of the matrix and to truncate the data before the A_0 mode reaches back wall.

The composite plate with a delamination generates a much more complex wavefield than the notched case. The primary reason for this is the two-dimensional area of the delamination. The delamination causes the wavenumber over it to increase generating a new mode. This is seen in both the spatial and Fourier Domains. Figure 2.21 (a) shows the wavefield at $t = 102.2\ \mu s$. Over the delamination, the trapped energy is apparent. The signal in the Fourier Domain along $k_x = 0$ is seen in Fig. 2.21 (b). The dispersion curves from the simulation (color map) compare very well to the dispersion curves from SAFE for the pristine plate (red line). The additional wave mode due to the damage is seen at higher wavenumbers. This additional mode necessitated a narrow bandwidth

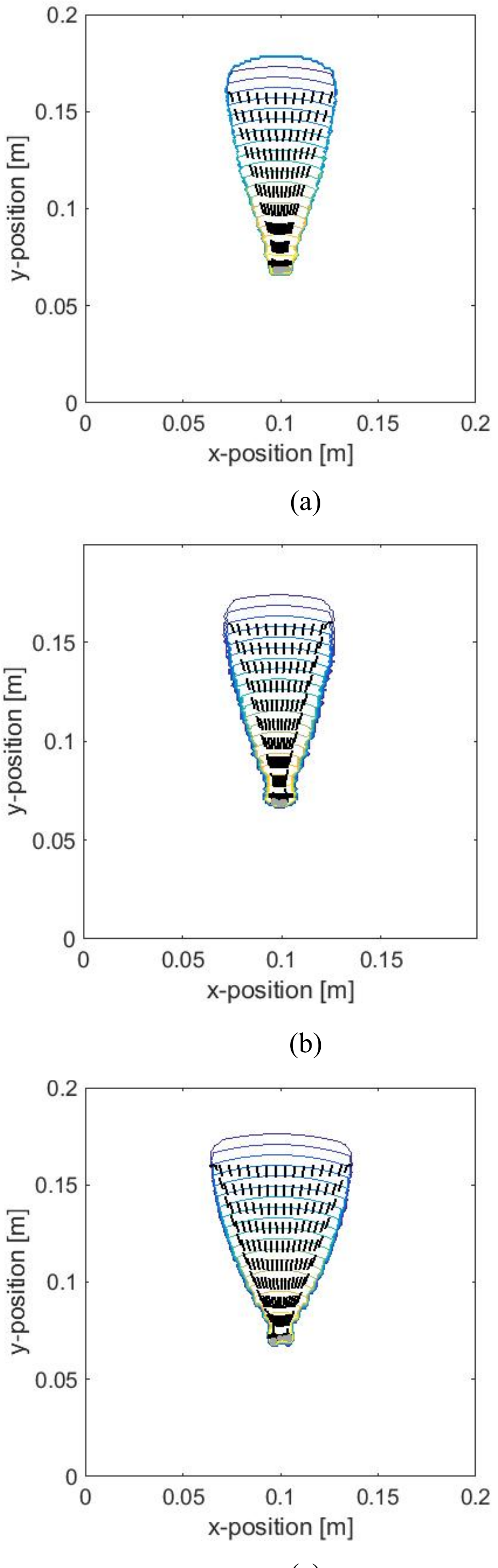

(a)

(b)

(c)

Figure 2.19 PG results for numerical notch model: (a) 40%, (b) 60%, (c) 70% notch thickness

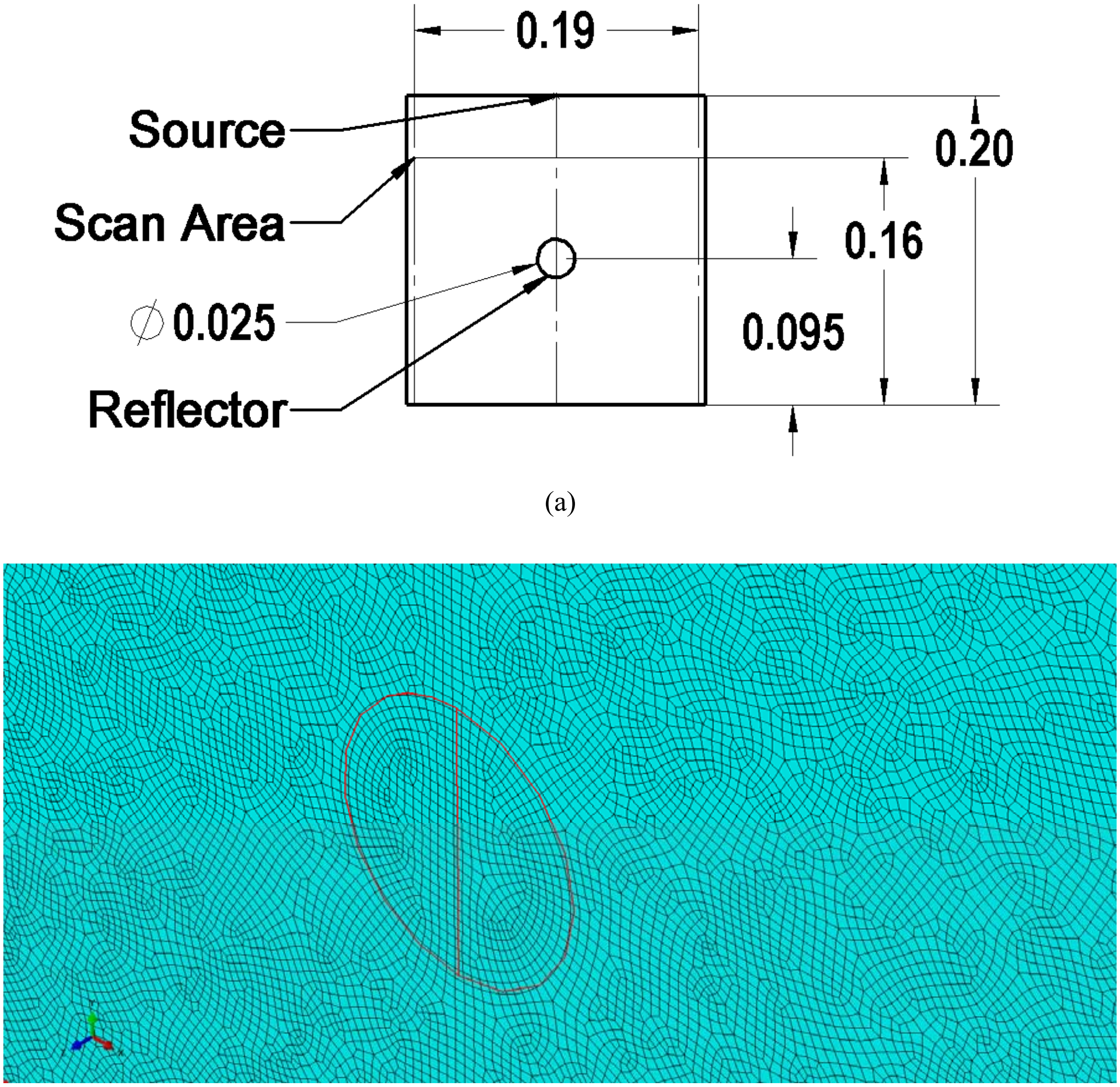

(a)

(b)

Figure 2.20 Schematic (dimensions in m) and mesh of delamination

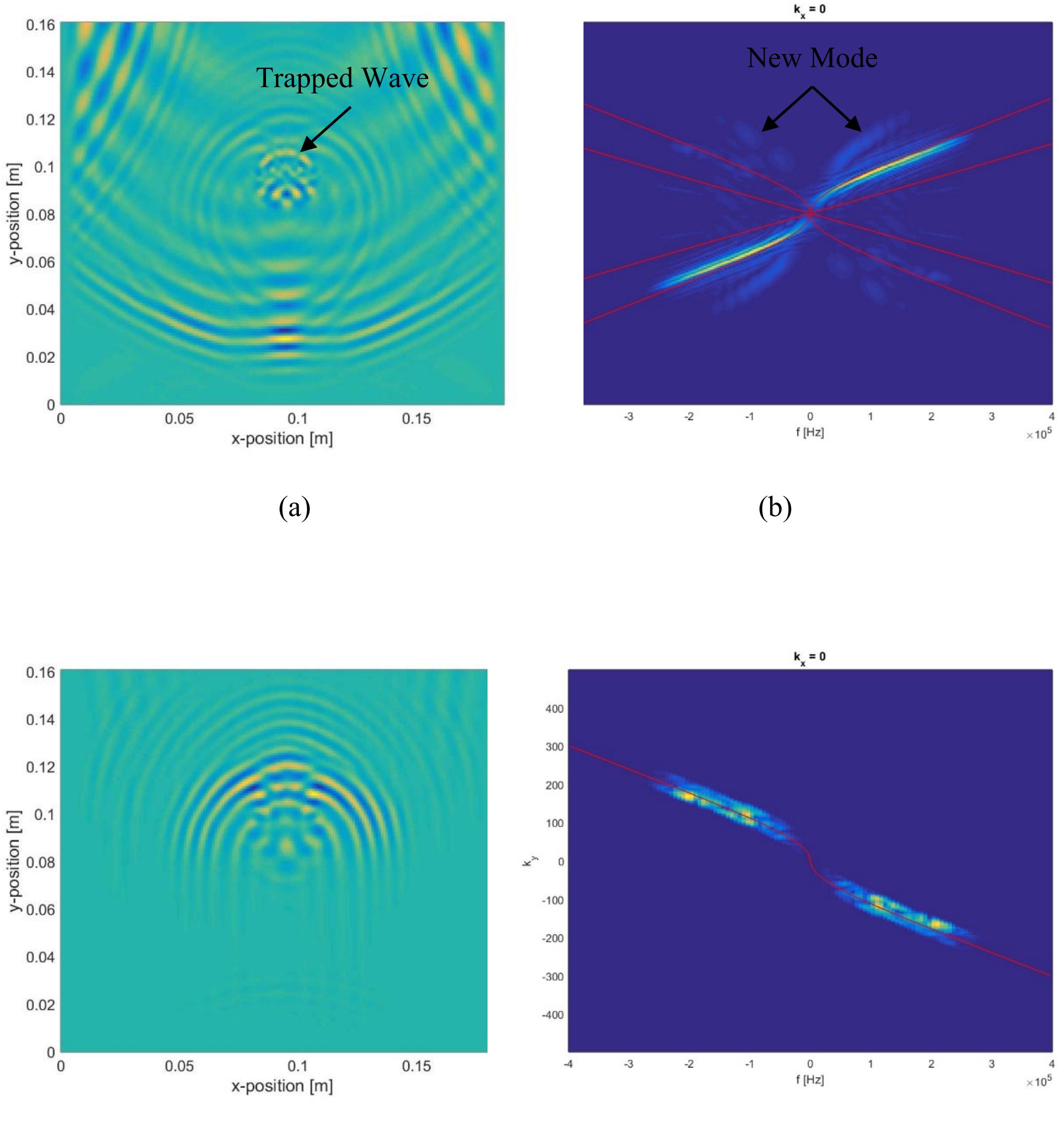

(a) (b)

(c) (d)

Figure 2.21 Displacements for numerical composite plate before filtering in the spatial-temporal domain (a) and in the Fourier Domain (b) and after directional and modal filtering in the spatial-temporal domain (c) and in the Fourier Domain (d) for the modal filtering. The filter had a width of 75 1/m, half the width of the filter used for the aluminum notch case. Despite the narrow filter (the results of which are seen in Fig. 2.21 (d)) the time-domain results in Fig. 2.21 (c) are quite acceptable as there is no obvious spreading in the filtered signal in Fig. 2.21 (c) compared to the original signal in Fig. 2.21 (a).

With a single mode isolated, the phase planes are now extracted and unwrapped. A slice of the phase plot along the y-direction and centered on the delamination is shown in Fig. 2.22. As in the numerical notch case, three frequencies are unwrapped: the center frequency of the excitation signal and the frequency bin above and below. These three phase fields are then averaged to reduce noise.

The unwrapped phase has the expected linear relationship with position. The gap in the phase plot is the area over the delamination. This area has a different wavenumber due to the smaller effective thickness of the layer (two plies over the delamination verses eight of the whole plate). Modal filtering reduces the amplitude of this content as it is a different mode, thus there is little signal or phase over the area of the delamination. The phase also contains a jump in the frequency band below the center frequency (*f*$_{-1}$) This may be due to the low amplitude waves behind the

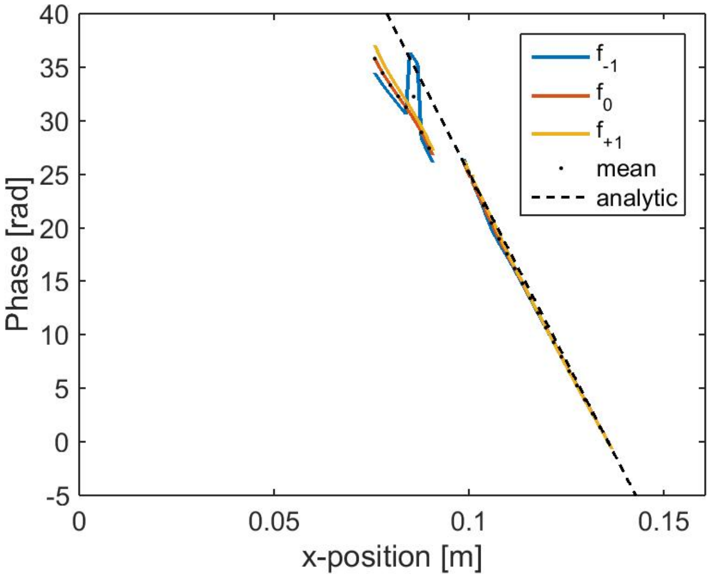

Figure 2.22 Unwrapped phase verse space for the numerical delamination model.

delamination seen in Fig. 2.21 (c) or the low amplitude content over the delamination remaining from the mode reduction process.

Results of the complete unwrapping process are seen in Fig. 2.23. In Fig. 2.23 (a) the contours illustrate the unwrapped phase field, the dashed lines indicate the path of the marching scheme, with the gray dots indicate the damage location estimates from the second derivative of phase along the path of the marching scheme. The black circle indicates the area of the simulated delamination. Figure 2.23 (b) gives just the estimation of the delamination (gray dots) relative to the actual location of the delamination (black line).

The bulk of the phase field above the delamination is a smooth with constant slope as indicated by the regular spacing of the contour lines indicating good results from the mode isolation, phase extraction and phase unwrapping techniques. Despite this, the gray points indicating the location of spikes in second derivative are clumped at the front and back of the delamination, thus limiting their ability to accurately estimate the damage location. Additionally, both groups are shifted significantly in the negative y-direction from the actual location of the damage. This shift is due to the FT and IFFT necessary for filtering. The FFT and IFFT process produces a smooth signal regardless of the discontinuities in the original signal since the basis function (sinusoid) is smooth. The smoothing stretches the discontinuity in space. Therefore, some signal is present beyond the discontinuity, allowing the source localization process to proceed past the discontinuity. Using local amplitude around the discontinuity identified by the source localization process may allow markers in the amplitude such as the Gibbs phenomena to be used to refine the estimate of the discontinuities location.

2.7 Experimental Results

Two experimental cases are considered that are analogous to the numerical cases. The first case presented is an aluminum plate with notches. The second is a fiberglass plate with a simulated

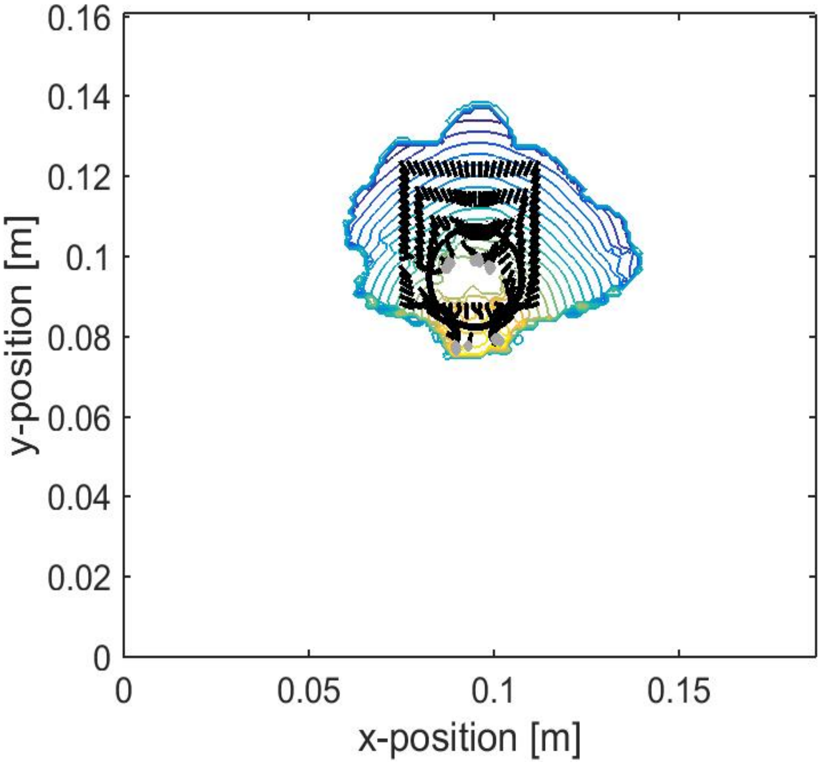

(a)

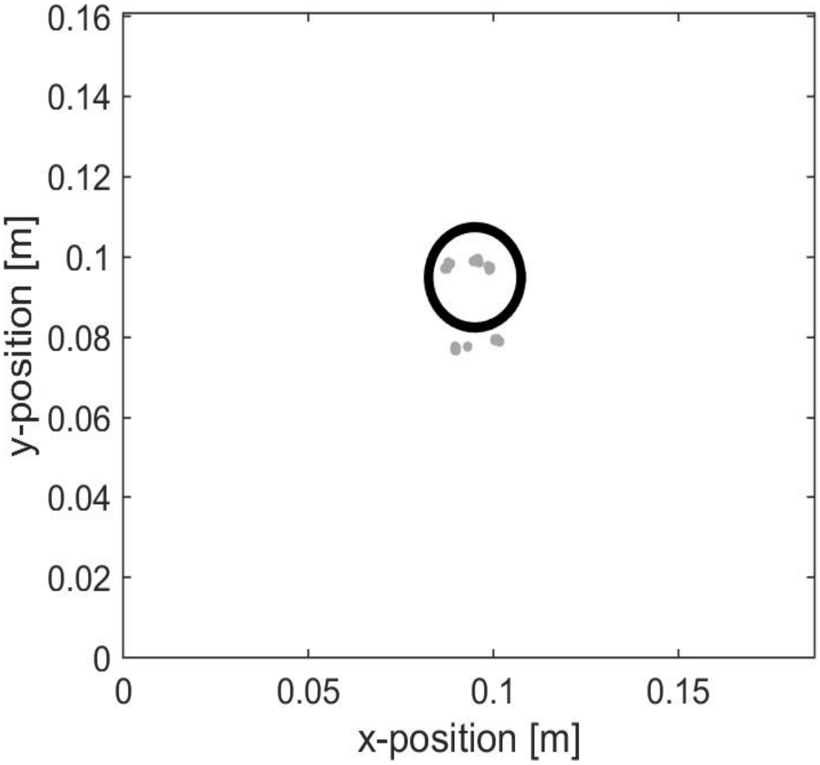

(b)

Figure 2.23 PG results for numerical delamination model delamination. The general experimental setup is consistent with the setup described in Section 1.4.

2.7.1 Notched Plate

The notched plate sample consisted of a 2mm thick aluminum plate with notches milled through a portion of the thickness (Fig. 2.24). The notches are 12.5 mm long by 2 mm wide. Four notches are used in this work with nominal notch depths of 1.2 mm, 1.4 mm, 1.6 mm and 1.8 mm. The plate's thickness is 2mm so the notches respectively represent 60%, 70%, 80% and 90% of the plate's thickness. Each of the scanned regions are covered with 3M Scotchlite Reflective Sheeting, a retroreflective tape. The tape enhanced the component of the laser beam that is reflected to the laser's scanning head and thus improves the measurement quality. The plate is oriented so that the notchse brake the surface of the plate on the opposite the measurement side. A function generator creates a 200 kHz four-cycle tone burst that is amplified to excite a 26 mm x 2 mm circular piezoelectric disk. The specimen is measured on a 113 x 115 point measurement grid with approximately 1.8 mm grid spacing.

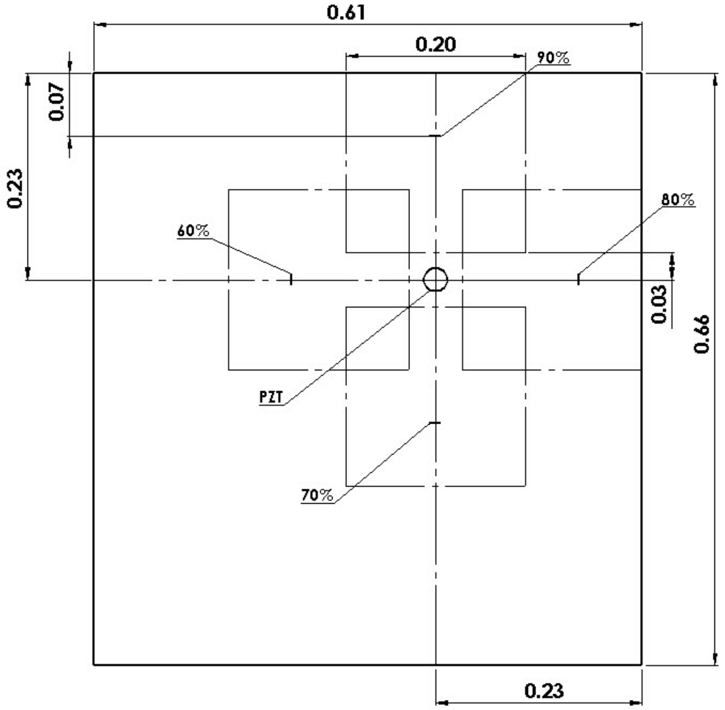

Figure 2.24 Schematic of experimental notch sample (dimensions in m)

The plate's normal surface velocity from the SLDV are the primary input to the PG method for the experimental samples. Four notch depths are considered in the experimental sample: nominally 1.2mm, 1.4 mm, 1.6 mm and 1.8mm. The analysis process described in Section 2.5 is followed to map the notches. Figure 2.25 illustrates the input data at $t = 77.7\mu s$ (a) along with its FT (b). The results of the modal and directional filtering are seen in panels (c) and (d).

To illustrate the results of the unwrapping procedure a slice of the unwrapped phase field for the A_0 mode of the reflected wave is shown in Fig. 2.26. This slice is taken along a vertical line passing through the center of the notch. The f_0 plot closely matches the phase gradient from SAFE calculations (the dashed line). The unwrapped phase is smooth and linear, consistent with the expectation of linear phase variation from the analytical analysis previously presented.

The results for the full procedure are shown in Fig. 2.27 - 2.28 for each notch depth. The contours are the unwrapped phase field, the dashed lines indicate the path of the marching scheme, the gray dots estimate the damage estimation from evaluating the second derivative of the phase along the paths of the dashed line and the thick solid black line locates the notch. Regular phase contours indicate that the phase unwrapped into a cone-like surface as predicted by the analytical models. The smooth and continuous phase field allows the marching scheme to converge on the notch.

The traces generally converge in straight lines towards the notch. In the case of the 60% notch, the amplitude of the reflected wave is small compared to the other cases. This in turn leads to a noisier phase plot as is evident in the waviness of the contour lines as well as the fact that the gradient traces are not straight. The traces converge on one another and follow the same path

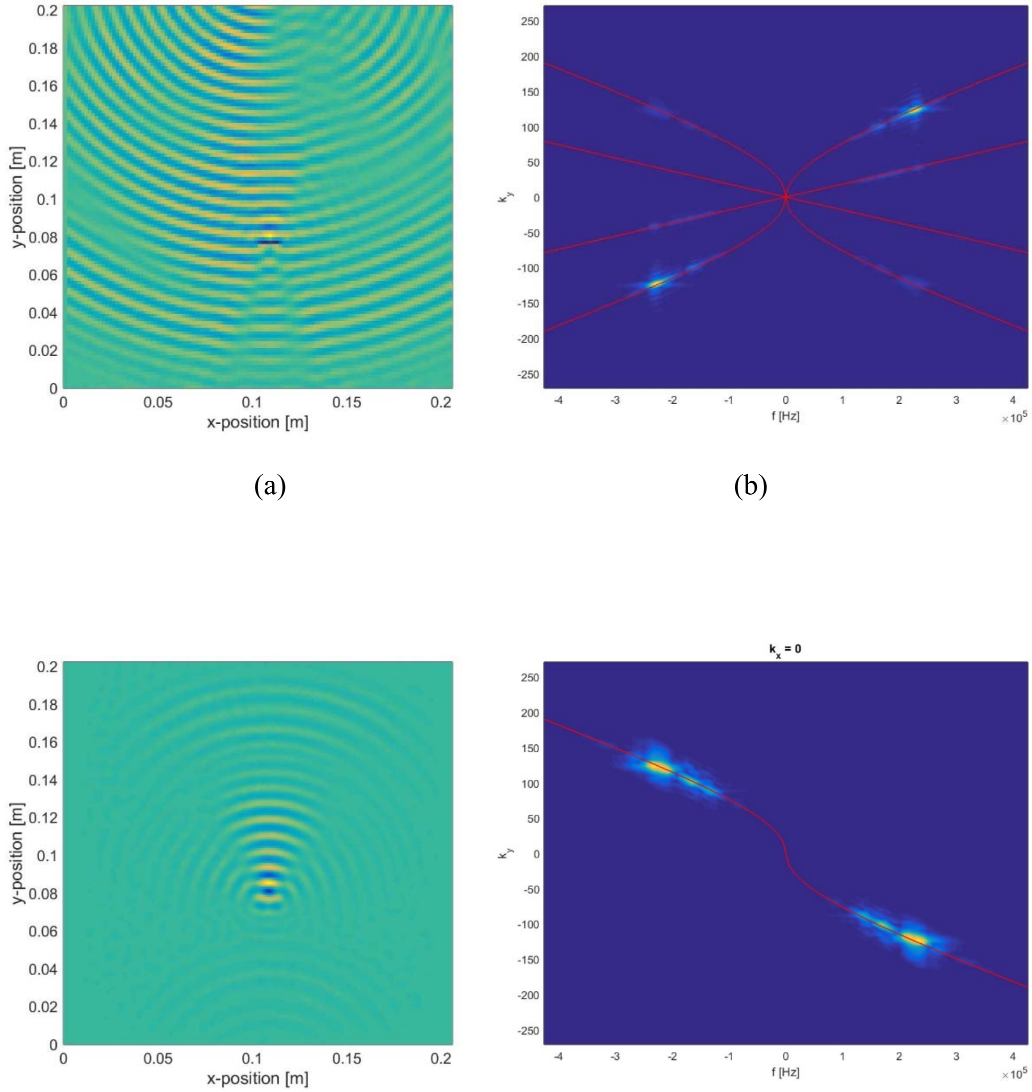

(a) (b)

(c) (d)

Figure 2.25 Experimentally measured displacements for a plate with a 1.4 mm deep notch before filtering in the spatial-temporal domain (a) and in the Fourier Domain (b) and after directional and modal filtering in the spatial-temporal domain (c) and in the Fourier Domain (d) towards the notch. This is due to the waviness in the phase field. The waviness leads to ridges and valleys in the surface. Since the marching scheme takes a path of greatest ascent, the scheme preferentially finds the ridges in the phase field and then follows them to the notch. Given that there are a finite number of ridges in the surface, multiple traces ascend the same ridge and follow that to the notch. Although this is not strictly speaking an issue, it does limit the number of unique estimates in the point cloud which describe the surface.

The trace terminations (gray dots) create point clouds that give a good estimation of the notches' span and position. The points in the 70% and 80% notch give the best estimation of both the span and position of the notch. This filtering procedure removes information in the wavenumber domain that leads to some spreading in the spatial domain. This causes the gradient traces to overshoot the notch by a small amount.

2.7.2 Composite with Delamination

For the experimental delamination case, the delamination is modeled by inserting a Teflon disk in between the second and third layers of a fiberglass plate. The plate geometry and delamination

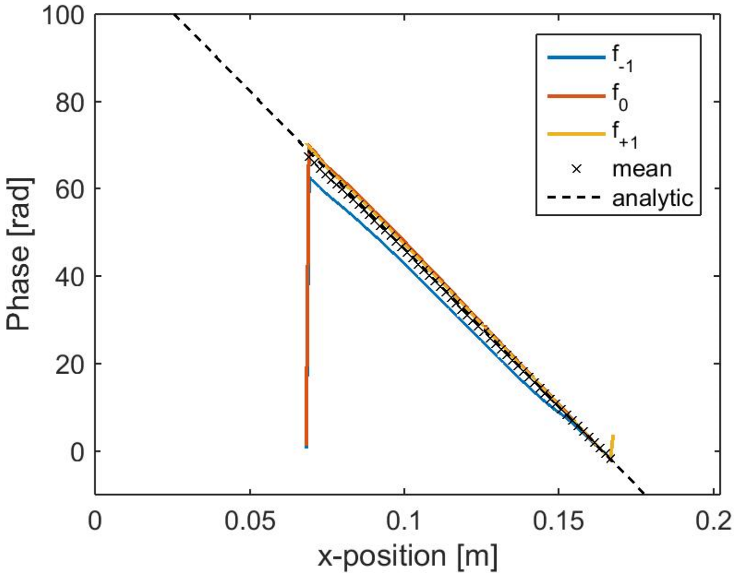

Figure 2.26 Phase unwrapping results for experimental notch sample (1.2mm depth)

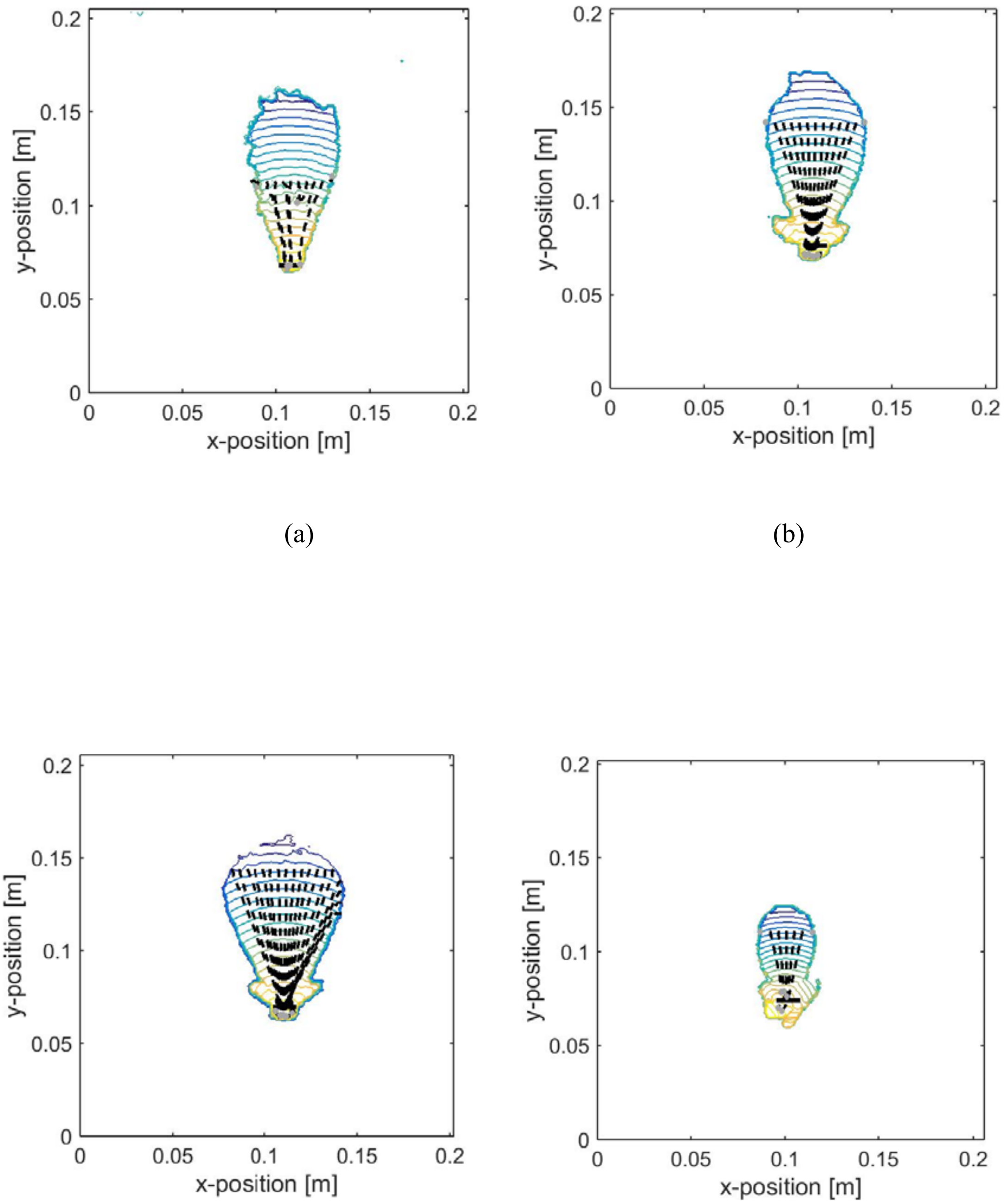

(a)

(b)

(c)

(d)

Figure 2.27 PG results for experimental notch sample: (a) 60% notch depth, (b) 70% notch depth, (c) 80% notch depth, (d) 90% notch depth

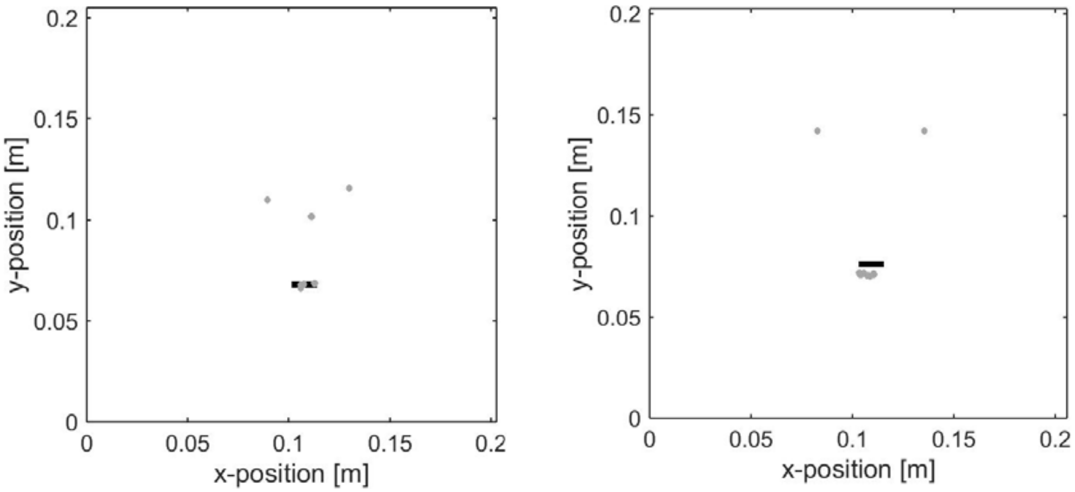

(a)

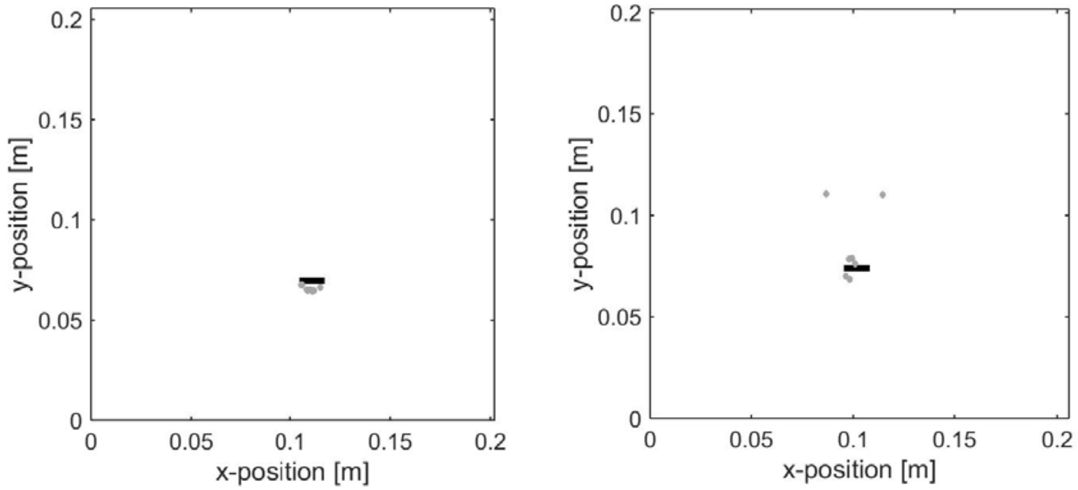

(b)

Figure 2.28 PG results for experimental notch sample: (a) 60% notch depth, (b) 70% notch depth, (c) 80% notch depth, (d) 90% notch depth location are seen in Fig. 2.29. Eight layers of S2 fiberglass with CYCOM 5216 epoxy are used to construct the plate giving a finished thickness of 1.6 mm. The ply orientation is consistent with the numerical model: $[0^\circ, 90^\circ, 45^\circ, -45^\circ]_s$.

Using the experimental set up described in Section 1.4 the sample is excited with a 15 mm x 2 mm circular piezoelectric disk driven by a four-cycle 264 kHz tone burst. The surface velocities are measured at 2.56 MHz on an 85 x 83 point grid with a nominally 1.3mm grid spacing. Five hundred and twelve samples are taken at each point giving the time series a 200 μs duration.

Again, the normal surface velocity measurements taken directly from the SLDV are used as the input to the PG method for the experimental samples. The procedure in Section 2.5 is used to analyze the measured data. First, the wavefield is reduced so that only the reflected A_0 mode remains. Figure 2.30 (a) shows a time slice of the data at $t = 9.73E - 5\ \mu s$ with panel (b) giving the dispersion curves at $k_x = 0$. The contours show the experimental data while the red lines give the SAFE solution. Panels (c) and (d) illustrate the reduced wavefield. In this case, the A_0 mode is

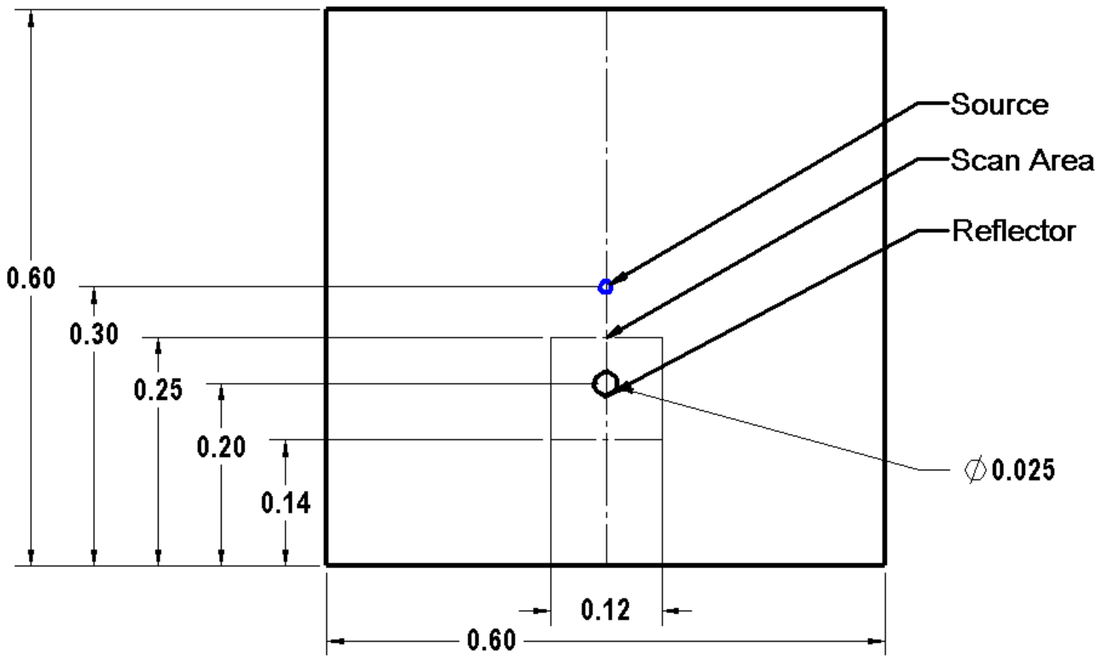

Figure 2.29 Schematic of experimental delamination sample (dimensions in m)

the retained.

Illustrating the unwrapped phase, a slice of the phase field along a line in the y-direction passing through the center of the notch is shown in Fig. 2.31 (a). As in the numerical case, three frequencies are unwrapped: the center frequency of the excitation signal and the two adjacent frequency bins. The slope of the mean value and the f_0 plots closely matches that of the analytical calculation given by the dashed line. The slopes are most constant on the right portion of the figure. This corresponds to the reflected wave propagating back towards the source. The center portion of the chart from $y = 0.039$ to 0.064 m corresponds to the section over the delamination. This area does not have a constant linear slope. Here, there is a second mode generated over the delamination that is partially filtered out. Comparing Fig. 2.31 (a) to Fig. 2.30 (c), the wavefield over and behind the delamination has a lower amplitude that then phase field above the delamination. The amplitude over the delamination results from the mode reduction, while the low amplitude below the delamination is the result of the directional separation. Despite these two reductions to the wavefield, there is still some energy over the delamination and behind the delamination. These low energy areas are causes noisy phase fields like what is seen in Fig. 2.31 (a) from approximately $y = 0.03$ to 0.064 m. This area also includes some large jumps, possibly due to the low amplitude, or the recombination of waves that wrapped around the discontinuity and then recombined behind it.

The PG results for the delamination are seen in Fig. 2.31 (b) and (c). Like in the numerical case, they are not as good as for the notch. In this figure, the phase plane is indicated by the contours, and the path of marching scheme by the dashed lines. The second derivative of the phase is taken along the path of the marching scheme and the discontinuities detected are the gray dots. The black circle indicates the location of the delamination.

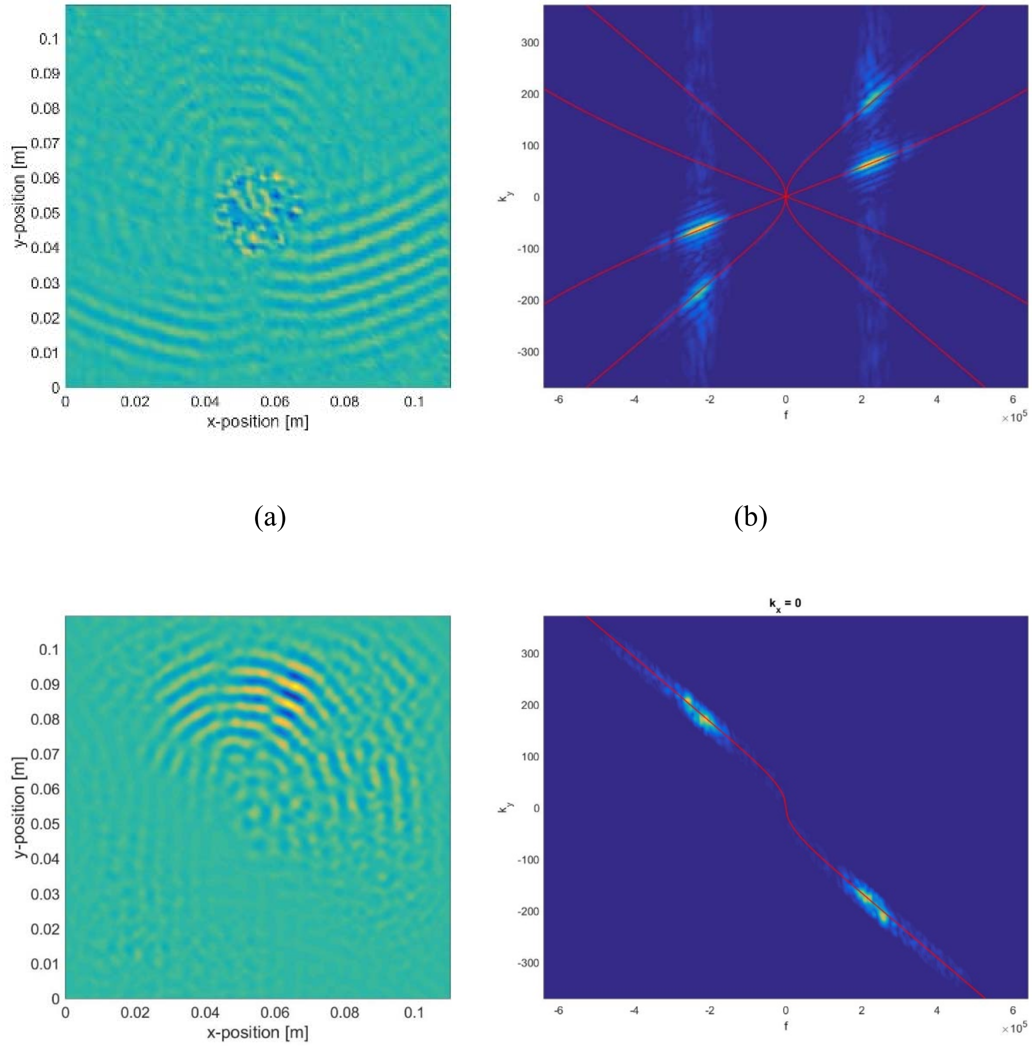

(a) (b)

(c) (d)

Figure 2.30 Experimentally measured displacements for composite plate before filtering in the spatial-temporal domain (a) and in the Fourier Domain (b) and after directional and modal filtering in the spatial-temporal domain (c) and in the Fourier Domain (d)

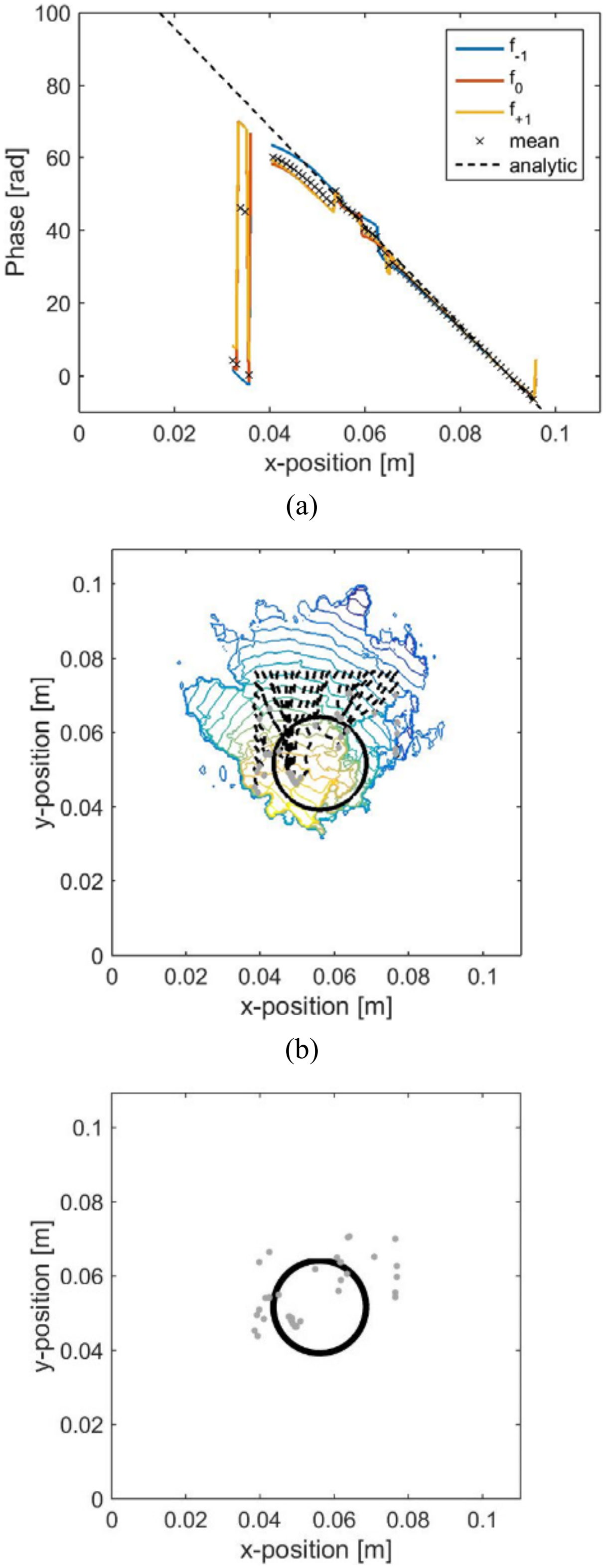

(a)

(b)

(c)

Figure 2.31 Results for the experimental delamination sample, (a) phase unwrapping results, (b) PG results with contours and without (c)

The more complex defect and reflected wavefield result in a less regular phase field. There are several lines in the phase plane contours running approximately perpendicular to the phase contour lines. These indicate distinct portions of the phase plane that did not line up with one another. These distinct portions occur because of directionality of the reflected wave. The directionality produced multiple lobes in the reflected wavefield.

These lobes formed boundary seen in Fig. 2.31 (b) which prevented the marching path from reaching the lower right side of the delamination. The marching path headed towards the delamination however the complexities of the phase field prevented accurate estimate of the phase field. Figure 2.31 (c) shows just the damage estimate (gray dots) compared with the actual damage location (black circle). It is clear that this estimate does not clearly represent the map of the delamination.

2.8 Conclusions

Two different types of defects are considered, a notch simulating a linear defect across the thickness of the plate and a delamination in the plane of the plate. The results from each of the two types vary substantially. The results for the notch are quite good. A reasonable approximation of the notches' extent and location is estimated for the numerical and experimental models in the range of notch depths considered. The delamination on the other hand fails to capture the shape of the delamination and had a considerable shift in space.

There are many possible reasons why the delamination estimates is not as good as the notch estimates. The first is in removal of the trapped wave over the delamination with the mode filtering process. The trapping of energy leads to high amplitude over the delamination relative to the reflected wave's amplitude. While much of the energy over the delamination is removed, enough remains that it is on the order of the reflected waves energy levels. Second, the reflected wave tends to radiate along six radial lines. The boundaries between several of these are seen as discontinuities in the phase field in Fig. 2.31 (b). The breaks in the phase field tend to force all traces to a single portion of the surface. This is seen in the cluster of points in the lower left of the delamination, while the lower right has no points to estimate its location. The discontinuities in the phase plane are seen to prevent the traces from reaching the lower right corner. This prevents complete estimation of the damage's extent.

In the case of the notch, although all four notch depth yield good estimations of the damage span and location, the lower amplitude reflections in the 60% notch depth case appear to approach the limits of the method. As the level of the reflected wave decreases towards the noise level, the noise has an increasing influence on the phase field. This influence is seen in the irregularities of the phase field and the convergence of the gradient traces on ridges of the phase field. This leads to fewer unique points in the point cloud estimating the notch, thus lower resolution of the defect.

The Phase Gradient process is well suited to crack like defects with strong reflection coefficients while weaker reflected wavefields reduce the resolution of the resulting point cloud. For more complex defects such as the delamination, the PG method is not able to define the full extent of the defect. Breaks in the phase field cause the traces to map limited sections of the damage. This leads to an incomplete map of the damage. This technique is most appropriate for crack like defects.

CHAPTER III

PHASE CONGRUENCY FOR DAMAGE MAPPING

3.1 Overview

Phase Congruency for damage mapping is a technique that maps damage by analyzing wavefield images. The method is adapted from an image processing technique for edge detection. This work modifies the method to map boundaries of damage in a wavefield. The method makes use of filter bank analysis to decompose the spatial domain of the wavefield and compare the phase of the components. Locations where the components have equal phase denote the presences of damage.

The first section of this chapter provides an overview of Phase Congruency as developed for image processing. The next section addresses adjustments to improve the method when used with GW for damage mapping. In the third section, the procedure for implementing the PC for damage mapping method is demonstrated on synthetic data.

3.2 Phase Congruency for Image Processing

The Phase Congruency method for mapping damage draws on the previous work done for image processing on edge detection [65]. Figure 3.1 (b) illustrates the use of Phase Congruency for detecting edges in the image in (a). The basic concept of Phase Congruency as it was developed for image processing will be reviewed in this section. Particular attention is paid to the use of filter banks as it will inform the adaptations of method necessary for use in wavefield analysis.

3.2.1 Concept

Researchers studying human visual processing noticed humans make use of the phase of components from a decomposition of an image in the spatial domain when detecting and locating edges [74-77]. This led the researchers to realize that one indicator of an edge in an image is the alignment of the phase of components from a spatial Fourier Expansion of the image [74, 75, 78, 79]. Here an edge is defined as a discrete change in luminance in the image (e.g. a step edge), a narrow change in luminance (e.g. a line) or a signal with a continuous luminance profile, but a discontinuity of the first derivative of the luminance profile (e.g. a triangle function). This concept forms the basis for the Phase Congruency method for edge detection in images.

Taking a square wave as an example of a 1-D image where the amplitude represents a signal with discontinuities.

$$u(x) = \text{signum}\left(\sin\left(\frac{2\pi}{P}(x - x_0)\right)\right) \tag{3.1}$$

where P denotes the period of the square wave and x_0 indicates the location of the fundamental discontinuity with subsequent discontinuities at $x = x_0 \pm \frac{mP}{2}$ where m is any integer. This signal can be decomposed into its Fourier Expansion of the signal. Taking the Fourier Expansion of the signal as

$$u(x) \cong u_N(x) = c_0 + \sum_{n=1}^{N} 2c_n \cos\left(\frac{2\pi n}{P}x - \theta_n\right) \tag{3.2}$$

with,

$$C_n = \frac{1}{P}\int_{x_0}^{x_0+P} u(x)e^{-\frac{i2\pi n}{P}x}dx \tag{3.3}$$

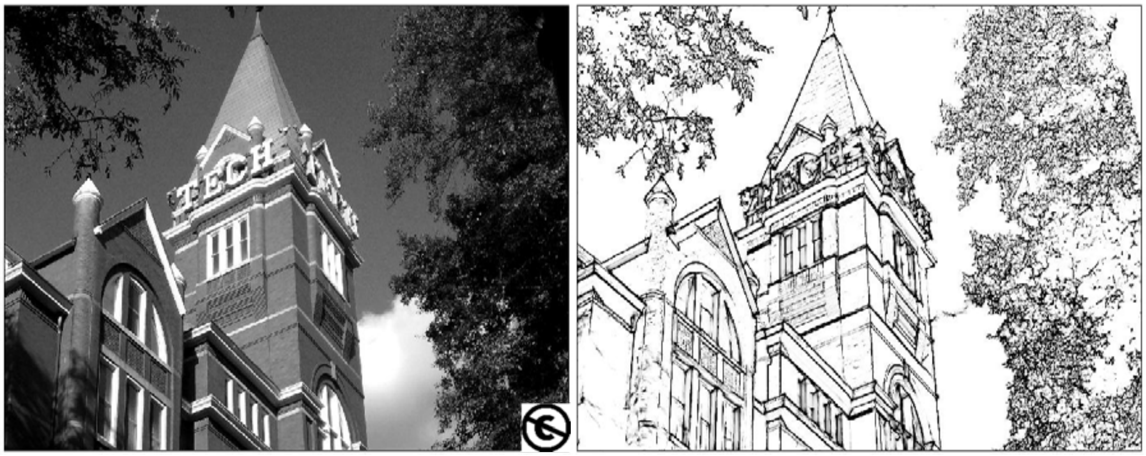
(a) (b)

Figure 3.1 Example of edge detection with PC [1]: the input image (a) , output of PC method (b)

$$C_n = c_n e^{i\theta_n} \tag{3.4}$$

This yields an approximation of the signal on a cosine basis,

$$u_N(x) = \sum_{n=1}^{N} \frac{2}{\pi n}((-1)^{n+1} + 1)\cos\left(\frac{2\pi n}{P}(x - x_0) - \frac{\pi}{2}\right) \tag{3.5}$$

When the phase of approximation is evaluated at the discontinuities, $x = x_0$ and $x = x_0 + \frac{P}{2}$ the value of each term in the summation is

$$\varphi_n(x_0) = -\frac{\pi}{2}, n = 1,3,5 \ldots N \tag{3.6}$$

$$\varphi_n\left(x_0 + \frac{P}{2}\right) = \frac{\pi}{2}, n = 1,3,5 \ldots N \tag{3.7}$$

It can clearly be seen from Eqn. (3.6) and (3.7) that for all odd values of n, u_n has constant phase at each discontinuity (even values of n have zero amplitude). At $x = x_0$ all components have a phase of $-\pi/2$ and at $x = x_0 + \frac{P}{2}$ all components have a phase value of $\pi/2$ (Fig. 3.2). The signal $u(x)$ and the reconstruction from three terms, $u_3(x)$, is shown in the upper panel (a) and the phase of each term is seen in the lower panel (b). The areas circled in red are the locations where the phase of each component aligns, i.e. points of phase congruency. Congruency occurs at the location of each edge, with phase values of $-\pi/2$ and $\pi/2$. The same exercise can be performed for edges represented by discontinuities in the first derivative of a signal such as a triangle wave. The results will be that the peak exhibits a phase values of zero for all components and that the valleys have phase values of π [79].

Since phase alignment is seen to be an indicator a metric for quantifying the phase alignment can be defined as [79],

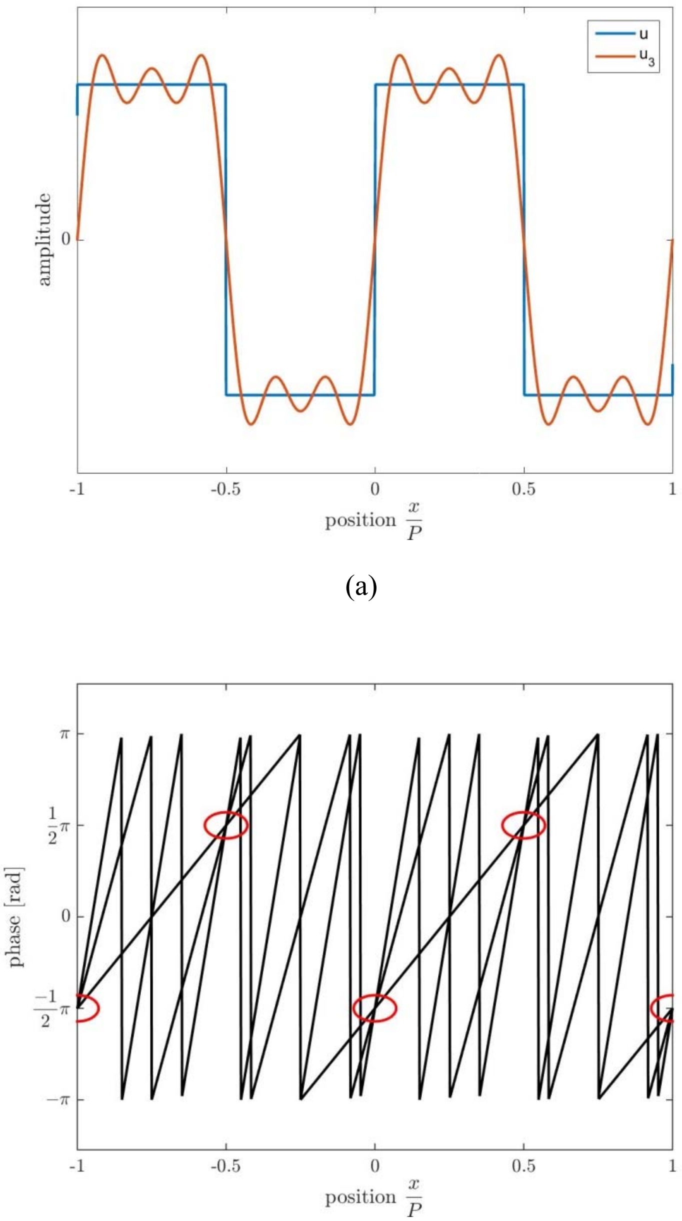

(a)

(b)

Figure 3.2 The signal $u(x)$ and its reconstructed estimate $u_3(x)$ from a Fourier Decomposition showing magnitude (a) and phase (b)

$$PC(x) = \frac{E(x)}{\sum_{n=1}^{N} a_n(x)} \tag{3.8}$$

Figure 3.3 illustrates a graphical way of describing Eqn. (3.8). On the left is a set of complex components plotted on the complex plane, where complex components are calculated from the real part using its Hilbert Transform,

$$A_n(x) = c_n \cos(nkx + \varphi_n) + ic_n \sin(nkx + \varphi_n) \tag{3.9}$$

and

$$E(x) = \left|\hat{E}(x)\right| = \left|\sum_{n=1}^{N} A_n(x)\right| \tag{3.10}$$

$$a_n(x) = |A_n(x)| \tag{3.11}$$

for an arbitrary position that is not a discontinuity. The sum of their magnitudes is greater than the magnitude of the resulting complex value, $\hat{E}(x)$ represented by the dashed line. On the right is a vector plot in the complex plane where the vectors do align. Here it is easily seen that the sum of vector magnitudes is exactly equal to the magnitude of the resulting vector. This illustrates that by Eqn. (3.8) the maximum value for $PC(x)$ is one and its lowest possible value is zero.

It is important to notice two points that are masked by the simplicity of the example square wave. First, there is no DC offset, a_0. For real signals, this will always be a real constant. For this

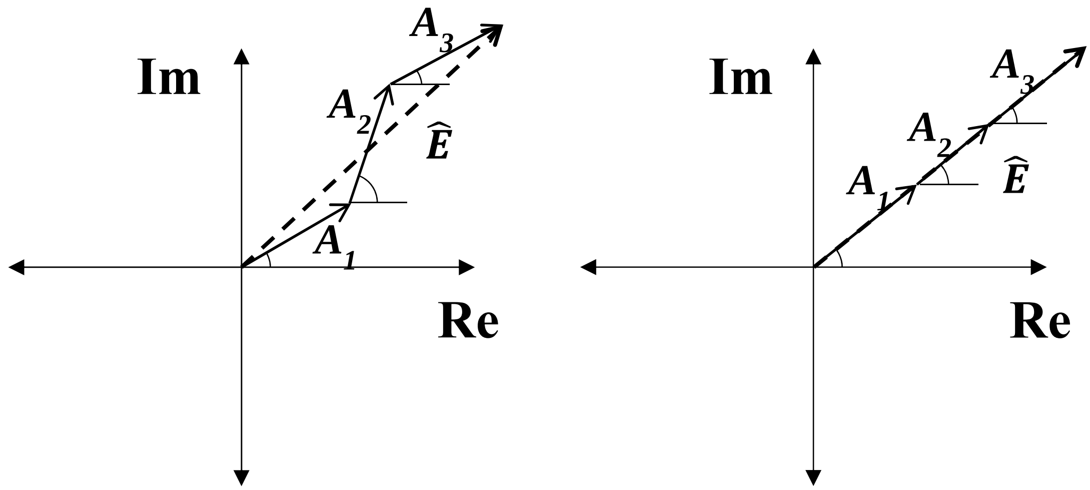

Figure 3.3 Illustration of three component vectors.

reason, it should be discarded, as it will not add any information regarding the discontinuity. Second, the choice of basis function for the Fourier Expansion has bearing on the results. Since the signal considered is purely real, the cosine basis with only positive values of n completely describes the signal. Had the decomposition basis been the complex exponential both positive and negative values of n would be required. The positive and negative indexes would form a pair of complex conjugate signal components. Their vector sum would always yield a real value thus the angle where the components align, the angle of congruity, would be confined to zero or π. Utilizing the cosine function retains the full range of possible congruency angles thus is the preferred basis function.

In this section, the basis of the Phase Congruency method is presented as developed by Venkatesh and Ownes [79]. Fundamentally, the method tests for alignment of phase components by comparing the sum of the vector magnitudes to the magnitude of the overall vector sum. This presentation uses a Fourier Expansion to decompose the signal. This works well for the simple square wave example used in this section. The next section will show how filter banks instead of the Fourier basis can be used to describe signals with coefficients that are a function of space.

3.2.2 Phase Congruency with Filter Banks

In the square wave example in Fig. 3.2 the signal has constant periodicity P. Therefore, the Fourier coefficients, which are constant in space, accurately describe the signal over all space. This is not representative of the signals of interest in general. In general, the spectral content of the signal may change in space. To describe this spatial change in wavenumber content, a method other than a Fourier Decomposition is needed. Gabor discusses this duality between the space and wavenumber domain and the inherent uncertainty in each domain when computing windowed FT [80]. Take for example a signal with a change in wavenumber at the midpoint as shown in Fig. 3.4 (a). If one are to take the FT of this signal, both wavenumber components would be present at all positions as is shown in Fig. 3.4 (b) (note that the spectrum of the FT is repeated for all points in space to illustrate its invariability in space). However, if one were to isolate only part of the signal with a spatial window and take the FT of the windowed signal, then the FT would represent the part of the signal within the window. By sliding the window in space such that a FT associated with each point in the signal are computed, then a spatially dependent spectrum like the one seen in Fig. 3.4 (c) would be created.

Signal analysis using traditional windowed FT is a common method for analyzing the wavenumber content of a signal as a function of space, and one that will be employed in this work. However, it can be more practically applied in the Fourier Domain [81, 82]. To show this consider a real signal, $u(\xi)$ on the dummy spatial domain ξ. A dummy wavenumber variable κ is used along with the windowing function, $g\big(\xi - x, a(\kappa)\big)$, which is both a function of space and wavenumber by the scaling factor $a(\kappa)$. The window $g\big(\xi - x, a(\kappa)\big)$ is evaluated at position x to yield the windowed signal $u'(\xi)$.

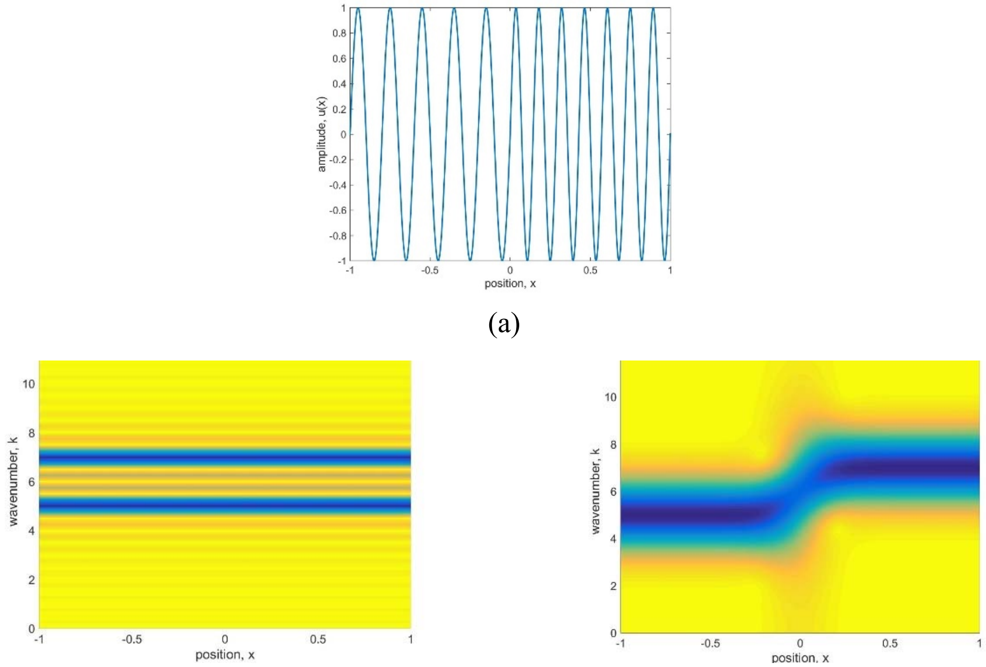

(a)

(b)

(c)

Figure 3.4 Example of signal with a change in spectral content at *x* = *0* (a) and it Fourier Transform (replicated over the spatial domain) (b) and the Short Time Fourier Transform of the signal (c)

$$u'(\xi) = u(\xi)g\big(\xi - x, a(\kappa)\big) \tag{3.12}$$

Taking the FT,

$$H(x,\kappa) = \int_{-\infty}^{\infty} u'(\xi)\, e^{-i\kappa\xi} d\xi = \int_{-\infty}^{\infty} u(\xi) g(\xi - x, a(\kappa))\, e^{-i\kappa\xi} d\xi \tag{3.13}$$

Equation (3.13) can be expressed as a convolution,

$$H(x,\kappa) = \int_{-\infty}^{\infty} u(\xi)\big(g(\xi - x, a(\kappa)) e^{-i\kappa(\xi - x)}\big)\, d\xi e^{-i\kappa x} \tag{3.14}$$

$$H(x,\kappa) = \big(u(x) * g(x, a(\kappa)) e^{i\kappa x}\big) e^{-i\kappa x} \tag{3.15}$$

By the convolution theorem,

$$H(x,\kappa) = \mathcal{F}_{\kappa}^{-1}\left\{\mathcal{F}_{x}\{u(x)\}\mathcal{F}_{x}\{g(x, a(\kappa)) e^{i\kappa x}\}\right\} e^{-i\kappa x} \tag{3.16}$$

$$H(x,\kappa) = \mathcal{F}_{\kappa}^{-1}\{U(k) G(k - \kappa, a(\kappa))\}\, e^{-i\kappa x} \tag{3.17}$$

Here it is seen that the windowing can be represented in the wavenumber domain as the multiplication of the FT of the signal and windowing function. Following the Inverse FT, the phase adjustment made to allow the convolution must be undone. As noted by Quatieri [82], the multiplication in the wavenumber domain is not of the window itself, but rather a modulated window. Thus, assuming that the window includes this modulation by the complex exponential,

$$u'(\xi) = u(\xi) g(\xi - x, a(\kappa)) e^{i\kappa x} \tag{3.18}$$

then,

$$H(x,\kappa) = \mathcal{F}_{\kappa}^{-1}\{U(k) G(k - \kappa, a(\kappa))\} \tag{3.19}$$

In Eqns. (3.18)-(3.19) there is a duality in the space and wavenumber domain. In each case, the envelope of the window in space, $g(\xi - x, a(\kappa))$ and the filler $G(k - \kappa, a(\kappa))$ in the wavenumber domain, can be translated. Thus $H(x,\kappa)$ can isolate specific locations and wavenumbers.

In PC analysis, the phase is the basis of the method and the magnitude is used for weighting.

This implies, that the filter bank analysis should not distort the phase or magnitude of the or the original FT, $U(k)$. Thus,

$$U'(k) \propto U(k)\ G(k-\kappa, a(\kappa)) \tag{3.20}$$

$$1 \propto G(k-\kappa, a(\kappa)) \tag{3.21}$$

where $U'(k)$ is the approximation of $U(k)$. Since PC is a normalized measure, $U'(k)$ and $U(k)$ need only be proportional. Only trivial windows satisfy Eqn. (3.21). However, using a set of L windows,

$$U'(k) \propto \sum_{l=1}^{L} U(k)\ G(k-\kappa_l, a(\kappa_l)) \tag{3.22}$$

$$1 \propto \sum_{l=1}^{L} G(k-\kappa_l, a(\kappa_l)) \tag{3.23}$$

a reasonably consistent approximation of the phase and magnitude of the components can be maintained. Now the complex signal components can be written as a set of L components where

$$H_{\kappa_l}(x) = \mathcal{F}_{\kappa_l}^{-1}\{U(k)G(k-\kappa_l, a(\kappa))\} \tag{3.24}$$

This section has laid out how a set of filter banks can be used to extract a space and wavenumber dependent components describing the signal. The section started with the approach of taking a FT of the signal windowed in space to compute the space-wavenumber relationship of the signal. Making use of the convolution theorem and a modulated window, it is shown how a discrete set of L spatially dependent signal components, $H_{\kappa_l}(x)$ could be calculated by multiplying the signal and the window in the Fourier Domain then performing and Inverse FT to return to the spatial domain. The next section will show how the signal components calculated from a filter bank can be used directly for calculating PC.

3.2.3 Spatial Windows as Quadratic Pairs

This section will show that by using a single filter that has two terms in quadrature, the real and imaginary parts of the signal component can be calculated at the same time. The signal $u(x)$ is approximated by the Fourier Series $u_N(x)$ by Eqn. (3.2). In Eqn. (3.9) the complex form of the signal components is constructed by adding the Hilbert Transform of the component (sine term) to the component itself (cosine term). The cosine and sine terms of Eqn. (3.9) form a quadrature pair. Venkatesh and Owens [79] showed that multiplication of a pair of filters in quadrature with the signal yields a pair of results which are in quadrature and can therefore be used to construct the complex component as is used in Eqn. (3.9). In other words, if a filter, $g_1(x)$ and its Hilbert transform $g_2(x)$ are convolved with a signal $u(x)$ then the results form a Hilbert transform pair as well.

$$u'_1(x) = g_1(x) * u(x), \quad u'_2(x) = g_2(x) * u(x) \tag{3.25}$$

Thus an analytic signal can be constructed following Bracewell's convention [83] as

$$u'(x) = u'_1(x) - iu'_2(x) = g_1(x) * u(x) - ig_2(x) * u(x) \tag{3.26}$$

Since the convolution function has the distributive property, Eqn. (3.26) can be rewritten,

$$u'(x) = \big(g_1(x) - ig_2(x)\big) * u(x) \tag{3.27}$$

Thus a single filter can be constructed,

$$g'(x) = g_1(x) - ig_2(x) \tag{3.28}$$

and the component vectors can be computed as,

$$u'(x) = g'(x) * u(x) \tag{3.29}$$

If $g'(x)$ is a real valued window envelope $g(\xi - x, a(\kappa))$ modulated with the complex exponential as in Eqn. (3.18) then $g'(x)$ is guaranteed to form a quadrature pair by the same reasoning that $u'(x)$ forms a quadrature pair as shown in Eqn. (3.25) and (3.26). This implies that the expression for $H_{\kappa_l}(x)$ in Eqn. (3.19) is equivalent to the complex signal component $A_n(x)$ in Eqn. (3.9) and can be used directly to compute PC as described in Eqn. (3.8).Thus,

$$A_n(x) = H_{\kappa_l}(x) = g_n(x) * u(x) \tag{3.30}$$

where the n^{th} component, A_n is calculated with the n^{th} filter g_n in a set of N filters. Making use of the convolution theorem, Eqn. (3.30) can be rewritten as

$$A_n(x) = \mathcal{F}_k^{-1}\left\{\mathcal{F}_x\,\{g_n(x)\}\mathcal{F}_x\,\{u(x)\}\right\} \tag{3.31}$$

By constructing of the filter from a real valued window modulated by the complex exponential the result of the filter bank analysis can be directly utilized in the PC expression, Eqn.(3.8). This provides a quick method of decomposing the signal while retaining significant flexibility in constructing the window.

3.2.4 Additional Filter Considerations

The last item to note with respect to the filters is that they must be bandlimited in the Fourier Domain. In Section 3.2.1 the Fourier Decomposition was shown using a cosine expansion for real signals. It is noted the complex exponential expansion would produce complex conjugate pairs of coefficients whose phase would cancel. This drove use of the cosine expansion. This is analogous to considering only one half-plane of the Fourier Domain. For this reason, the filters in the wavenumber domain must be limited to the positive wavenumber domain. This requires that they be band limited.

3.2.5 Considerations for Degenerate Cases

This section will present modifications to the Phase Congruency expression developed by Kovesi to address two degenerate cases; zero signal amplitude and pure sinusoidal signals [65]. Kovesi suggests the following modification to Eqn. (3.8) [65],

$$PC(x) = \frac{W(x)\, E(x)}{\sum_{n=1}^{N} a_n(x) + \varepsilon} \tag{3.32}$$

The first parameter ε is added to prevent division by zero. The only requirements on ε is that it must be greater than zero but very small relative to the vector summation in the denominator.

For this work all computations will use machine precision, 4.94e-324.

The weighting factor, $W(x)$, addresses the issues encountered when one dominant component is present. For example, a pure sine wave would result in a PC equal to one at all positions as there would only be one component to the signal in the Fourier Domain. Therefore, the numerator and denominator would have equal values resulting in a PC value of one. A single wave component aligned with itself is a degenerate case. To account for this, a measure of signal width is introduced,

$$w(x) = \frac{\frac{\sum_{n=1}^{N} a_n(x)}{\max\big(a_n(x)\big) + \varepsilon} - 1}{N - 1} \tag{3.33}$$

Utilizing the vector component amplitudes, a location dependent width factor is computed. There are two limiting cases in this expression. The first is if $a_n$is constant for all n components. In this case, the signal is perfectly wide. The limit of the width factor when all components have equal magnitude as ε tends to zero,

$$w(x) = \lim_{\varepsilon \to 0} \frac{\frac{\mathrm{N}a_n(x)}{a_n(x) + \varepsilon} - 1}{N - 1} = 1 \tag{3.34}$$

Thus for a wide spectrum the weighting factor would not alter the PC expression. However, in the opposite limiting case only one component has a non-zero value. This is the perfectly narrow signal case.

$$w(x) = \lim_{\varepsilon \to 0} \frac{\frac{a_n(x)}{a_n(x) + \varepsilon} - 1}{N - 1} = 0 \tag{3.35}$$

Here the PC expression is driven to zero by the weighting factor. The weighting factor is used to preferentially pass broadband signals while penalizing narrow signals.

Rather than using this width directly, it is fit to a sigmoid function to obtain the final weighting value. Fitting to the sigmoid function allows a non-linear weighting based on the width measure and thus a sharper divide between spectra that are considered wide and those which are not. The weighting function is defined as,

$$W(x) = \frac{1}{1 + \exp(\gamma(c - w(x))} \tag{3.36}$$

Figure 3.5 illustrates the relationship between the width factor, and the weighting factor when fit to this sigmoid function for parameters, $c = 0.5$ and $\gamma = 10$. The sigmoid function acts as a soft threshold for passing or stopping values. The sharpness of the signal can be modified by changing the parameter γ and the cutoff point is set with c.

3.2.6 Handling Noise in a Normalized Metric

Since this is a normalized measure, points with meaningful signal content and those without cannot be discerned based on the PC value alone. Kovesi also introduced an approach for handing noise [65]. To address noise a requirement is set such that the magnitude of the sum of components must be greater than the noise threshold *T*. This is implemented by taking the larger of two values: the energy less the noise, $E(x) - T$, or 0.

$$PC(x) = \frac{W(x)\max(E(x) - T, 0)}{\sum_{n=1}^{N} a_n(x) + \varepsilon} \tag{3.37}$$

The noise floor of the signal should be calculated or estimated to select an appropriate

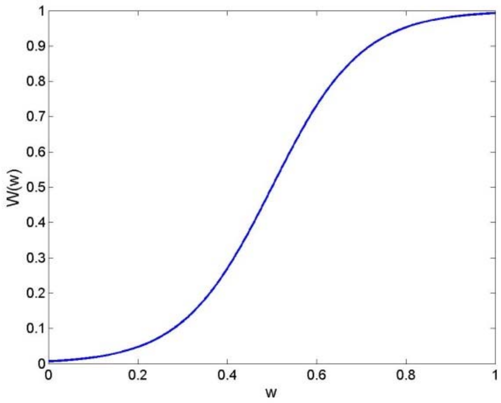

Figure 3.5 The width factor is fit to a sigmoid function to determine the weighting value

value for T. This approach sets all PC values to zero if the signal is locally below the noise floor. Therefore, only points with meaningful signal will have non-zero PC values.

3.2.7 2-D PC

The filters described in Section 3.2.2-3.2.3 are all 1-D. To extend the filters to 2-D the 1-D filters are given a shape in the second dimension [65]. For example, a Gabor filter can be used as it preserves phase. Considering the filters on a polar coordinate system in the 2-D wavenumber domain [65] the angular shape of the filters is given by ,

$$G_m(\theta) = \exp\left(\frac{-\left({}^{\theta}/_{\theta_m}\right)^2}{2{\sigma_\theta}^2}\right) \tag{3.38}$$

The angular filter shape is then multiplied by the 1-D filter shape, which is now the radial filter shape,

$$G_{n,m}(k_r,\theta) = G_n(k_r)G_m(\theta) = G_n(k_r)\exp\left(\frac{-\left({}^{\theta}/_{\theta_m}\right)^2}{2{\sigma_\theta}^2}\right) \tag{3.39}$$

where the subscript *r* refers to wavenumber and filter width in the radial direction, and the subscript m gives the index of the filters in the angular direction. The choice of filter in the radial direction is kept general and will be discussed in the next section. Figure 3.6 shows an example of a 2-D filter. The surface gives the 2-D filter while the black line illustrates the radial shape of the filter and the red line illustrates the angular shape of the filter.

Now that there are a discrete set of filters in both the radial and angular direction, they can be multiplied by the signal in the wavenumber domain to determine the 2-D signal components.

$$a_{n,m}(\vec{x}) = \left|A_{n,m}(\vec{x})\right| = \mathcal{F}_k^{-1}\{G_{n,m}(\vec{k})\mathrm{U}(\vec{k})\} \tag{3.40}$$

An additional summation is needed in the PC measure to include the M angular orientations. Equation (3.37) becomes,

$$PC(\vec{x}) = \frac{1}{\mathrm{M}} \sum_{m=1}^{M} \frac{W_m(\vec{x}) \max(E_m(\vec{x}) - T, 0)}{\sum_{n=1}^{N} a_{n,m}(\vec{x}) + \varepsilon} \tag{3.41}$$

3.3 Phase Congruency for Damage Mapping

The PC method for images is given by Eqn. (3.41). This form was constructed with images in mind. Taking Fig. 3.1 as an example there are a wide range of elements in this picture: regular components in the brickwork and building trim, as well as irregular components in the leaves and clouds. Thus, few assumptions are made about the signal in the development of the PC equation, Eqn. (3.41). However, for GW the problem is more bounded. A wavefield will typically contain only a few sinusoidal components as described in Section. Further, a wavefield carries information in the time domain that an image does not. Using these characteristics of wavefields, this section will explore methods for adapting PC to damage mapping with wavefields.

3.3.1 Presence of GW

The dominant feature in all measurements will be the GW. If the wavefield is considered a sum of

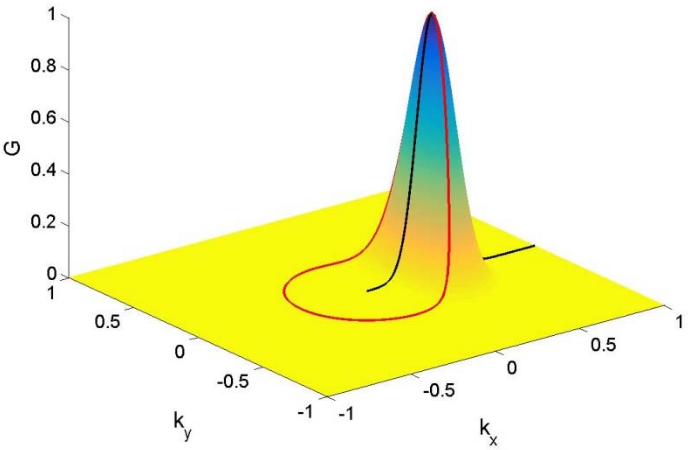

Figure 3.6 Example of two-dimensional filter

discrete areas with an associated wave as is done in Eqn. (2.10), then the wavefield can be considered a summation of harmonic components modulating rectangular functions describing the area the harmonic components is acting on. For example, the rectangle function in Fig. 3.7 (a) describes the area that the component of a wavefield in Fig. 3.7 (b) is acting on. If the rectangular function, $f(x)$, has a FT, $F(k)$ (Fig. 3.7 (c) – black line, a sinc function), then $f(x)$ modulated by the harmonic component has the FT, $F(k-k_0)$, plus its complex conjugate (Fig. 3.7 (d) – black line),

$$f(x)cos(k_0x) = \frac{f(x)}{2}\left(e^{ik_0x} - e^{-ik_0x}\right) = F(k-k_0) + F^*(k+k_0) \tag{3.42}$$

where the asterisk denotes the complex conjugate. The boundaries of these regions are the discontinuities the PC method should plot. One way to achieve this would be to demodulate the signal and then perform the PC analysis on just the rectangle function with a filter bank that spans the zero wavenumber to the maximum wavenumber (Fig. 3.7 (c)). However, a simpler way is

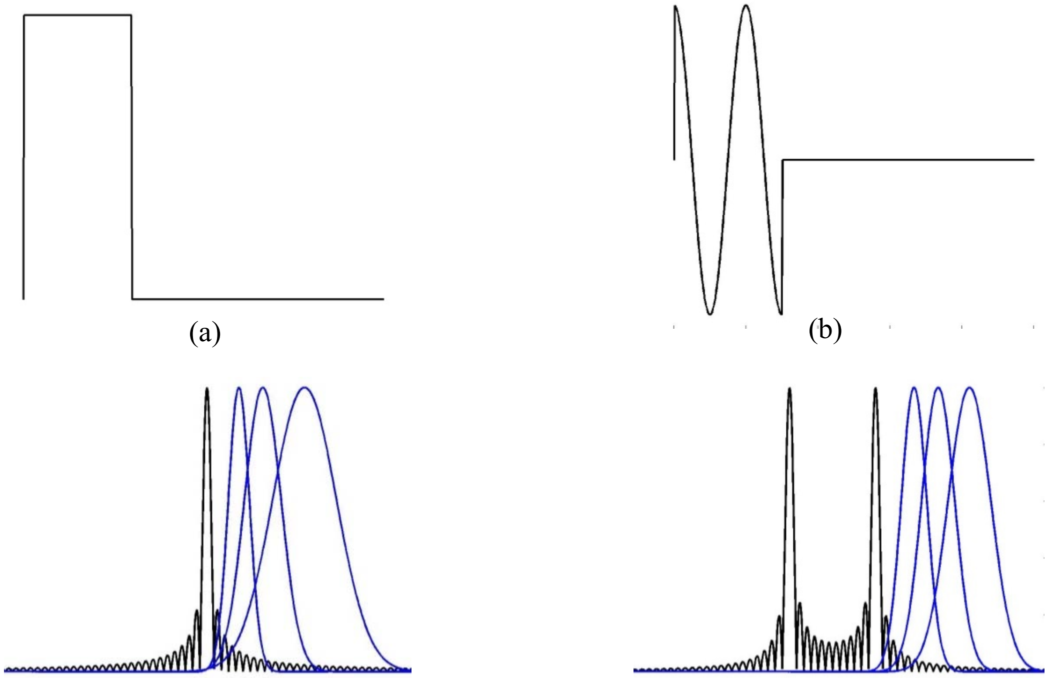
(a) (b)

(c) (d)

Figure 3.7 Rectangular function (a) and modulated rectangular function (b) with FT of the rectangular function (black line) and filter banks (blue lines) and the FT of the modulated rectangular function (black line) and filter bank (d) (blue lines) simply to shift the range of wavenumbers covered by the filter bank to be from the highest modulating wavenumber to the maximum wavenumber (Fig. 3.7 (d)). Now the filter bank decomposition of the modulated rectangular function is analogous to the filter bank decomposition of the rectangle function but without performing a demodulation.

The ultimate goal is to map the discontinuities. Limiting the range of the analyzed wavenumber domain to the portion above the highest modulating wavenumber creates a decomposition analogous to analyzing a rectangular function where only one-half of wavenumber domain is analyzed by the filter bank.

3.3.2 Time dependent signals

The next adaptation that needs to be made is to include the time dimension. This is a simple adaptation to make. If the 2-D PC measure is taken at each time slice then each of the time slices can be summed to give a single PC result. Equation (3.41) can be modified to include J time slices as follows,

$$PC(\vec{x}) = \frac{1}{\mathrm{JM}} \sum_{j=1}^{J} \sum_{m=1}^{M} \frac{W_{m,j}(\vec{x}) \max(E_{m,j}(\vec{x}) - T, 0)}{\sum_{n=1}^{N} a_{n,m,j}(\vec{x}) + \varepsilon} \tag{3.43}$$

3.3.3 Characteristic Evaluation of Candidate Filters

This section will consider a range of candidate filters for use in PC for damage mapping. A list of characteristics for suitable filters is derived from the development of PC presented in Section 3.2. Then a range of potential filters is evaluated based on the filter characteristics. In Section 3.3.4 a quantitative comparison is made against the remaining filters.

Four characteristic criteria are identified for candidate filters. First, for a windowed FT to reflect only the local wavenumber content the window must be compact in the spatial domain

(Section 3.2.2). The next item identified was that the envelope of the signal must be real, and the bank of filters should approximately sum to a constant (Section 3.2.2). Third, the filter must represent the sum of two filters in quadrature for $E(x)$ to be calculated (Section 3.2.3). Lastly, the filters must be bandlimited in the wavenumber domain (Section 3.3.1). Summarizing the four requirements for filter design the filters must have:

1. a real positive value envelope in the wavenumber domain,
2. compact support in the space domain,
3. be bandlimited in the wavenumber domain, and
4. must represent a sum of filters in quadrature.

With these requirements, a set of prospective filters is composed. Many of the filters are common filters from the literature. A summary of the filters considered is shown in Table 3.1 along with the results of the characteristic analysis of their suitability.

The Gaussian, Mexican Hat, Gabor and Log-Gabor filters are included in the evaluation for their ability to minimize the ambiguity between space and wavenumber domain [80, 84, 85]. The Haar is selected due to its ability to detect discontinuities and its compactness in space [86]. The Complex Shannon, is selected for its compactness in the wavenumber domain [87]. The Meyer, Daubechies family, Symlets family, Coiflets family and Frequency B-spline are all considered as they are common general purpose wavelets and could make suitable filters [84, 87]. Additionally custom filter, the Complex Boxcar, is considered.

The first set of filters considered are those based on the Gaussian function: Gaussian, Mexican Hat, Gabor and Log-Gabor. Although compactness in both the space and wavenumber domain is not strictly possible [80], the Gaussian function is approximately compact in both domains. This makes filters based on the Gaussian function likely candidates since compactness is

Table 3.1 List of filters evaluated for PC.

Filters Name	Const. phase in wavenumber	Compact in space	Bandlimited	Form quadrature pair
Gaussian	Yes	Approx.	Approx.	Yes
Mexican Hat	Yes	Approx.	Approx.	Yes
Gabor	Yes	Approx.	Approx.	Yes
Log-Gabor	Yes	Approx.	Approx.	Yes
Haar	No	Yes	No	Yes
Complex Shannon	No	No	Yes	Yes
Meyer	No	Approx.	Yes	Yes
Daubechies	No	Yes	No*	Yes
Symlets	No	Yes	No*	Yes
Coiflets	No	Yes	No*	Yes
Frequency B-spline	Approx.	No	Yes	Yes
Complex Boxcar	No	Yes	No	Yes
* For certain parameter choices the filter can be approximately compact/bandlimited .				

required in both domains. Gaussian filters are generally described as a family of filters based on derivatives of the Gaussian function and centered at zero wavenumber in the wavenumber domain. The Mexican Hat is the first derivative of the Gaussian function [88]. The Gabor filter is simply the Gaussian function modulated by the complex exponential. This filter is known to minimize the uncertainty trade-off between the space and wavenumber domain [80]. For this reason, the Gabor filter is a good candidate. The Log-Gabor is the Gabor filter on a logarithmic wavenumber axis. All of the filters described above meet the general criteria outlined for use in PC and are thus included in the analysis.

The Haar filter is well known for its use detecting discontinuities [86]. This filter is compact in space. However, it is broadband in the wavenumber domain, thus unsuitable for use in PC. The Shannon filter is analogous to the Haar filter in the wavenumber domain [87]. This filter has the benefit of being compact in the wavenumber domain and allows Eqn. (3.23) be exactly satisfied. However, the sharp edges to this filter in the wavenumber domain make it broadband in the spatial domain and therefore is not considered further.

The Meyer filter is a convenient function due to its bandlimited nature and although it is not strictly compact, it is approximately compact in space [84]. The filter however does not have constant phase and therefore cannot be used for PC.

The discrete wavelets considered include the Daubechies, Symlets and Coiflets families. Discrete filters have no analytic description [84]. They are constructed on a grid of points in an iterative fashion. Generally they are not bandlimited although with higher order constructions (i.e. higher number of iterations used to generate the waveform) and higher numbers of vanishing moments they typically approximate bandlimited filters [84]. However, none of these filters are constant in phase are not considered further.

The Frequency B-Spline is a more general form of the Complex Shannon filter [87]. In fact, the Complex Shannon filter is a first order Frequency B-Spline filter. Thus the Frequency B-Spline has similar bandlimited features as the Complex Shannon filter but it is not compact in space. Therefore it is not a suitable filter.

The Complex Boxcar filter is simply a rectangular function modulated by the complex exponential. This filter is contrived for use in this work since modulated rectangle functions are the building blocks of wavefield models used in this work. In the wavenumber domain, it is the sinc function shifted to the frequency of the complex exponential. Clearly, this filter is not bandlimited nor is it of constant phase. Thus, it is not a suitable filter.

Table 3.1 summarizes the analysis of the filter characteristics based on the four criteria developed at the beginning of this section. Based on the analysis above, the four Gaussian based filters are the only filters to all met the criteria defined above. A comparison of each of them is run against a set of ideal signals. In addition to these filters, two filters are also included as a basis of comparison for filters that are not expected to yield good results: the Haar and Complex Boxcar.

3.3.4 Quantitative Filter Comparison

To compare the suitability of the filters three test signals are developed. These three signals represent the basic building blocks of expected wave behavior. The step edge is the most fundamental discontinuity.

$$g_1(x) = \begin{cases} 1 & x < 0 \\ 0 & x \geq 0 \end{cases} \tag{3.44}$$

This test signal allows a direct comparison between filters for their performance detecting discontinuities. The second represents an ideal signal in the presence of a rigid boundary at the midpoint. This test signal is a step edge multiplied by a wave.

$$g_2(x) = g_1(x)\cos(k_1 x) \tag{3.45}$$

The last signal represents a discrete change in wavenumber at the midpoint. This signal is comprised of two step functions, $g_1(x)$ and its inverse. Each of these step edges is multiplied by a sinusoid of different wavenumbers with the requirement that the amplitude is continuous at the intersection of the two parts. This is the most important test signal since changes of wavenumber are common features in wavefields for damaged specimen

$$g_3(x) = g_2 - (g_1(x) - 1)\cos(k_2 x) \tag{3.46}$$

The test signals are illustrated in Fig. 3.8. These signals are considered to be appropriate test signals due to the scaling and translation of the filter and signal in the spatial domain. All of the considered filters are compact or approximately compact in the spatial domain. Therefore they effectively window the signal in space. Additionally, the signal translates in space due to the convolution. As this is the case, when the convolution centers the filter over the discontinuity and the scaling causes the window to be compact in space, a signal can be approximated with these simple models.

The four Gaussian based filters, the Haar and Complex Boxcar are evaluated against this set of three test signals. The first filter tested is the first order Gaussian expressed in the wavenumber domain as,

$$G_n^{Gaus}(k) = (2\pi c_n{}^3)^{\frac{1}{4}} e^{\left(-\frac{1}{4}k^2 c_n{}^2\right)}(k+|k|) \tag{3.47}$$

where,

$$c_n = \frac{N}{k_{max}} 2^{n-1} \tag{3.48}$$

The dilation parameter is used to control the location of the peak response, and arrange a set of filters to span the wavenumber domain of interest (Fig. 3.9 (a)).

The next set of filters considered are the Mexican Hat filters [88]. When scaled to have even coverage over the supported wavenumber range.

$$g_{1,n}^{MH}(x) = \frac{1}{c_n\sqrt{2\pi}}\left(1-\left(\frac{x}{c_n}\right)^2\right) e^{\left(-\frac{x^2}{2c_n{}^2}\right)} \tag{3.49}$$

Taking the sum of the original filter and its Hilbert Transform in the Fourier Domain, the following expression containing the quadrature pair of filters in the Fourier Domain is,

$$G_n^{MH}(k) = c_n{}^2 e^{\left(-\frac{k^2 c_n{}^2}{2}\right)}(k^2 + k|k|) \tag{3.50}$$

The scaling parameter controls the peak location of the filter, thus controlling the primary range of

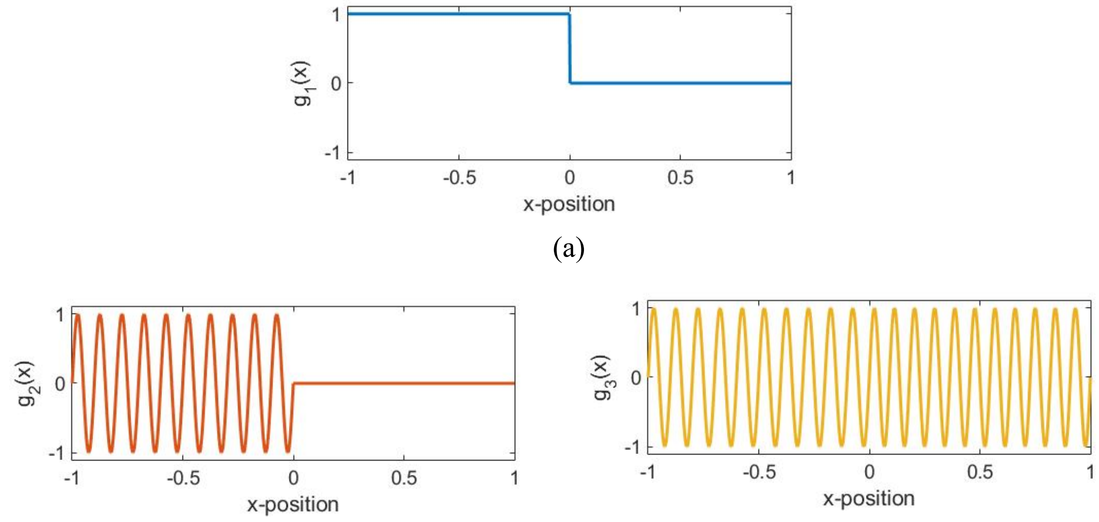

(a)

(b) (c)

Figure 3.8 The three test signals used for quantitative comparison of the filters.

wavenumber the filter covered (Fig. 3.9 (b)).

$$c_n = \frac{N}{k_{max}} 2^{n-1} \tag{3.51}$$

The Gabor filter [80] is a Gaussian function multiplied by the complex exponential. The complex exponential allows the quadrature pair of filters to be represented in a single term. The Gabor filter can be expressed as,

$$G_n^{Gabor}(k) = \exp\left(-\frac{{c_n}^2}{2}(k_n - k)^2\right) \tag{3.52}$$

The filter width is given by the parameter c_n and the center of the Gaussian is given by k_n. The parameters are used in combination to create filter sets that spans the positive half of the wavenumber axis (Fig. 3.9 (c)).

The Log-Gabor filter is simply the Gabor filter on a logarithmic axis. Thus, the shape of the filter in the wavenumber domain is given by,

$$G_n^{LGabor}(k) = \exp\left(-\frac{\log\left({}^{k}/_{k_n}\right)^2}{2\log(c)^2}\right) \tag{3.53}$$

The width parameter, c, is held constant for all scales and center wavenumber, k_n, evenly spaced on the logarithmic axis [85]. Figure 3.10 (a) illustrates an example set of filters Log-Gabor filters.

The Haar filter is a very simple filter in the spatial domain as seen in Fig. 3.10 (b). However, in the Fourier Domain the Haar is more complex.

$$G_n^{Haar}(k) = -\frac{2i}{k\sqrt{c_n}}\left(2\sin\left(\frac{c_n k}{4}\right) - \sin\left(\frac{c_n k}{2}\right) + \cos\left(\frac{c_n k}{2}\right) - 1\right) \tag{3.54}$$

where,

$$c_n = 2^{\frac{n}{2}} \quad \text{for } n = 1 \dots N \tag{3.55}$$

Only the dilatation parameter, c_n, is available to vary the center wavenumber since there is no modulation component [86].

The Complex Boxcar is simply the complex exponential multiplied by a boxcar function.

$$g(x) = \begin{pmatrix} |x - x_0| < c & 1 \\ |x - x_0| \geq c & 0 \end{pmatrix} e^{i(k_n x + \varphi)} \tag{3.56}$$

The Complex Boxcar is a rectangle function multiplied by the complex exponential with the real and imaginary parts forming the quadrature pair. In the wavenumber domain, the filters are given by,

$$G_n^{CBox}(k) = \sqrt{c}\,\mathrm{sinc}\left(\frac{c}{2}(k_n - k)\right) \tag{3.57}$$

The parameters are set such that there are N copies of the filter linearly spaced with the first having a zero crossing at $k = 0$ and the last having the first zero crossing at the maximum wavenumber permitted by the grid spacing.

$$c = \frac{2\pi(N + 1)}{k_{max}} \tag{3.58}$$

Sample illustrations of the filters in the spatial and wavenumber domain are shown in Fig. 3.10 (c).

The six filters are tested against the signals in Fig. 3.8. To compare the results, the variance between the ideal case and the normalized PC results is computed. The PC results are normalized to span the range zero to one since PC will be used in as a relative measure going forward. As can be seen in (Table 3.2), the Gabor and Log-Gabor filters performed the best by over one order of magnitude in the modulated step function and change of wavenumber case. These two cases are most relevant to wavefields. The Gabor's results are consistently better than the Log-Gabor's so

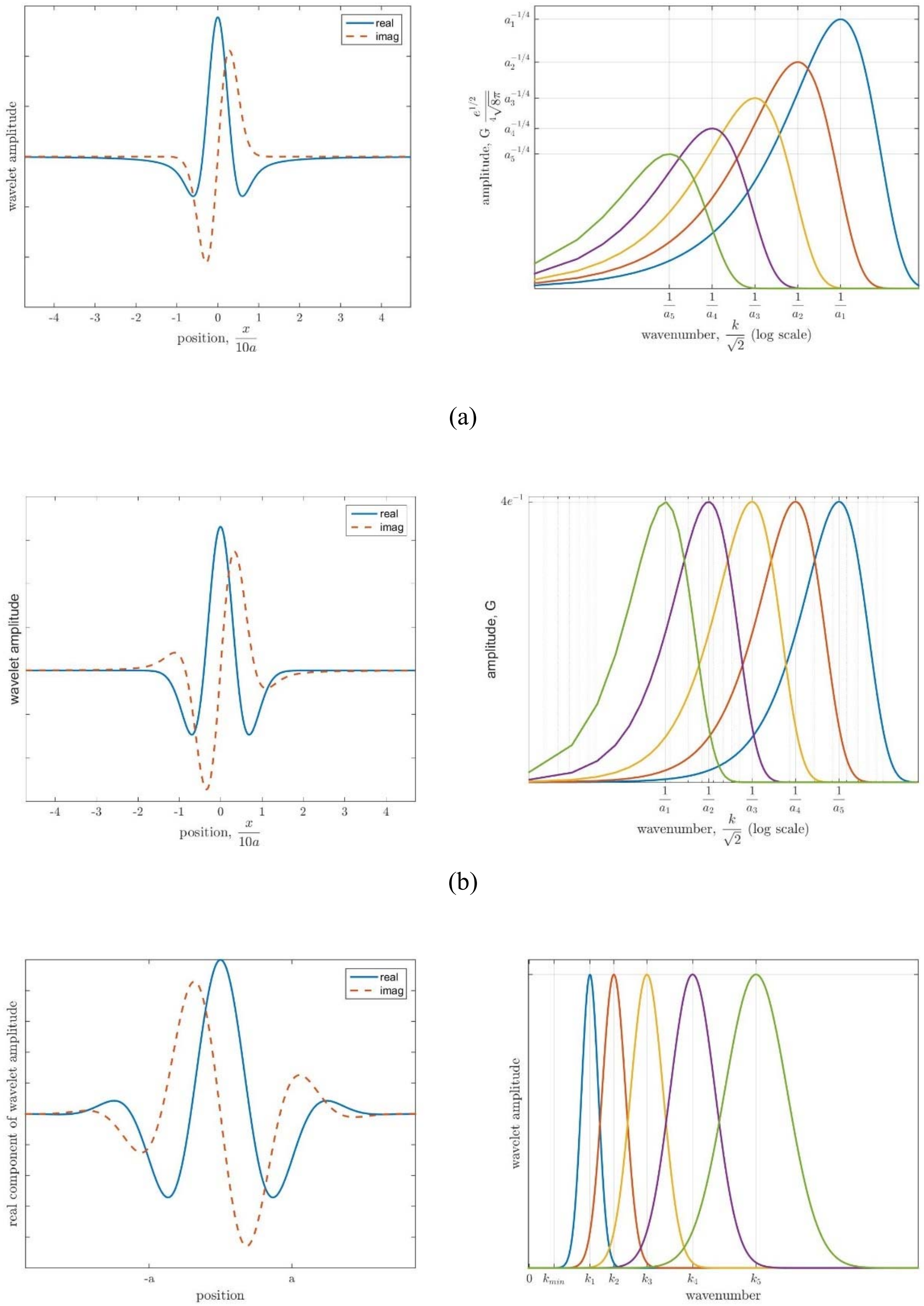

(a)

(b)

(c)

Figure 3.9 Examples of the First-Order Gaussian (a) Mexican Hat (b) and Gabor (c)

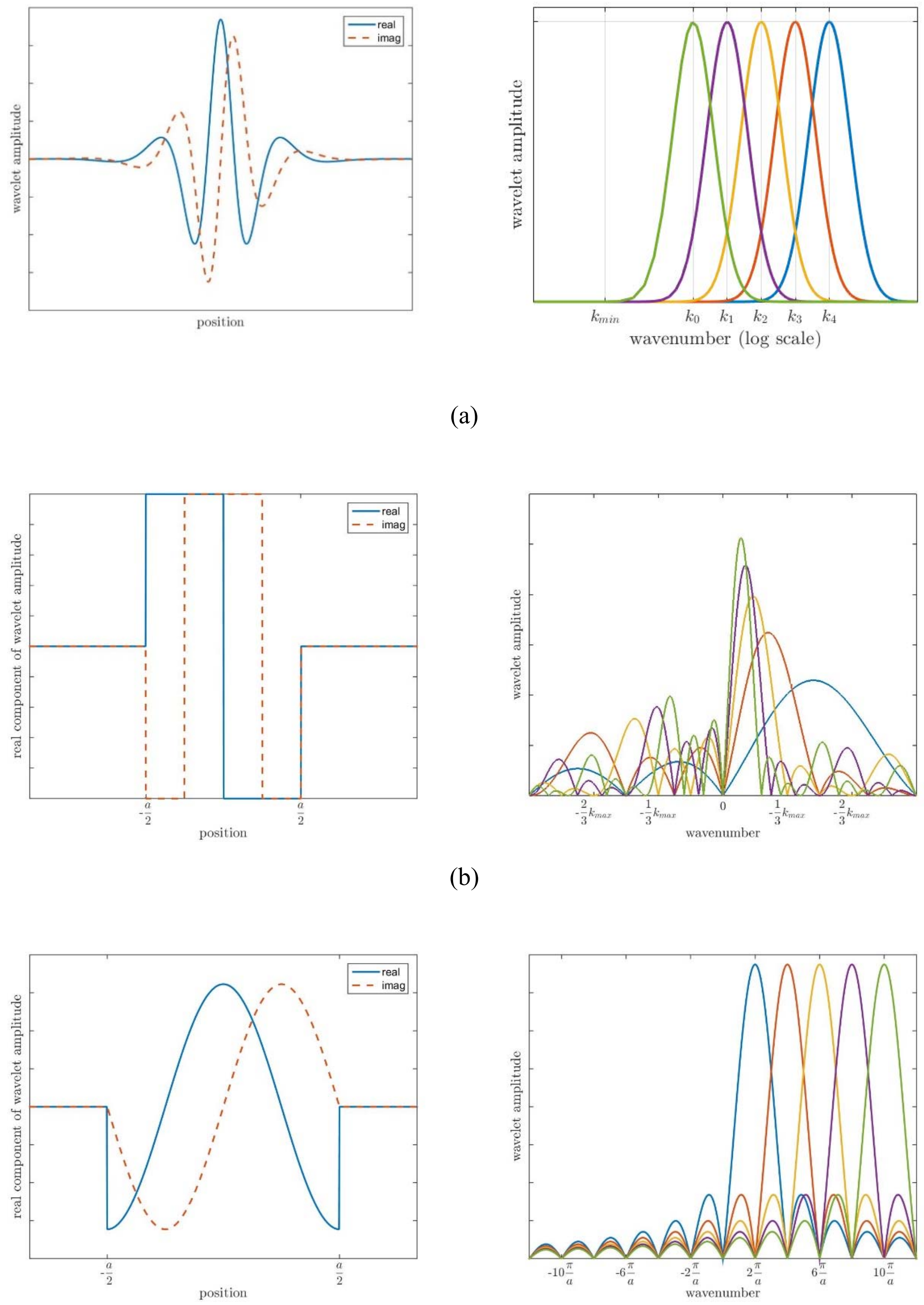

(a)

(b)

(c)

Figure 3.10 Examples of the Log-Gabor (a) Haar (b) and Complex Boxcar (c)

Table 3.2 Variance in $PC(x)$ for test signals compared with ideal results

Var. in PC(x)	Step	Modulated Step	Change in k
Haar	0.0132	0.3091	0.6105
Complex Boxcar	**0.0059**	0.3255	0.7614
Gabor	0.0177	**0.0184**	**0.0214**
Log Gabor	0.0201	0.019	0.0238
Mexican Hat	0.1183	0.257	0.3747
Gaussian	0.3890	0.4832	0.6729

the Gabor will be used as the filter in all cases going forward.

This section considered a range of candidate filters and selected the best of the set based on the characteristics of the filters as well as quantitative comparison of the most likely filters. The next section will give a detailed analysis of parameter selection for the Gabor filter.

3.3.5 Gabor Filters for Wavefield Decomposition

This section gives an analytic method for determining appropriate parameters to construct a Gabor filter bank. There are three parameters that must be set; the number of filters, the width of the filter and the center wavenumber of the filter. Therefore three independent conditions must be set so these three parameters can be determined.

The first condition is the upper bound and lower bounds of spanned range of wavenumbers. From a practical standpoint the crossing value at the end points is set to be 10^{-2} times the maximum value of the filter for the lower edge of the first mode, $n = 1$, and higher edge of the last mode, $n = N$, in Eqn. (3.52) crosses the Nyquist frequency at 10^{-3}. These values are chosen because they effectively approximate zero but maximize the value to filter summation over the desired range.

The next condition is that the crossing point of successive filters is held constant. The width parameter, c_n, is set to ensure the half power width of each filter is a constant multiple, d, of the wavelength corresponding to the center wavenumber of the filter. This ensures the filter's size is appropriate for the wavelength it is testing.

With three unknowns, the filter width parameter, the center wavenumber of the lowest filter and the spacing between them, and the three constraints, the upper boundary, lower boundary and requirement for filter crossings to be at equal amplitude the system is fully defined. The three-equation system can then be solved numerically,

$$m = \frac{\pi d - \sqrt{-2\log\left(\frac{1}{\sqrt{2}}\right)\log(2)}}{\pi d + \sqrt{-2\log\left(\frac{1}{\sqrt{2}}\right)\log(2)}} \tag{3.59}$$

$$d = \frac{2k_1\sqrt{\log(10)\log(2)}}{\pi(k_1 - k_{min})} \tag{3.60}$$

$$k_1 = \frac{k_{max}\pi d}{m^{1-n}\left(\pi d + \sqrt{6\log\left(\frac{1}{\sqrt{2}}\right)\log(2)}\right)} \tag{3.61}$$

giving,

$$k_n = k_1 m^{(1-n)}, \quad n = 1 \ldots N \tag{3.62}$$

$$c_n = \frac{d\pi}{k_n\sqrt{\log(2)}} \tag{3.63}$$

These parameter choices guarantee that the filter bank will span only the range of wavenumbers specified, and have regular size and spacing. Now that the filters are completely defined, the next section will detail the mapping procedure with two examples.

3.4 PC for Damage Mapping Examples

To demonstrate the procedure for damage mapping two examples will be given with synthetic data sets. The first is a 1-D example. This 1-D case is used for its simplicity. The basic components of PC for damage mapping apply equally to 1-D as well as 2-D so it is an instructive example. Second, a 2-D example will be given. This example will illustrate a full 2-D case with the time domain. The procedure used in the 2-D example will be the same as used for all results in this Chapter.

3.4.1 Phase Congruency Example for 1-D Signal

The simple 1-D signal is a change of wavenumber example. This example uses synthetic data from Eqn. (3.46) and seen in Fig. 3.11 (a). The input signal is evaluated between $x = -1$ and 1. The wavenumber on the left half is 10 m^{-1} and on the right half 9 m^{-1}. With the sample wave velocities, the first step is to take an FFT of the signal (Fig. 3.11 (b)). Since this is a synthetically generated wave, the signal is padded not with zeros, but by extending the signal according to Eqn. (3.46). This will reduce edge effects in processing. Leakage is not a concern because the wavelengths divide evenly into the span of the signal so both ends of the signal have an amplitude of zero.

With the signal in the wavenumber domain, the signal is decomposed by Eqn. (3.30). Per the analysis in Section 3.3.4 the Gabor filter will be used as the analysis filter. The Gabor filter is constructed per Eqns. (3.52)-(3.63). There are ten filters in the filter bank (Fig. 3.11 (c)). The lower bound of the wavenumbers spanned by the filter bank is the highest wavenumber of the signal, 10 m^{-1}. The upper bound is the highest wavenumber from the FFT which is $(2dx)^{-1}$ where dx is the sample spacing. The number of filter is chosen so that the filter half-power width in the spatial domain is one to three times the size of the center wavelength of the filter. In this case, the ratio of half power width to center wavelength is 1.81. This ensures that the filter's width is larger than the wavelength of the signal it is sampling, yet compact so that the filter captures only wavenumber content that is locally present at the analysis point. Figure 3.12 (a) illustrates the first filter in the filter bank (n=1) in the spatial domain. Both the real and imaginary components are shown along with lines indicating the half-power points. These lines cross the envelope of the wave at $1/\sqrt{2}$. Between them there are just less than two cycles of the filter.

With the filter bank and the signals in the wavenumber domain each filter can be multiplied by the signal and then returned to the spatial domain via a IFFT per Eqn. (3.31). The results for selected filters are seen in Fig. 3.12 (b). These can then be used to compute $E(x)$ per Eqn. (3.10). This quantity is plotted for comparison against the summation of component magnitudes in Fig.

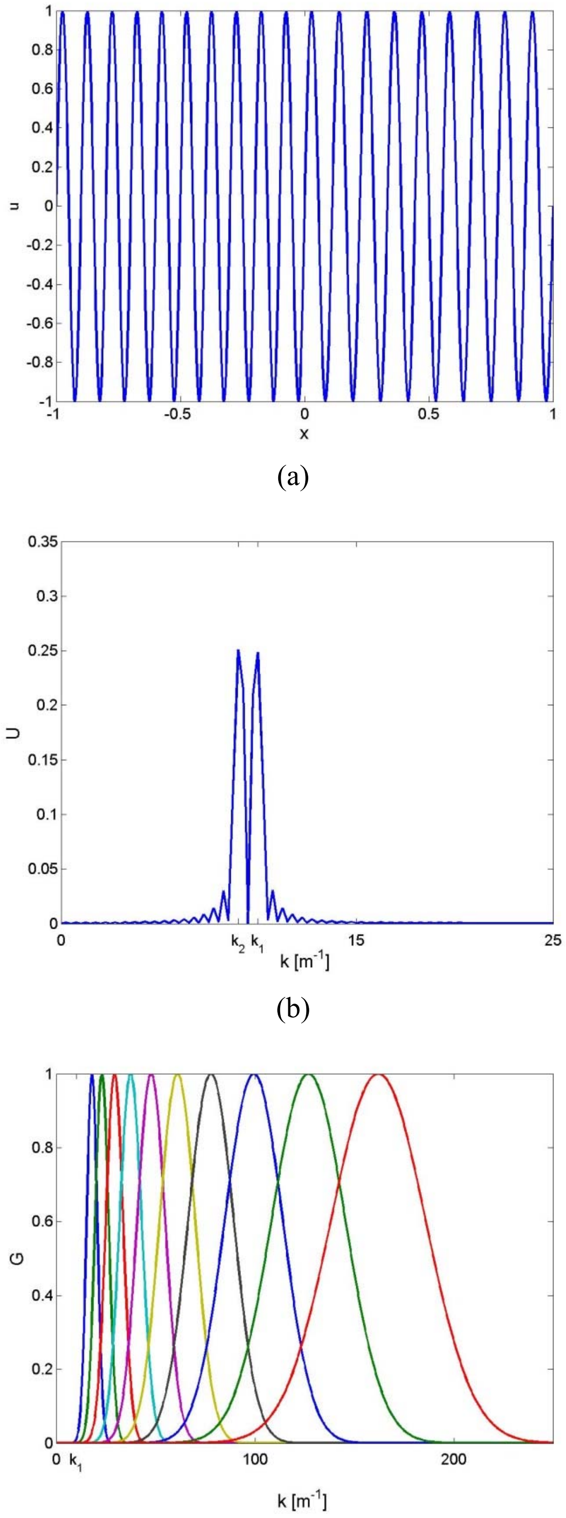

(a)

(b)

(c)

Figure 3.11 The 1-D wave example in the space domain (a) and the wavenumber domain (b) along with the bank of filters in the wavenumber domain (c)

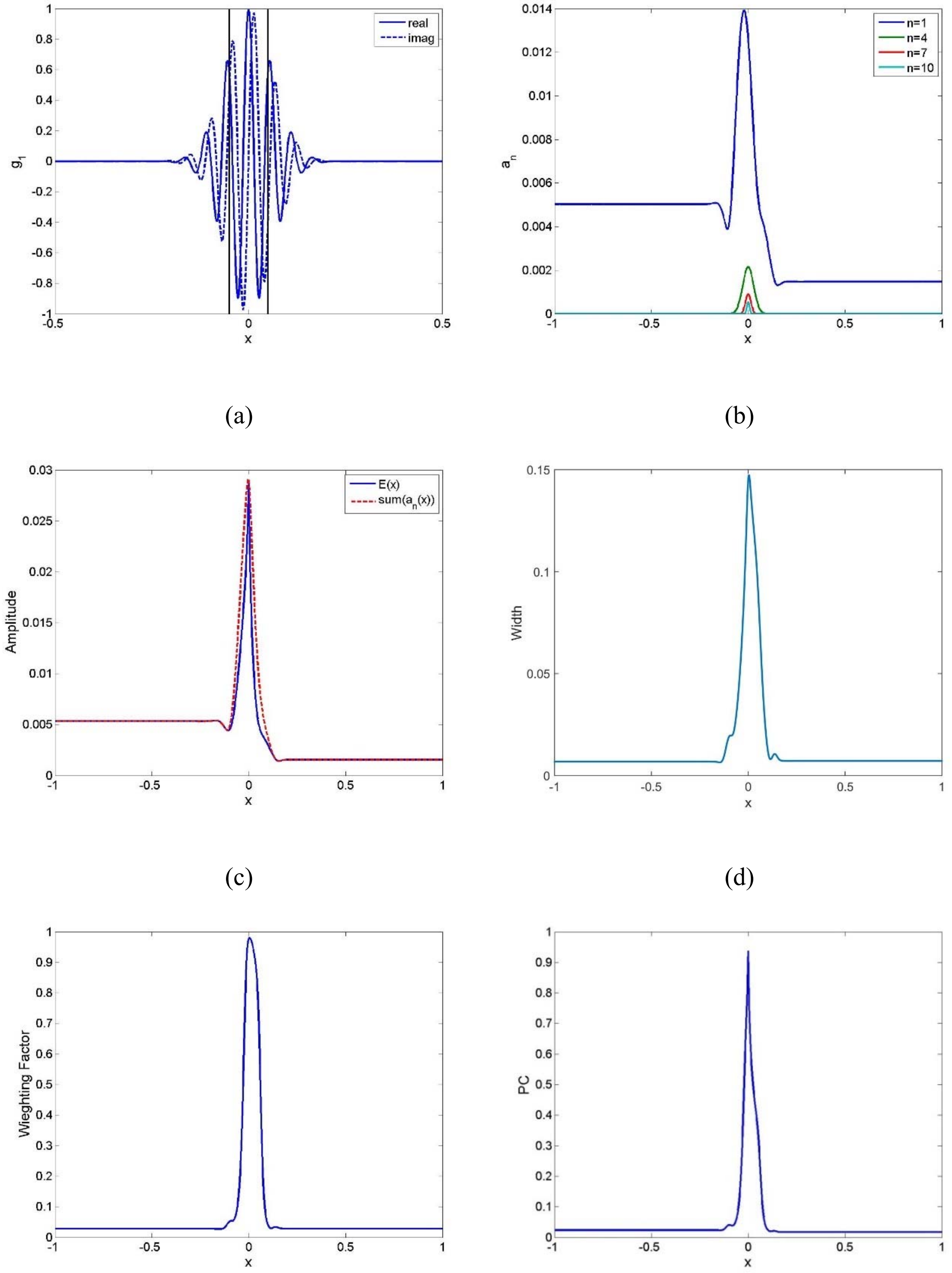

(a) (b)

(c) (d)

(e) (f)

Figure 3.12 An example of a filter in spatial domain (a) along with the computed components A_n (b), the sum of components compared with the magnitude of the vector sum (c),the width function (d), the weighting function (e) and PC result (f)

3.12 (c). This plot illustrates the issue of signals with local single harmonic components discussed in Section 3.2.5. The two quantities $E(x)$ and $\sum a_n$ are plotted in Fig 3.12 (c). Away from the discontinuity the two quantities have equal values. This would give PC a value of one in these regions per Eqn. (3.8) despite the fact that there is no discontinuity in the region. This is precisely what motivates the use of the weighting factor. The weighting factor is computed with Eqn. (3.33) then scaled via the sigmoid function with Eqn. (3.36). These functions are plotted in Fig. 3.12 (d) and (e). The width function in Fig. 3.12 (d)) clearly penalizes the areas with a single harmonic. This follows through to the weighting function in Fig. 3.12 (e). Since this dataset is synthetic, the noise threshold is set to zero.

All the terms necessary to compute PC by Eqn. (3.37) are available. The PC values are seen in Fig. 3.12 (f). The computed PC values clearly indicate the change in wavenumber a $x = 0$.

Summarizing the steps used to calculate PC

1. Take the FFT of the signal,
2. Construct the filter bank in the Fourier Domain (Eqns. (3.52)-(3.63)),
3. Multiply each filter by the signal and take an IFFT to get the signal components $A_n(x)$ as a function of space (Eqn. (3.31)),
4. Using the signal components $A_n(x)$, $E(x)$ (Eqn. (3.10)) and $W(x)$ (Eqn. (3.33) and (3.36)) can be computed,
5. Set the noise threshold and calculate $PC(x)$ (Eqn. (3.37))

3.4.2 Phase Congruency Example for 2-D Wavefield

In this section, a two-dimensional wavefield will be used to as an example for describing the PC for damage mapping process with two-spatial dimensions and time. The procedure laid out in this section will be the same as that used in all subsequent analysis of numerical and experimental data. A synthetic wavefield will be used for this analysis. The same analytic signal used in Section 2.5

with the one exception. This example will approximate a line source using a sum of point sources. To do this Eqn. (2.41) will be modified to accept multiple reflectors,

$$u(\vec{x},t) = \frac{1}{r_i} u_{S_0^i}(r_i,\theta_i,t) + \frac{1}{N}\sum_{n=1}^{N}\left[A\left(r_{s,n},\theta_{s,n},t\right)u_{S_0^s}\left(r_{s,n},\theta_{s,n}\right) + A\left(r_{s,n},\theta_{s,n}\right)u_{A_0^s}\left(r_{s,n},\theta_{s,n},t\right)\right] \tag{3.64}$$

where, the index n refers to the reflecting source index. In this example, 20 reflecting sources are spaced evenly spaced between $x = 0.0875$ and $0.1125\ m$ representing a 1 cm long discontinuity.

All other equations and parameters are used as described in Section 2.5 to compute the synthetic wavefield. A snapshot of the wavefield is seen in Fig. 3.13 (a) at $t = 107.8\mu s$. The first step in the process is to take the 2-D FFT of the single time step (Fig. 3.13 (b)).

The next step is to create the filter bank. The filter bank for this analysis is shown in Fig. 3.13 (c). The filters are constructed according to Eqns. (3.39),(3.52)-(3.63). In this analysis there are three filters in the radial direction (*n=1..3*) and six in the angular direction (*m=1..6*). The three filters in the radial direction give a filter half power width to center wavelength ratio of approximately 2.8. Pointwise multiplication in the wavenumber domain of the signal and each of the filters results in a set of 18 signal components at each point (6 angular filters x 3 radial filters) for each time step.

$$a_{n,m,j}(\vec{x}) = \left|A_{n,m,j}(\vec{x})\right| = \mathcal{F}_k^{-1}\left\{G_{n,m,j}\left(\vec{k}\right)U_j\left(\vec{k}\right)\right\} \tag{3.65}$$

A single signal component for the fourth angular orientation ($m = 4$ centered on $-\pi/2$) and first radial orientation ($n = 1$, lowest center wavenumber 179 m^{-1}) at time $t = 107.8\mu s$ ($j = 45$) is seen in Fig. 3.14 (a). To compute $E(\vec{x})$ the magnitude of the sum of components along the radial direction is taken,

$$E_{m,j}(\vec{x}) = \left|\sum_{n=1}^{N} A_{n,m,j}(\vec{x})\right| \tag{3.66}$$

Figure 3.14 (b) illustrates $E_{m,j}(\vec{x})$ for the same angular position and time increment. The widths and weighting factors are calculated at each orientation and time frame as

$$w_{m,j}(\vec{x}) = \frac{\dfrac{\sum_{n=1}^{N} a_{n,m,j}(\vec{x})}{\max_n\left(a_{n,m,j}(\vec{x})\right) + \varepsilon} - 1}{N - 1} \tag{3.67}$$

and

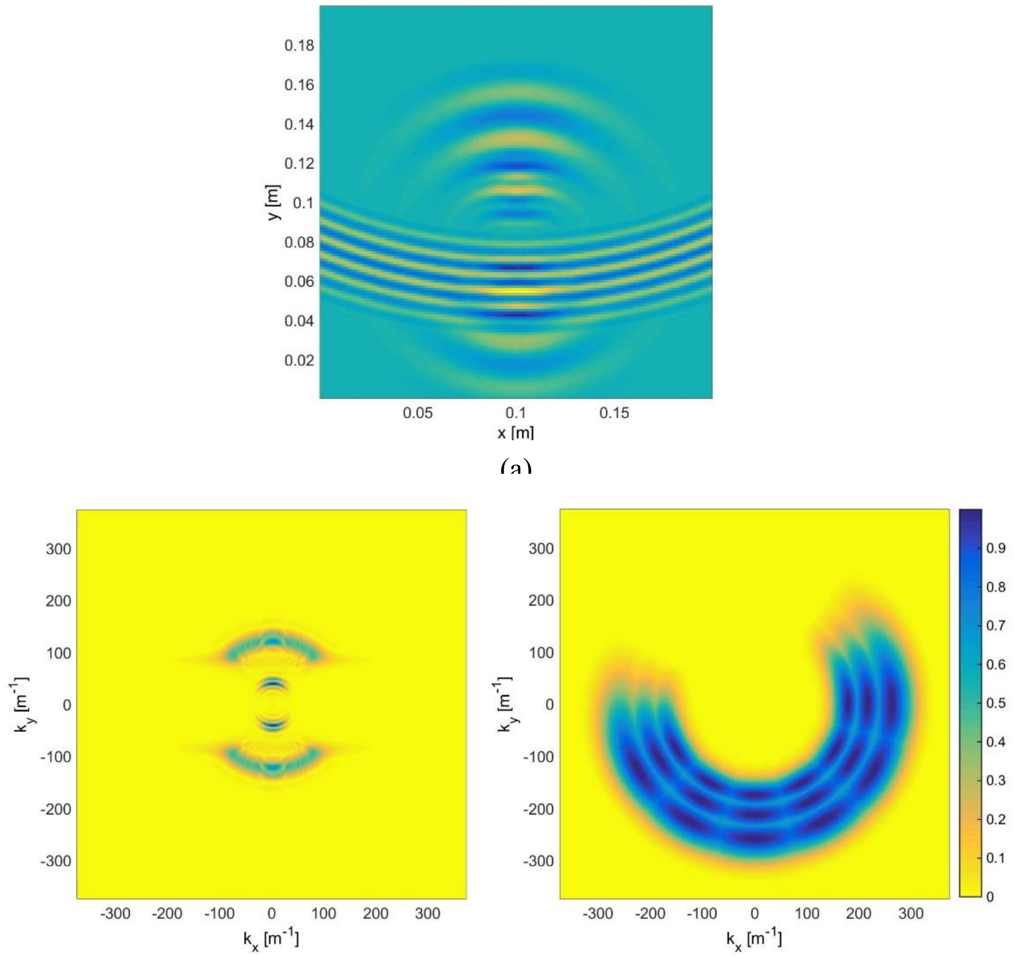

(a)

(b) (c)

Figure 3.13 The 2-D wave example in the space domain (a) and the wavenumber domain (b) along with the bank of filters in the wavenumber domain (c)

$$W_{m,j}(\vec{x}) = \frac{1}{1+\exp(\gamma(c-w_{m,j}(\vec{x}))} \tag{3.68}$$

At this point PC can be calculated by Eqn. (3.41), the results of which are seen in Fig. 3.14 (c). The PC plot clearly indicates the location of the discontinuity in the wavefield.

3.5 Conclusions

In this chapter, the Phase Congruency method is adapted for use mapping damage in plate-like structures. First the method as described by Kovesi [65], and Venkatesh and Owens [79] for edge detection in images was summarized. Then the method was considered in the context of GW. Adaptations are made to accept the time domain, and to reflect the dominant sinusoidal nature of the wavefield. This resulted in changing the range of wavenumbers evaluated. Next the procedure

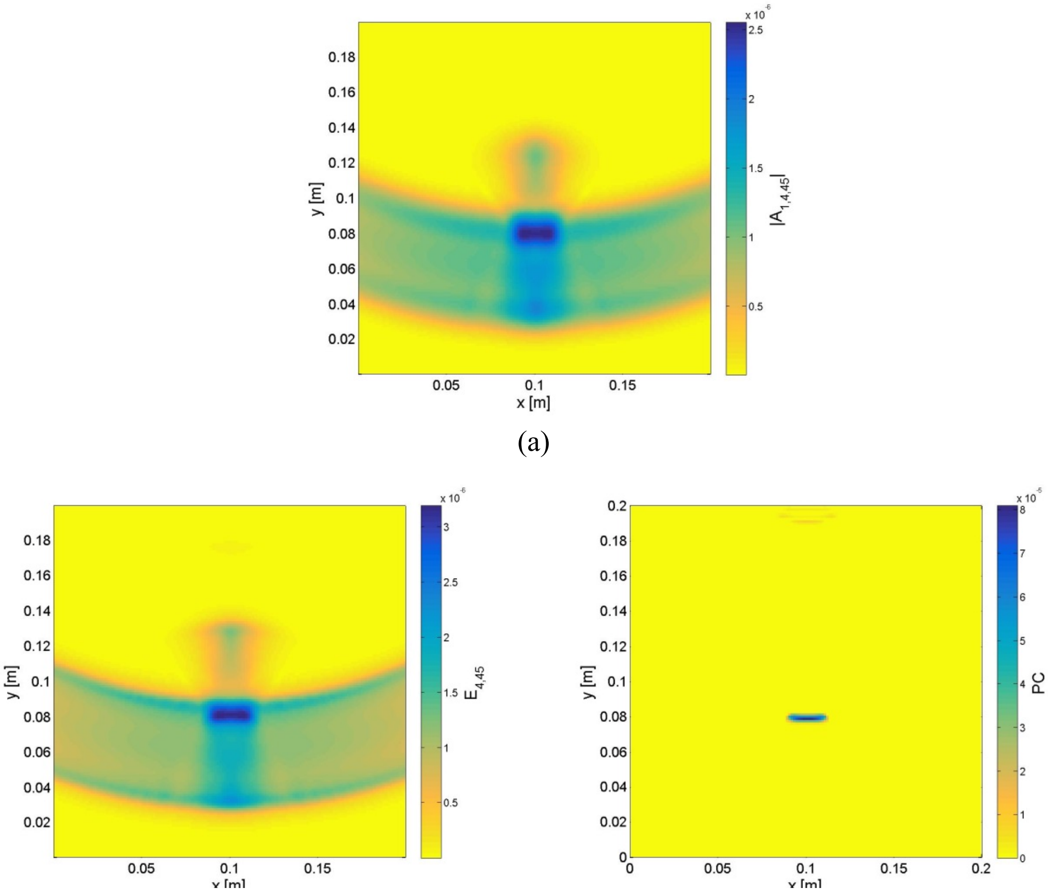

(a)

(b) (c)

Figure 3.14 An example of the computed components $a_{1,4,45}$ (a) along with $E_{4,45}$ (b) and PC (c) for calculating the PC for damage mapping is described for both 1-D and 2-D measurement fields.

The most important adaptation of the method is recognizing that by limiting the range of wavenumbers considered the underlying structure of the wavefield could be detected. Since the wavefield is modeled as a set of rectangular functions modulated by a wave, shifting filter banks in the Fourier Domain so that the lower bound is the modulating wavenumber, approximates edge detection of the rectangular wave.

The second adaptation is incorporating the time dependence of the signal. A simple summation is added to the PC equation to account for time. By keeping the time slices independent of one another, the process can be parallelized for computation.

The last adaptation of the method for use with GW is the choice of filter shape. The Gabor filter proved to be the best choice for GW based on characteristic criteria and quantitative evaluation with sample signals. This was not surprising since Gabor predicted that this filter has the best tradeoff between localization in space and wavenumber [80]. The choice of logarithmic spacing of filters allowed the filter width to scale with the center wavelength of the filter.

The last section of this chapter detailed the Phase Congruency for damage mapping procedure. This was done with a 1-D and 2-D example. The procedure shown here will be used in the next chapter to for mapping damage on numerical and experimental samples.

This chapter utilizes the similarity between the detecting discontinuities in images and in GW while proposing improvements to increase the sensitivity of the method to discontinuities in wavefields. The method described here is attractive for NDE as is does not require any a priori knowledge of the specimen. The inputs and parameters for the analysis can all be gleaned from the measured wavefield.

CHAPTER IV

PHASE CONGRUENCY RESULTS

4.1 Overview

The Phase Congruency for damage mapping method as developed in the previous chapter is demonstrated on a series of numerical and experimental datasets. In the first section, three numerical models are presented. In the next section, six experimental samples are considered. In both the numerical and experimental cases, the complexity of the models increases bringing added realism to the damage. Following these evaluations a method for characterizing the damage is given.

4.2 Numerical Results

This section will present three numerical models: the aluminum plate with a notch and fiber glass plate with a delamination described in Section 2.6 and a model of an aluminum bar with a change in thickness. This series of models spans a range of complexity. The first model approximates the 1-D analytical model used to develop the method. The second model adds a 2-D wavefield but still only has a linear damage analog. The third and final numerical simulation is for a 2-D wavefield with a 2-D damage analog. The PC for damage mapping results are compared to damage maps computed with the root mean square of the surface displacements over time.

4.2.1 Aluminum Bar

The first numerical model simulates an aluminum bar with the center third of the bar reduced to half thickness. The bar is 45 cm long, with the center 15 cm reduced from a nominal thickness of 6.35 mm (0.25 inches) to 3.175 mm (0.125 inches) (see Fig. 4.1). The material properties are those given in Table 2.1. One end of the bar is forced with a four-cycle tone burst at 50 kHz. The other end of the bar is held fixed. The bar is discretized into 8-node linear brick, reduced integration, hourglass control elements (C3D8R) roughly 1 mm cubed. The simulation is solved in ABAQUS with the Standard Explicit solver. The simulation is run for 2e-4 seconds with 5.3e-8 s steps. The surface displacements are recorded for the surface opposite the notch.

The results from the aluminum bar consider a simple change of wavenumber with reflections. The surface displacements are input to the PC for damage mapping method as described in Section 3.4.2. For this analysis, four filters are used in the radial direction and only one filter in the angular direction as this simulation approximates a 1-D case. The orientation of this filter is aligned with the long axis of the bar. With the number of filters in both the radial and angular directions the signal components $A_{n,m,j}(x)$ are calculated for each point, filter and time instance then used to calculate PC according to Eqn (3.43). The results are seen in Fig. 4.2.

Comparing the PC results (blue line) from this data set with a simple root mean square (RMS) along the time domain (red line), the advantages of PC are clear. Phase Congruency for damage mapping only gives indications where the discontinuity is located, while the RMS can only indicate changes in the bar's response over space. Since the displacement amplitude increases over the thin section of the bar, RMS transitions between high and low values over the thin and thick sections respectively. This infers a change in geometry. However, PC only gives an indication where the discontinuity occurs. Therefore, interpretation of the PC results is quite straightforward.

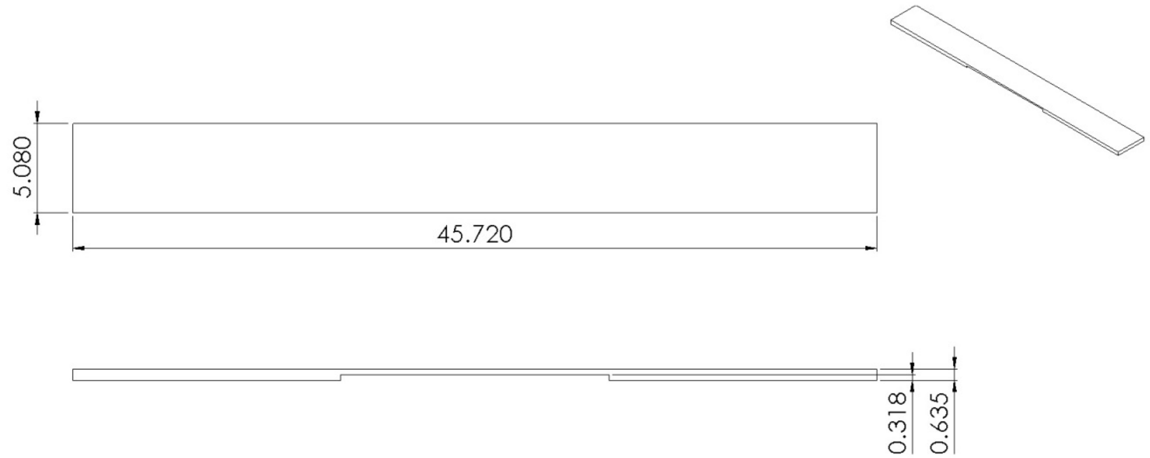

Figure 4.1 Schematic of numerical aluminum bar (dimensions in cm)

4.2.2 Aluminum Plate with Notch

The surface displacements from the numerical simulation of the aluminum plate with a notch described in Section 2.6.1 are used to in the PC for damage mapping method as well. Since the component calculation happens independently of time, the time domain of this dataset is decimated by a factor of four to reduce the computational load. Again, PC is calculated as described in Section 3.4.2. In this case, six angular filter orientations are used along with five filters in the radial direction. Phase Congruency is computed with these parameters. The results for the 60% notch in the aluminum plate clearly indicate the location of the notch (Fig. 4.3 (a)).

The RMS plot for the same dataset is more challenging to interpret (Fig. 4.3 (b)). The notch is evident but it is obfuscated with the variations in RMS due to the reflected and transmitted waves interfering with the incident wave. These interactions are clearly noticed in the area just in front of the notch where there is a high RMS value due to constructive interference of the reflected wave

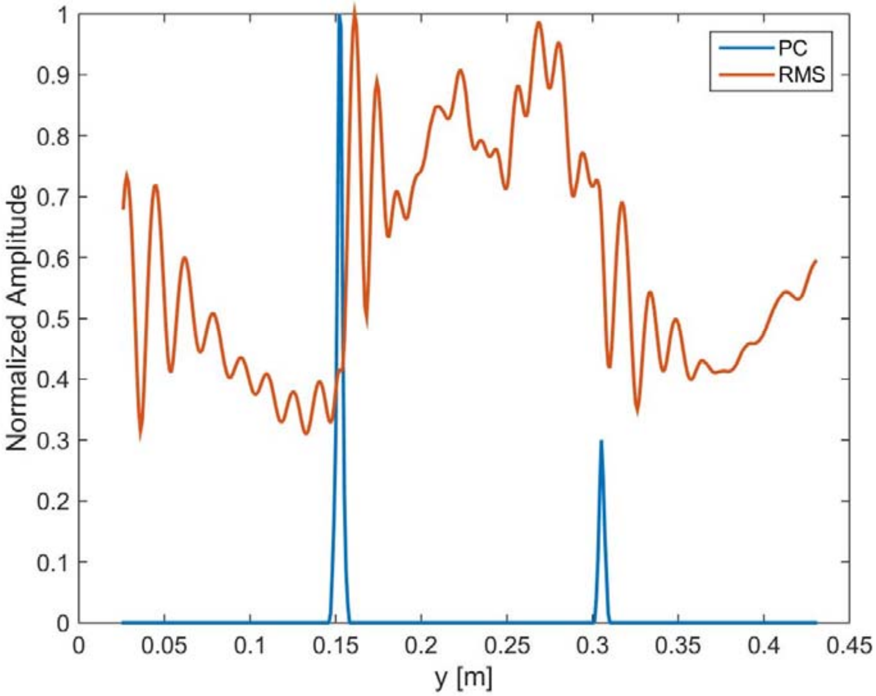

Figure 4.2 Results for the numerical simulation of an aluminum bar with a thickness change in the center third of its length; PC (blue line) and RMS (red line)

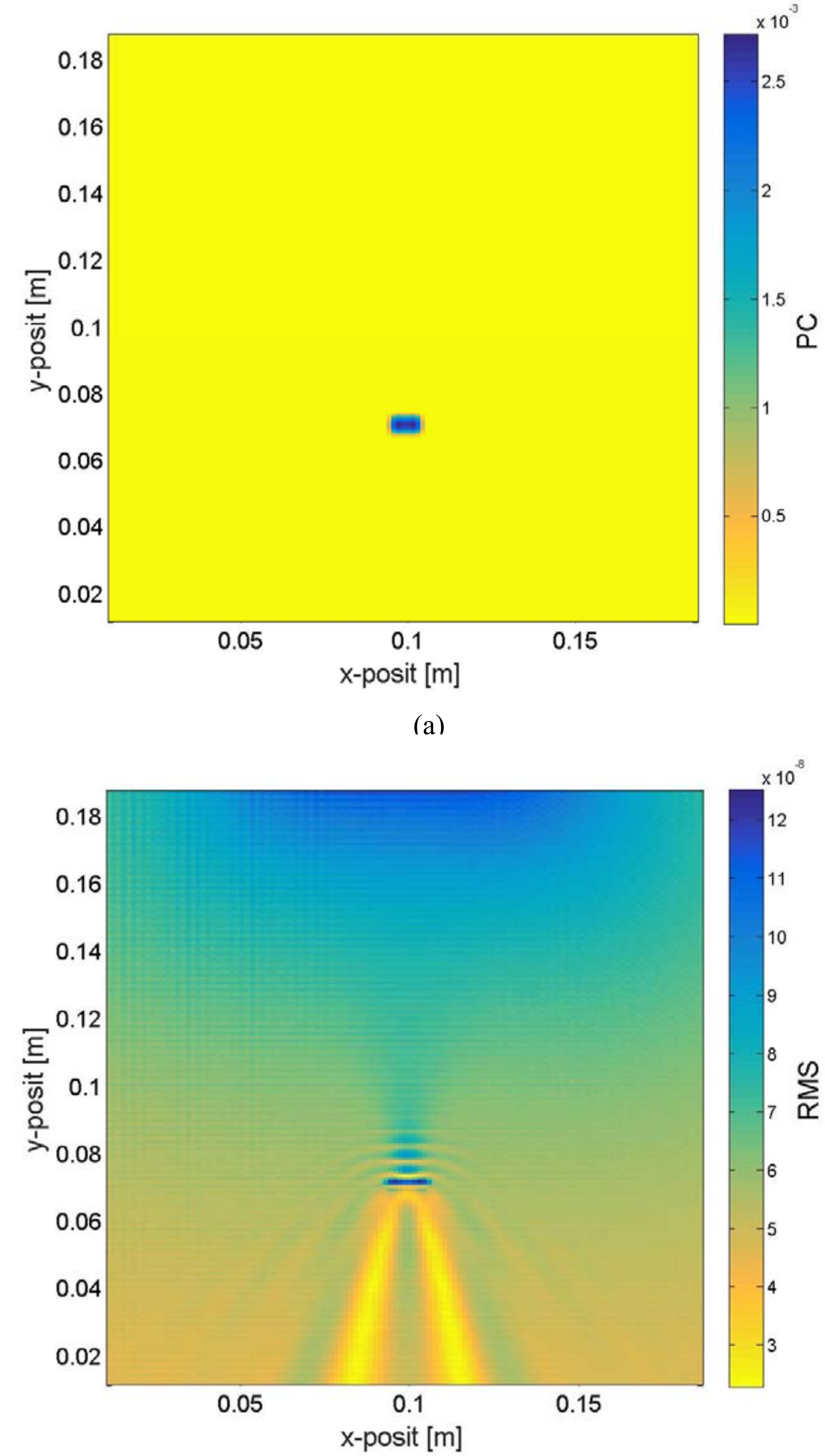

(a)

(b)

Figure 4.3 Results for the numerical simulation of a 60% thickness notch in an aluminum plate; PC (a) and RMS (b).

and the incident wave. Conversely, destructive interference between the transmitted wave and the wave passing around the notch is evident in the low amplitude tails extending from the notch's edge. None of these features are evident in the PC plot. The other notch depths modeled in Section 2.6.1 are considered as well with very comparable results.

4.2.3 Composite with Delamination

The fiberglass plate with a simulated delamination from Section 2.6.2 is considered as well. The surface displacements from this model are input to the PC method. The dataset is decimated by a factor of four as was done for the aluminum plate in the previous section. This method uses six filter orientations in the angular direction. Three filters in the radial direction are used. As in the previous section, the procedure for computing PC from Section 4.2.3 is used; the results of which are seen in Fig. 4.4 (a).

The results from the delamination model further indicate the strengths of the PC approach. Here a neat circle clearly indicates the boundary of the delamination. In contrast, the RMS plot (Fig. 4.4 (b)) has raised amplitudes over the delamination indicating the presence of the simulated damage. There are variations in amplitude in this region however. A practitioner would have no way of knowing if these variations are due to changes in the specimen or interference between wave components as is the case here. Despite the small spurious indication at the lower boundary of the delamination, the PC plot in Fig. 4.4 (a) would give an inspector a clear indication of the shape and location of the damage.

The results from the numerical models match the expectations from the analytical modeling. Discrete indicators are seen at all damage boundaries but the bulk of the area over the damage / geometry changes do not give indications. This is an improvement over simple RMS calculations of the surface velocities. In the next section corresponding experimental models will be evaluated.

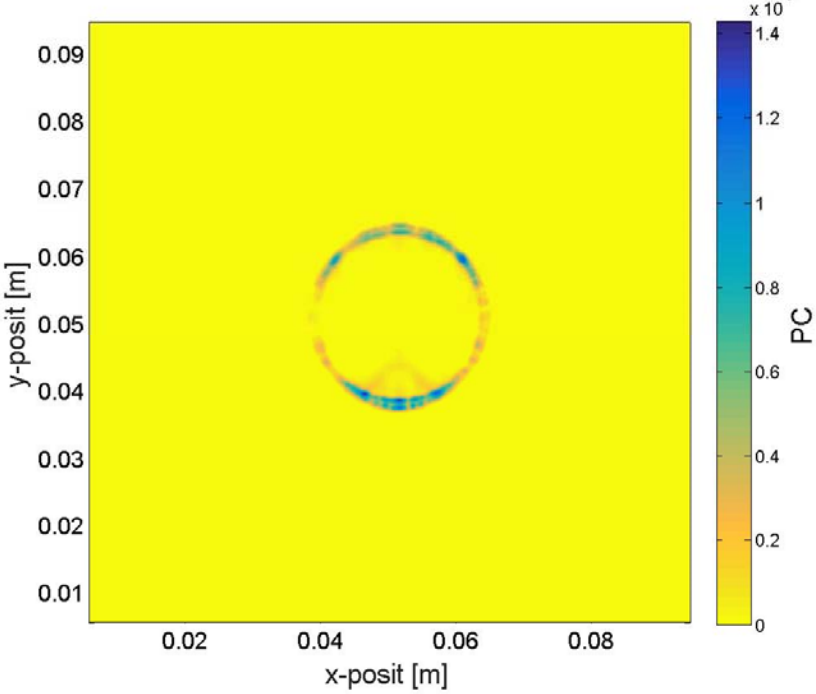

(a)

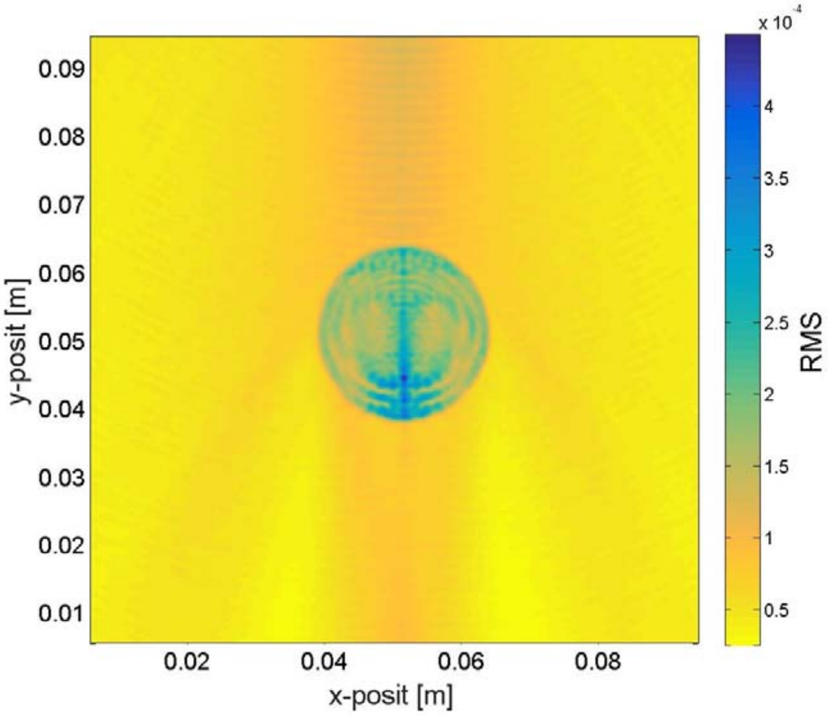

(b)

Figure 4.4 Results for the numerical delamination simulation; PC (a), RMS (b)

4.3 Experimental Results

The experimental models corresponding the numerical models from the previous section are considered along with two more complex cases. A plate with a complex cross-section and an added mass to simulate a defect is considered as well as impact damage in carbon fiber plates. These models are developed to evaluate the PC for damage mapping method as well as to compare against the numerical results described in the previous section.

4.3.1 Aluminum Bar

The first sample is a simple aluminum bar with the profile machined such that the center third of the bar is half as thick (3.175 mm, 0.125 inches) as nominal bar thickness (6.35mm, 0.25 inches) (see Fig. 4.5). The thinned length is approximately 15.24 cm (6 inches) while the total scanned length is 45.72 cm (18 inches) centered around the thinned portion of the bar. The bar is nominally 5.1 cm (2 inches) wide. A row of rectangular ceramic plate piezoelectric transducers from STEMInc are epoxied to one end of the bar while the other end is clamped in a bar clamp with rubber shoes on the jaws. The row of transducers is excited simultaneously with a 100 kHz, four-cycle tone burst. The surface velocities are sampled on a grid of 229 x 17 points with 2.2 x 2.3 mm spacing respectively. The sampling rate is 2.56 MHz for 0.8 ms. The PC values are calculated independently for each time slice, so the spacing in time does not need to obey the Shannon-Nyuist sampling theorem. Therefore, to reduce computational load, the time dimension is decimated by a

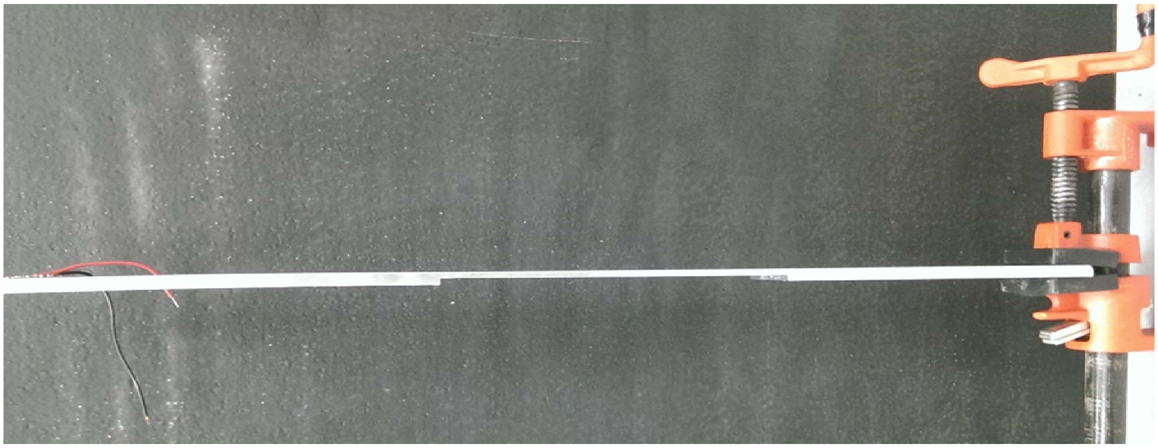

Figure 4.5 Profile of aluminum bar

factor of five and truncated after 238 μs. Section 1.4 details the experimental set up for measuring the surface velocities of the plate.

This sample approximated a simple 1-D case. As such only one filter orientation aligning with the bars major axis is used, along with three filters in the radial direction. The procedure outline in from Section 4.2.3 is used to compute the PC map seen in Fig. 4.6. The results shown in Fig. 4.6 align closely with those for the numerical results in Fig. 4.2. The PC plot (blue line) clearly indicates the location of the changes of thickness in contrast to the RMS plot (red line). The nominal RMS values do change over the thinned region however. As in the numerical case, the signal is complicated by the interference between mode reflections. In the PC result, none of this is seen, only single lines of indications denoting the boundaries of the change in thickness.

4.3.2 Aluminum Plate with Notch

The next sample in order of increasing complexity is the notch in the aluminum plate. This is again a simple case of an isotropic material, with a simple simulated defect. This sample utilizes the full 2-D analysis by incorporating multiple filter orientations in the angular direction in contrast to the

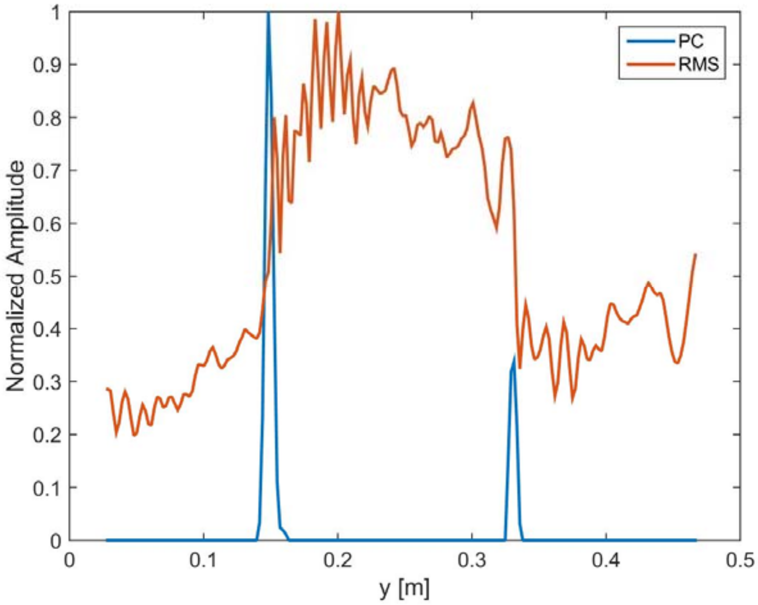

Figure 4.6 Experimental results for an aluminum bar with a change of thickness; PC (blue) and RMS (red).

aluminum bar that only utilizes one filter orientation.

The dataset described in Section 2.7.1 is used in this analysis. This data set was collected with an excitation frequency of 200 kHz. As is done with many datasets in this chapter the time domain is decimated by a factor of two to reduce the computational load. It is also truncated between $t = 27.0$ and $105.1 \mu s$. This time window is selected because it incorporates the time in which the wave and notch are interacting. Five radial filters are used along with six angular filter orientations.

The PC map is developed using the method described in Section 3.4.2. The results for the 60% notch depth are shown in Fig. 4.7 (a). This case appears to be approaching the limits of the analysis method. The noise in the signal in the upper right corner of the scanned area causes PC values that are in the range of the PC values related to the notch. The reflected wave's low amplitude, relative the incident wave's causes very little change in the wavefield for the PC method to detect. Even with the noise in the upper right corner of the plot however, the notch is clearly shown in the center of the figure. Contrasting that with the RMS results which do not clearly show the notch. For all other notch depths, 70%, 80% and 90%, the notch is clearly seen without spurious indications in the field. Figure 4.8 (a) illustrates this with the results for the 90% notch depth. Comparing the results with the RMS plots in Fig. 4.8 (b), the notch is evident in the PC results without the background oscillations in the rest of the field resulting from the wave interactions in the RMS plots.

4.3.3 Composite Plate with Delamination

Two different measurements are made of the composite plate with the simulated delamination. The first set of data is the set described in Section 2.7.2. A 15 mm x 2 mm piezoelectric wafer transducer is used to excite this sample with a four-cycle 264 kHz tone burst. This type of transducer is broadband but relatively low amplitude. The dataset is decimated in the time domain by a factor of two and truncated to the range $t = 15.2$ to $99.6 \mu s$.

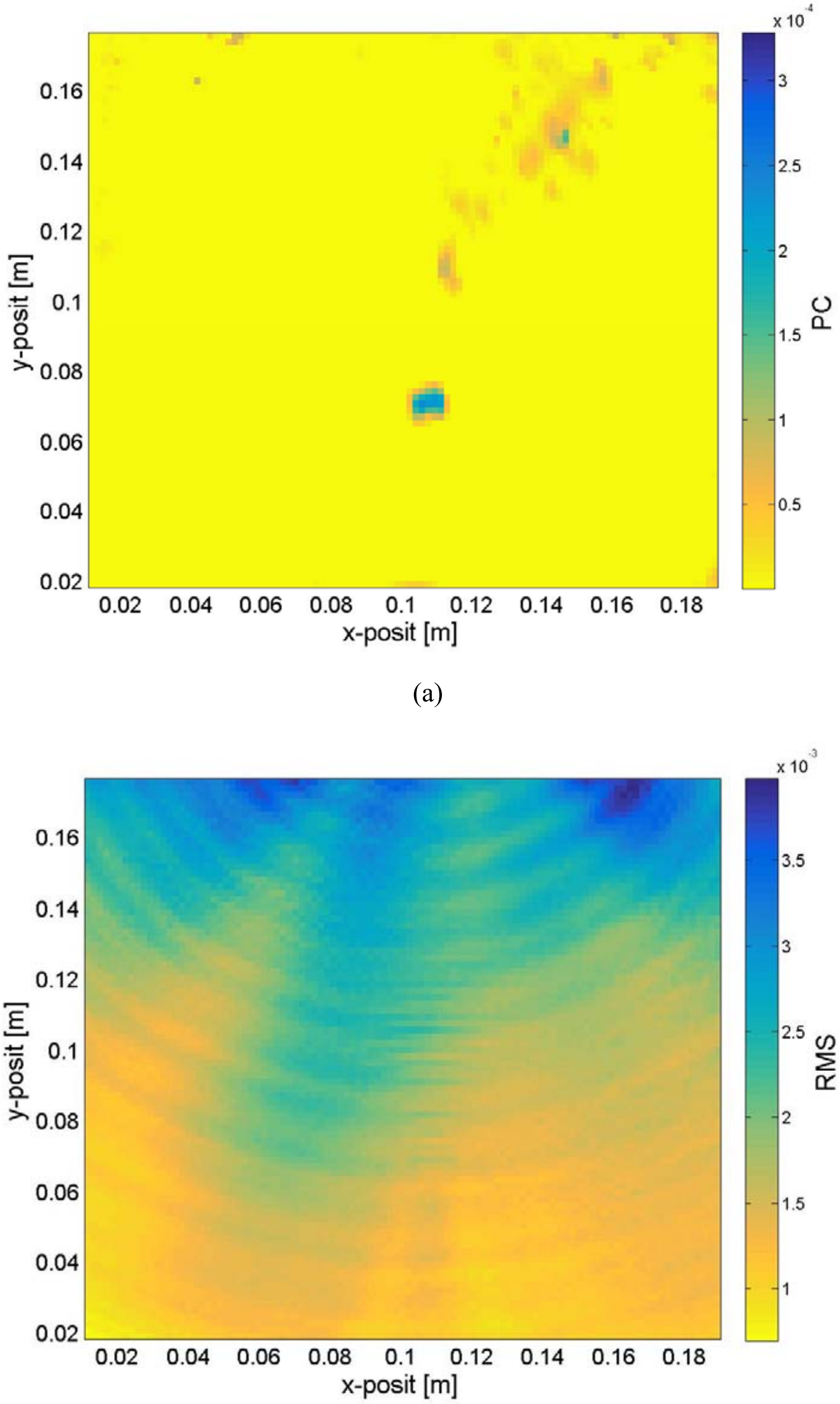

(a)

(b)

Figure 4.7 Experimental results for aluminum plate with a notch 60% the depth of the plate thickness; PC (a), RMS (b)

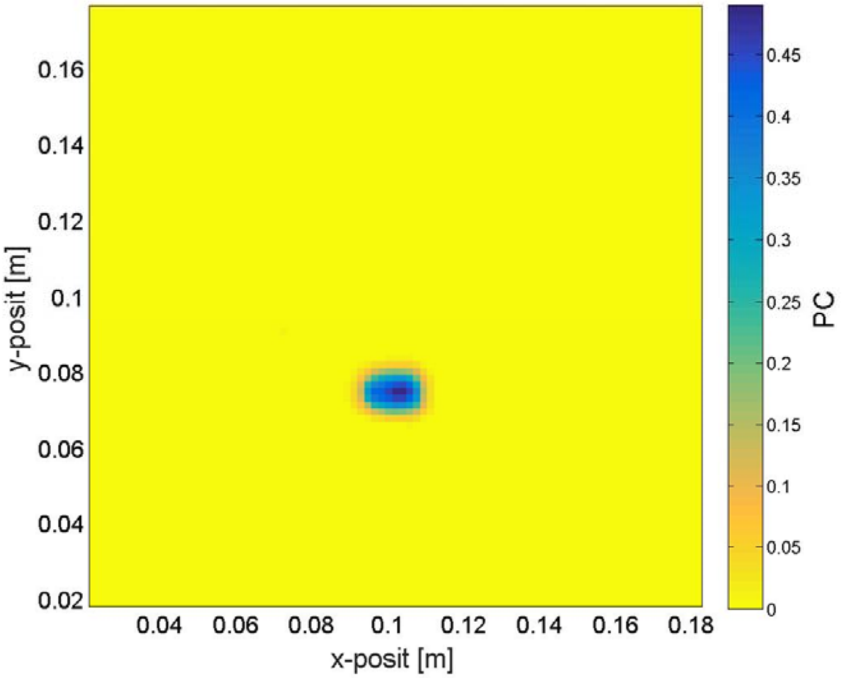

(a)

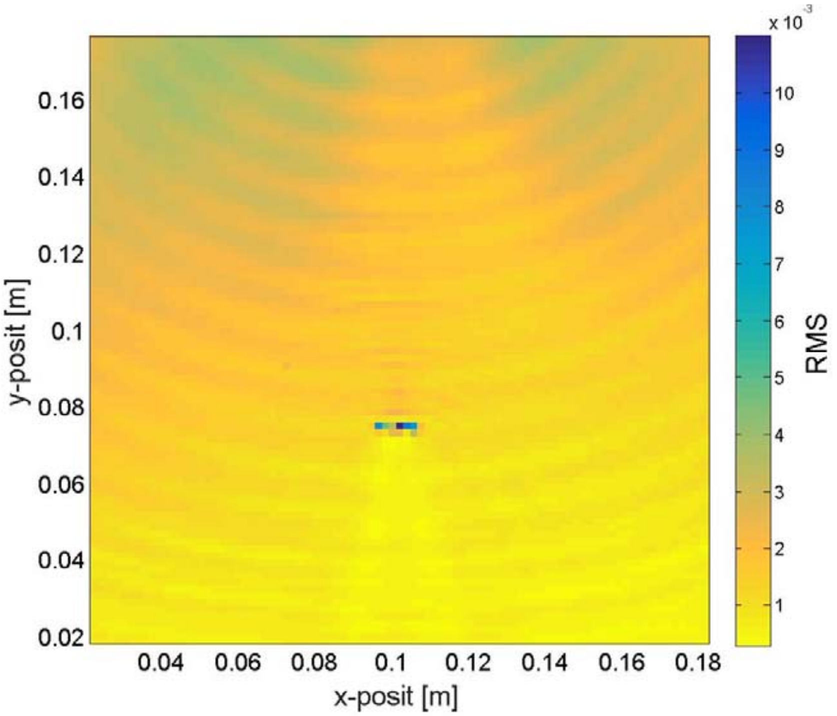

(b)

Figure 4.8 Experimental results for aluminum plate with a notch 90% the depth of the plate thickness; PC (a), RMS (b)

Following the procedure laid out in Section 3.4.2 a map of PC is given in Fig. 4.9 (a). The PC method highlights the delamination quite well. Although, the results are not as clean as in the numerical case (Fig. 4.4(a)) which highlighted just the delamination boundary, the strongest indications are at the boundary of the delamination. In comparison to the RMS results in Fig. 4.9 (b), the PC method only has indications over the delamination.

There is a fundamental difference in the delamination between the numerical case and the delamination case. In the numerical case, there is no contact between nodes on either side of the delamination. Given this, there is a distinct mode created over the delamination. This mode is very clearly seen in Fig. 2.21 (b). However, in the frequency-wavenumber domain for the experimental case the second mode is not clearly seen (Figure 2.30 (b)). This is likely due to the fact that the interactions between the opposing sides of the delamination are much more complex. There are kissing interactions as well as contact shear forces between the sides of the delamination that complicate the wavefield over the delamination. As these distributed interactions cause discontinuities in the wavefield throughout the area of the delamination. The PC content across the delamination is likely reflecting the cross-delamination interactions. Therefore, it is unlikely that a singular boundary around the delamination will be identified. That aside, considering the PC values in a radial direction from the center of the delamination, the boundaries are generally higher than the interior section along the radial direction.

This set of results also highlights another aspect of the PC for damage mapping method The resolution is limited to the center wavelength of the last filter. Since the last filter tapers to zero at the maximum wavenumber, it suppresses this high wavenumber content which leads to results that appear to have a lower resolution than a comparable result with no filtering in the spatial domain. Comparing Fig. 4.9 (a) and (b) illustrates this point. The PC results Fig. 4.9 (a) in the area over delamination have a more blurred appearance than the RMS results in Fig. 4.9 (b). The RMS results are computed node-wise directly from the measured data so no filtering occurs in this

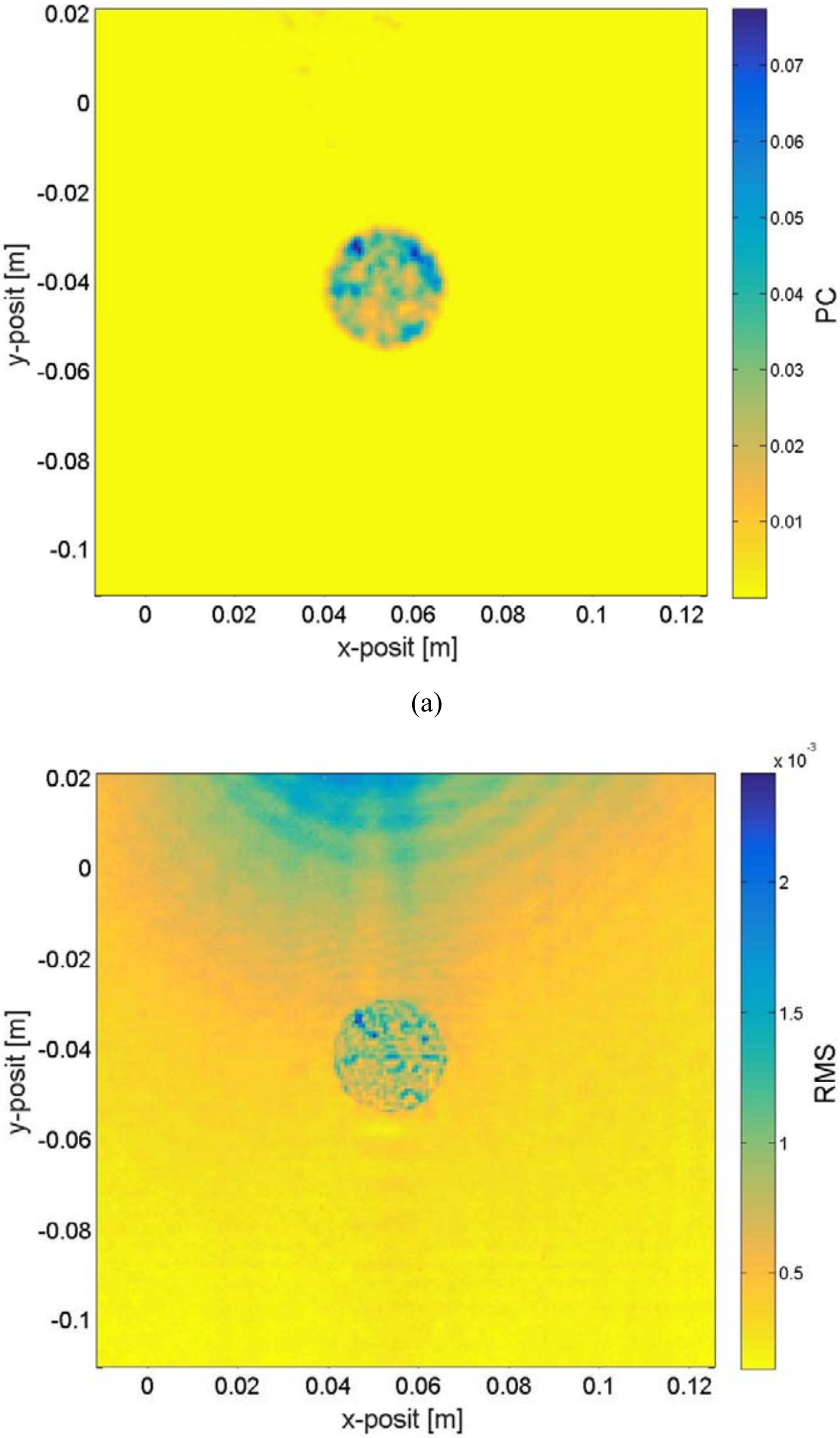

(a)

(b)

Figure 4.9 Results for a delamination simulated in a fiberglass plate excited at 264 kHz; PC (a) and, RMS(b) dataset, while the filter bank decomposition suppresses the high wavenumber content.

Despite the content over the interior of the delamination, the PC results give a very clear indication of the delamination as compared to the RMS results are values near the transducer at the top of the field are on the order of the signal over the delamination. This is a primary example of one of the primary attributes of phase based methods due to their independence from amplitude.

The same composite plate is used in a second experiment. This experiment utilized the experimental setup from Section 1.4 to measure the wavefield. The transducer in this case is a resonance type transducer, which has very limited bandwidth but high amplitudes. The transducer is an APC International, Ltd. Ultrasonic Cleaning Transducer, P/N 90-4050. The transducers is clamped to the sample with a bar clamp with rubber shoes over the jaws. This transducer is used at its lowest measured resonance frequency of 16.5 kHz. The corresponding wavelength for this frequency is 2.45 cm. This is nearly the same as the diameter of the delamination, 2.54 cm. This allows the method to be evaluated when the wavelength of the signal is roughly equal to the size of the defect sought.

For this experiment, an eleven-cycle tone burst at 16.5 kHz is used to excite the transducer. The sample is measured on 197 x 235 point grid with .78 x .76 mm spacing between nodes. The SLDV samples the signal at 1.28 MHz for 4 ms. The data is truncated to $t = 0.188$ to $1.2\ ms$ for analysis.

The dataset is processed with three filters in the radial direction and six filters in the angular direction. The calculated PC values are seen in Fig. 4.10 (a). There is a clear difference in the results of the PC and RMS (Fig. 4.10 (b)) approaches. In this example, the wavelength is on the order of the size of the delamination. As seen in the RMS plot, there is very little disturbance of the wavefield due to the delamination. However, the PC method clearly picks out the delamination. The results are not as good as the higher frequency example in Fig. 4.9 (a), although still an

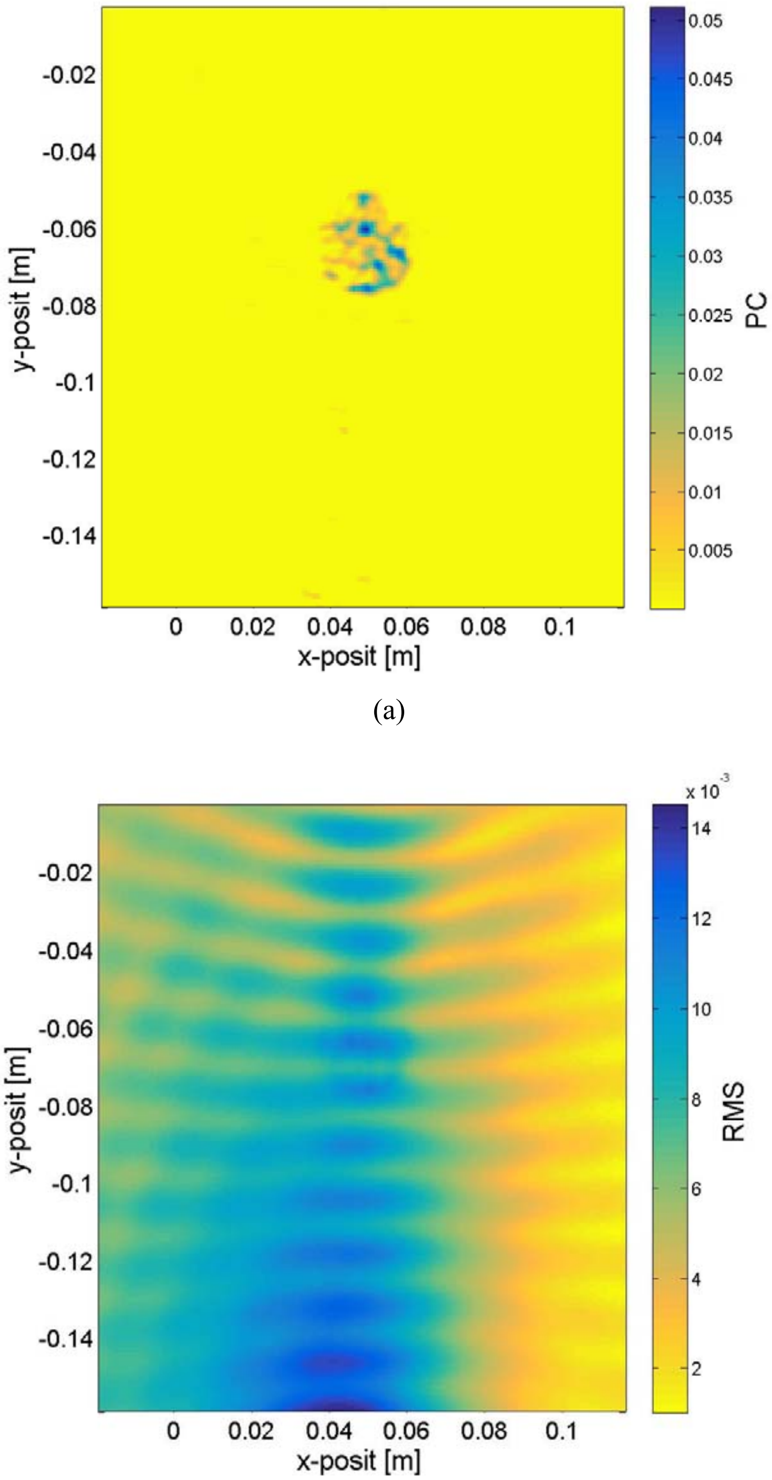

(a)

(b)

Figure 4.10 Results for a delamination simulated in a fiberglass plate excited at 16.5 kHz; PC (a) and, RMS(b) improvement over the RMS estimate the damage. This result demonstrates the ability of the method to discern even small disturbances in the wavefield.

4.3.4 T-stringer

The next sample is a sample with complex geometry provided by NASA Langley Research Center. The sample is a T-stringer composite plate with two reinforcing stiffeners as shown in Fig. 4.11. To simulate damage, a mass is adhered with shear gel to the back of the plate. For this sample, the resonance type piezoelectric transduce described in the previous section is used. The transducer is excited at its second measured resonance at 38.5 kHz when coupled to the plate. The transducers is clamped to the sample with a bar clamp with rubber shoes over the jaws and excited with a four-cycle tone burst at 38.5 kHz.

The surface velocity of the plate is measured using the experimental set-up described in Section 1.4. A grid of 203 x 144 sampling points is used with spacing of approximately 1.2 mm in each direction. The plate's response is sampled at 640 kHz for approximately 0.8 ms with resulting time series decimated by a factor of four for analysis. This sample has a rough surface texture due to the woven fabric construction. To improve the signal received by the SLDV 3M Scotchlite™ Reflective Sheeting is applied to the surface.

The PC values are computed according to the process described in Section 3.4.2. In this case, five filters are used in the radial direction and six in the angular direction. Four features are seen in the results shown in Fig. 4.11 (a). The response due to the added mass is seen at approximately (0.06 mm, 0.095 mm). At approximately (0.1 mm, 0.035mm) a surface defect is seen. This surface defect leads to the SLDV measuring the large displacements of the retroreflective tape rather than plate motion and appears as a strong discontinuity in the wavefield. The PC method reflects this strong discontinuity with large PC values. The left and right edges of one of the stringers are seen around x = 0.11 mm and x = 0.16 mm. These represent changes in thickness thus give larger PC values. The last feature is the surface texture. Due to the fiber weave, there are

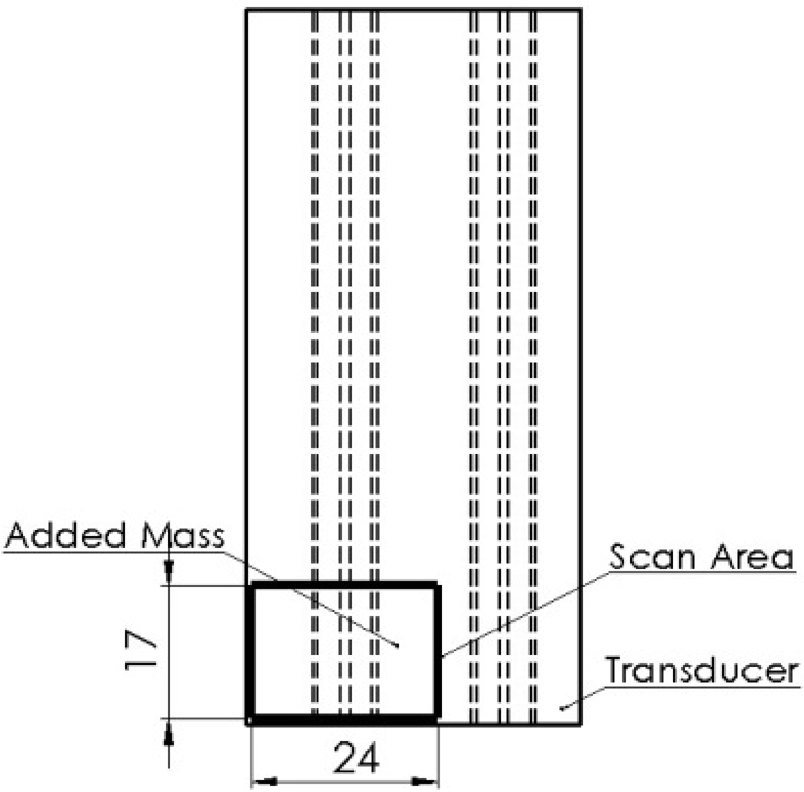

(a)

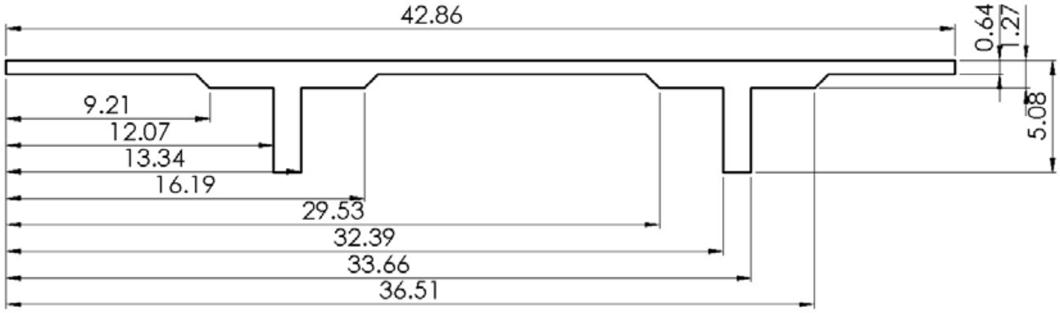

(b)

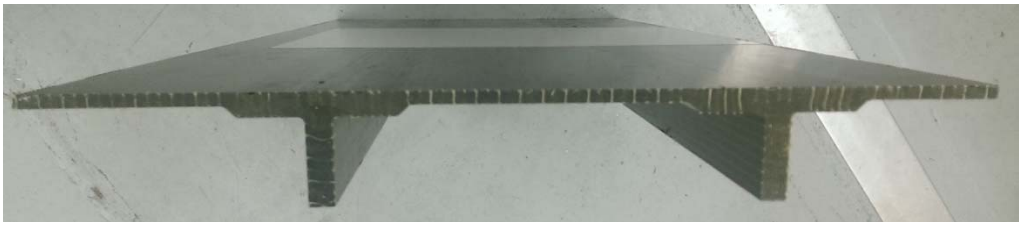

(c)

Figure 4.11 Schematic (a) (b) (dimensions in cm) and photograph of the T-stringer plate (c).

bumps along the surface in straight parallel lines. The detail provided here is far richer than that provided by the RMS values shown in Fig. 4.12 (b). The RMS fails to capture any of the features seen in the PC results. The PC results again show an ability to capture small changes in wavenumber that the RMS maps are not able to.

4.3.5 Plate with Impact Damage

To evaluate the PC for damage mapping method on a set of actual impact damage, two carbon fiber plates (Rockwest Composite P/N 48222) are impacted. These impacts cause complex damage with multiple transverse cracks and delaminations that resemble damage likely to be seen in the field. These plates provide realistic samples to evaluate the PC for damage mapping method.

The impact damage is created by dropping a 2.15 kg weight onto a steel ball that concentrates and transfers the force to the plate. The weight is suspended above the sample and released. The weight strikes the 3.175 cm diameter steel ball bearing that is placed on the plate. The weight is dropped from heights ranging from 0.61 to 1.22 m (2 to 4 ft.) above the plate in 0.1524 m (0.5 ft.) increments. The ball bearing is held in place laterally by a piece of Styrofoam. Following the initial impact, the Styrofoam is slid forward, moving the ball from between the impactor and the plate while moving the Styrofoam between the plate and the weight to prevent additional damage from any secondary impacts. Four impacts are made on each plate at different locations. The nominal locations of the impacts are shown in Fig. 4.13.

The APC transducer previously described is used for this series of measurements. This experiment utilizes the third resonance of the transducer at 122 kHz. The transducer is driven by a continuous sine excitation. The transducer is clamped with a pipe clamp at the center of the edge nearest the defect to be inspected. This excitation gives large enough amplitudes that no surface preparation is needed to get adequate velocity measurements from the SLDV. The measurements are taken using the experimental set-up described in Section 1.4. A 113 x 127 point measurement grid is used with approximately 0.72 x 0.70 mm spacing respectively for each impact location. Each

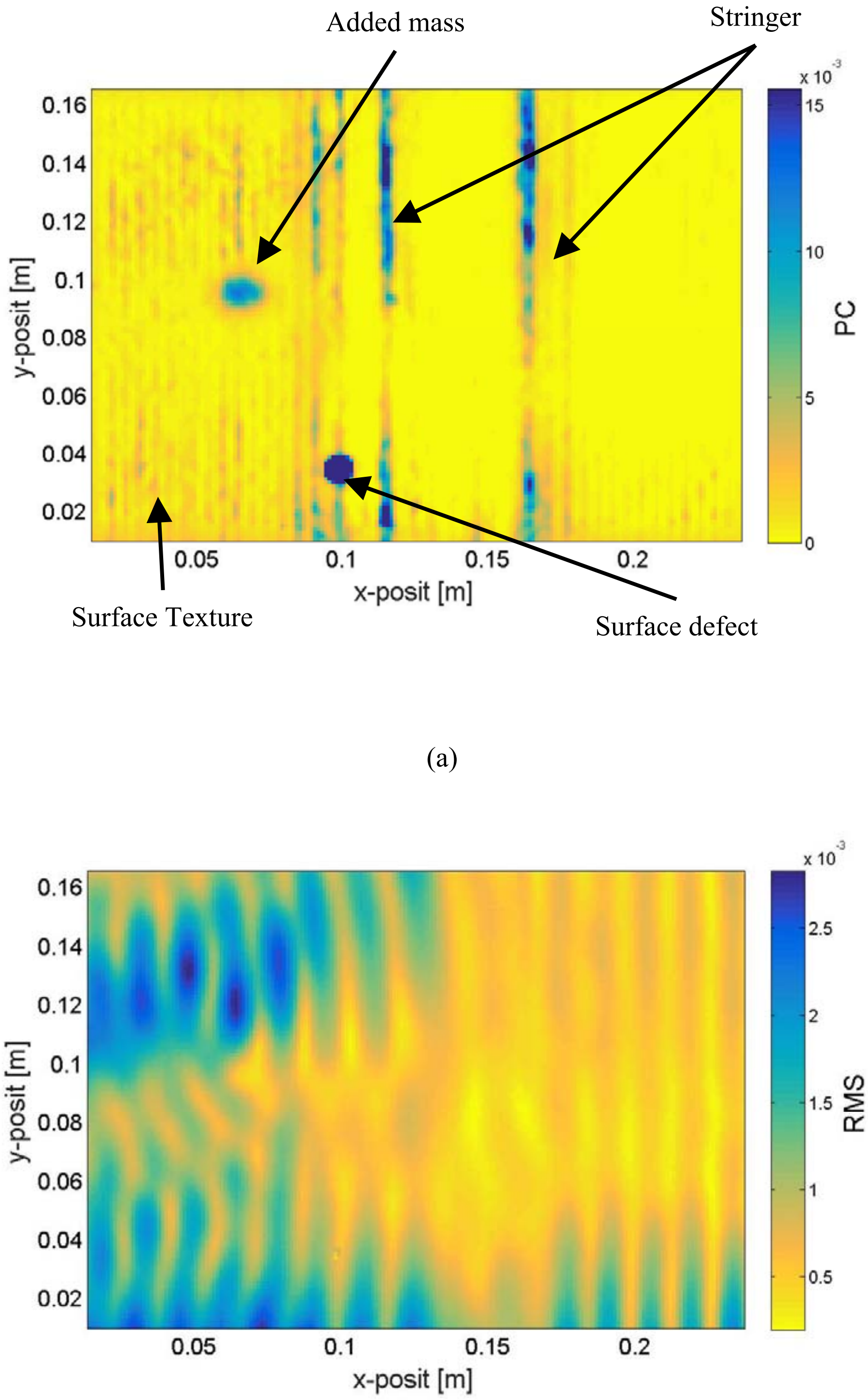

(a)

(b)

Figure 4.12 Results for T-stringer plate; PC (a) and, RMS(b)

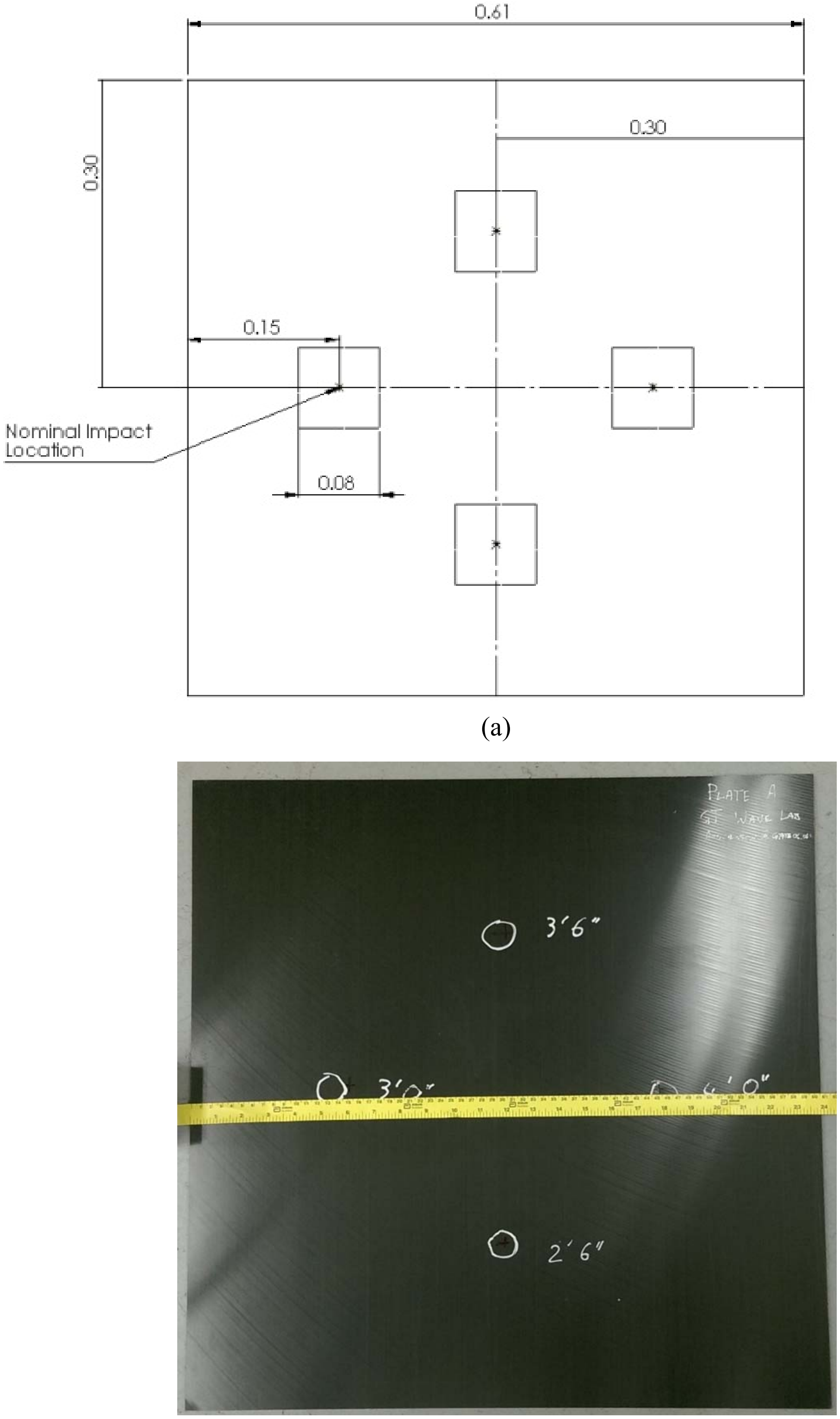

(a)

(b)

Figure 4.13 Schematic (a) (dimensions in m) and photograph of one of the impacted plates with impact locations and drop heights (in feet and inches) marked in white (b) of the grid points are sampled at 2.56 MHz for 0.8 ms.

To form a basis of comparison for these complex damages, x-ray computed tomography (CT) scans were performed by NASA's Langley Research Center. The CT scans provide very high resolution (35.8 μm) and sensitivity to defects. Scans were provided in each of the three dimensions of the plate: the in plane, and two orthogonal out of plane scans as seen in Fig. 4.14. This set of scans allows detailed mapping of the damage.

The PC analysis for all results in this section used four filters in the angular direction and six in the radial direction. The signal is truncated after only 38.7 μs since the excitation is continuous, therefore there is no need to wait for the interrogating wave to pass through the full scan area. The time duration corresponded to 4.7 cycles of the excitation frequency.

4.3.6 CT Scan Imagery

The raw CT scan data for each impact is a set of three x-ray scans. Each set represents x-ray images in one orientation Fig. 4.14 (a). The three sets consists of a of x-ray images taken at even intervals through the plate as illustrated in Fig. 4.14 (b). The images in these sets contain dark spots in the location of voids caused by cracks or delaminations as seen in Fig. 4.14.

To convert the raster images to plots of damage, the PC for image processing technique is used according to Eqn. (3.41) since damage is represented by a change in from light to dark values. Each image is processed with the PC method independently. Then all three orientations are arranged into 3-D data cubes. The data cubes from each orientation are summed together, then summed along the depth direction giving a single 2-D representation of the data from all three orientations and at all depths. Accordingly, defects at all layers are superimposed in the resulting plots. The result of the summation is that transverse cracks give stronger indications than delaminations because transverse cracks are present in multiple layer images and their indications compound. Conversely, delaminations are present in just a few scan layers thus their indications

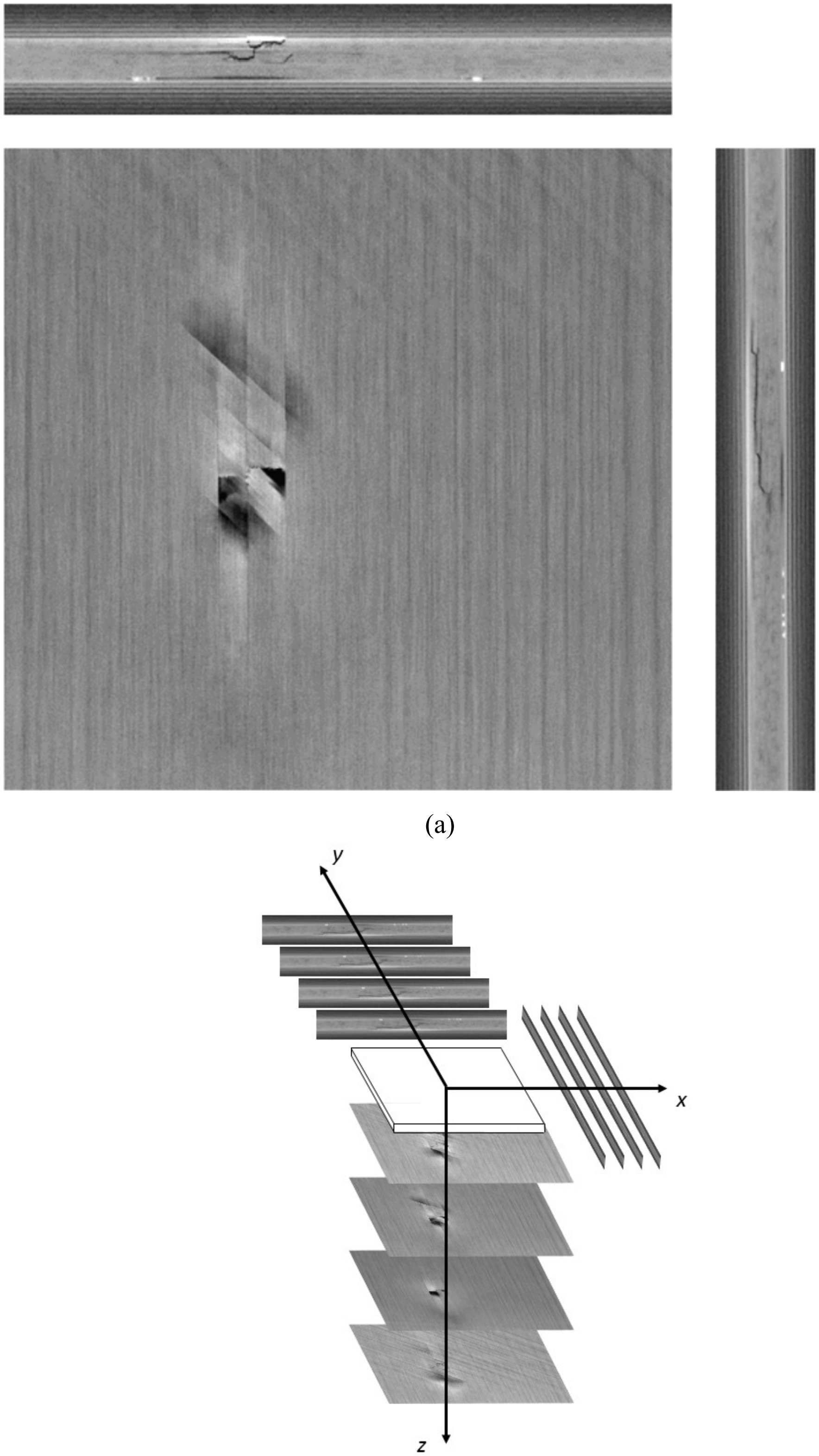

(a)

(b)

Figure 4.14 Sample of raw x-ray images in each of the three orientations (a) and a schematic three x-ray sets taken for each impact site (b) do not compound in the summation to the extent transverse cracks do.

The results for the SLDV and x-ray CT scans for each case are seen in Fig. 4.15 - 4.17 for the drop heights between 0.61 m and 1.22 m. Damage is not visible in the PC results for damage from drop heights lower than 0.61 m (2 feet). In each set the upper panel gives the results for the PC analysis, the middle panel RMS maps and the bottom panel gives the results for CT scans. The CT scans provided very high resolution images of the defects. For this reason, the scale of the CT scans (approximately 2.7 cm x 2.6 cm) are much finer than the PC results (approximately 7.5 cm x 8.3 cm square). The red boxes in the PC and RMS plots give the size and approximate location of the CT scans relative to the SLDV measurement.

Comparing the RMS and PC plots the shape of the mapped damage is similar between the two, although the PC results remove background content and help illuminate the damage. Neither RMS nor PC provides the richness of information available in the CT scans. The CT scans contain bright narrow lines indicating transverse cracks. Typically, the transverse cracks only span one layer of the composite layup due to the orientations of the fibers. These cracks are generally oriented parallel to the fiber orientation. The exception being the pair of cracks that are approximately perpendicular to fiber orientation in Fig. 4.17 (c).

The other features evident in the scans are delaminations. These delaminations typically extend from one of the transverse cracks and are characterized by the lighter colors spanning between transverse cracks. The sides of delaminations that are not associated with transverse cracks appear to transition gradually to the fully bonded background value. The cross section in Fig. 4.18 illustrates this. The end of the delamination at point A terminates at a transverse crack while the end of the delamination at point B tappers off. Comparing the CT scans with the PC results, the PC method appears to be most sensitive to the delaminations. Given that the transverse cracks are shallow, typically only as thick as one layer, it is not surprising that the cracks do not give indications. Second, the multitude of small individual components to the damage make for a

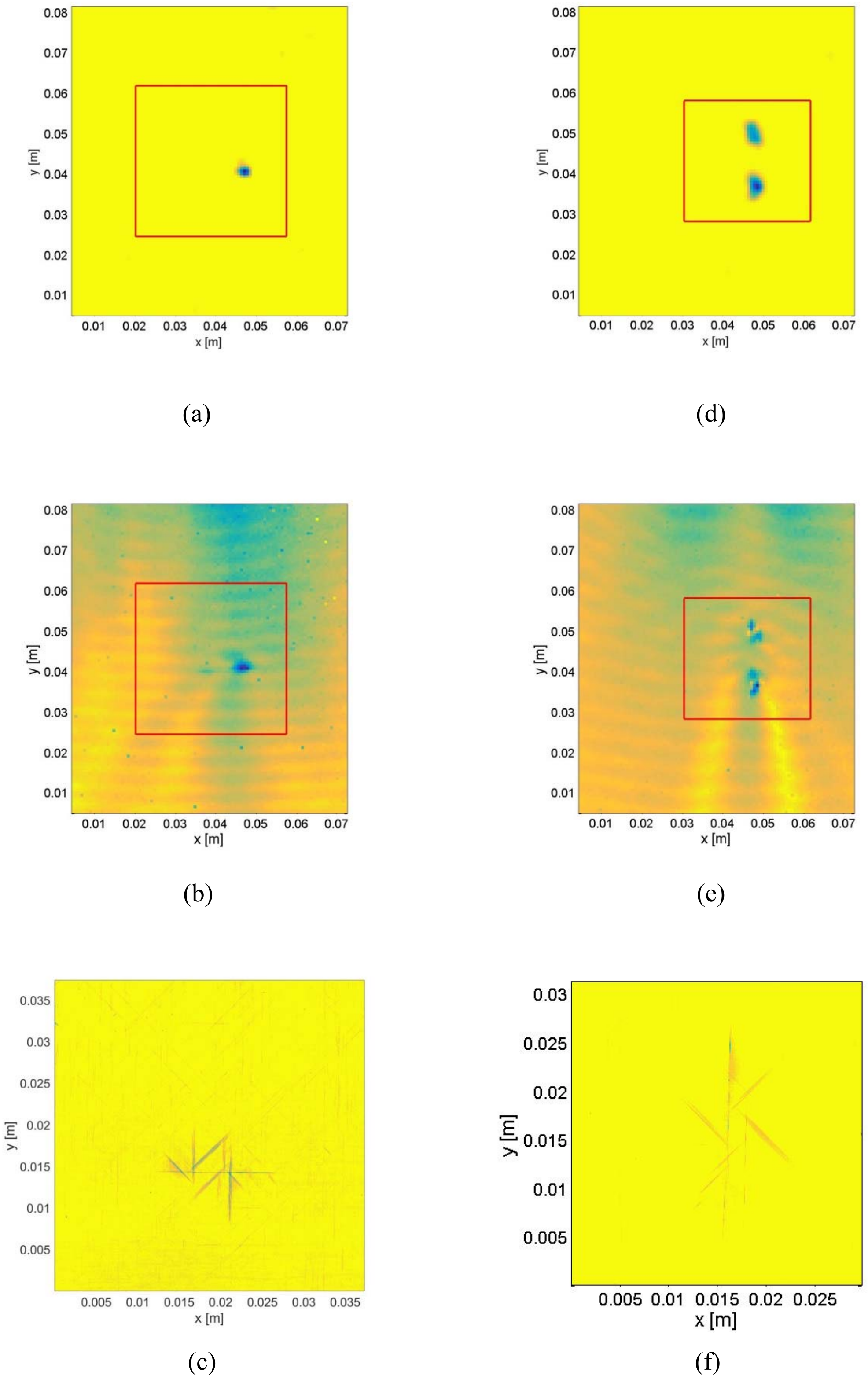

(a) (d)

(b) (e)

(c) (f)

Figure 4.15 Impact damage in a carbon fiber plate for a 0.61 m(a)-(c) and 0.76m (d)-(f) drop height; top: PC, middle: RMS, bottom: x-ray CT scan respectively

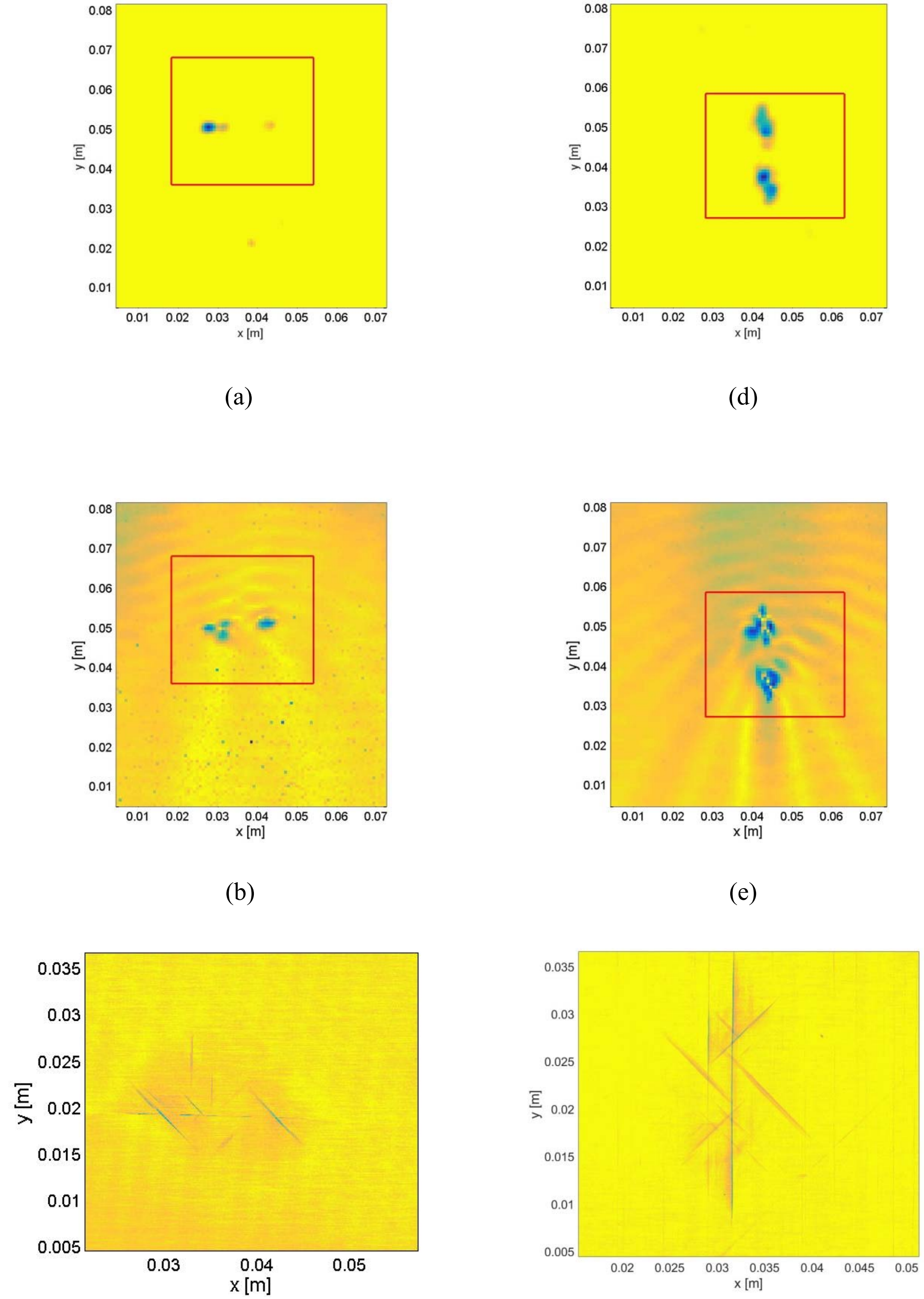

(a)

(d)

(b)

(e)

(c)

(f)

Figure 4.16 Impact damage in a carbon fiber plate for a 0.91 m(a)-(c) and 1.07 m (d)-(f) drop height; top: PC, middle: RMS, bottom: x-ray CT scan respectively complex distributed defects. This is in contrast to the damage analogs created with the Teflon disk in the fiberglass plate and thickness reduction in the aluminum bar that had single, distinct changes in the cross-sectional profile.

4.4 Damage Characterization

4.4.1 Overview

This section explores characterizing the damage identified by the PC for damage mapping method developed in the previous section. The damage is characterized based on the phase angle at which the components align at the location of a discontinuity. This angle allows two groups of damage to be characterized: those which infer a continuity condition at the surface of the plate at the damage

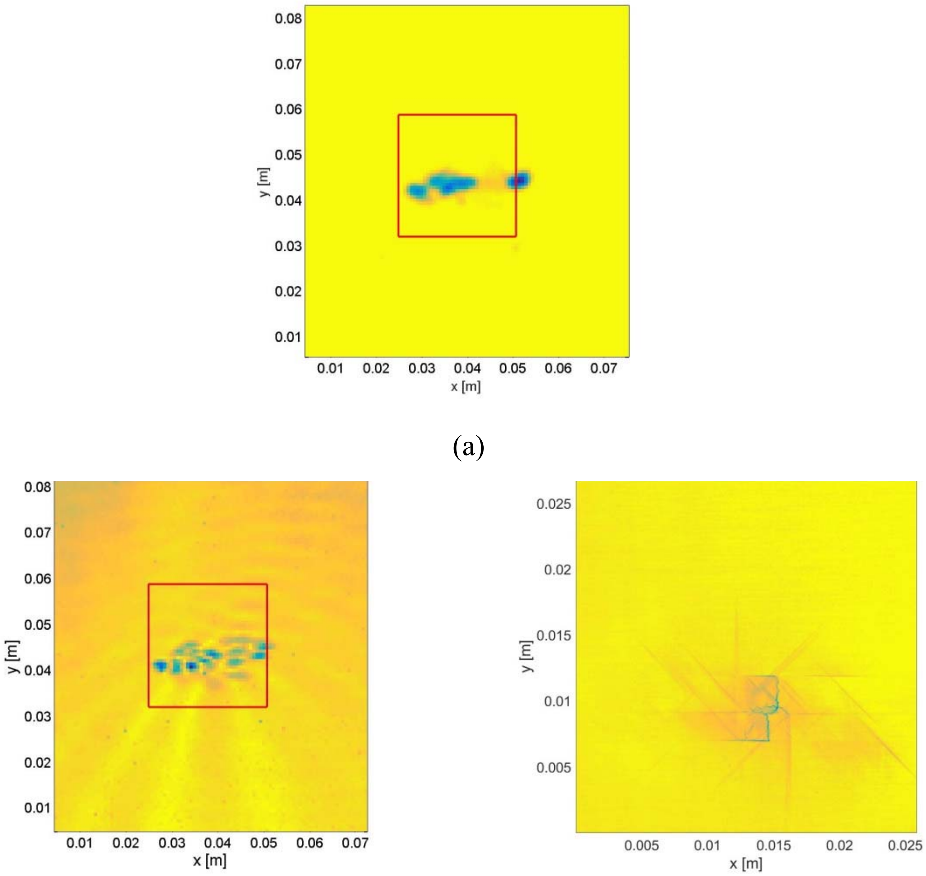

(a)

(b) (c)

Figure 4.17 Impact damage in a carbon fiber plate for a 1.22 m drop height; top: PC, bottom: x-ray CT scan location and those that do not. Damage that infers continuity includes all subsurface damage and is predicted by a characteristic angle of congruity of ± π/2. On the other hand, surface breaking cracks are an example of damage that does not infer continuity and has a characteristic angle of congruity at zero and π.

The angle of congruity is the phase angle of the sum of N complex components A_n at a local maximum in PC. The characteristic angle of congruity is the angle that an idealized discontinuity exhibits under a set of assumptions. This section uses an analytical model of a wavefield adapted from Section 2.2.1 to determine the characteristic angles of congruity for the two damage types and the conditions under which these characteristic angles of congruity are seen. Numerical simulations are presented to validate these findings.

4.4.2 Characteristic Angle of Congruency for a Single Wavefield Component

Since the PC for damage mapping analysis method is linear, analysis of single wavefield component is addressed first. This section analytically develops the characteristic angle of congruency for a single term of a wavefield model. The wavefield model is adapted from Eqn. (2.10) with following modifications:

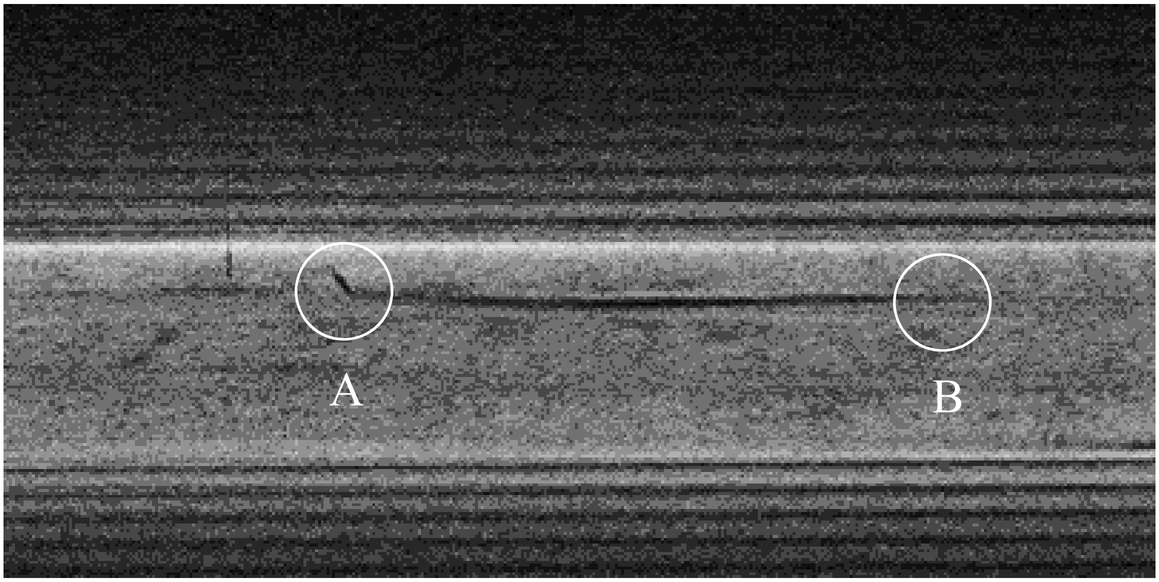

Figure 4.18 Transverse scan from 0.914 m drop height impact damage.

- the span of each segment is finite having length L to reflect the limited span of a wavefield measurement, and
- PC is calculated independently of time so the phase contribution from time, ωt, is assumed constant and contained in the general phase term, φ,

Taking only the real part of incident term in Eqn. (2.10) becomes,

$$u(x) = a_{A_0^i}\cos\left(k_{A_0}(x - L_1 - x_1) - \varphi\right)\begin{cases}0, & x \leq x_1 \\ 1, & x_1 < x \leq x_1 + L_1 \\ 0, & x_1 + L_1 < x\end{cases} \tag{4.1}$$

To determine the characteristic angle of congruity, $A_n(x)$ is computed directly, as the convolution in Eqn. (3.30),

$$A_n(x) = u(x) * g_n(x) = \int_{-\infty}^{\infty} u(\xi) g_n(\xi - x) d\xi \tag{4.2}$$

The function $g_n(\xi - x)$ is simply the Gabor filter from Eqn. (3.52) in the spatial domain utilizing the parameters as described in Eqns. (3.59)-(3.62). Evaluating the integral in Eqn. (4.2) and evaluating it at $x = x_1 + L_1$

$$\begin{aligned} A_n(x_1 + L_1) = -\frac{a_{A_0^i}}{4}\Bigg(&\left(\mathrm{erf}(i\Phi_n^-) - \mathrm{erf}\left(\frac{L_1}{c_n\sqrt{2}} + i\Phi_n^-\right)\right)e^{-(\Phi_n^-)^2}e^{i\varphi} \\ &+ \left(\mathrm{erf}\left(\frac{L_1}{c_n\sqrt{2}} + i\Phi_n^+\right) - \mathrm{erf}(i\Phi_n^+)\right)e^{-(\Phi_n^+)^2}e^{-i\varphi}\Bigg) \end{aligned} \tag{4.3}$$

$$\Phi_n^{\pm} = \frac{c_n\left(k_{A_0} \pm k_n\right)}{\sqrt{2}} \tag{4.4}$$

The filter's center wavenumber, k_n, and the width, c_n, have a fixed relationship by the half-power width, W_{HP}, of the filter and the multiple, m, as discussed in Section 3.3.5.

$$W_{HP} = 2\sqrt{\ln(2)}c_n = \frac{m}{k_n} \tag{4.5}$$

Combining Eqn. (4.3) through (4.5),

$$
\begin{aligned}
A_n(x_1 + L_1) = -\frac{a_{A_0^i}}{4}\Bigg(\Bigg(&\mathrm{erf}\bigg(\frac{i\pi m}{\sqrt{2\ln(2)}}\bigg(\frac{k_{A_0}}{k_n} - 1\bigg)\bigg) \\
&- \mathrm{erf}\bigg(\frac{i\pi m}{\sqrt{2\ln(2)}}\bigg(\frac{k_{A_0}}{k_n} - 1\bigg) \\
&+ 2\pi\sqrt{\frac{\ln(2)}{2}}\frac{L_1}{\lambda_n m}\bigg)\Bigg) e^{-\frac{\pi^2 m^2}{2\ln(2)}\left(\frac{k_{A_0}}{k_n}-1\right)^2} e^{-i\varphi} \\
&+ \Bigg(\mathrm{erf}\bigg(\frac{i\pi m}{\sqrt{2\ln(2)}}\bigg(\frac{k_{A_0}}{k_n} + 1\bigg) - 2\pi\sqrt{\frac{\ln(2)}{2}}\frac{L_1}{\lambda_n m}\bigg) \\
&- \mathrm{erf}\bigg(\frac{i\pi m}{\sqrt{2\ln(2)}}\bigg(\frac{k_{A_0}}{k_n} + 1\bigg)\bigg)\Bigg) e^{-\frac{\pi^2 m^2}{2\ln(2)}\left(\frac{k_{A_0}}{k_n}+1\right)^2} e^{i\varphi}\Bigg)
\end{aligned}
\tag{4.6}
$$

In this description of the component, it is dependent only on two non-dimensional quantities, $\frac{k_{A_0}}{k_n}$and $\frac{L_1}{\lambda_n}$ as well as the multiple m.

Next, suitable bounds for the two dimensionless ratios can be determined such that the phase of A_n does not depend on n. If $\frac{L_1}{\lambda_n} > m\left(\frac{k_{A_0}}{k_n} + 1\right)$ the error functions with complex arguments become small relative to the error functions with purely imaginary arguments and can be set to zero. Thus, Eqn. (4.6) reduces to,

$$
A_n(x_l + L_l) = \frac{a_{A_0^i}}{4}\left(D_+\left(k_{A_0}, k_n\right)e^{-i\varphi} + D_-\left(k_{A_0}, k_n\right)e^{i\varphi}\right) \tag{4.7}
$$

where,

$$
D_\pm = \pm\mathrm{erf}\left(\frac{i\pi m}{\sqrt{2\ln(2)}}\left(\frac{k_{A_0}}{k_n} \pm 1\right)\right)e^{-\frac{\pi^2 m^2}{2\ln(2)}\left(\frac{k_{A_0}}{k_n}\pm 1\right)^2} \tag{4.8}
$$

Now the terms, $D_{\pm}$ have phase values of $\pm\pi/2$ respectively. For the expression as a whole to have a constant phase value for any n, D_+ and D_- should have equal magnitude also. Since $D_{\pm}$ are scaled by the Gaussian, as k_n increases the magnitude of D_+ and D_-will converge as seen in (Fig. 4.19). Convergence can be approximated when the center wavenumber, k_n, is two orders of magnitude bigger than the incident wavenumber.

Based on this approximation, for large segment length to wavelength ratios, $\frac{L_1}{\lambda_n}$, and small wavenumber ratios, $\frac{k_{A_0}}{k_n}$, the component A_n, at $x = x_1 + L_1$tends to phase values of $^{\pi}/_{2}$. To bound the ratios for which this approximation is valid, Eqn. (4.7) is considered for the limiting multiplier values $m = 1$ and $m = 3$ defined in Section 3.3.5. The phase approximated by Eqn. (4.7) is within 2% percent from the phase calculated from full expression in Eqn. (4.6) for $\frac{L_1}{\lambda_n} > 2$, $\frac{k_{A_0}}{k_n} > 0.1$ and $1 \leq m \leq 3$. The value of the phase of the components at a discontinuity, $x = x_1 + L_1$ is approximately $^{\pi}/_{2}$ at segment length, L_1, greater than two wavelengths and filter center wavenumbers, k_n, larger than ten times the incident wavenumber k_{A_0}.

4.4.3 Multiple Wavefield Components

The above section analytically solved for the wavefield components, A_n, for a single term in the

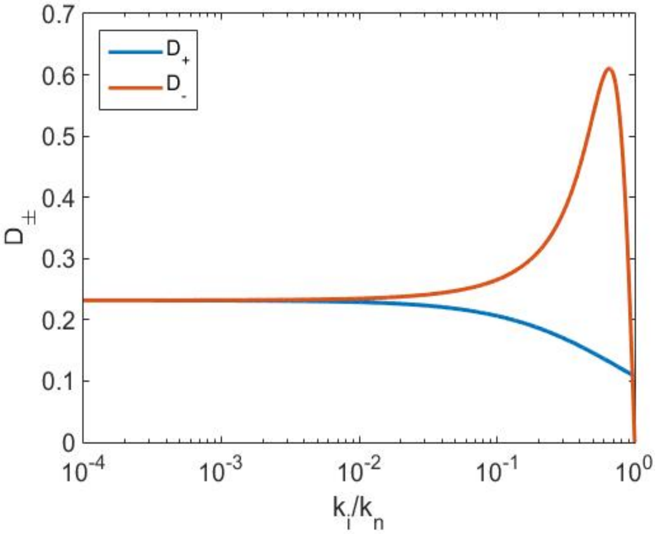

Figure 4.19 Ratio of approximate terms $D_{\pm}$ as a function of the wavenumber ratio for $m = 1$.

analytical wavefield model given by, Eqn. (4.1). If a second term on the right side of the spatial domain is considered so that the two terms form an adjoining set in space, the modified model becomes,

$$u(x) = \begin{cases} a_{A_0^i}\cos\left(k_{A_0^i}(x - L_1 - x_1) - \varphi_1\right) & x_1 < x \leq x_1 + L_1 \\ a_{A_0^t}\cos\left(k_{A_0^t}(x - L_2 - x_2) - \varphi_2\right) & x_2 < x \leq x_2 + L_2 \end{cases} \tag{4.9}$$

where $x_2 = x_1 + L_1$

Repeating the above analysis for the second term for the position $x = x_2$ phase of the components, A_n, associated with this term tend towards $-{}^{\pi}/_{2}$ (Fig. 4.20). Summing the component contributions for each term,

$$A_n(x_2) = A_{n,i}(x_1 + L_1) + A_{n,t}(x_2) \tag{4.10}$$

The analysis now considers the two types of damage: those that infer continuity at the discontinuity and those that do not. Starting with those that assume continuity at the surface, the amplitudes of the two components must be equal so,

$$\begin{aligned} A_n(x_2) = \frac{a_{A_0}}{4}\Big(&D_+\left(k_{A_0^i}, k_n\right)e^{i\varphi_1} + D_-\left(k_{A_0^i}, k_n\right)e^{-i\varphi_1} \\ &- D_+\left(k_{A_0^t}, k_n\right)e^{i(k_2x_2+\varphi_2)} - D_-\left(k_{A_0^t}, k_n\right)e^{-i(k_2x_2+\varphi_2)}\Big) \end{aligned} \tag{4.11}$$

The vector sum of all A_n components is then dominated by the lowest center wavenumber component since at high k_n the component will tend to zero magnitude as the phase tends to zero(π) for k_1 greater (less) than k_2 (Fig. 4.21). The lowest component has the largest magnitude as well as the largest deviation from the characteristic phase angle. As $k_n$increases, the phase angle of that vector component tends towards the characteristic phase angle however, its magnitude decreases. Therefore, the contribution of vectors with phase angles closer to the characteristic phase angle become small, thus they do not help drive the vector sum to the characteristic phase angle (Fig. 4.22). The resulting vector (seen in black) is approximately the same phase angle of the first vector

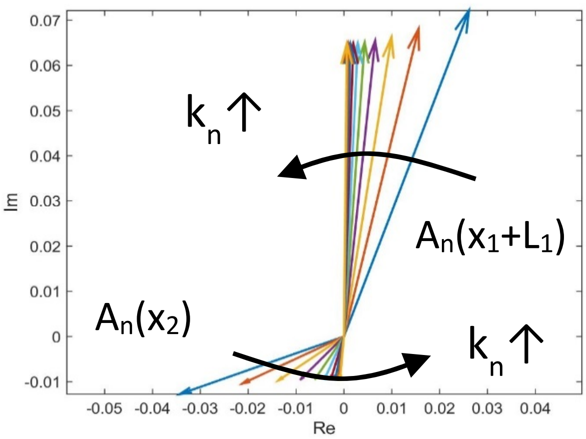

Figure 4.20 Component vectors for the left and right edges of a modulated rectangular function for a range of filters

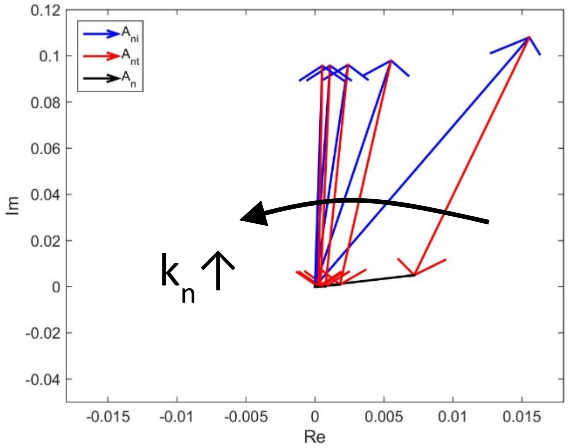

Figure 4.21 Components $A_{n,i}(x_1 + L_1)$, $A_{n,t}(x_2)$, and $A_n(x_2)$ as a function of k_n.

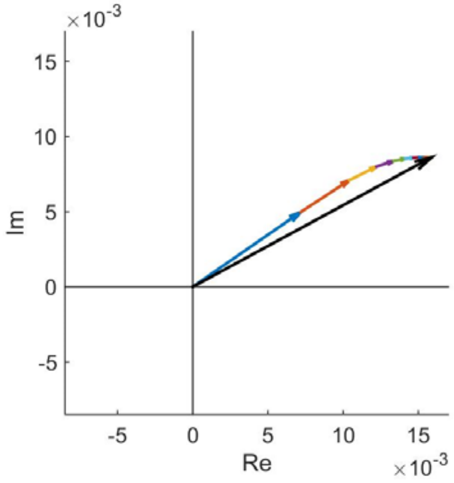

Figure 4.22 Sum of ten vector components.

component.

In general, it is impractical to only use filters with center wavenumbers, k_n, two orders of magnitude greater than the interrogating wave for two reasons. The first is that the sampling density required for large wavenumbers becomes very high and may become impractical. The second is that at these high wavenumbers, far from the interrogating wavenumber, the signal amplitude becomes very small relative to the noise. Therefore, additional information is needed to make use of the characteristic angle of congruity.

The phase terms, φ, captures any constant phase shift associated with wavefield, as well as the time varying component, ωt. This implies φ will sweep through all unique phase values as time progresses. Figure 4.23 illustrates both the dependence of the angle of congruity on φ with the marker shading a function of PC as calculated from Eqn. (3.8). As φ approaches the characteristic phase values (zero and π), the value of PC increase as noted by color scale of the marker in Fig. 4.23. Thus the characteristic angle at a discontinuity can be determined in practice by considering the PC value over a range of phase angles. Given that the phase term includes the time varying component, ωt, computing PC over time at the location of the discontinuity allows one to determine the characteristic angle of congruency.

The constraint on the model that determines the characteristic angles of congruity is the continuity of displacement requirement that lead to equal magnitudes and phases between components. However, defects that do not infer a continuity of displacement constraint such as surface breaking cracks would not exhibit this characteristic angle of congruency. Performing a similar analysis when the amplitudes of each component are not equal reveals that the characteristic angle of congruency in this case must be $\pm {}^{\pi}/_{2}$.

Given the model and analysis describe above, two damage types can be distinguished from one another. Fundamentally, these two types can be characterized as those that infer continuity of displacement at the surface and those that do not. The former group includes internal damage such as delaminations, porosity, thickness changes and internal cracks as well as cracks that break the far surface and have characteristic phase angles of zero and π. The latter group is mainly comprised of cracks that break the measured surface and have characteristic phase angles of $\pm {}^{\pi}/_{2}$.

4.4.4 Comparison with Numerical Models

A numerical simulation corresponding to the analytical model given by Eqn. (4.9) is constructed for comparison to the analytical results. The model has two segments with matching impedances to ensure there is no reflection at the interface (Fig. 4.24). The forced end of the rod has the properties of aluminum given in Table 4.1. The fixed end of the rod has properties that did not relate to a specific material but were selected so that the impedance ($Z = \rho c$) matched aluminum. To prevent multiple modes a longitudinal wave in a rod is simulated in ABAQUS [73]. The excitation is an oscillating pressure applied evenly across the left face at 264 kHz while right boundary is fixed. Two-node linear elements (B21) are used in ABAQUS' Standard Explicit solver. The surface displacements from the simulation are seen in Fig. 4.25 (a).

Phase Congruency results from this model were compared to two PC calculations from the analytical model. The first calculates the signal components analytically from Eqn. (4.10) and

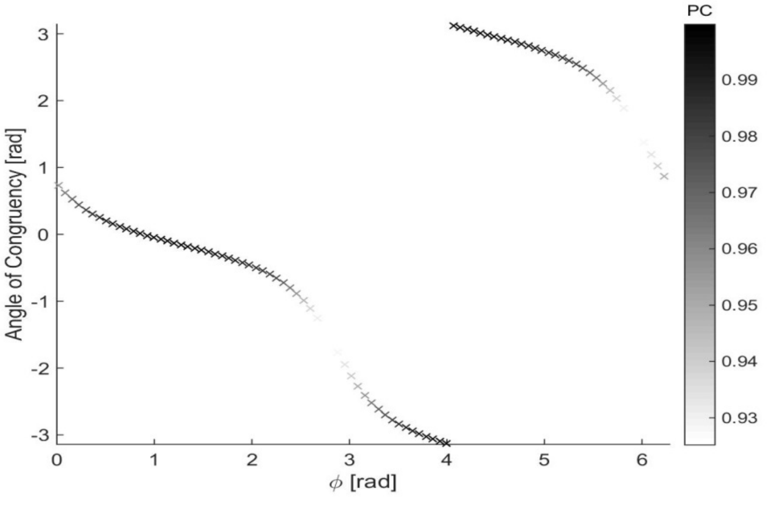

Figure 4.23 Vector sum of the two components as a function of φ.

Table 4.1 Properties of Impedance matched model

Material	Density [kg/m^3]	Elastic Modulus [Gpa]	Speed of Sound [m/s]	Impedance [kg/m^{2}s]
Material 1 (Aluminum)	2700	71e9	5128	13.8e6
Material 2	1800	106.5e9	7692	13.8e6

computes PC using Eqn. (3.8). The second comparison to PC computed from synthetic values from Eqn. (4.9). Phase Congruency for the synthetic and numerical models is computed as described in Section 3.4.1 and the time domain is mapped to phase values by ωt.

Figure 4.25 (b) shows the angle of congruity as a function of the constant phase value, φ. The closer the angle of congruency is to the characteristic angle of congruency the stronger the PC response. The synthetic data and numerical simulations agree well with the analytical results.

Next numerical tests of a damage that breaks the inspection surface and damage that does not are conducted for comparison to the analytically calculated characteristic angles of congruency in Section 4.4.3. To validate this analysis a 0.152 m x 0.019 m x 0.006 m (12 in x ¾ in x ¼ in) aluminum bar is modeled in ABAQUS with a crack at the midpoint (Fig. 4.26). One end is held fixed while the other is used to excite the bar with a four cycle tone burst pressure load at 50 kHz. ABAQUS' Standard Explicit solver is used with 1539 1.3e-7 s time increments totalling 2e-4 s. The model is discretized with C3D8R elements approximately 1mm cubed in size. The crack is modeled by decoupling the elements on either side of the crack so they could move independently

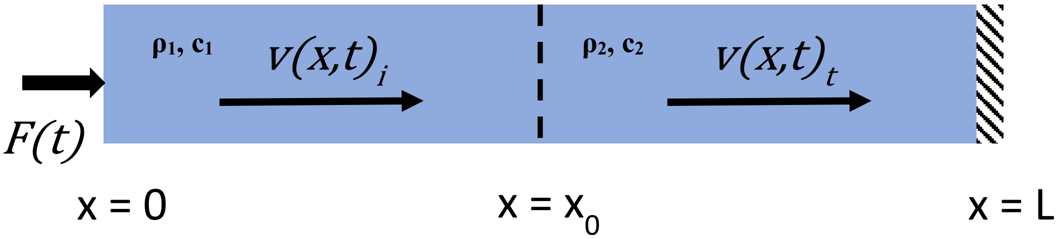

Figure 4.24Schematic of 1-D two component problem.

of one another. Then the surface displacements on both sides are used for a compartive analysis. The top surface represents a surface breaking defect (i.e. not inferring a continutity requierment) while the bottom represents a defect which does infer a continutity of displacement requirement at the inspection surface.

Taking these displacements and applying the PC method, the angle of congrency is plotted as a function of time. Figure 4.27 illustrates the results at the location of the crack along the centerline of the bar. As before, the color scale of the markers corresponds to thier PC values. The distinct characterisitc angles of congreuency are consistent with the analytical predictions. The surface breaking crack yeilds characteristic values of $\pm {}^{\pi}/_{2}$ and the non-surface breaking side yields values of 0 and π. In this section an analysis of two characterisitic defect types, surface breaking and non-surface breaking were evaluated. An analytical analysis determined that each type had a pair of characteristic angles of congruity. Synthetic data and numerical simulations were used to validate that these characterisitic angles can be observed and correlate well with the analytical predictions.

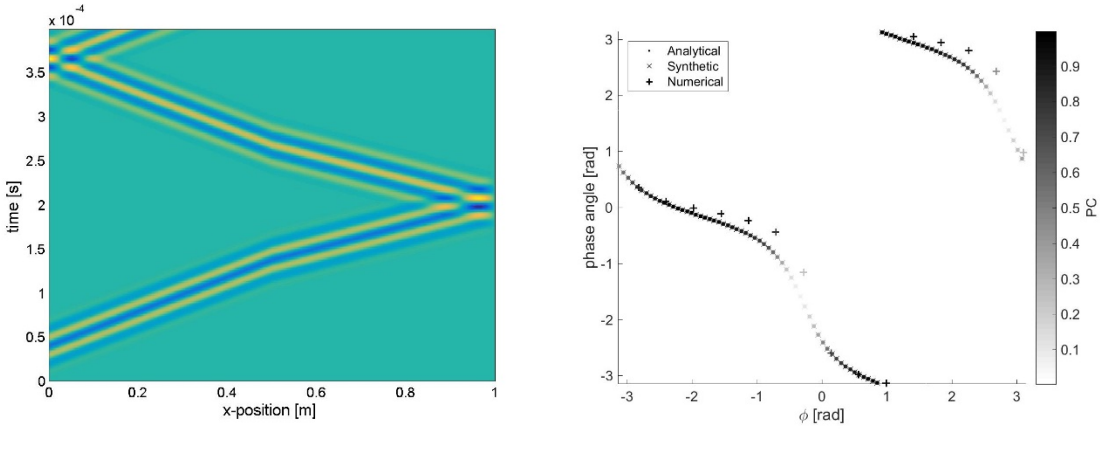

(a) (b)

Figure 4.25 Displacement data for the numerical simulation and a comparison of the angle of congruency as a function φ from an analytical calculation (.), synthetic dataset (x), and numerical simulation (+) all weighted by PC

4.5 Conclusions

This chapter presents PC results for numerical and experimental models as well as a method of characterizing the damage. The first set of models, the aluminum bar with a change of thickness, approximates a 1-D case. The results of the numerical and experimental model are very consistent. The PC method only gives indications where the changes in thickness occur providing a clear picture of the simulated defect to a user. The notched aluminum plate gives a clear indication of the simulated damage for deep notches with strong reflections. As the amplitude of the reflected and transmitted waves decreased (caused by the shallower notch depths) the indications for the notch become increasingly weaker, approaching the level of the background. The delamination in the fiberglass plate increases the complexity of the damage. For simple interactions across the delamination in the numerical case, a very clear ring indicates the outline of the delamination. In the experimental results, the shape is clear, however, the distinct ring indicating the boundary is not present. Despite this, the results of the PC method are an improvement over the RMS results as the background response is greatly reduced, thus highlighting the delamination. Further, at low wavenumbers, the PC method continues to map the delamination while the RMS results fail to identify the damage.

The T-stringer sample considered more complex wavefields. In this model, both a scatterer and thickness changes are present. The PC clearly indicates the added mass acting as a scatterer as well as the changes in thickness. Neither of these features are present in the RMS plot. The final specimens considered are the impact-damaged plates. These are the most complicated damages

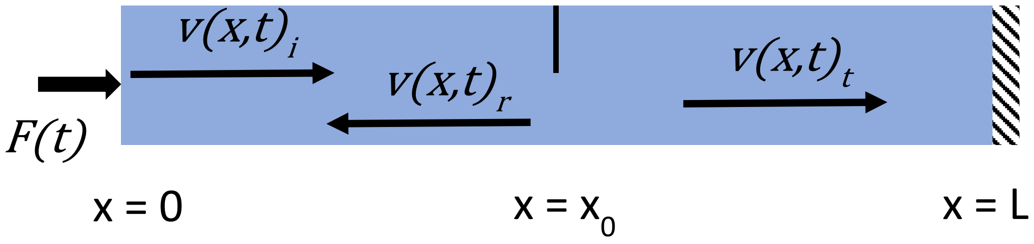

Figure 4.26 Schematic of numerical crack model.

considered in that they are composed of multiple delaminations, of relatively small size, on multiple layers intermixed with transverse cracks. Comparing these results to x-ray CT scans which represent a very high resolution, high confidence estimates of the damage, the PC results do not illustrate the complexity of the damage seen in the CT scans. It appears that the PC results give the strongest indications corresponding to delaminations in the plates. Despite this, the PC method still indicates the location of the damage and reasonably approximates the span of the delamination. The map of the damage is much more consistent between the RMS and PC plots. As in previous cases, the PC method is able to remove the background content that is visible in the RMS plots.

The damage characterization section identified two categories for classifying damage. Altering whether nor not continuity is enforced at the intersection defines these two damage categories: those that enforce continuity at the surface (e.g. any damage which does not break the surface being measured, sub-surface cracks, delaminations, etc.) and those that do not impose a continuity requirement (e.g. a surface breaking crack on the inspection side). Each of these types is shown to have its own pair of characteristic angles of congruity. Numerical models are used to validate the findings of the analytical analysis. The numerical models compared very well with the analytical solutions and demonstrated the characterization approach. However, high sampling rates

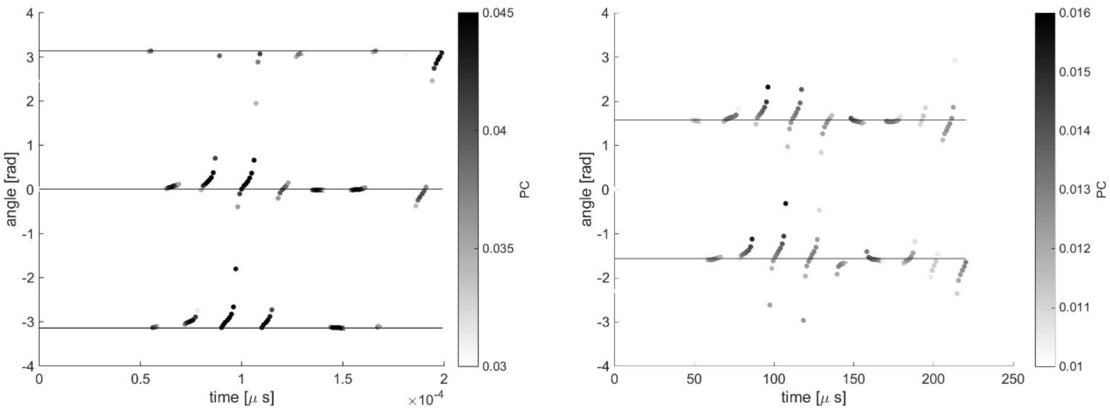

(a) (b)

Figure 4.27 Results for the numerical simulation of an aluminum bar with a crack; PC of non-surface breaking side (a), PC of surface breaking side (b).

and dense grids are needed for characterization. This method is most limited by the categories of damage that can be categorized. The first category, surface breaking cracks is very narrow, while the second category encompasses a wide array of damage types.

For a simple wavefield, the PC method generates an easily understandable map of thickness changes and cracks. For large delaminations, the method clearly indicates the extent of the damage while filtering out waves in the pristine region, although indications are given over the delamination beyond just the boundary location. In these simple cases the improvement over the RMS of the surface velocity is quite dramatic, particularly when considering the aluminum bar. Even in the more complex case of the T-stringer the difference is quite marked. The RMS results do not yield any useful information about the defect while the PC results indicate both the simulated scatterer and the changes in geometry. However, for the impact damage the methods results are not as good as the x-ray CT scans. This comparison does come with practical trade-offs. The price for the increased resolution is practical limitation on use.

CHAPTER V

OPTICAL GUIDED WAVE MEASUREMENTS

5.1 Overview

Guided wave techniques using full field measurements require repeated excitation-measurement events to measure the full field pointwise capturing the time-histories one node at a time. This chapter will explore an alternative method for GW measurement that captures the time histories of all nodes in the field simultaneously using an optical technique.

The measurement method utilizes a high speed camera to capture the evolution of a GW propagating across a plate. Using multiple measurements, the signal's SNR is improved through averaging. A method to achieve effective sampling rates satisfying the Shannon-Nyquist sampling criteria from a multiple datasets collected with sampling rates below the Shannon-Nyquist sampling rate is used to facilitate analysis in the Fourier Domain. Once in the Fourier Domain, the presence of the GW can be verified by comparing signal peaks in the Fourier Domain with the dispersion curves for the particular sample. If a GW is present, then there will be a peak in the signal along dispersion curves at the excitation frequency. For display in the time-space domain, further signal processing is done to reduce noise. The signal is filtered in the frequency domain to remove known narrowband noise sources with a Tukey filter. Then an IFFT of the signal is taken to return to the time-space domain.

5.2 Optical Measurement Concept

The measurement concept for this method is built around two assumptions. First, the surface displacements caused by the GW will disturb the light received by the camera from a particular point on the plate. This will be recorded by the camera as a change in intensity for the pixel corresponding to the location on the plate. The second assumption is that the signal is a linear superposition of components that can be separated. This section will discuss these assumptions and how they are used to extract the wavefield from the captured video.

This work utilizes a high speed video camera (HSC) that captures monochromatic images. Each pixel in the image is represented by one digital value at each time instance. The digital values are proportional to the light reflected from a particular point on the surface being imaged. This method assumes that the light reflected to the camera will vary as a function of disturbances to the plate caused by the GW. The primary mode for disturbing the light captured by the camera is expected to be out-off-plane surface displacements caused by the wave will cause the local angle of the plate to change relative to the camera. If the surface is specular, changes in the angle of the surface relative to the camera will cause a change the intensity measured by the camera for a particular point on the plate. If these changes can be measured and isolated in the video captured by the camera, then wavefields can be extracted.

The second assumption is that the signal can be modeled as a linear super-position of parts. The video captured by the camera of a transient wave contains at least three components: the time invariant intensity dominated by the static image of the plate, $I_{DC}(x, y)$, a time variant component consisting of the changes in intensity caused by the wave, $I_{wave}(x, y, t)$, and a noise intensity component, $I_{noise}(x, y, t)$.

$$I(x, y, t) = I_{DC}(x, y) + I_{wave}(x, y, t) + I_{noise}(x, y, t) \tag{5.1}$$

The data processing method for this technique removes the static and noise component leaving only the signal component. The time invariant component is removed by subtracting the mean value computed over time for each pixel. Then the remaining signal consists of the wavefield plus any other time varying noise. Sources of noise include motion of the plate from ambient air-borne and structure-borne noise (i.e. HVAC and other mechanical equipment), light flickering, sensor noise and other transient changes in illumination (e.g. shadows from object motion outside the frame, etc.). Some of these sources are easily recognizable in the data such as flickering lights (120 Hz) while others, transient illumination changes and sensor noise are broadband and uncorrelated. Identifiable correlated noise can be removed with traditional filtering techniques provided it is separable in time, space, frequency or wavenumber. Uncorrelated noise on the other hand can be reduced by averaging. By removing the DC component as well as the correlated noise and uncorrelated noise, the wave, $I_{wave}(x, y, t)$ can be isolated.

5.3 Experimental Set-up

The experimental set-up is very similar to the one used for measurements made with the SLDV however in place of the SLDV a single Photron Fastcam SA1.1 HSC is used to acquire the signal. An external trigger starts the camera. The camera then controls the synchronization of the excitation and measurement aspects of the setup (Fig. 5.1). Once recording begins, the camera triggers a one cycle square wave burst from the Function Generator (FG1) (Agilent 33120A). The square burst functions as a controllable delay. Function Generator 2 (FG2) (Agilent 33220A) triggers the excitation on the falling side of the square wave from FG1. The signal is passed through an amplifier (E&I 1040L) and on to the APC transducer described in Section 4.3. The data was

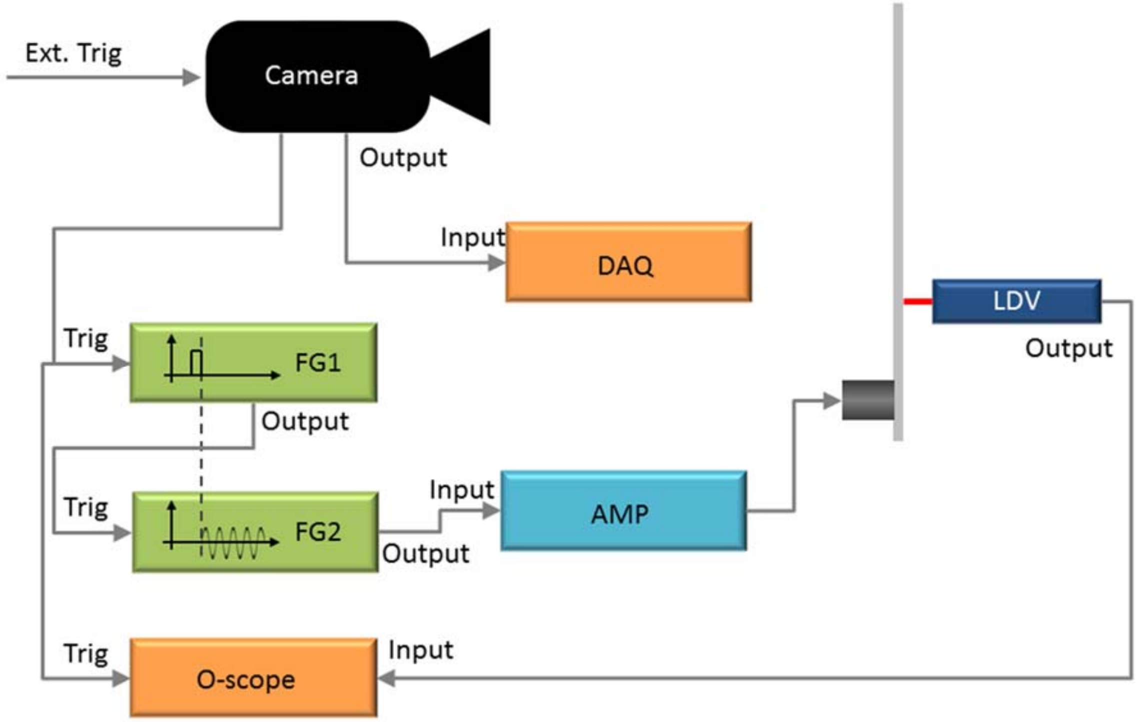

Figure 5.1 Wiring schematic for triggering and data acquisition

recorded on a laptop using software provided by the camera's manufacturer (Photron FASTCAM Viewer [89]). The software outputs the video as a series of Tagged Image Format File (TIFF), one for each instance of time.

The camera has limited throughput of data thus imposing a trade-off between frame rate and frame size. As the frame rate goes up, the maximum size of the frame goes down and vice versa. To obtain a reasonable frame size (320 x 320 pixels) the frame rate was limited to 45 kfps giving a Nyquist frequency of 22.5 kHz. Two excitation frequencies are used: 16.5 kHz and 36 kHz. With this frame rate only the 16.5 kHz excitation frequency was below the Nyquist frequency. To capture data for the 36 kHz excitation frequency a higher effective frame rate is needed. By taking multiple captures and interleaving them together to form a single dataset a higher effective sampling rate is created. The time between frames Δt_{raw} at 45 kfps is 2.22e-5 s. Taking three videos with an delay one-third frame spacing, 7.41e-6, between each video, the effective time between frames, Δt_{eff}, is 7.41e-6 s. Interleaving them (Fig. 5.2) gives an effective Nyquist frequency of 67.5 kHz, well above the 36 kHz excitation.

The plates are excited with the APC transducer. The transducer is modified with a bolt to

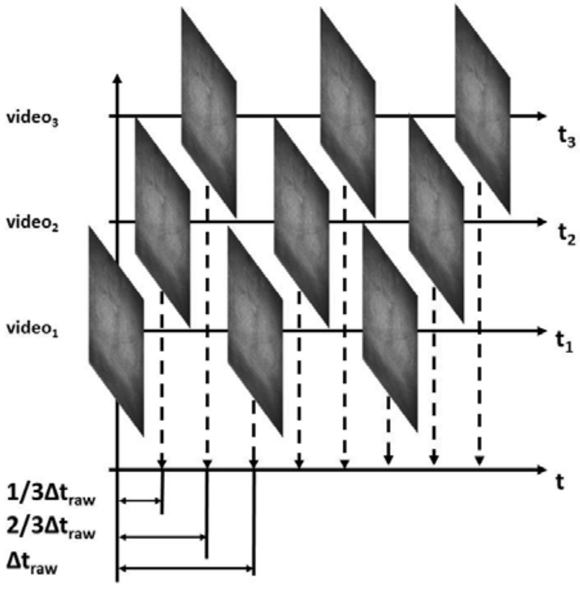

Figure 5.2 Schematic of interleaving method.

extend the length of transducer enhancing the amplitude of the displacement at resonance [90]. A bar clamp with rubber shoes on the jaws holds transducer on the bottom edge of the plate just below the scanned area as indicated in Fig. 5.3.

The camera requires a large amount of ambient light at these high frame rates. Configurations using two or three high-intensity lights are used to provide even illumination depending on the sample (see Fig. 5.4). The first configuration is direct illumination of the plate. In this configuration, two of the three lights are used. The two lights are placed on either side of the camera and pointed directly towards the plate. In the second configuration, all three lights are used. The lights are arranged with two on either side of the camera and the third above the camera. In this configuration the lights were pointed at a piece of sheet metal behind the camera. This metal acted as both a reflector and diffuser. This cast a more even light although with lower intensity. This arrangement is used for the carbon fiber and aluminum plates since the samples have a highly aligned surface texture orientation. This surface texture prevented even illumination with direct

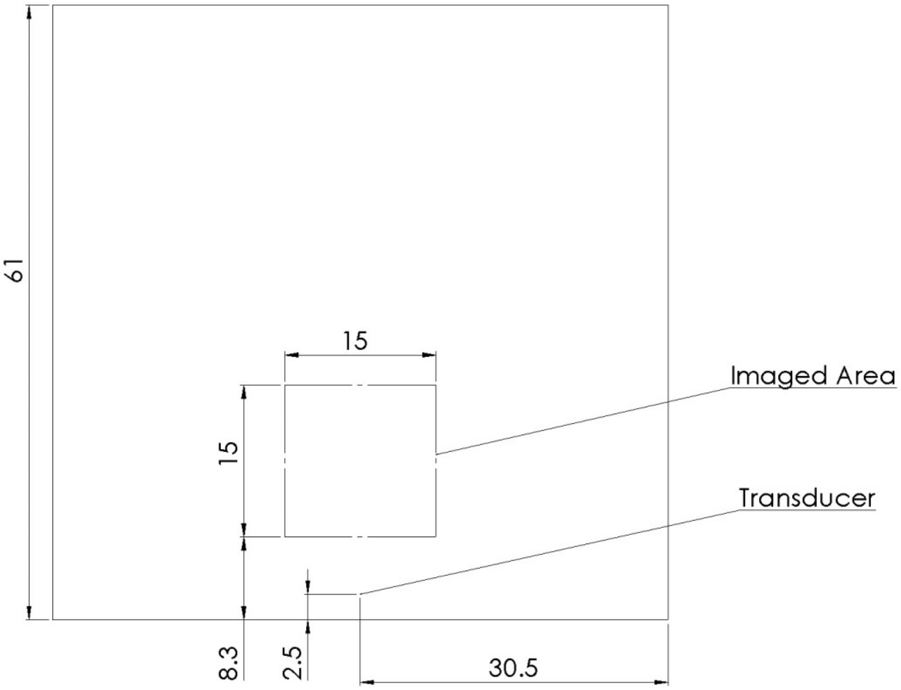

Figure 5.3 Nominal layout for all three samples measured with the High Speed Camera (all dimensions in cm)

lighting. By using the plate as a diffuser, more even illumination of the plate is achieved.

Fundamentally, the set-up for this method is as straightforward as taking any other video. The two primary differences are synchronizing the excitation and the camera, and providing sufficient light for the high shutter rates.

5.4 Data Analysis Approach

To analyze the data, a post-processing method is needed to isolate the signal from the noise as discussed in Section 5.2. There are four components of the signal: the time invariant component, correlated noise, uncorrelated noise and the wavefield. The analysis approach addresses each one individually. The time invariant component is easily removed by subtracting the mean value. The narrowband noise sources can be filtered with traditional signal processing techniques. With these two components removed, the uncorrelated noise and GW signal are all that remains. Even with only these two components, the data has a very low SNR. Typical signal levels at this point are around one discrete intensity level. Therefore, any measurable noise must be of the same order as the signal or greater. Averaging is an appropriate method for dealing with signals and uncorrelated

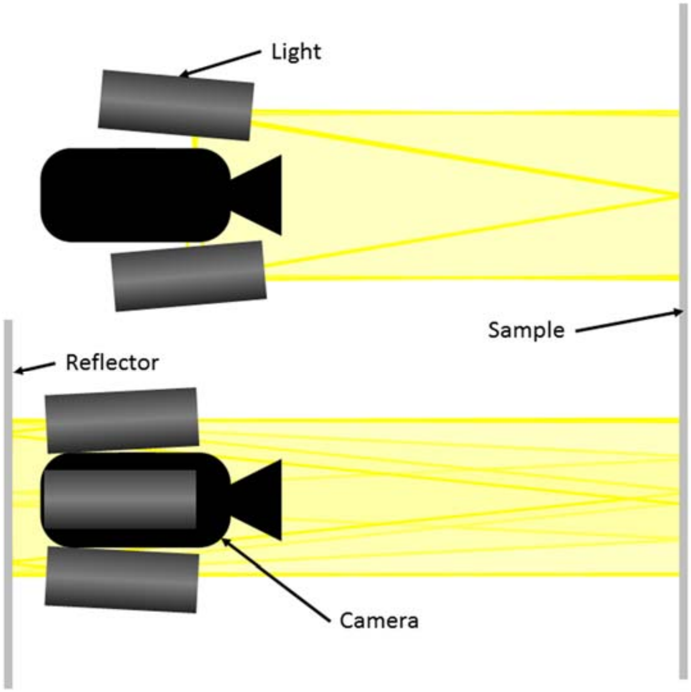

Figure 5.4 Lighting arrangements used for even illumination

noise at nominally one intensity value. Therefore, averaging is used to improve the SNR and isolate the wavefield.

The first post-processing step is to reduce the uncorrelated noise through averaging. It is known for uncorrelated noise, averaging reduces the standard deviation by the number of averages to the negative half power. Denoting the intensity values for equivalent points in time in space over repeated excitation-measurement events with the index n as $I_n(x, y, t)$, if N measurements are taken, then the standard deviation, σ, of the intensity values decrease as,

$$\sigma\big(\bar{I}_n(x, y, t)\big) = \frac{1}{\sqrt{N}}\sigma\big(I_n(x, y, t)\big) \tag{5.2}$$

This holds for only uncorrelated noise. Correlated noise will in general not be reduced by averaging. To confirm that the noise of the signal is dominated by uncorrelated noise, Eqn. (5.2) is compared against a set of measured data with no excitation present. Twenty individual videos are captured using the experimental setup described in Section 5.3. Each video contained 15, 320 x 320 pixel frames. The standard deviation is calculated across all pixels and time frames as a function of the number of takes N that were averaged together. The reduction in the standard deviation of the noise is seen to closely fit the uncorrelated noise model. Figure 5.5 displays the calculated values (blue x) and compares them with the analytical model (red line). Despite the known presence of some correlated noise (flickering lights) the noise is dominated by the uncorrelated component. Thus, averaging 20 takes will result in a reduction in the standard deviation of the noise by 78%.

The next step is to remove the DC component. In the captured video, the DC component is the static image. The static image is the strongest component of the video spanning most of the 256 intensity levels when the camera is properly adjusted. To remove this and isolate the time varying component, the signal average over time is subtracted from each point.

At this point, the presence of the wave in the capture signal can be determined. By taking a three-dimensional FFT and comparing the results to expected dispersion curves, the presence of the wavefield can be confirmed. If the wave is present, localized high amplitude content is seen at the frequency and wavenumber associated with the excitation signal.

If visualization is required, additional processing is done to address the correlated noise. Given the noise is correlated, targeted filtering can be used to remove these components if they are known. In this work, the AC power source for the lights caused a strong noise component at 120 Hz. This noise source, while very strong, is well outside the domain of interest thus does not affect the processing. A high pass filter can easily remove this component with minimal effect on the frequencies of interest. A second known narrowband noise source is noise due to the interleaving of datasets. Misalignment between the datasets in the interleaving process results in significant noise around the raw framerate and multiples of the framerate (45 kHz, and 90 kHz in this work). The largest cause of misalignment is likely differences in phase of the light flicker and video. This noise is at a known frequency thus a low pass filter can be used to isolate this noise. These two components can be removed with one band pass filter that passes frequencies between 120 kHz and

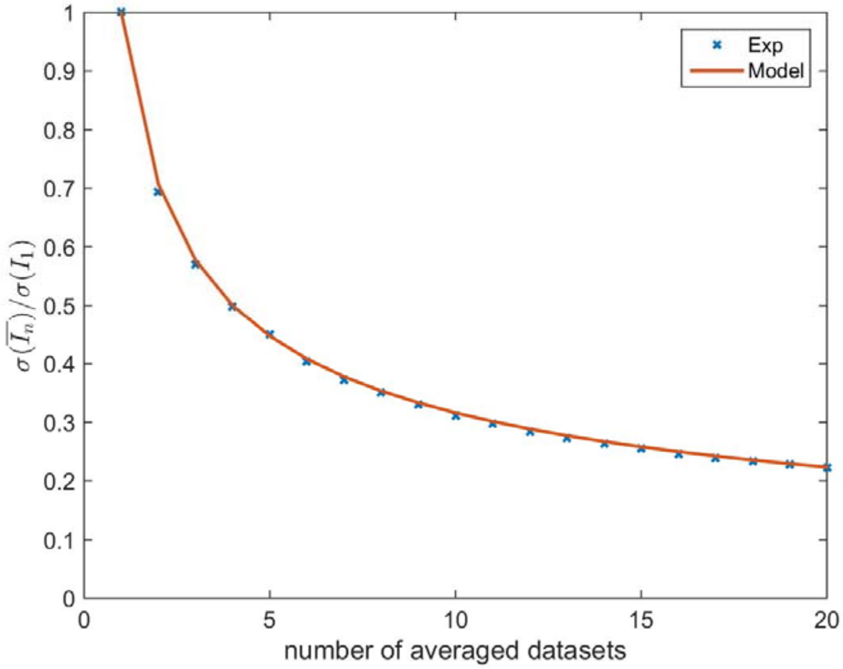

Figure 5.5 Standard deviation of measurement noise as a function of number of averages

the interleaving frequency

Given the low SNR, visualization the wave requires an additional post-processing step. A band-pass filter around the excitation frequency is used to reduce the amount of uncorrelated noise. In the specific case of this work, the long length of the excitation signal relative to the length of the measurement allowed a relatively narrow band pass filter to be used with low distortion.

Narrow filters in the wavenumber domain can be used depending on the purpose of the output. For wave visualization, modal filtering as described in Section 2.3.3 produce a very clean image of the wave at the expense of spatial spreading of the signal. This inhibits the ability to clearly depict damage. Alternatively, the wavenumber domain can be left unfiltered to retain sharpness in the spatial domain while also retaining noise. This trade-off must be evaluated based on the intended purpose of the visualization.

In the next section, the process described above will be compared against unfiltered signals using SNR calculated as, the ratio of maximum energy in a frame divided by the frame with the minimum energy.

$$SNR = \frac{\max\left(\sum_{x,y} I^2\,[x,y,t]\right)}{\min\left(\sum_{x,y} I^2\,[x,y,t]\right)} \tag{5.3}$$

Here, $I[x, y, t]$, is the intensity of the signal. The squared intensity values are summed across a single time frame, then the maximum and minimum of these values are used to compute the SNR. These SNR ratios are used to evaluate the ability of the post-processing procedure described here to isolate the signal from the noise.

5.5 Results

The experimental set-up described in Section 5.3 is used along with the post-processing and analysis procedure described in the preceding section to demonstrate the feasibility of using a high-speed camera to acquire signals from GW in plates. Three samples are considered in this evaluation:

the fiberglass plate with a Teflon disk described in Section 2.7, an undamaged carbon fiber plate with the same dimensions and properties as those described in Section 4.3, and a 1 mm aluminum plate with the assumed properties given in Table 2.1. All three plates were nominally 0.61 m (2 ft.) square.

The surface is prepared so that they behave specularly. The measured surface of the plate is painted with Rust-Oleum® Mirror Effect spray paint along with speckling from flat black spray paint (Rust-Oleum® ChalkBoard paint) to give texture to the plate's surface.

Datasets are taken for two excitation frequencies for all three samples. The first dataset is taken using an excitation frequency of 16.5 kHz for the fiberglass plate. Although this excitation frequency is below the Nyquist frequency (22.5 kHz) for the 45 kfps frame rate used, three sets of captures are taken offset from one another by 7.41 μs giving an effective Nyquist frequency of 67.5 kHz. A sample of a single frame is seen in Fig. 5.6 (a) along with an accompanying spatial slice in panel (b). This is the first frame of the video so no signal is present therefore, the range of values is dominated by the static (DC) component of the signal and noise. This range of values is from 40 to 160 representing half of the dynamic range of the photodiodes for a single time frame. Once the DC component in time is removed, only the signal and noise remain. There is a known correlated noise source from the lighting. This is seen in the large low frequency variation in Fig. 5.6 (c). The span of the time domain is approximately two-thirds of the period of the 120 Hz lighting noise. Since this component is known and easily filtered, it is removed as well. The corresponding time and spatial domain plots of the remaining signal are seen in Fig. 5.7 (a) and (b). What remain then is uncorrelated noise and the signal from the GW. A histogram of the remaining values for the first 15 frames is shown in Fig. 5.7 (c). The first 15 frames are used since no signal is present in these frames. Here it is easy to see that the bulk of the values are on the order of one intensity value. Since one is the smallest discrete value that can be measured by the camera, more data is needed to reduce the value of the uncorrelated noise.

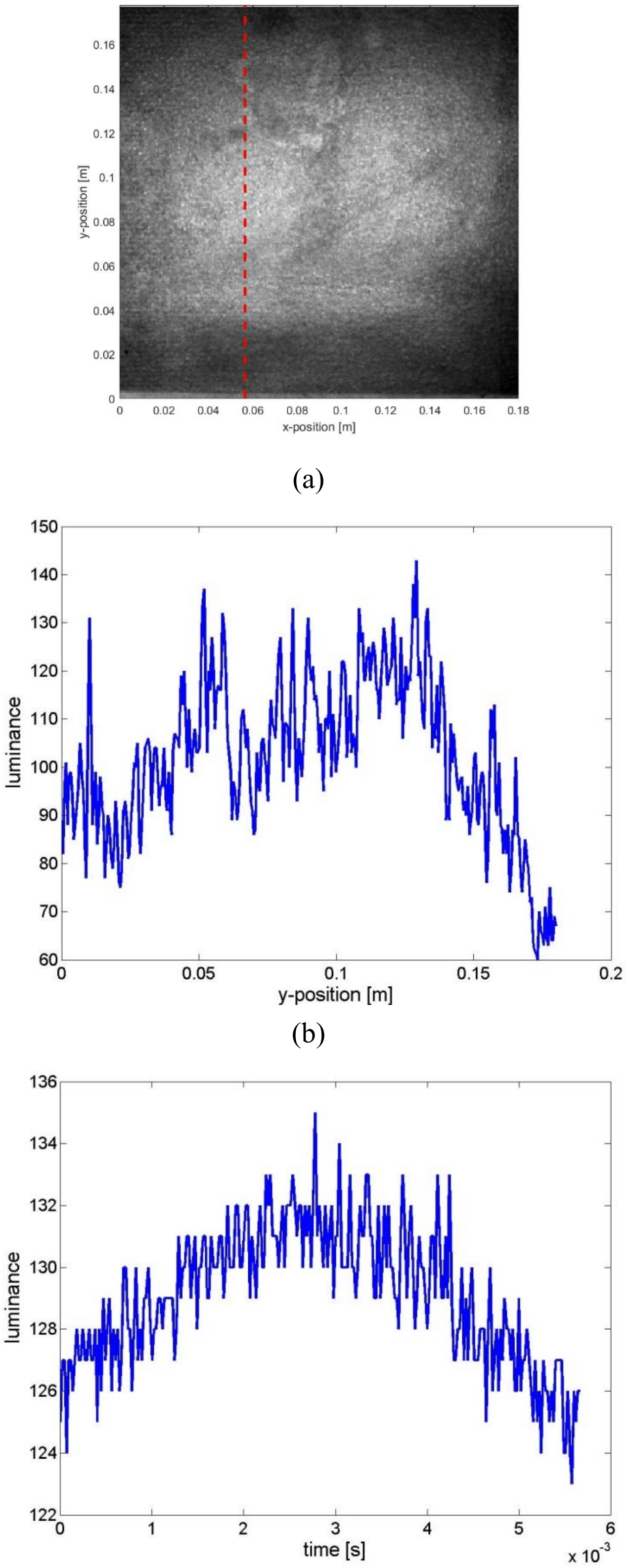

(a)

(b)

(c)

Figure 5.6 Raw video frame (a) along with slice along x = 0.0564 m (b) and time history for center point (c)

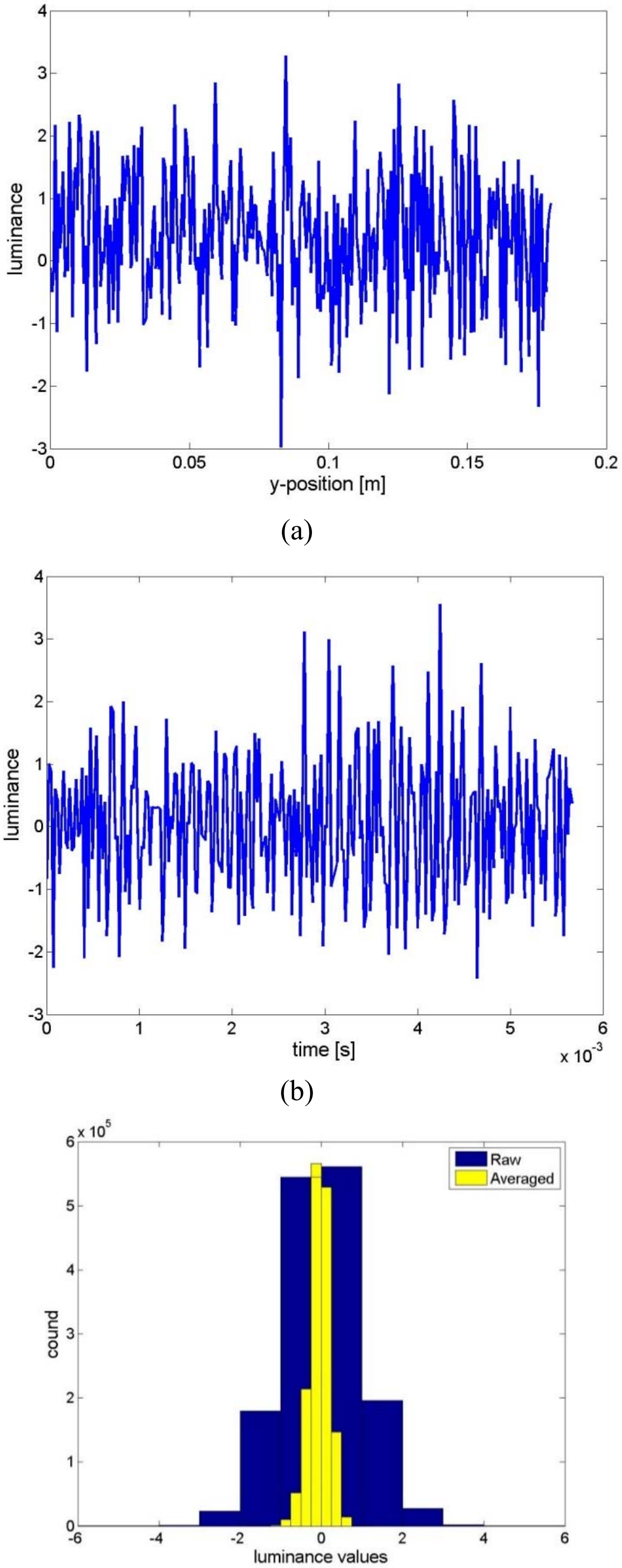

(a)

(b)

(c)

Figure 5.7 Luminance data along x = 0.0564 m after filtering (a) and time history for center point (b) along with histogram for the raw and averaged datasets (c).

To reduce the level of the uncorrelated noise an average of twenty video captures is taken. The standard deviation of the same fifteen frames is seen after averaging in Fig. 5.7 (c). In Fig. 5.8 (a) the dispersion curves in the wavenumber – frequency domain and the wavenumber-wavenumber domain (b) are shown for data with no averaging. The colormap illustrates the signal compared with the theoretically calculated dispersion curves given by the line. The wave is barely discernable in this figure. Figure 5.9 illustrates the dispersion curve after averaging. Here the wave can clearly be seen in both representations. The uncorrelated noise away from the axes is clearly reduced through averaging. Since multiple datasets are interleaved together, an additional low pass filter was applied with an upper bound of 45 kHz to account for the interleaving. In practice the high pass filter for to account for the lighting noise and the low pass filter for interleaving noise were implemented as Tukey filter from 1kHz to 45kHz. At this juncture the DC component, and known noise due to interleaving and lighting have been filtered, and the uncorrelated noise has been reduced through averaging. The normalized signal energy is seen in Fig. 5.10 (a). The SNR from Eqn. (5.3) was calculated to be 1.293. The signal smoothed with the moving average over 15 frames was used in calculating the signal energy as it remove some of the high frequency content seen in the raw signal thus allowing the SNR to reflect the more temporally stable changes in the signal due to the presence of the wave. Since the SNR for this signal is quite low, for visual display of the wave in the time-space domain, additional filtering was performed to improve the SNR.

To further isolate the wave, a more narrow frequency filter was applied between 12-21 kHz as well as applying the modal filtering technique as described in Section 2.3.3. The normalized signal energy was plotted following this filtering step in Fig. 5.10 (a) as well. In the signal energy plot, the presence of the wave is clearly seen from time 0.5e-3 to 2.5e-3 seconds. This filtering step greatly improves the SNR to 18.220. In the resulting spatial domain plot of the filtered wavefield, the wave is clearly seen emanating from the lower edge of the frame in the lower panel of Fig. 5.10 (b).

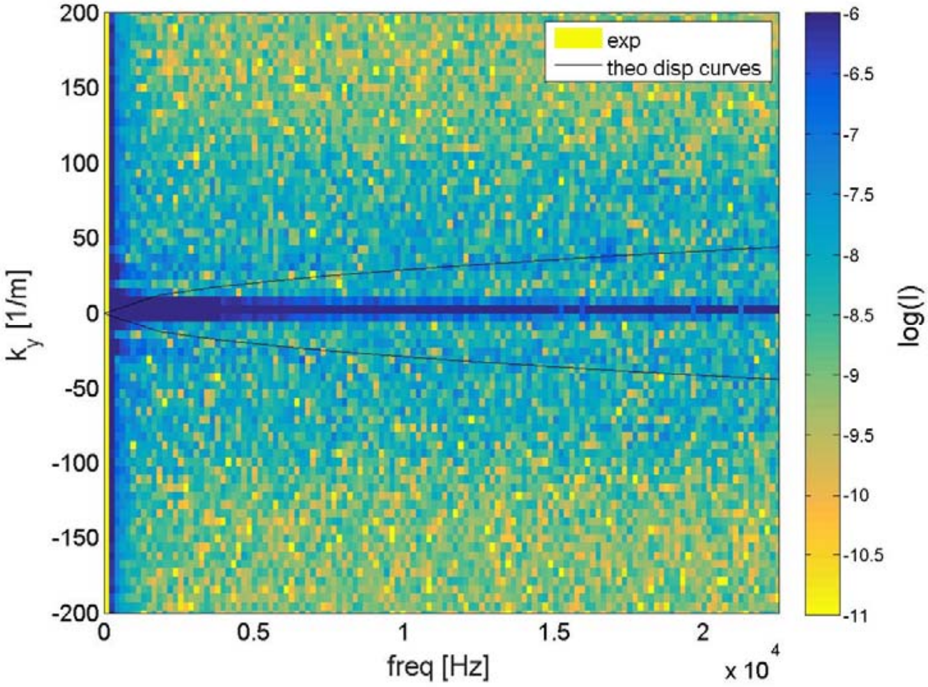

(a)

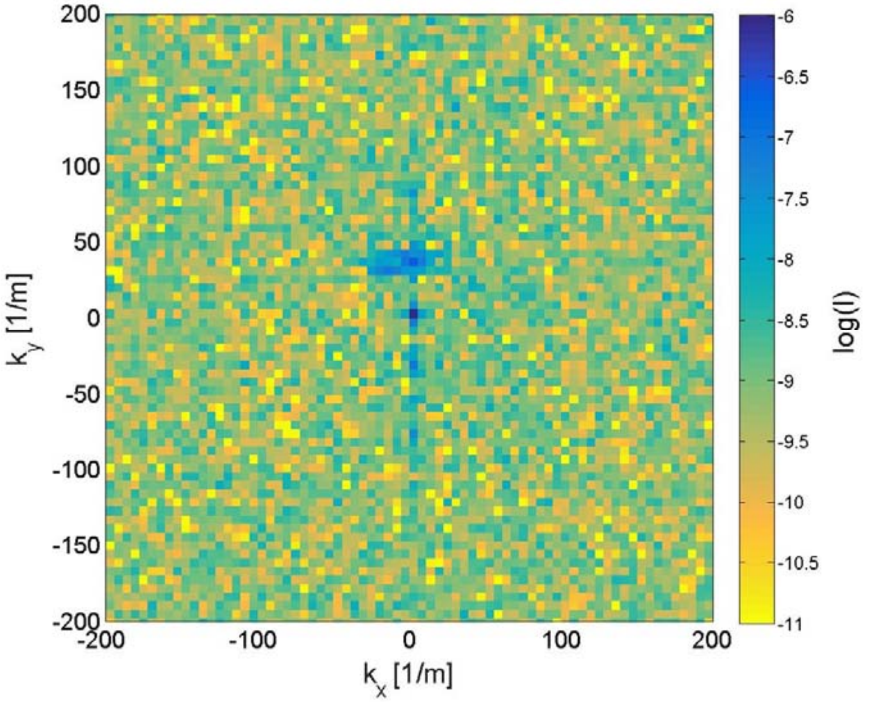

(b)

Figure 5.8 Dispersion curves for the fiberglass plate at 16.5 kHz excitation with no averaging; frequency vs. wavenumber (a), wavenumber vs. wavenumber (b)

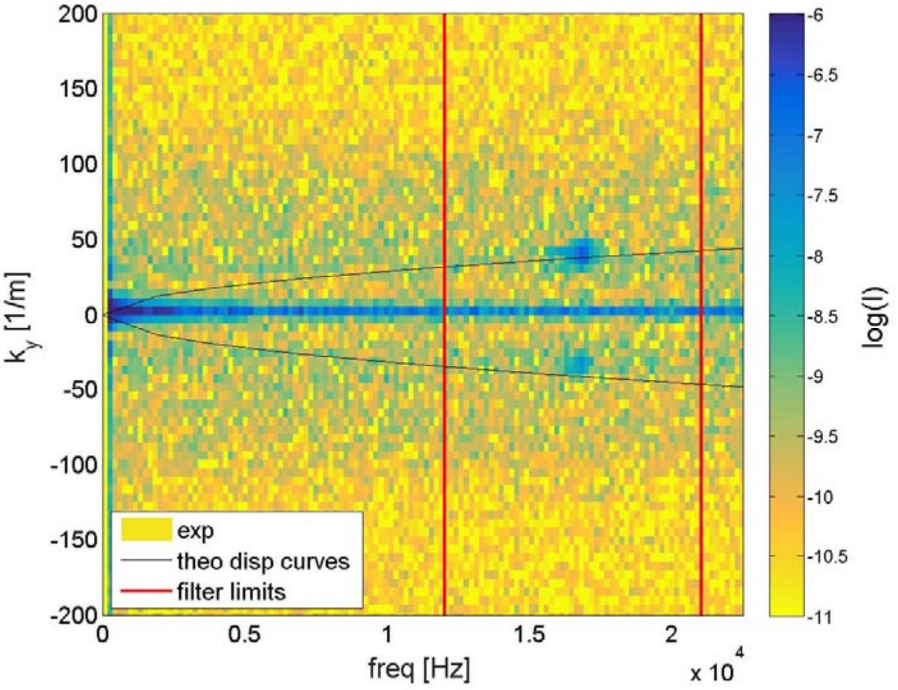

(a)

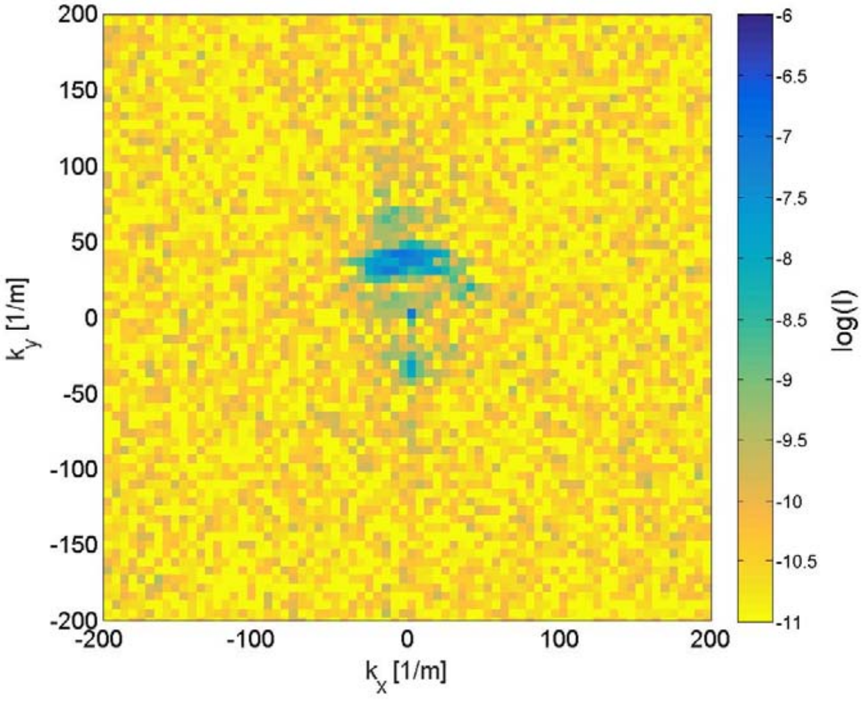

(b)

Figure 5.9 Dispersion curves for the fiberglass plate at 16.5 kHz excitation after 20 averages; frequency vs. wavenumber (a), wavenumber vs. wavenumber (b)

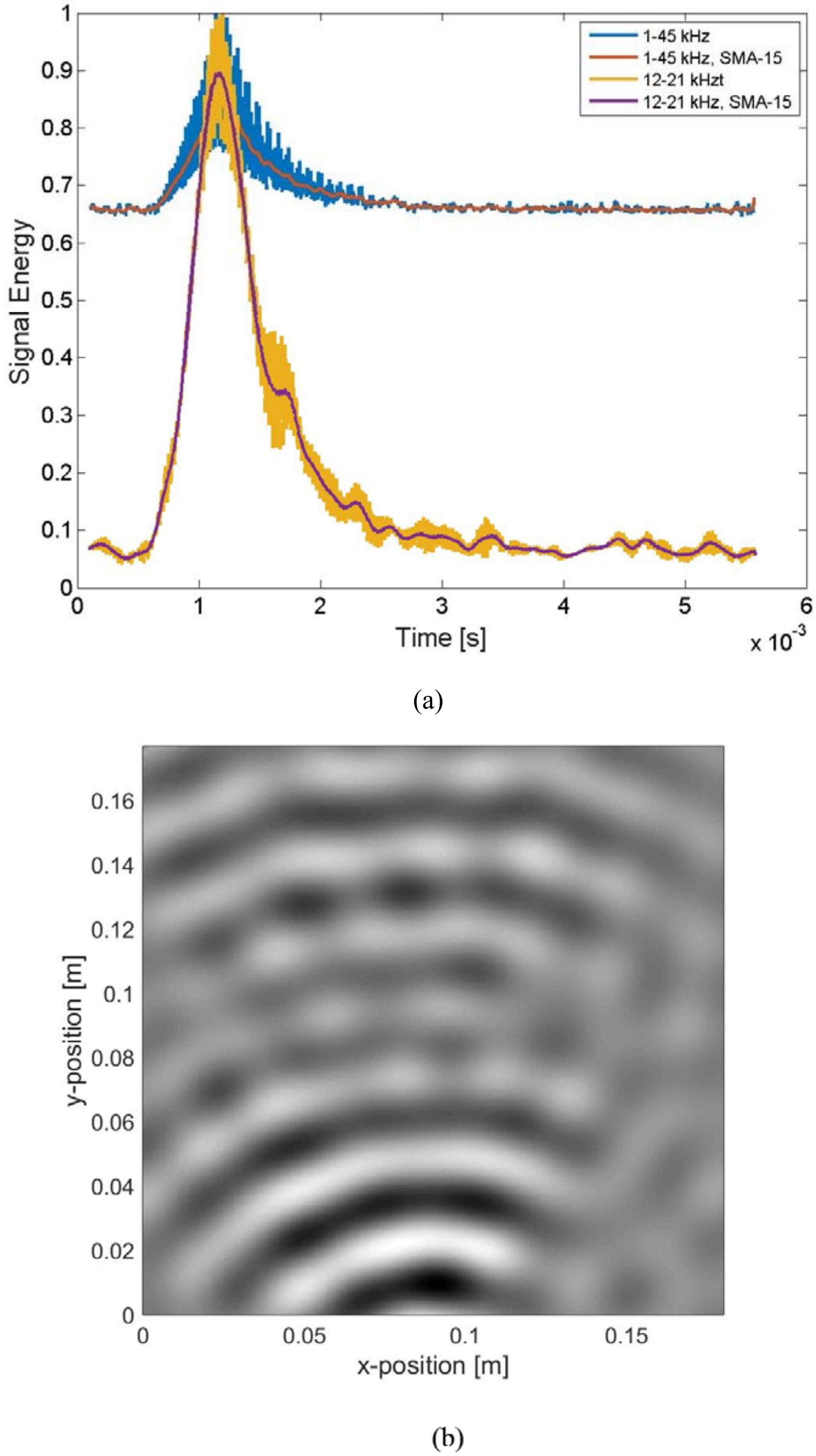

Figure 5.10 Normalized signal energy vs. time (a), and time-space domain results (b) for the fiberglass plate at 16.5 kHz excitation

Figure 5.11 compares these HSC measurement results to a dataset collected with a SLDV. A single point-wise comparison is made in Fig. 5.11 (a) and (b). In Fig. 5.11 (a) the signal envelopes closely match although the HSC measurement contains additional noise. The zoomed in comparison in Fig. 5.11 (b) further illustrates the agreement between the signals. The measured signals are compared at a snapshot in time in Fig. 5.11 (c) and (d). Again, close agreement between the HSC and SLDV measurements is seen.

The first broad filtering step minimizes signal distortion while removing known correlated noise. Since this noise is far from the signal in the Fourier Domain, a broad filter is used to minimize the distortion of the signal. In the second stage, the narrow filter improves the visualization of the wavefield but does so at the expense of distortion from heavy filtering. The specific circumstances of an individual use case need to be considered when evaluating this trade off.

Results for the remaining combinations of excitation frequencies and plates are seen in Figs. 5.12-5.21 and SNR before and after the narrowband frequency and wavenumber filters were applied are seen in Table 5.1. Table 5.1 also lists the range of the narrowband filter in the frequency domain and the range of the wavenumber domain filter relative to the analytically computed wavenumber at the excitation frequency. In all cases, the dispersion curves indicate the presence of a wave. In the signal energy plots, the wave is hard to discern before the second filtering step except in the fiberglass plate at 16.5 kHz. Following the second filtering step however, the wave is clearly visible

Table 5.1 Signal to Noise Ratio of processed datasets

	Fiberglass 16.5 kHz	**Fiberglass 36 kHz**	**Aluminum 16.5 kHz**	**Aluminum 36 kHz**	**Carbon Fiber 16.5 kHz**	**Carbon Fiber 36 kHz**
Frequency Filter Range [kHz]	12-21	30-42	12-21	30-42	12-21	30-42
Wavenumber Filter Range [1/m]	±15	±30	±50	±30	±50	±30
SNR-pre	1.293	1.197	1.041	1.085	1.064	1.070
SNR-post	18.220	2.413	1.356	1.764	2.320	1.998

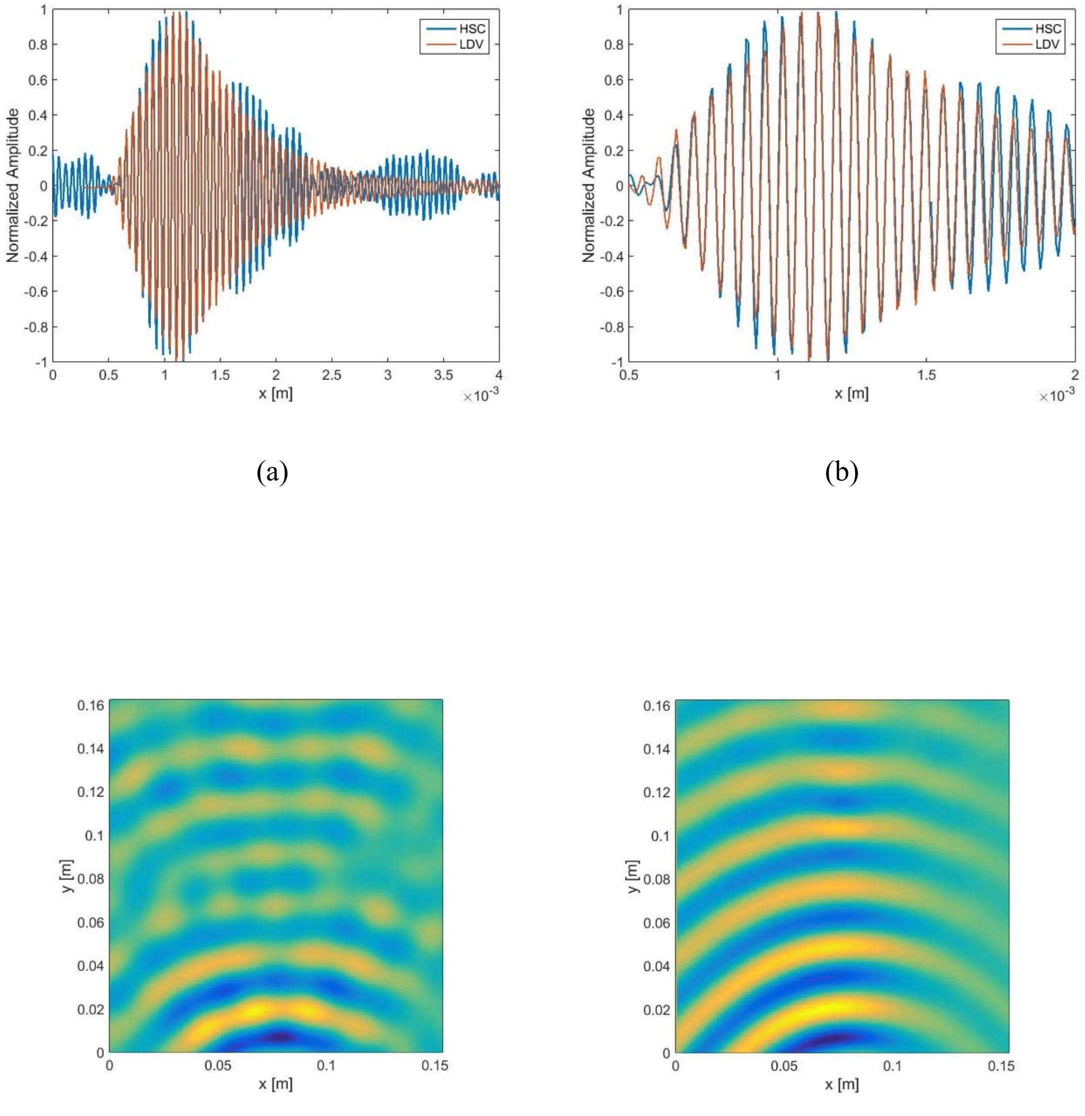

(a) (b) (c) (d)

Figure 5.11 Single point comparison of High Speed Camera results compared to SLDV results (a) (b) and snapshot comparison of High Speed Camera wavefield (c) and SLDV wavefield (d)

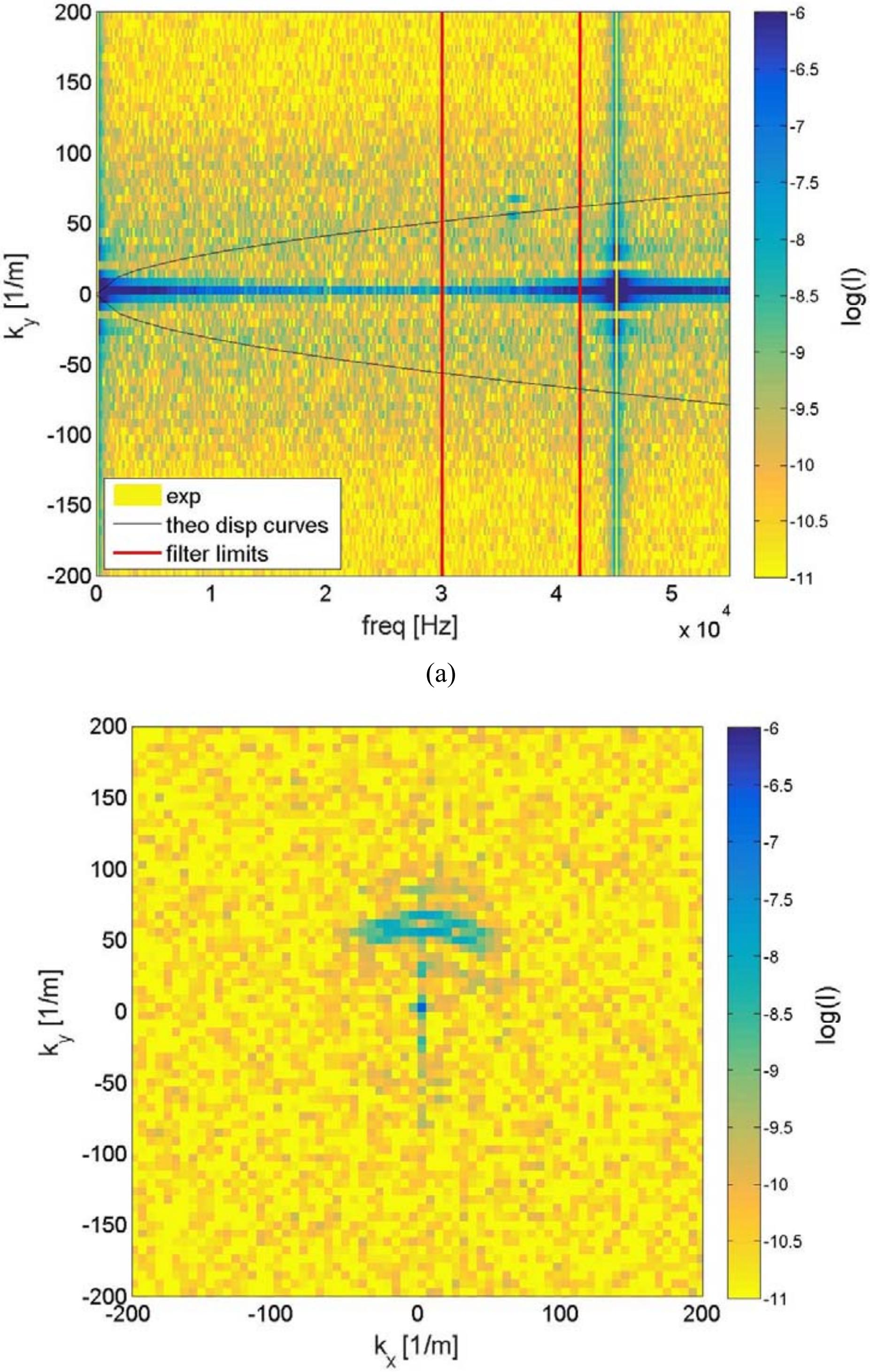

(a)

(b)

Figure 5.12 Dispersion curves for the fiberglass plate at 36 kHz excitation with 20 averages; frequency vs. wavenumber (a), wavenumber vs. wavenumber (b)

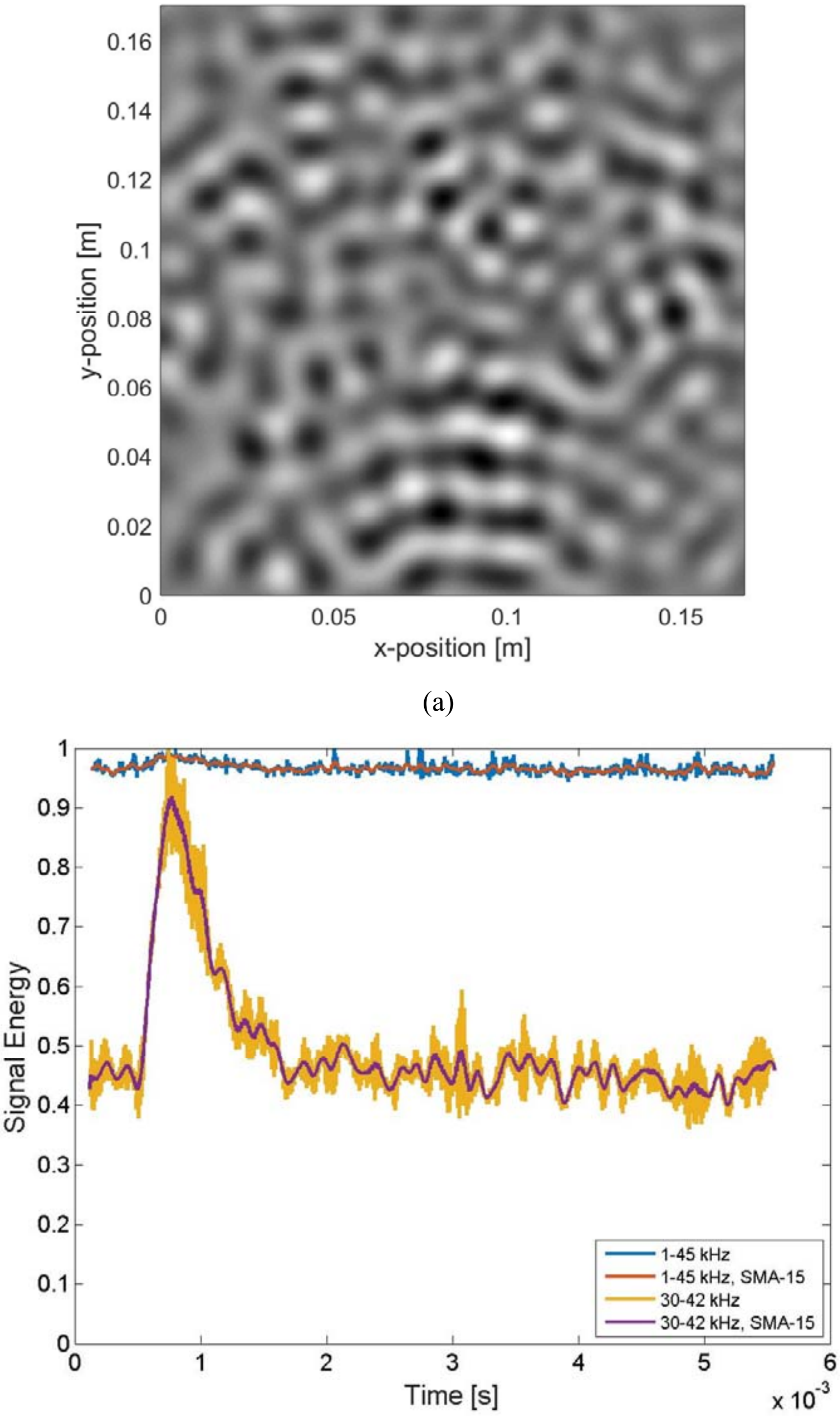

(a)

(b)

Figure 5.13 Time-space domain results for the fiberglass plate at 36 kHz excitation; spatial domain (a), normalized signal energy vs. time (b)

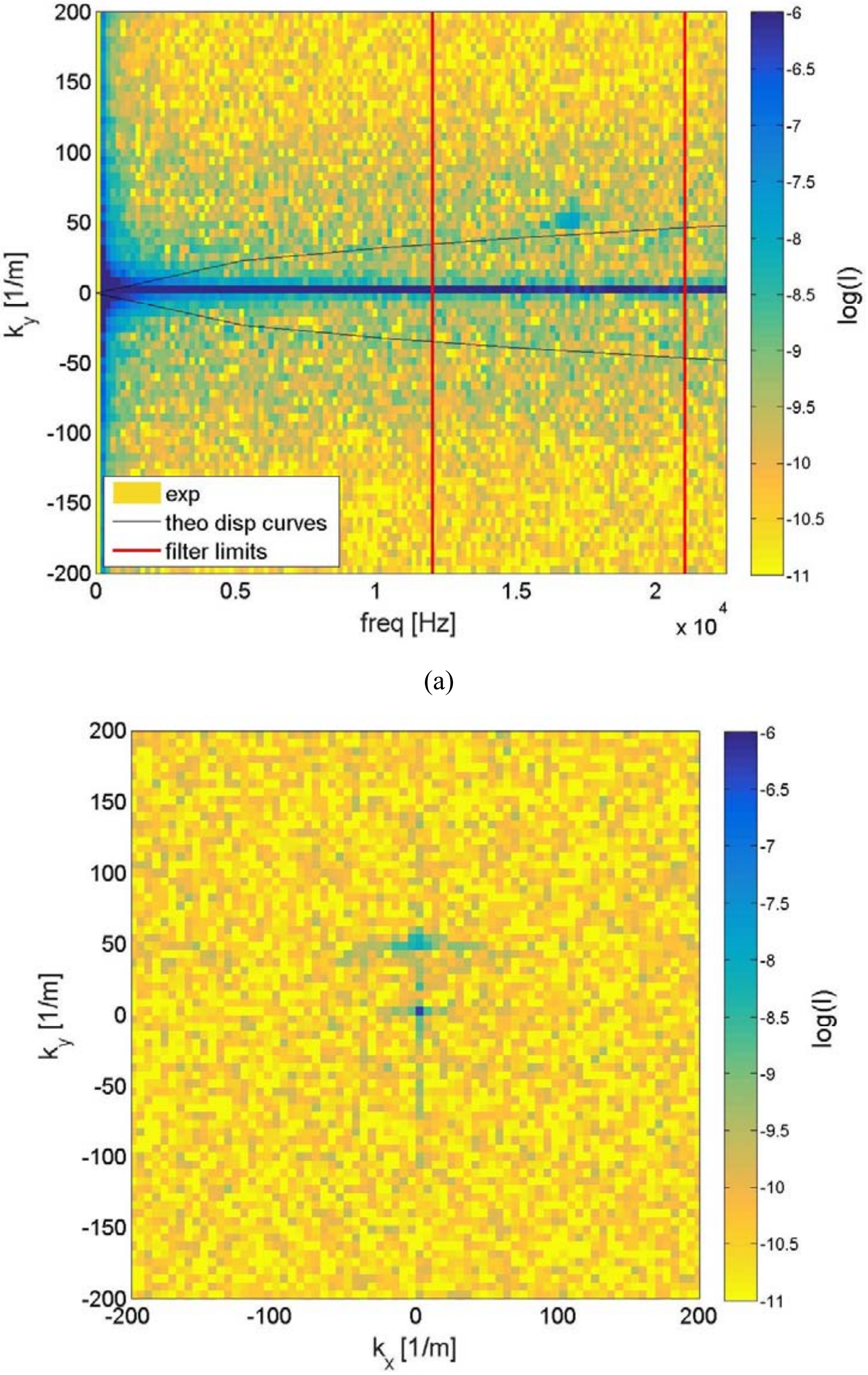

(a)

(b)

Figure 5.14 Dispersion curves for the aluminum plate at 16.5 kHz excitation with 20 averages; frequency vs. wavenumber (a), wavenumber vs. wavenumber (b)

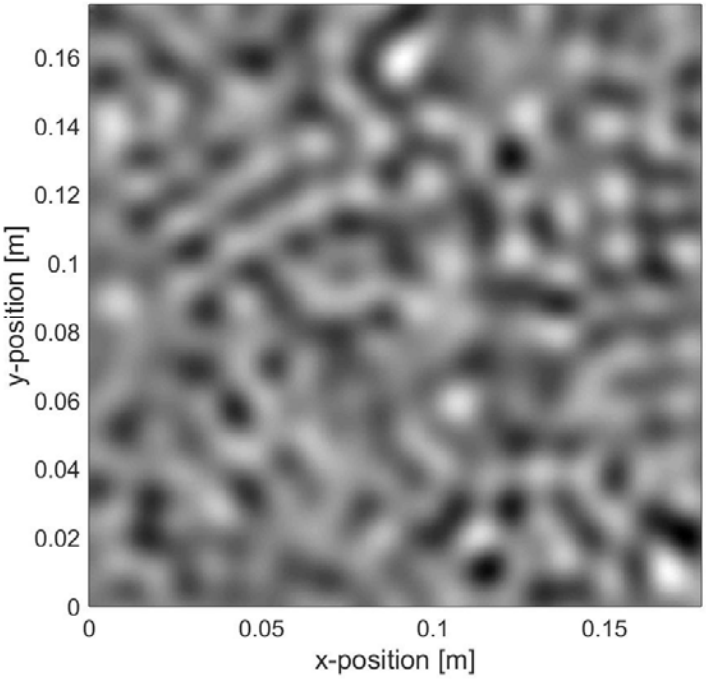

(a)

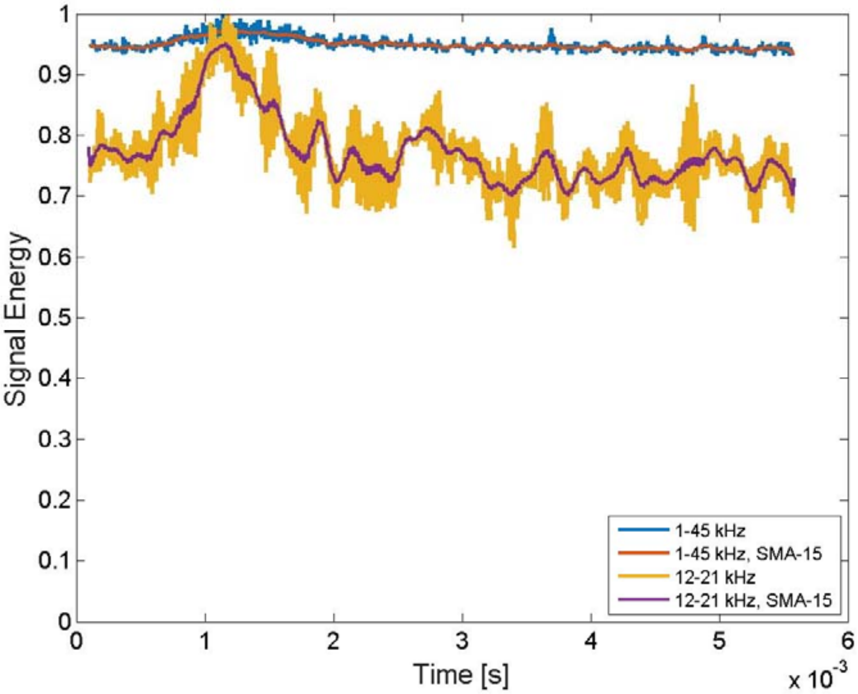

(a)

Figure 5.15 Time-space domain results for the aluminum plate at 16.5 kHz excitation; spatial domain (a), normalized signal energy vs. time (b)

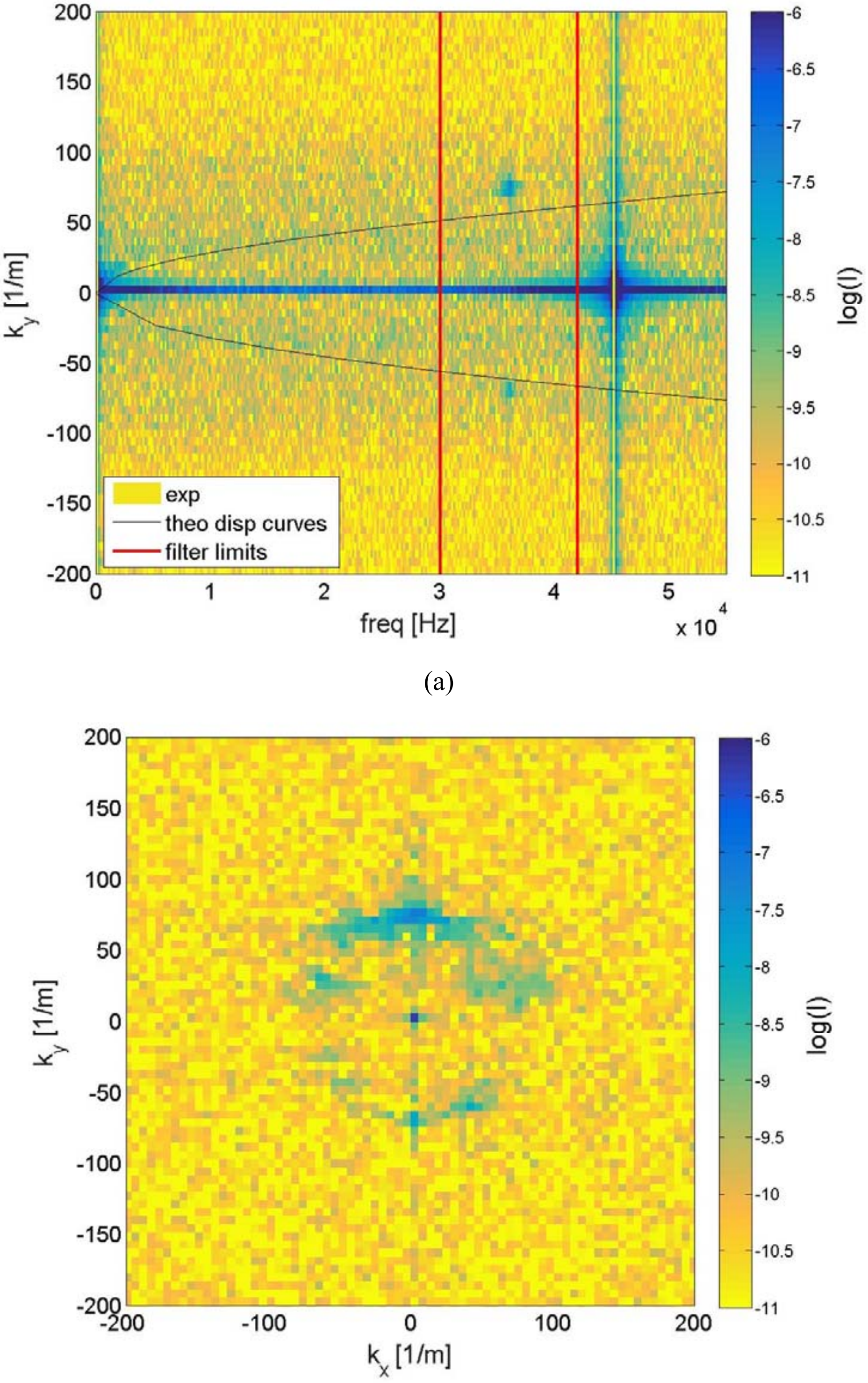

(a)

(b)

Figure 5.16 Dispersion curves for the aluminum plate at 36 kHz excitation with 20 averages; frequency vs. wavenumber (a), wavenumber vs. wavenumber (b)

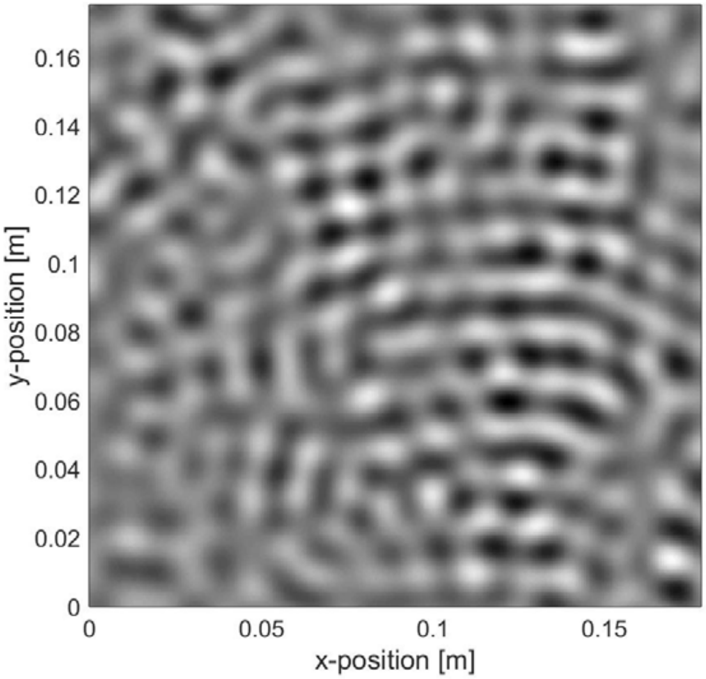

(a)

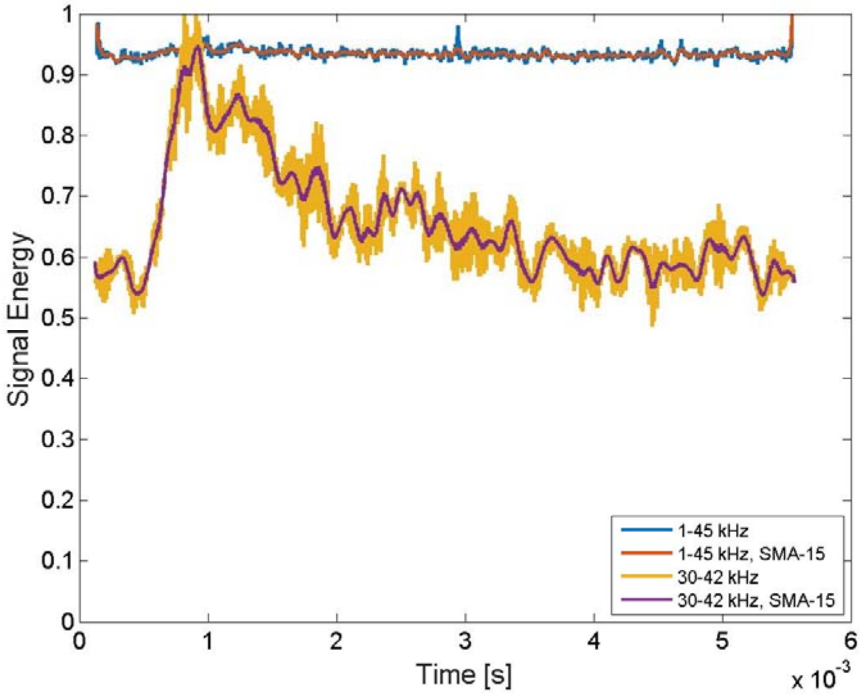

(b)

Figure 5.17 Time-space domain results for the aluminum plate at 36 kHz excitation; spatial domain (a), normalized signal energy vs. time (b)

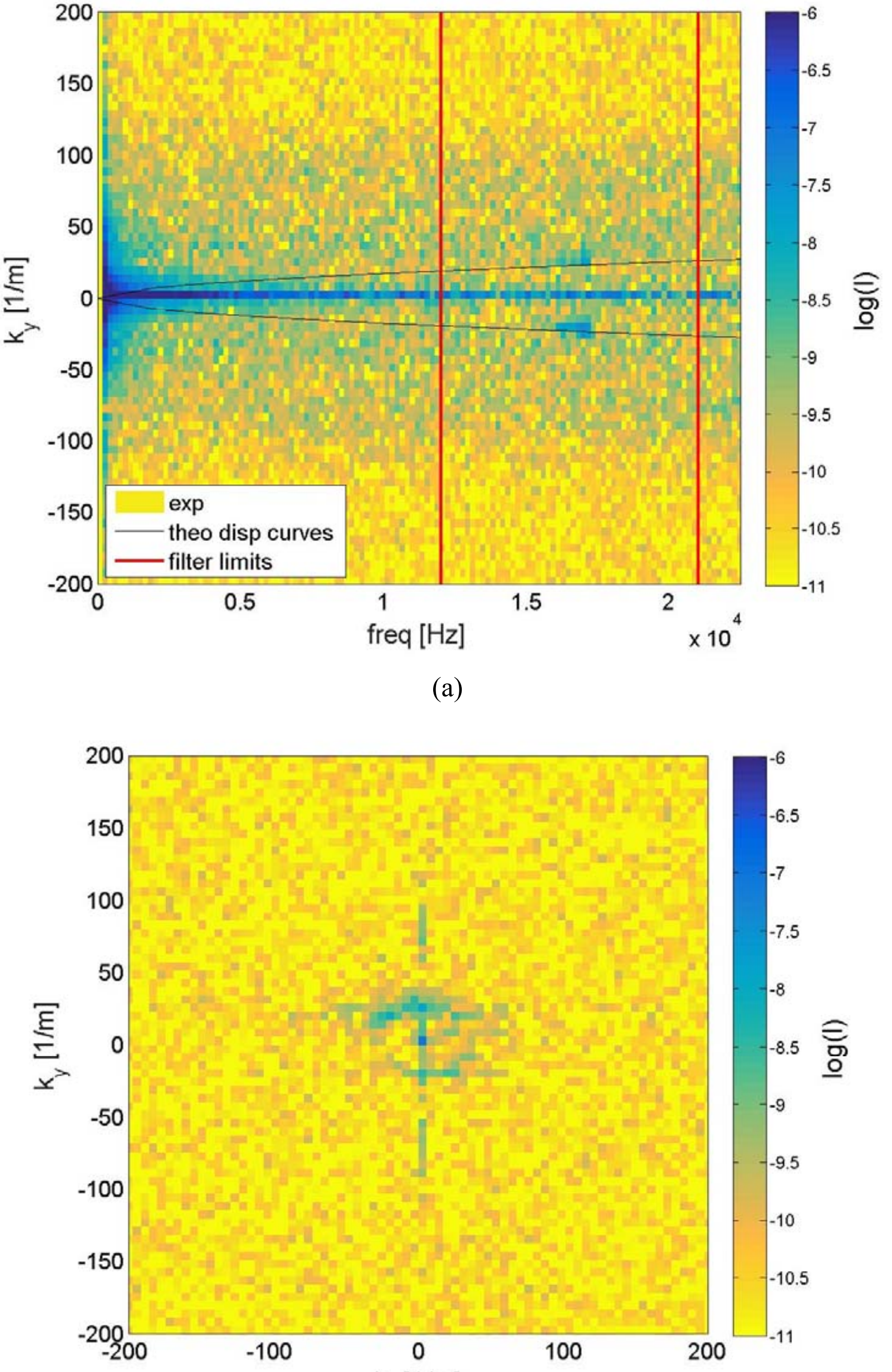

(a)

(b)

Figure 5.18 Dispersion curves for the carbon fiber plate at 16.5 kHz excitation with 20 averages; frequency vs. wavenumber (a), wavenumber vs. wavenumber (b).

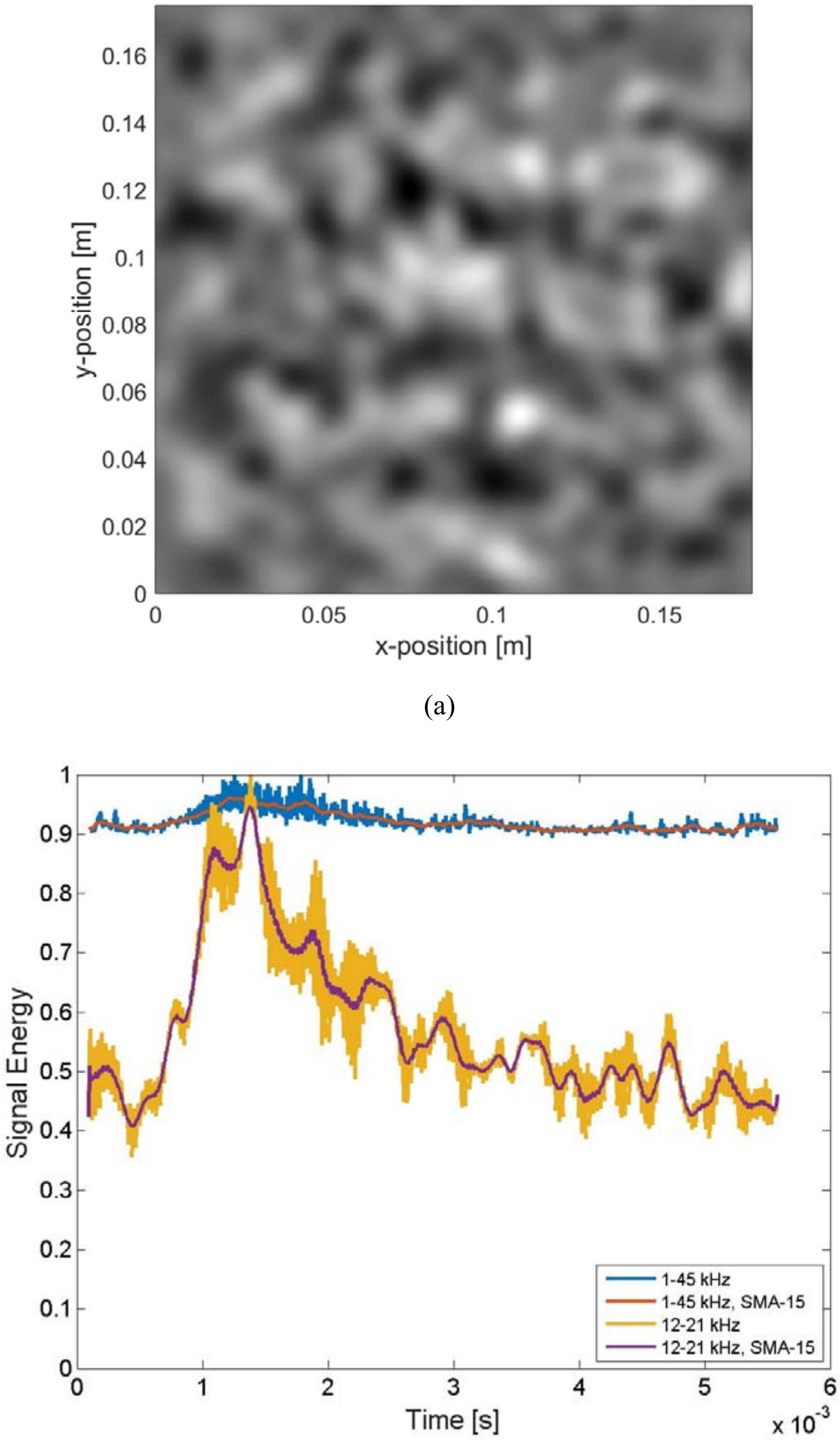

(a)

(b)

Figure 5.19 Time-space domain results for the carbon fiber plate at 16.5 kHz excitation; spatial domain (a), normalized signal energy vs. time (b)

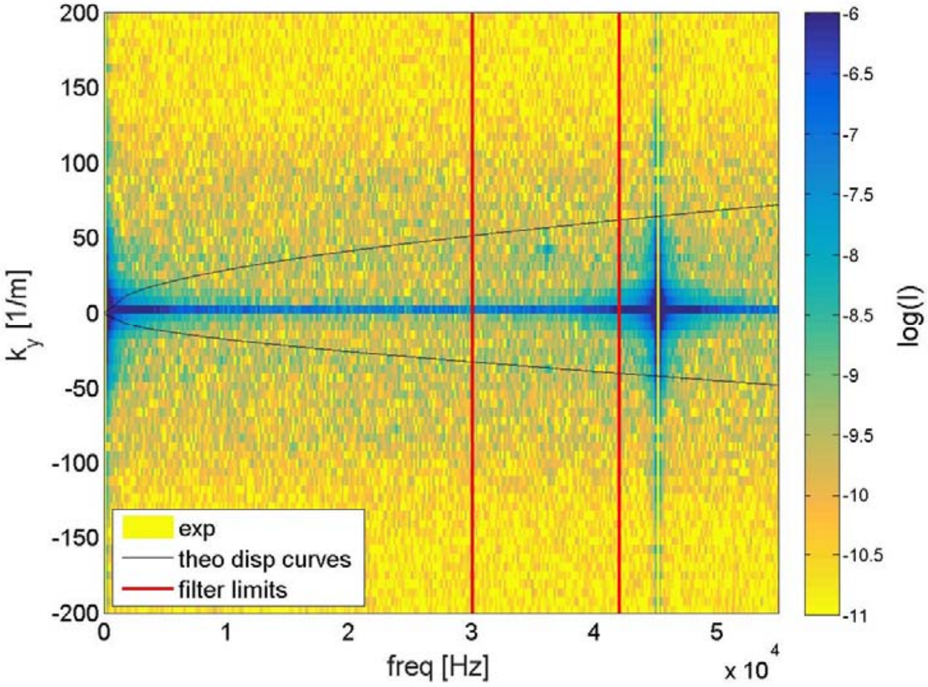

(a)

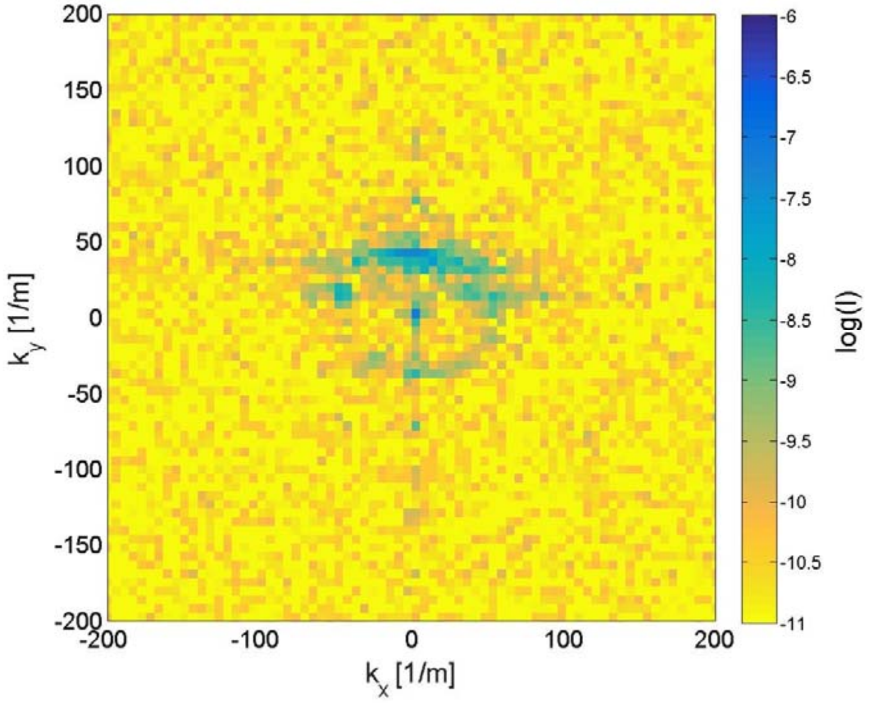

(b)

Figure 5.20 Dispersion curves for the carbon fiber plate at 36 kHz excitation with 20 averages; frequency vs. wavenumber (a), wavenumber vs. wavenumber (b)

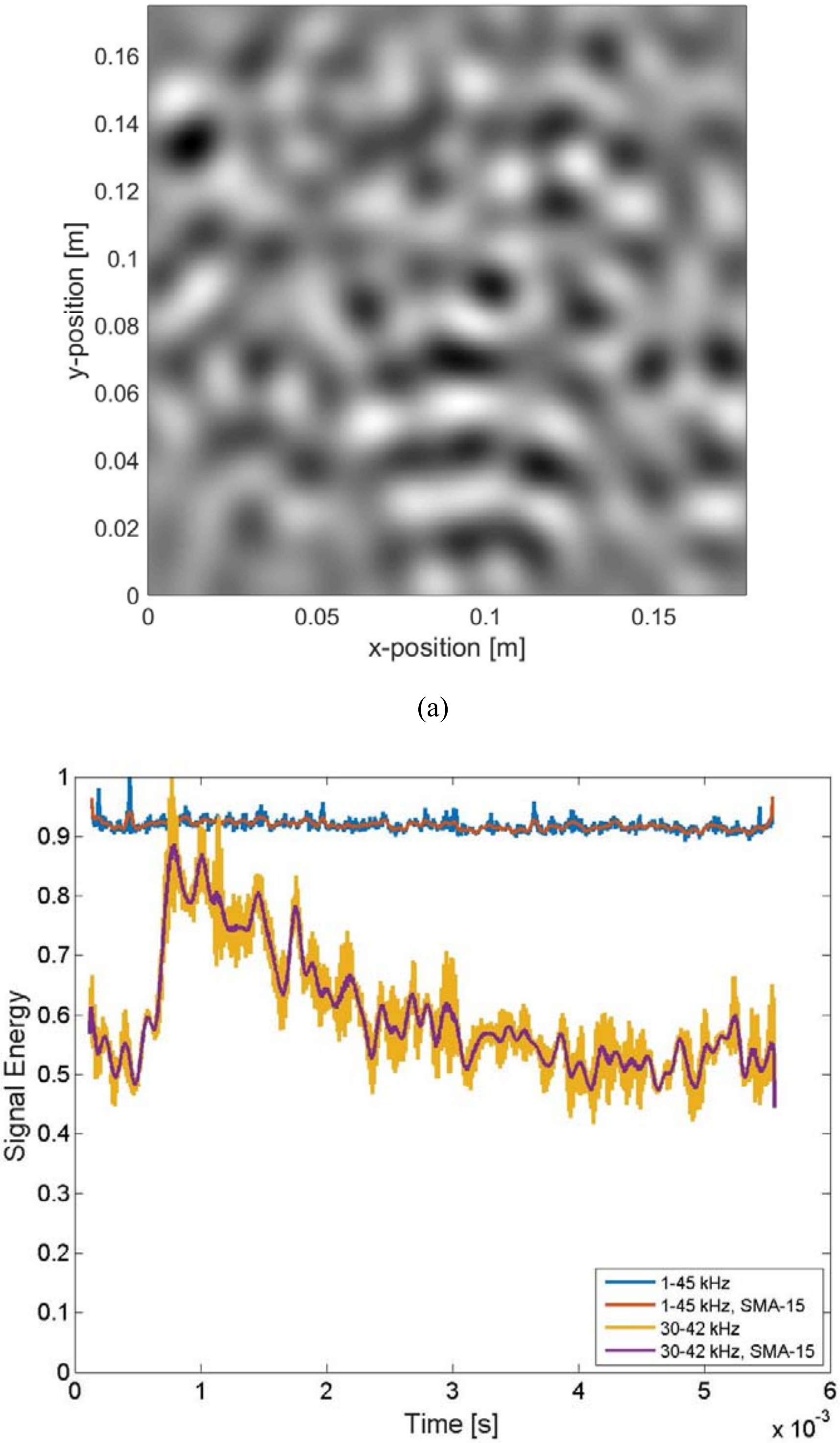

(a)

(b)

Figure 5.21 Time-space domain results for the carbon fiber plate at 36 kHz excitation; spatial domain (a), normalized signal energy vs. time (b) in all the normalized signal energy plots.

The spatial domain plots do not clearly indicate a wave except in the fiberglass plate at 16.5 kHz. In the fiberglass plate at 36 kHz, aluminum plate at 36 kHz and in both carbon fiber plate some regular order can be seen emanating from the x-axis at approximately x=0.11m. The results illustrate the benefits of filtering process. By increasingly focusing the filtering procedure on the wave in the Fourier Domain, more obvious indications of the wave's presence is seen. However, this comes at the expense of spreading caused by these narrow filters. Care should be taking when evaluating this tradeoff.

5.6 Discussion

The results of the optical wave measurements and data analysis reveal that GW can be measured by a high speed camera. This was evident by the fact that in all six datasets indications are present in the dispersion curves and plots of energy over time. However, even in the best case, the SNR was quite low without heavy filtering in both the frequency and wavenumber domain.

There are several limitations to the optical measurement approach with high speed cameras. The first and most important is the low SNR ratio. This is likely driven largely by hardware, however experimental procedure may play a role as well. The limitations on hardware also impose a tradeoff of framerate and frame size. The hardware will likely improve with time, thus also improving the SNR and framerates for a given frame size. Intrinsic limitations include the fact that only relative measurements are made. It is not possible to directly compute displacements from the captured video. The video only measures the intensity, which is indirectly related to displacements. Conversely, the method provides a large decrease in time to acquire the data, from around 90 minutes to approximately nine minutes, even when collecting 20 captures for averaging each of three video sets for interleaving. In addition, the frame size provides a relatively dense sampling grid. As hardware continues to improve, SNR is likely to increase, broadening the potential for using high speed cameras for GW measurements.

CHAPTER VI

CONCLUSIONS

6.1 Summary

This thesis presents two phase-based methods for mapping guided waves (GW) and explores a novel method of optical GW measurement. Guided waves have long been regarded as an important and powerful tool for Non-Destructive Evaluation. However, applications of GW techniques to field use are very limited. This is in part due to the complex nature of the wavefields produced by GW as well as the difficulty in measuring the wavefield. In this research, efforts are focused on minimizing the amount of a priori information necessary to implement the methods as well as propose a novel method for acquiring the wavefield.

The first method explored is the Two-Dimensional Phase Gradient method. This thesis extends the 1-D method previously developed to two-dimensions. The method is evaluated numerically and experimentally on both crack and delamination type damage analogs. It is clear that the method lends itself to linear crack like damage modeled as notch. However, the method is not suitable for 2-D delamination type damage. This drives development of a second damage mapping method.

The Phase Congruency for damage mapping method recasts an existing tool for edge detection in images as a damage mapping technique. Through development of a linear wavefield model, the method is analyzed and adapted to use for mapping damage. In particular, analysis of model wavefields in the wavenumber domain drove a new prescription for the wavenumber band considered in the analysis. Additionally, the models allow characteristic and quantitative comparison of potential filters. The PC for damage mapping method is evaluated on numerical and experimental datasets of increasing complexity. The best damage maps are found for the simplest cases of damage, notches, geometry changes and simulated delaminations. In case of mixed scatterer types, both geometric and mass additions, the method performs well, identifying both types of scatterers. In the most complex case of impact damage, the method identifies and localizes damage well, giving good estimates of the span of the delaminations contained in the damage. However, the complexities of the damage are not captured. In all cases, no a priori information is needed for this method. The PC for damage mapping reduces the amount of information needed and increases the amount of information provided to inspectors by means of a damage map.

Finally, this research explores the possibility of using an optical method for acquiring GW signals. A high speed camera and high intensity lighting was used to detect GW in three plates at two excitation frequencies. By looking at the acquired wavefields in the Fourier Domain, the presence to the GW could clearly be seen. Further development of both the hardware and data processing could provide NDE practitioners with a very simple and robust method for capturing wavefields on geometrically complex specimen.

In summary, this work has two focus areas. The first is to make improvements in the data available to NDE practitioners about damage by providing a map of the damage. Second, important first steps were made in a novel GW acquisition technique.

6.2 Contributions

This thesis provides three main contributions to the field of NDE research:

1. Two-Dimensional Phase Gradient Technique

The Phase Gradient technique is expanded to 2-D resulting in a new method for mapping linear damage such as cracks. This method requires the dispersion curves for modal filtering. These could be provided from known material properties or estimated from the measured wavefield. The method is not well suited to 2-D damage types however, the results for linear damage shapes are quite good.

2. Phase Congruency for damage mapping

A well-known image processing technique is analyzed and recast for use mapping damage in GW wavefields. By exploiting the particular case of wavefields, a marked increase in damage map quality was achieved when compared to plotting the RMS of a wavefield. Additionally, this method provides good results even in complex wavefields with no a priori knowledge of the sample's material characteristics. This greatly enhances its utility to NDE practitioners by both reducing the knowledge of the specimen required and by providing clear maps of damage and geometric changes in the specimen.

3. Optical Wavefield Acquisition

Wavefield acquisition with a high speed camera is demonstrated. Although the signal to noise ratio is low, it is an order of magnitude faster in acquiring the data than comparable SLDV measurements. Current fielded techniques for acquiring damage maps are limited to ultrasonic C-scans performed either by hand or robotically. These methods are both slow and in the case of robotic scans, highly restricted in the geometries they can scan. The optical camera is both fast and flexible compared to the current fielded systems. Even compared to typical laboratory systems such as the Scanning Laser Doppler Vibrometer, the optical method is an order of magnitude faster. While the scope of the exploration of this technique was limited in this research, it clearly demonstrated the potential of the method.

6.3 Future work

The work described in this thesis has several opportunities for future work.

6.3.1 Damage Mapping

1. Phase Congruency Modeling

The Phase Congruency for damage mapping method works well in cases that closely matched, or could be reduced to the analytical model developed for describing wavefields. However as the damage became more complex, the damage map became less complete. The interplay between the limits of the GW interactions with the damage and limits of the PC for damage mapping method should be explored to determining which is the limiting factor. Additionally, if the sampling grid density is high enough and the wavelengths are low enough, the damage again takes on the characteristics of the simple model with well-spaced damage elements. The grid densities and wavelengths necessary to approximate complex damage with a simpler model need to be considered. Further analysis should examine the relationship between these characteristics and the limitations of experimental systems, thus providing guidelines for hardware requirements to resolve features at these length scales and vice versa.

2. Explore the influence of Signal-to-Noise Ratio

The SLDV measurements typically had very high Signal-to-Noise Ratios (SNR) thus the influence of SNR was not considered. However, the SNR of the optical measurements wave are very low, the best case being 1.2. The datasets from the optical measurement did not produce a useful damage map. It is likely that this is due to the very low SNR, since for the same sample and excitation measurements with the SLDV yielded acceptable damage maps. Analysis of SNR and its influence on the PC method's ability to map damage would provide important markers for hardware requirements, or limitations of mapping capability for a specified SNR. This information would then provide benchmarks for experimental and post-processing techniques to address the SNR.

3. Comparison with comparable wavefield analysis techniques

This work compared the PC for Damage Mapping results to RMS plots and CT X-ray scans however, additional comparisons could be warranted. Comparison of both qualitative and quantitative metrics would allow trade-offs between methods to be assessed. Qualitative comparisons examining the type of a priori information required (baselines, material parameters, specimen geometry) would address field feasibility, while quantitative performance criteria (accuracy of mapping, probability of detection, false positive rates) would compare suitability for meeting specific inspection requirements. Methods for comparison include delay and sum type approaches [58, 59], wavenumber methods [49, 50, 52] and amplitude based techniques [39]. The 2-D Phase Gradient technique could be compared along similar lines to other crack detection methods [42, 51].

4. Explore alternative characterization schemes

This work considered one approach for quantitative characterization utilizing the angle of congruency in the PC method. However, additional approaches should be explored. The PC method has information available that is yet unused. In particular the PC at individual orientations as well as the evolution of PC over time. Utilizing the orientations, it may be possible to discern quantitatively rather than qualitatively zero thickness defects (cracks) from similar defect with a discernable width, corrosion damage or delaminations. Alternatively, the evolution of PC overtime may allow detection of trapped waves that could help discriminate broad damage shapes such as delaminations from cracks. Further exploration of this area could allow quantitative characterization rather than experiential qualitative characterization.

6.3.2 Optical Wavefield Acquisition

1. Better understand conversion of surface displacements to intensity

This thesis did not attempt to understand the relationship between the surface displacements caused by the GW and the change in intensity detected by the camera. In developing the experimental procedure it is assumed that the change in intensity was due to local changes in the angle between the surface of the plate, the camera and the lights. However, no verification of this assumption is performed. A concerted effort to understand the relationship between the GW and the acquired signal would allow researchers to develop experimental and analytic procedures that will maximize the GW signal captured by the camera.

2. Improve sensitivity to Guided Wave signal

The high-speed cameras are limited in both the discretization of the signal and the dynamic range of the sensors. Avenues should be explored to maximize the dynamic range of the camera occupied by the oscillatory component of the signal associated with the GW. In this work, the signal from the GW typically only spanned one or two of the digital values. Methods to increase the sensitivity of the camera to the GW signal by means of analog pre-filtering or otherwise to reduce the signal range across space of the DC signal components. Simple examples include even illumination of the captured area, and painting to remove color variation and features.

6.4 Concluding Remarks

Guided wavefields provide a rich amount of information on the medium through which they propagate. The concept of this work was to developing novel methods of presenting the information available in the wavefield to NDE practitioners as well as framing a new method for GW measurement. Non-Destructive Evaluation practitioners are charged not just with identifying damage but determining how that damage ultimately affects the component and system it is a part of. Therefore, researchers must seek to extract more and more information from the available data. To this end, the analysis methods presented here focused on the extracting information out of the spatial domain to provide a picture of subsurface damage.

In addition, the development of the methods focused on minimizing a priori knowledge required. The methods presented here did not rely on models or baselines and only made cursory use of dispersions curves. This makes the methods robust to uncertainties in material parameters or changes in the sample over time. This in turn makes the methods more suitable for field use.

The concept for optical guided wave acquisition makes GW measurements more flexible and faster. High speed cameras are non-contact, portable, low power and do not require tight control of location relative to the inspected surface. High speed cameras are much faster than point-wise measurement methods such as the SLDV. Measurements made in this work were ten times faster with the high speed camera than with the SLDV. The potential speed and flexibility of high speed cameras would be an asset to NDE practitioners in the field.

These steps by themselves do not provide the complete basis for fieldable system. First, much more work is needed to bring the sensitivity of the optical method to a point that it is useful even in a lab. The persistent trend of improvement in digital hardware observed for nearly half a century will likely continue and solve a great deal of the signal-to-noise ratio short comings of the method. To speed the process along, improvements in experimental procedure and data processing through rigorous analysis of the conversion from surface displacement to the camera's detected change in intensity must occur.

As GW measurement techniques improve, either the optical method or others, so that full wavefield measurements can be made in the field, then true field demonstrations and evaluations of GW methods can begin. Until then, GW methods will be confined to lab use. In the meantime, persistence of the research community in extracting ever more information from wavefields will ultimately allow NDE practitioners not only the ability to detect and locate damage but assess its implications to the suitability of the system, as that is ultimately the goal of NDE.

REFERENCES

1. Mistercontributer, "Tech Tower," 2013 (Photograph) Wikipedia.

2. G. Johnson, Ultrasonic Flaw Detectors...And Beyond A history of the discovery of the tools of nondestructive technology. in Quality Magazine BNP Media, 2013, Vol. 52, pp. 22-24.

3. D. Canonico, "The History of ASME's Boiler and Pressure Vessel Code," Retrieved from www.asme.org on March 5, 2015.

4. *Acceptable Methods, Techniques and Practices - Aircraft Inspection and Repair*, AC 43.13-1B, 1998.

5. M. P. Papaelias, C. Roberts and C. L. Davis, "A review on non-destructive evaluation of rails: state-of-the-art and future development", *Proceedings of the Institution of Mechanical Engineers Part F-Journal of Rail and Rapid Transit,* vol. 222, no. 4, pp. 367-384, 2008.

6. P. R. Muduli and U. C. Pati, "A novel technique for wall crack detection using image fusion," Computer Communication and Informatics (ICCCI), 2013 International Conference on, 2013, pp. 1-6.

7. H.-N. Nguyen, T.-Y. Kam and P.-Y. Cheng, "An Automatic Approach for Accurate Edge Detection of Concrete Crack Utilizing 2D Geometric Features of Crack", *Journal of Signal Processing Systems,* pp. 1-20, 2013.

8. *Non-destructive Testing - Penetrant testing*, 3452-1:2013, I. O. f. Standardization, 2013.

9. R. C. McMaster, "The History, Present STatus and Future Developments of Eddy Current Tests," Workshop on Eddy Current Nondestructive Testing, 1977, pp. 1-32.

10. *Electromagnetic testing*, Columbus, Ohio: Columbus, Ohio : American Society for Nondestructive Testing, 2004.

11. *Infrared and thermal testing*, 3rd ed.. ed. Columbus, OH: Columbus, OH : American Society for Nondestructive Testing, 2001.

12. S. P. Sachin and P. Kara, "Through-the-thickness identification of impact damage in composite laminates through pulsed phase thermography", *Measurement Science and Technology,* vol. 24, no. 11, pp. 115601, 2013.

13. Z. Liu, M. Genest and D. Krys, "Processing thermography images for pitting corrosion quantification on small diameter ductile iron pipe", *NDT & E International,* vol. 47, no. pp. 105-115, 2012.

14. W. C. Rontgen, "On a New Kind of Rays", *Science,* vol. 3, no. 59, pp. 227-231, 1896.

15. G. W. C. Kaye, "X-rays in industry", *Nature,* vol. 117, no. pp. 123-126, 1926.

16. V. Deutsch, "History of NDT-Instrumentation," 15th World Conference on Non-Destructive Testing, 2000.

17. "NDT Resource Center," Retrieved from https://www.nde-ed.org/index_flash.htm on Aug, 14 2015.

18. C. W. Chan, "Lamb waves in highly attenuative plastic plates", *The Journal of the Acoustical Society of America,* vol. 104, no. 2, pp. 874, 1998.

19. H. Lamb, "On Waves in an Elastic Plate", *Proceedings of the Royal Society A Mathematical Physical and Engineering Sciences,* vol. 93, no. 648, pp. 114-128, 1917.

20. L. Gavrić, "Finite Element Computation of Dispersion Properties of Thin-Walled Waveguides", *Journal of Sound and Vibration,* vol. 173, no. 1, pp. 113-124, 1994.

21. D. C. Worlton, "Experimental confirmation of Lamb waves at megacycle frequencies", *Journal of Applied Physics,* vol. 32, no. 6, pp. 967-971, 1961.

22. H. P. Hatch and K. A. Fowler, "Applications of Lamb Waves to Examination of Steel Strip for Laminar Defects", *Materials Evaluation,* vol. 23, no. 10, pp. 496, 1965.

23. H. Berger, "An Ultrasonic Imaging Lamb-Wave System for Reactor-Fuel-Plate Inspection", *Ultrasonics,* vol. 5, no. 1, pp. 39-41, 1967.

24. S. Mazumdar, What Will Drive Composites Growth in 2015 in Composite Manufacturing American Composites Manufacturing Association, Arlington, 2015, Vol. Jan/Feb.

25. C. Red, Composites in Aircraft Interiors, 2012-2022 in Composites World Gardner Business Media, Inc, 2012.

26. J. Hale, Boeing 787 from the ground up in Aeromagazine Boeing Corp., 2006, pp. 16-23.

27. M. R. LeGault, DDG-1000 Zumwalt: Stealth Warship in Composites World Gardner Business Media Inc., 2010.

28. "Robotic Manufacturing System Will Build Biggest Composite Rocket Parts Ever Made", 2015. Accessed on: Jan. 1, 2016, [Online].

29. W. G. Knauss, "Global Failure Modes in Composite Structures," California Institute of Technology.

30. M. J. S. Lowe, D. N. Alleyne and P. Cawley, "Defect detection in pipes using guided waves", *Ultrasonics,* vol. 36, no. pp. 147-154, 1998.

31. Z. Q. Sun, Y. W. Mao, W. H. Jiang and D. Zhang, "Investigation on interaction of Lamb waves and circumferential notch in pipe by means of wavelet transform," 2000 IEEE Ultrasonics Symposium Proceedings, Vols 1 and 2, eds S. C. Schneider, M. Levy and B. R. McAvoy, 2000, pp. 827-830.

32. P. Cawley, M. Lowe, D. Alleyne, B. Pavlakovic and P. Wilcox, "Practical long range guided wave inspection-applications to pipes and rail", *Materials Evaluation,* vol. 61, no. 1, pp. 66-74, 2003.

33. S. Pavlopoulou, C. Soutis and G. Manson, "Non-destructive inspection of adhesively bonded patch repairs using Lamb waves", *Plastics, Rubber and Composites,* vol. 41, no. 2, pp. 61-68, 2012.

34. E. Le Clézio, M. Castaings and B. Hosten, "The interaction of the S0 Lamb mode with vertical cracks in an aluminium plate", *Ultrasonics,* vol. 40, no. 1–8, pp. 187-192, 2002.

35. R. Sicard, J. Goyette and D. Zellouf, "A SAFT algorithm for lamb wave imaging of isotropic plate-like structures", *Ultrasonics,* vol. 39, no. 7, pp. 487-494, 2002.

36. N. Hu, T. Shimomukai, C. Yan and H. Fukunaga, "Identification of delamination position in cross-ply laminated composite beams using S_0 Lamb mode", *Composites Science and Technology,* vol. 68, no. 6, pp. 1548-1554, 2008.

37. J. C. P. McKeon and M. K. Hinders, "Lamb wave scattering from a through hole", *Journal of Sound and Vibration,* vol. 224, no. 5, pp. 843-862, 1999.

38. Z. S. Chang and A. Mal, "Scattering of Lamb waves from a rivet hole with edge cracks", *Mechanics of Materials,* vol. 31, no. 3, pp. 197-204, 1999.

39. G. R. Liu, K. Y. Lam and H. M. Shang, "Scattering of waves by flaws in anisotropic laminated plates", *Composites Part B-Engineering,* vol. 27, no. 5, pp. 431-437, 1996.

40. W. B. Williams, J. E. Michaels and T. E. Michaels, "Characterization of propagation and scattering via wavefield imaging for improved in situ imaging of damage in composites," Health Monitoring of Structural and Biological Systems 2016, eds T. Kundu, 2016, pp. 980502-980502-980510.

41. J. Koreck, Computational characterization of adhesive bond properties using guided waves in bonded plates, M.S., Civil and Environmental Engineering, Georgia Institute of Technology, 2006.

42. S. A. Meguid and X. D. Wang, "Wave scattering from cracks and imperfectly bonded inhomogeneities in advanced materials", *Mechanics of Materials,* vol. 31, no. 3, pp. 187-195, 1999.

43. J. L. Rose, "Guided wave nuances for ultrasonic nondestructive evaluation", *Ultrasonics, Ferroelectrics and Frequency Control, IEEE Transactions on,* vol. 47, no. 3, pp. 575-583, 2000.

44. S. Huo and H. Ries, "Estimation of adhesive bond strength in laminated safety glass using guided mechanical waves: Part 1. An energy velocity approach", *Insight: Non-Destructive Testing & Condition Monitoring,* vol. 50, no. 3, pp. 146-152, 2008.

45. M. Santos and J. Perdigão, "Leaky Lamb waves for the detection and sizing of defects in bonded aluminium lap joints", *NDT & E International,* vol. 38, no. 7, pp. 561-568, 2005.

46. J. L. Blackshire and S. Soni, "Lamb wave propagation in a restricted geometry composite pi-joint specimen," AIP Conference Proceedings, 2012, pp. 1299-1306.

47. Z. Fan, M. Castaings, M. J. S. Lowe, C. Biateau and P. Fromme, "Feature-guided waves for monitoring adhesive shear modulus in bonded stiffeners", *NDT & E International,* vol. 54, no. pp. 96-102, 2013.

48. H. Reed, G. Harvey, A. Dick, J. Dobson and C. Leckey, "A Parameterized Delamination Model for Use in Complex Damage Characterization of Composite Laminates in Ultrasonic Inspections," presented at 43rd Annual Review of Progress in Quantitative Nondestructive Evaluation (QNDE), Atlanta, GA, 2016.

49. Z. Tian, L. Yu and C. A. C. Leckey, "Guided wave propagation study on laminated composites by frequency-wavenumber technique," Proc. SPIE, Nondestructive Characterization for Composite Materials, Aerospace Engineering, Civil Infrastructure, and Homeland Security, 2014.

50. O. Mesnil, C. A. Leckey and M. Ruzzene, "Instantaneous and local wavenumber estimations for damage quantification in composites", *Structural Health Monitoring,* vol. 14, no. 3, pp. 193-204, 2015.

51. L. Yu, Z. Tian and C. A. C. Leckey, "Crack imaging and quantification in aluminum plates with guided wave wavenumber analysis methods", *Ultrasonics,* vol. 62, no. pp. 203-212, 2015.

52. P. D. Juarez and C. A. C. Leckey, "Multi-frequency local wavenumber analysis and ply correlation of delamination damage", *Ultrasonics,* vol. 62, no. pp. 56-65, 2015.

53. C. A. Paget, S. Grondel, K. Levin and C. Delebarre, "Damage assessment in composites by Lamb waves and wavelet coefficients", *Smart Materials & Structures,* vol. 12, no. 3, pp. 393-402, 2003.

54. C. Leckey, M. Rogge, Z. Tian and L. Yu, "Crack Detection with Lamb Wave Wavenumber Analysis."

55. Y. N. Al-Nassar, S. K. Datta and A. H. Shah, "Scattering of Lamb Waves by a Normal Rectangular Strip Weldment", *Ultrasonics,* vol. 29, no. 2, pp. 125-132, 1991.

56. M. G. Gustafsson and T. Stepinski, "Split spectrum algorithms rely on instantaneous phase information-a geometrical approach (US NDE)", *IEEE Transactions on Ultrasonics Ferroelectrics and Frequency Control,* vol. 40, no. 6, pp. 659-665, 1993.

57. V. L. Newhouse, N. M. Bilgutay, J. Saniie and E. S. Furgason, "Flaw-to-grain echo enhancement by split-spectrum processing", *Ultrasonics,* vol. 20, no. 2, pp. 59-68, 1982.

58. J. Rajagopalan, K. Balasubramaniam and C. V. Krishnamurthy, "A phase reconstruction algorithm for Lamb wave based structural health monitoring of anisotropic multilayered composite plates", *The Journal of the Acoustical Society of America,* vol. 119, no. 2, pp. 872-878, 2006.

59. J. E. Michaels, A. J. Dawson, T. E. Michaels and M. Ruzzene, "Approaches to hybrid SHM and NDE of composite aerospace structures," Proc. SPIE, Health Monitoring of Structural and Biological Systems, 2014.

60. J. Camacho, M. Parrilla and C. Fritsch, "Phase Coherence Imaging", *IEEE Transactions on Ultrasonics Ferroelectrics and Frequency Control,* vol. 56, no. 5, pp. 958-974, 2009.

61. L. Rayleigh, "On the Free Vibrations of an Infinite Plate of Homogeneous Isotropic Elastic Matter", *Proceedings of the London Mathematical Society,* vol. s1-20, no. 1, pp. 225-237, 1888.

62. N. Guo and P. Cawley, "The Interaction of Lamb Waves with Delaminations in Composite Laminates", *Journal of the Acoustical Society of America,* vol. 94, no. 4, pp. 2240-2246, 1993.

63. J. Ayers, N. Apetre, M. Ruzzene and V. K. Sharma, "Phase gradient and mode conversion estimation in 1D damaged structures", *Structural Health Monitoring,* vol. 10, no. 1, pp. 65-82, 2011.

64. D. C. Ghiglia and M. D. Pritt, *Two-Dimensional Phase Unwrapping Theory Algorithms and Software*, New York: John Wiley & Sons, 1998.

65. P. D. Kovesi, "Image Features from Phase Congruency", *Videre: Journal of Computer Vision Research,* vol. 1, no. 3, pp. 2-27, 1999.

66. D. N. Alleyne and P. Cawley, "The Interaction of Lamb Waves with Defects", *IEEE Transactions on Ultrasonics Ferroelectrics and Frequency Control,* vol. 39, no. 3, pp. 381-397, 1992.

67. M. Ruzzene, "Frequency–wavenumber domain filtering for improved damage visualization", *Smart Materials & Structures,* vol. 16, no. 6, pp. 2116-2129, 2007.

68. T. E. Michaels, J. E. Michaels and M. Ruzzene, "Frequency-wavenumber domain analysis of guided wavefields", *Ultrasonics,* vol. 51, no. 4, pp. 452-466, 2011.

69. G. R. Liu and J. D. Achenbach, "A Strip Element Method for Stress-Analysis of Anisotropic Linearly Elastic Solids", *Journal of Applied Mechanics-Transactions of the ASME,* vol. 61, no. 2, pp. 270-277, 1994.

70. M. J. S. Lowe, Disperse, 2008.

71. Y.-C. Lee and S.-P. Ko, "Measuring dispersion curves of acoustic waves using PVDF line-focus transducers", *NDT & E International,* vol. 34, no. 3, pp. 191-197, 2001.

72. B. Spottiswoode, 2D phase unwrapping algorithms, 2008.

73. Abaqus, 2013.

74. M. C. Morrone and R. A. Owens, "Feature Detection from Local Energy", *Pattern Recognition Letters,* vol. 6, no. 5, pp. 303-313, 1987.

75. M. C. Morrone, J. Ross, D. C. Burr and R. Owens, "Mach bands are phase dependent", *Nature,* vol. 324, no. 6094, pp. 250-253, 1986.

76. A. V. Oppenheim and J. S. Lim, "The importance of phase in signals", *Proceedings of the IEEE,* vol. 69, no. 5, pp. 529-541, 1981.

77. M. C. Morrone and D. C. Burr, "Feature Detection in Human Vision: A Phase-Dependent Energy Model", *Proceedings of the Royal Society of London B: Biological Sciences,* vol. 235, no. 1280, pp. 221-245, 1988.

78. S. Venkatesh and R. Owens, "An energy feature detection scheme," International Conference on Image Processing, 1989.

79. S. Venkatesh and R. Owens, "On the classification of image features", *Pattern Recognition Letters,* vol. 11, no. 5, pp. 339-349, 1990.

80. D. Gabor, "Theory of communication. Part 1: The analysis of information", *Electrical Engineers - Part III: Radio and Communication Engineering, Journal of the Institution of,* vol. 93, no. 26, pp. 429-441, 1946.

81. J. Allen, "Short-term spectral analysis, and modification by discrete Fourier transform", *IEEE Transactions on Acoustics Speech and Signal Processing,* vol. 25, no. 3, pp. 235-238, 1977.

82. T. F. Quatieri, *Discrete-time speech signal processing principles and practice*, Upper Saddle River, N.J.

Upper Saddle River, NJ: Upper Saddle River, N.J. : Prentice Hall, 2002.

83. R. N. Bracewell, *The Fourier transform and its applications*, 2nd ed., rev.. ed. New York: New York : McGraw-Hill, 1986.

84. I. Daubechies, *Ten lectures on wavelets*, Philadelphia, Pa.: Society for Industrial and Applied Mathematics 1992.

85. P. D. Kovesi, "Phase congruency: A low-level image invariant", *Psychological Research-Psychologische Forschung,* vol. 64, no. 2, pp. 136-148, 2000.

86. A. Haar, "On the Theory of Orthogonal Function Systems", *Mathematische Annalen,* vol. 69, no. 3, pp. 331-371, 1910.

87. A. Teolis, *Computational signal processing with wavelets*, Birkhäuser: Boston, 1998.

88. D. Marr and E. Hildreth, "Theory of edge detection", *Proceedings of the Royal Society of London B: Biological Sciences,* vol. 207, no. 1167, pp. 187-217, 1980.

89. Photron FASTCAM Viewer (PVF), 2006.

90. M. Schaeffer, Static and Dynamic Properties of Reconfigurable Magneto-elastic Metastructures, PhD, Mechanical Engineering Georgia Institute of Technology, Atlanta, 2016.